Detection and Visualization of Moving Targets in Medical Ultrasound Imaging

Steinar Bjærum

Norwegian University of Science and Technology

February, 2001

Detection and Visualization of Moving Targets in Medical Ultrasound Imaging
Steinar Bjærum

NTNU Trondheim
Norges teknisk-naturvitenskapelige universitet
Doktor ingeniøravhandling 2001:2
Institutt for datateknikk og informasjonsvitenskap
IDI-rapport 2001:1

ISSN 0802-6394

ISBN 82-7984-163-6

Abstract

This thesis, containing an introduction and ten separate papers, is a contribution to the field of medical ultrasound imaging. Specifically, the thesis contains theoretical development and experimental evaluation of algorithms that improve the detection and visualization of moving targets in medical ultrasound imaging.

When a wave is reflected from a moving scatterer, the frequency of the reflected signal is changed compared to the frequency of the incident signal. By utilizing this Doppler effect, ultrasound can be used to measure the velocity of moving scatterers inside the human body. The scattered echoes from the red blood cells are used to measure blood flow velocities, and the signal from scatterers in the heart muscle are used to measure the velocities of contractions and relaxations of the heart muscle.

The signal scattered from blood is corrupted by signals scattered from stationary and slowly moving tissue such as vessel walls. Such clutter signals are typically 40-100dB stronger than the signal from blood. Without sufficient clutter suppression, the detection of low velocity blood flow will be poor, and the velocity estimates will have a large bias. The signal scattered by the rapidly moving blood cells has a larger Doppler shift than the signal reflected from slowly moving tissue. A high-pass filter can therefore be used to separate the signals from blood and the clutter signals. In Papers A-E the goal is to improve this clutter filtering. A broad range of clutter filters are analyzed, and we use statistical theory to evaluate the blood detection performance of different filters. We also propose new algorithms to improve the clutter rejection. These algorithms are described theoretically, and tested on experimental data. These papers provide a theoretical foundation, as well as practical algorithms that have the potential to improve the image quality in color flow imaging.

In Paper F we present and analyze an acquisition technique that improves the temporal resolution in color flow imaging by using a combination of beam interleaving and transmission of pulses with double repetition frequency. A typical example gives a 70% increase in frame rate when the blood flow through the heart valves is imaged with the probe in the apical position. This acquisition technique is used in the clinical study presented in Paper G. In patients with atrial fibrillation, there are significant variations in the duration of the heart beats. Because of this variation, it is impossible to reconstruct flow patterns based on data from several heart beats. To get a correct "snap-shot" of the cross-sectional velocity profile in the left ventricular outlet tract in patients with atrial fibrillation, around 100frames/second are necessary. The study showed no significant difference between two heartbeats of different lengths, and velocity time integrals from heartbeats of different lengths can also be averaged in patients with atrial fibrillation.

The blood motion imaging (BMI) technique presented in Paper H provides a more intuitive display of blood flow than that provided by conventional color flow imaging. As opposed to conventional color flow imaging, BMI preserves and enhances the speckle pattern. The speckle pattern can be visually tracked from frame to frame, giving the user a correct perception of the blood flow direction and magnitude. BMI is also useful

to separate true blood flow from wall motion artifacts. The technique has been tested by post-processing of recorded ultrasound data. The best results are obtained when imaging the blood flow in peripheral vessels. The lateral velocity component is then clearly visualized, and we get an impression of the parabolic velocity profile across the vessel. BMI processing can be applied both to continuously acquired data which are uniformly sampled in time, and to data acquired using conventional color flow "packet" acquisition. Continuous acquisition results in a very high temporal resolution, but the width of the image sector is limited.

The continuous acquisition technique developed for BMI is also applied to tissue Doppler imaging (TDI) and strain rate imaging (SRI). The temporal resolution is improved by calculating the Doppler-based images from the same pulse transmissions as the tissue B-mode images. In Paper I we show that when imaging a heart wall, i.e. the interventricular septum, frame rates above 300frames/second are possible with a lateral resolution equal to a conventional B-mode image. Tissue velocity estimates calculated from these data suffer from a lot of aliasing, but a robust technique is presented that corrects the aliased velocities. A significant advantage is the continuous stream of data with constant sampling intervals. Doppler spectra and sound signals can thus be calculated at arbitrary points in the 2D image. This acquisition technique is used in the clinical study presented in Paper J, where the spatial-temporal events in the interventricular septum are studied with a temporal and spatial resolution not previously available in tissue Doppler techniques.

Preface

This thesis is submitted to the Norwegian University of Science and Technology (NTNU) in partial fulfillment of the requirements of the degree "Doktor Ingeniør". The work was carried out at the Department of Physiology and Biomedical Engineering (IFBT), NTNU in the period 1996-2000. Formally, I was affiliated to the Department of Computer and Information Science (IDI), NTNU. My supervisors have been Professor Hans Torp, IFBT, and Professor Bjørn Olstad, IDI. In the period 1996-1998 the work was supported by the Research Council of Norway, and in the period 1999-2000 in collaboration between the Research Council of Norway and GE Vingmed Ultrasound AS.

Acknowledgments

This work had not been possible without help from other people. First of all I wish to thank Hans Torp. His ideas, knowledge and support have been invaluable for me during the work of this thesis. Working together with Hans and watching his technical skills has been a pleasure. I am very grateful to Bjørn Olstad for his friendly advice, support and constructive feedback. I also wish to thank Bjørn Angelsen for introducing me to the field of medical ultrasound and for encouraging me to start a doctoral study, and Kjell Kristoffersen for important encouragements and for valuable discussions.

Sincere thanks go to all my colleagues at IFBT. The friendly atmosphere at the department has been very important to me. In particular, I would like to thank my fellow (post-)doctoral students Sevald Berg, Andreas Heimdal, Sigve Hovda, Tonni Franke Johansen, Johan Kirkhorn, Stein Inge Rabben, Vidar Sørhus, and Gunnar Taraldsen for fruitful discussions and a lot of fun.

Working with the medical community was very inspiring. Many thanks to Bjørn Olav Haugen, Stein Samstad, Stig Slørdahl and Asbjørn Støylen for sharing their medical expertise with an electronics engineer.

Nancy Lea Eik-Nes revised the text of the thesis. Many thanks.

The financial support from the Research Council of Norway and GE Vingmed Ultrasound is greatly appreciated.

Finally, I wish to thank Marit for her invaluable patience and encouragements during the five years of this study. Our son Øyvind has been my greatest inspiration during the last months of the work.

Horten, February 2001

Steinar Bjærum

Contents

Paper C – **Blood Detection Performance in Moving Tissue**
In *Proceedings of the 1998 IEEE Ultrasonics Symposium,* vol. 2, pp. 1571-1574, Oct. 1998.
Steinar Bjærum and Hans Torp

Paper D – **Statistical evaluation of clutter filters in color flow imaging**
Ultrasonics, 38:376–380, Mar. 2000
Steinar Bjærum and Hans Torp

Paper E – **Automatic Selection of the Clutter Filter Cut-off Frequency in Ultrasound Color Flow Imaging**
Steinar Bjærum, Hans Torp, Torbjørn Bakke and Kjell Kristoffersen

Paper F – **High Frame Rate Color Flow Imaging**
Steinar Bjærum, Hans Torp, Kjell Kristoffersen and Dagfinn Sætre

Paper G – **A New Method Describing Cross-Sectional Blood Flow Velocity Profiles in the Left Ventricular Outflow Tract of Patients with Atrial Fibrillation with the Use of High Frame-Rate 2-Dimensional Color Flow Imaging**
Journal of the American Society of Echocardiography, 14(1):50–56, Jan. 2001
Bjørn Olav Haugen, Steinar Bjærum, Stein Olav Samstad, Terje Skjærpe and Hans Torp

Paper H – **Blood Motion Imaging: A New Blood Flow Imaging Technique**
Based on the U.S. patent applications *Method and Apparatus for Visualization of Motion in Ultrasound Flow Imaging Using Packet Data Acquisition,* Serial No. 09/449,391, and *Method and Apparatus for Visualization of Motion in Ultrasound Flow Imaging Using Continuous Data Acquisition,* Serial No. 09/449,389, both filed Nov. 26, 1999.
Steinar Bjærum and Hans Torp

Paper I – **High Frame Rate Tissue Doppler and Strain Rate Imaging**
Steinar Bjærum, Andreas Heimdal, Hans Torp, Brage H. Amundsen, Stig A. Slørdahl and Bjørn Olstad

Paper J – **High Frame Rate Strain Rate Imaging of the Ventricular Septum in Healthy Subjects**
Submitted for publication, 2000
Stig A. Slørdahl, Steinar Bjærum, Brage H. Amundsen, Asbjørn Støylen, Andreas Heimdal, Stein Inge Rabben and Hans Torp

Introduction

This thesis is divided into two parts. The first part contains an introduction with five sections. A brief introduction to ultrasound imaging and Doppler measurements is given in sections one and two. Section three discusses factors affecting the quality of ultrasound color flow imaging. Based on the discussion in section three, section four summarizes the contribution of the papers in part two of the thesis. The introduction ends with concluding remarks and directions for future studies. The second part of the thesis consists of ten separate papers. The papers are self-contained and complete with abstracts and references.

The journal papers, conference articles, and conference abstracts produced during this work are listed in the References [12, 14–21, 37, 60, 61, 67, 68, 73].

1 Ultrasound Imaging

The first use of ultrasound in medical applications were reported in the early 1950s [27, 41, 82]. The basic principles of an ultrasound imaging system are as follows: A voltage signal consisting of a few oscillations with frequency in the MHz range is applied to a piezo-electric transducer which converts the applied voltage to a vibration of the transducer surface. When this vibrating surface is put in contact with the body, an ultrasonic pulse is transmitted into the tissue. The pulse propagates through the tissue and is partly reflected and scattered by changes in density and compressibility of the tissue. When the back-scattered sound wave impinges on the transducer, the vibrations are converted back to an electric signal which is processed and displayed.

A sound wave that is reflected by a tissue structure at depth r, travels a total distance $2r$ before it reaches back to the transducer. With sound propagation velocity c, the depth r is related to the time after pulse transmission t by

$$t = \frac{2r}{c} \tag{1}$$

The sound wave is attenuated when it propagates through the tissue, and the attenuation increases with propagation distance. To compensate for this attenuation, the signal is amplified with a gain that increases with time. This amplifier is termed a time gain compensation (TGC) amplifier. The envelope of the signal is found, and the amplitude undergoes a logarithmic compression in order to display the large dynamic range of the ultrasound signal. The received signal can be displayed in several ways.

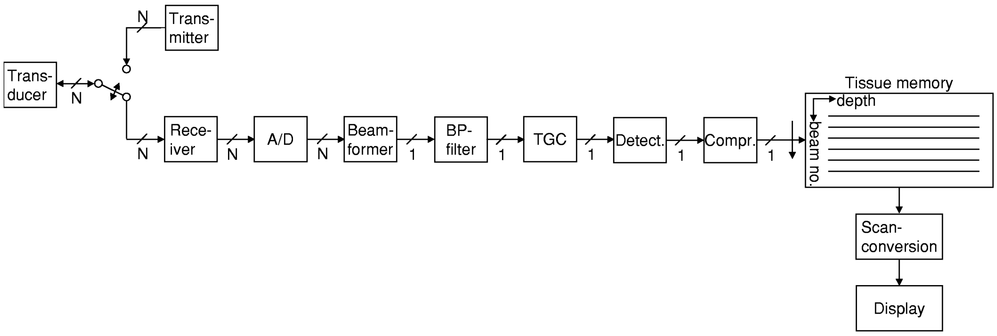

Figure 1: A digital ultrasound imaging system using an electronically steered and focused transducer array with N elements.

The first systems showed the received signal as a trace on an oscilloscope. This technique is called Amplitude-mode or A-mode. A better perception of motion was obtained by converting the amplitude to gray-scale values, and displaying the signal from consecutive pulse transmissions side by side on a computer screen. This technique is called Motion-mode or M-mode, since the motion of the tissue structure along the beam direction is easily perceived.

Brightness-mode or B-mode systems provide two-dimensional images of tissue structures. The main building blocks of a B-mode system are shown in Figure 1. A number of A-mode lines are collected by sweeping the ultrasound beam over the region of interest. The sweeping is done either mechanically or with a multi-element transducer. Figure 1 illustrates a system using a transducer with N elements. The transmitter imposes different delays of the voltage pulse applied to each individual transducer element in order to focus and steer the ultrasound beam in the desired direction. On receive, the beam former similarly delays the received signal from each element before the signals are summed. Advanced systems use beam formers capable of dynamically changing the focus as the pulse propagates deeper into the body. The band-pass filter in Figure 1 is tuned to the bandwidth of the pulse in order to improve the signal-to-noise ratio. Recently it was discovered that the image quality is improved by using the frequency band around the double of the transmitted ultrasound frequency [24, 69]. Second harmonic frequency components are generated by non-linear wave propagation, and the second harmonic generation increases with wave amplitude and propagation distance. The most severe reverberation noise is generated while the pulse propagates through the body wall. The propagation distance from the probe to the reverberating layers in the body wall is, however, so small that the second harmonic signal level is low, and the reverberation noise is lower than when the fundamental frequency band is used. The second harmonic image also has better lateral resolution since the sidelobe power level is not high enough to generate second harmonic frequency components. Such second harmonic imaging is achieved by doubling the center frequency of the band-pass filter in Figure 1.

When a complete scan is performed, the scan converter maps the data to a rect-

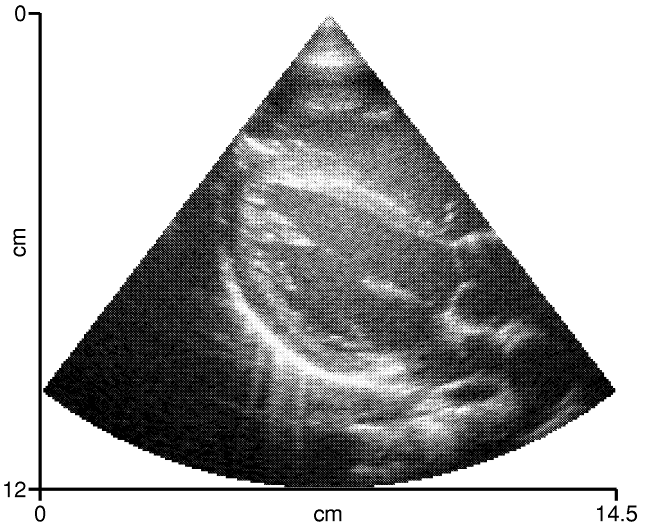

Figure 2: Ultrasound B-mode image of a young boy's heart.

angular display grid, and the data are displayed as a gray-scale image. In cardiac applications, typically 50frames/seconds are obtained. A B-mode image of a young boy's heart is shown in Figure 2.

2 Ultrasound Doppler Measurements

When a wave is reflected from a moving scatterer, the frequency of the reflected signal is changed compared to the frequency of the incident signal. By utilizing this Doppler effect, ultrasound can be used to measure the velocity of moving scatterers inside the human body. The scattered echoes from the red blood cells are used to measure blood flow velocities, and the signals from scatterers in the heart muscle are used to measure the velocities of contractions and relaxations of the heart muscle. In this section we develop mathematical expressions for the Doppler shift, then discuss systems for ultrasound Doppler measurements.

2.1 The Doppler Effect

An ultrasonic signal is transmitted at time $t = 0$. The received signal from a stationary point scatterer at depth r_0 in the far field of the transducer can be written as

$$y_{r_0}(t) = x\left(t - \frac{2r_0}{c}\right) \tag{2}$$

where c is the speed of sound, and $2r_0/c$ is the time needed for the ultrasound pulse to travel back and forth to the depth r_0. To simplify the development, we assume that

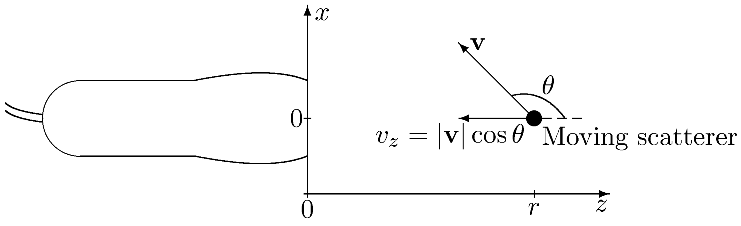

Figure 3: A scatterer moving towards the probe.

the shape of the received signal x does not vary for small displacements of the point scatterer around r_0. A scatterer moving with a velocity $\mathbf{v}$ is illustrated in Figure 3. The signal that is received at time t was reflected from the scatterer at depth

$$r = r_0 + v_z \left(t - \frac{r}{c}\right) \tag{3}$$

where r_0 is the depth when the pulse was transmitted at $t = 0$, v_z is the component of the velocity along the ultrasound beam, and $t - r/c$ is the time of interaction between the scatterer and the ultrasound pulse. Reorganizing Equation 3, the depth r can be written

$$r = \frac{r_0 + v_z t}{1 + v_z/c} \tag{4}$$

Inserting this expression for r in Equation 2 gives

$$y(t) = x\left(\frac{c - v_z}{c + v_z}\left(t - \frac{2r_0}{c - v_z}\right)\right) \tag{5}$$

where we see that the received signal is a delayed and compressed version of the signal that is received from a stationary scatterer. When a sinusoidal signal with frequency f_0 is transmitted, the received signal from a stationary scatterer is given by

$$y_{r_0}(t) = \cos\left(2\pi f_0\left(t - \frac{2r_0}{c}\right)\right) \tag{6}$$

For a moving scatterer, the received signal becomes

$$y(t) = \cos\left(2\pi f_0 \frac{c - v_z}{c + v_z}\left(t - \frac{2r_0}{c - v_z}\right)\right) \tag{7}$$

The change in frequency of the received signal compared to the transmitted signal is

$$f_d = f_0 \frac{c - v_z}{c + v_z} - f_0 = -\frac{2v_z}{c + v_z} f_0 \approx -\frac{2v_z}{c} f_0 \tag{8}$$

and is termed the Doppler shift. The velocity of the scatterer is related to the Doppler shift by the Doppler equation

$$v_z = -\frac{c}{2f_0 + f_d} f_d \approx -\frac{c}{2f_0} f_d \tag{9}$$

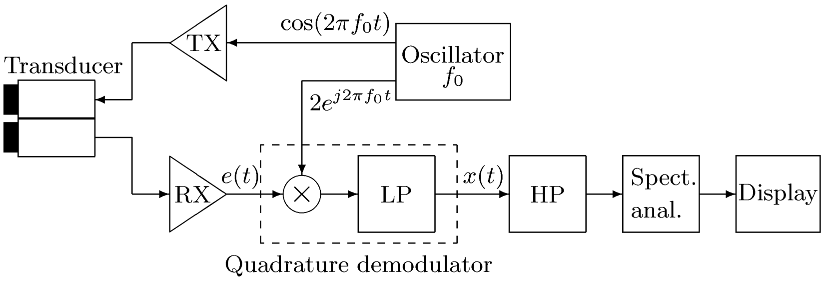

Figure 4: Continuous wave Doppler system.

and can be calculated from estimates of the Doppler shift. In the following sections, several methods that use the Doppler shift to measure blood velocities are discussed. A thorough treatment of Doppler ultrasound can be found in [9, 28, 42].

2.2 Continuous Wave Doppler

The first use of continuous wave (CW) Doppler for the measurement of blood velocities was reported in [63]. Figure 4 shows a block diagram of a simple CW Doppler instrument. Separate transducers are used for transmit and receive, but they are usually mounted in the same housing. The instrument is sensitive to red blood cells travelling in the interception of the transmit and receive beams. This region is called the sample volume. Each blood cell thus produces a signal as in Equation 7, but of finite time duration and thus non-zero bandwidth. This phenomenon is called the transit-time effect. At any time instant, the received signal is a sum of the contributions from a large number of blood cells within the sample volume, and is therefore modelled as a Gaussian random process [8]. Velocity gradients within the sample volume result in different Doppler shifts from the different blood cells, and broaden the power spectrum of the received signal. If the transit time effect is neglected, and the sample volume is uniformly insonified, the power spectrum of the received signal corresponds directly to the axial component of the velocity distribution within the sample volume [8]. The constant of proportionality between velocity and the Doppler shift is given by the Doppler equation. It is therefore common to use spectral analysis to extract the velocity information from the received signal. Since the blood velocity is much smaller than the speed of sound, the Doppler shift is much smaller than the transmitted ultrasound frequency. The received signal $e(t)$ in Figure 4 is thus a band-pass signal, and it is convenient to perform the signal analysis after demodulating the signal to base-band. The band-pass signal $e(t)$ can be written as [38]

$$e(t) = Re\left\{x(t)e^{j2\pi f_0 t}\right\} = \frac{1}{2}\left(x(t)e^{j2\pi f_0 t} + x^*(t)e^{-j2\pi f_0 t}\right) \tag{10}$$

where $*$ denotes complex conjugation and $x(t)$ is the complex envelope of the received signal. Multiplication with $2e^{-j2\pi f_0 t}$ in Figure 4 gives $x(t) + x^*(t)e^{-j2\pi 2 f_0 t}$, and the term centered around $-2f_0$ is removed by the low-pass filter (LP). The transmitted

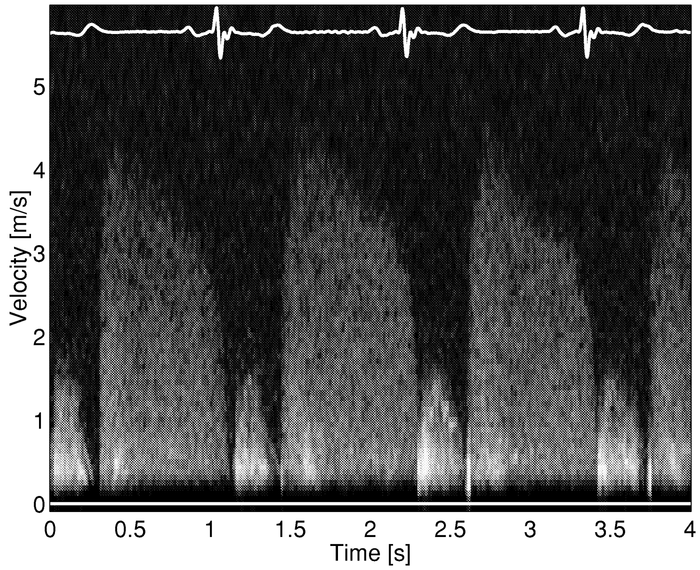

Figure 5: CW Doppler spectrum from a patient with aortic valve leakage.

frequency f_0 is known, and all the information is contained in the complex envelope $x(t)$ which is termed the Doppler signal.

The Doppler signal from blood is obscured by high-intensity echoes from tissue and vessel walls. These clutter signals can be 80-100dB stronger than the signal from blood. However, tissue structures move more slowly than blood, and the clutter signals can therefore be removed by the high-pass filter (HP) in Figure 4. This filter is a critical part of the system, since the clutter signal from tissue should be removed without also removing the signal from slowly moving blood.

The Doppler shift is in the audible range for the ultrasound frequencies commonly used, and by listening to $Re\{x(t)\}$ or $Im\{x(t)\}$ the operator can detect the presence of a Doppler signal and qualitatively evaluate the center frequency and bandwidth of the signal. Directional information can be obtained by separating positive and negative Doppler shifts, and feeding the resulting signals to the left and right channel in a stereo system. For visual display and quantitative measurements, frequency spectra from subsequent time windows are stacked side by side and displayed as shown in Figure 5. The Doppler spectrum in Figure 5 is from a patient with aortic valve leakage with reverse flow velocities up to 4m/s.

2.3 Pulsed Wave Doppler

A CW Doppler instrument is sensitive to flow throughout the region where the transmit and receive beams overlap, and therefore provides no range resolution. Pulsed wave (PW) Doppler instruments solve this problem and were first reported by Baker and

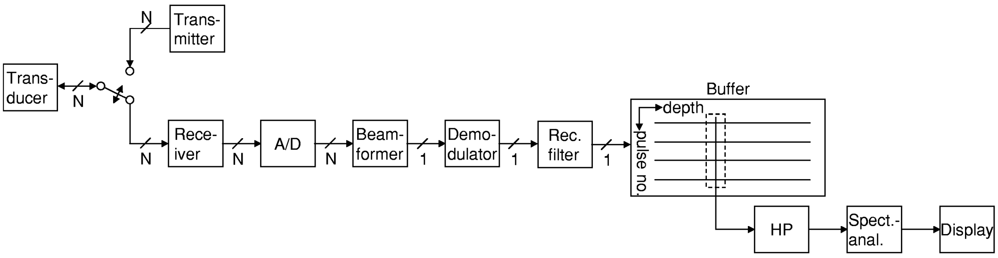

Figure 6: A digital pulsed wave Doppler system with N transducer elements.

Watkins [11]. The velocity can not be estimated from the Doppler shift of a single pulse since the frequency spectrum of the signal is changed considerably more by the frequency dependent attenuation than it is by the Doppler shift. The blood velocity is therefore estimated from the change in phase and/or delay of the signals received from several pulse transmissions. A pulsed wave Doppler system is schematically illustrated in Figure 6. The same transducer is used for both transmission and reception. When a sinusoidal soundburst with center frequency f_0 is transmitted, the received signal from a stationary point scatterer at depth r_0 is given by

$$x(t) = a(t)\cos\left(2\pi f_0\left(t - \frac{2r_0}{c}\right)\right) \tag{11}$$

where $a(t)$ is the pulse envelope. By using Equation 5, the received signal from a moving scatterer following the transmission of such a pulse is given by

$$x(t) = a\left(\frac{c-v_z}{c+v_z}\left(t - \frac{2r_0}{c-v_z}\right)\right)\cos\left(2\pi f_0\frac{c-v_z}{c+v_z}\left(t-\frac{2r_0}{c-v_z}\right)\right) \tag{12}$$

where r_0 is the position of the scatterer when the pulse is transmitted at $t = 0$. Pulses are transmitted with time interval T_s, and between two pulse transmissions the scatterer has moved a distance v_zT_s. The received signal from pulse n is thus given by

$$\begin{aligned}&x(t,n) = \\ &a\left(\frac{c-v_z}{c+v_z}\left(t - \frac{2(r_0+v_z(n-1)T_s)}{c-v_z}\right)\right)\cos\left(2\pi f_0\frac{c-v_z}{c+v_z}\left(t-\frac{2(r_0+v_z(n-1)T_s)}{c-v_z}\right)\right)\end{aligned} \tag{13}$$

If the signal is sampled at the time corresponding to the depth r_s we get

$$\begin{aligned}x(2r_s/c,n) &= a\left(-\frac{2v_z}{c+v_z}nT_s+\alpha\right)\cos\left(2\pi f_0\left(-\frac{2v_z}{c+v_z}nT_s+\alpha\right)\right)\\ &= a\left(-\frac{2v_z}{c+v_z}nT_s+\alpha\right)\cos\left(2\pi\frac{f_d}{f_s}n+\phi\right)\end{aligned} \tag{14}$$

where $\alpha = \frac{c-v_z}{c+v_z}\left(\frac{2r_s}{c} + \frac{2(v_z T_s - r_0)}{c-v_z}\right)$, $\phi = 2\pi f_0 \alpha$, and $f_d = -\frac{2v_z}{c+v_z} f_0$ is recognized as the Doppler shift. The frequency f_s equals $1/T_s$ and is termed the pulse repetition frequency (PRF). To avoid aliasing, the Nyquist theorem tells us that the maximum Doppler shift is limited by

$$|f_{d,\max}| < \frac{1}{2} f_s \tag{15}$$

The corresponding limit on the velocity is given by

$$|v_{z,\max}| = \frac{c}{2f_0}|f_{d,\max}| < \frac{c}{4f_0} f_s \tag{16}$$

and is termed the Nyquist velocity. To avoid spurious sample volumes between the transducer and the depth r_s, the PRF is limited by

$$f_s \leq \frac{c}{2r_s} \tag{17}$$

and the unambiguous range-velocity product is limited by

$$r_s v_z \leq \frac{c^2}{8f_0} \tag{18}$$

Increasing the PRF above the limit in Equation 17 creates an extra sample volume closer to the transducer, giving ambiguity in range of where the velocity is measured. It is often possible, however, to position the transducer so that there is little or no blood flow in the extra sample volume, and the high PRF (HPRF) technique can be used to measure high blood velocities [36].

With pulse-length T_p, a sample of the received signal at a time T_d after pulse transmission originates from a localized sample volume extending from $cT_d/2$ to $c(T_d - T_p)/2$. The receiver filter in Figure 6 increases the radial length of the sample volume. The purpose of the receiver filter in Figure 6 is to maximize the signal-to-noise ratio (SNR), but it also increases the radial length of the sample volume. It has been shown that a receiver filter with a rectangular impulse response with duration equal to the pulse length is close to maximizing the SNR [47]. Several techniques have been proposed to avoid aliasing of high velocities in PW Doppler [74, 84]. Common to these techniques are wideband pulses and the use of samples from several depth ranges to estimate the velocity.

The PW spectrum in Figure 7 shows normal blood velocities through the mitral valve. Compared to Figure 5, the spectrum is narrower since the velocity is measured at a localized position resulting in a smaller velocity spread.

2.4 Color Flow Imaging

Real-time color flow imaging was first reported by Namekawa et al. [52] and Kasai et al. [45]. A PW Doppler system can be extended to estimate the velocities at several depths along the ultrasound beam. This technique is called multigated Doppler [58]. A further extension is to scan the beam over a two-dimensional region, and measure the velocity at several depths along each beam direction.

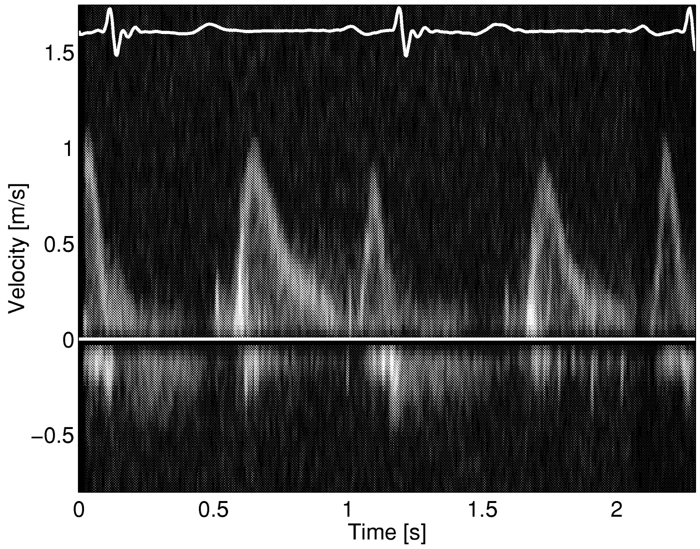

Figure 7: PW Doppler spectrum.

Several parameters describing the blood flow are calculated for each sample volume, and encoded in a color. The resulting color image is combined with a tissue B-mode image, and a two-dimensional map of the blood flow is obtained. A color flow imaging system is schematically illustrated in Figure 8. The flow parameters that are calculated are commonly the mean velocity, signal power, and bandwidth. Velocities towards the transducer are usually encoded in different shades of red depending on the magnitude of the velocity. Velocities away from the probe are usually encoded in different shades of blue. The signal power determines the intensity of the color. The mapping of bandwidth is motivated by the fact that in regions with disturbed flow, there are large velocity gradients in the sample volume and correspondingly, a large bandwidth of the Doppler spectrum. Sample volumes where a large bandwidth is measured are assigned a green color. In addition to determine the color, the parameters are used in the tissue/flow arbitration block in Figure 8b which for each pixel determines whether a B-mode or color value should be shown. An example of a color flow image is shown in Figure 9, where the reverse flow jet through a leaky aortic valve is visualized with red and green.

To get adequate frame rates, typically only 8-16 pulses are transmitted in each beam direction. With so few samples available, the suppression of clutter signals from stationary and slowly moving tissue is a difficult task, but crucial for the image quality.

Parameter estimation techniques can be divided into narrowband and wideband techniques [29]. Narrowband techniques use relatively long pulses, and estimate the velocity based on samples from one range gate. Examples of narrowband techniques are the “autocorrelation” technique [45], Fourier-based techniques, and techniques based on autoregressive (AR) modelling [1]. Wideband techniques use a train of short pulses

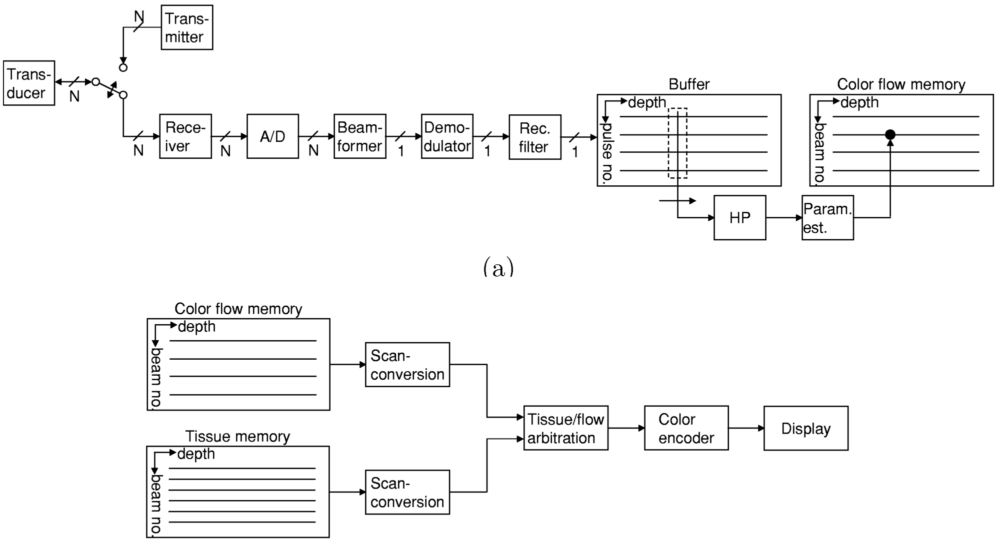

(a)

(b)

Figure 8: (a) Acquisition and processing of data for one beam direction in a color flow image. (b) Combination of tissue and color flow data to display one image frame.

to track a group of red blood cells using the intensity of their echoes. This tracking is achieved by using samples from several range gates. Examples of wideband techniques are the crosscorrelation technique [23], the sum-absolute-difference technique [22], and the wideband maximum likelihood estimator [30].

2.5 Tissue Doppler Imaging

PW Doppler can be used to measure the velocity of contraction and expansion at discrete sample volumes in the heart muscle. To ease the assessment of regional myocardial function, the two-dimensional color flow imaging technique was adapted to measure tissue velocities [51]. An example of a tissue Doppler image of the left ventricle is shown Figure 10. Additional information can be obtained by imaging the rate of deformation of the myocardium which is termed strain rate imaging (SRI) in [39]. SRI is a “local” measure of the elongation/contraction of the myocardium, and may ease the differentiation of active elongation/contraction from passive motion induced by elongation/contraction in other parts of the myocardium [39].

2.6 Clinical Applications of Doppler Ultrasound

Ultrasound Doppler instruments have proven to be of clinical importance for non-invasive assessment of blood flow. Color flow imaging is used qualitatively to get an overview of the flow and to ease the detection of abnormal flow patterns. Spectral

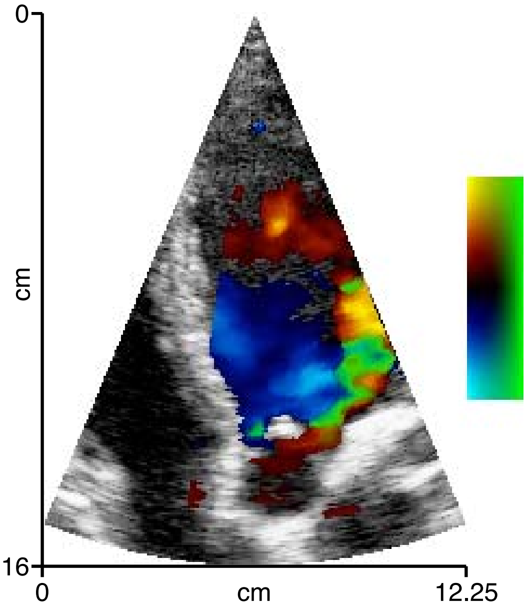

Figure 9: Color flow image of a leaking aortic valve.

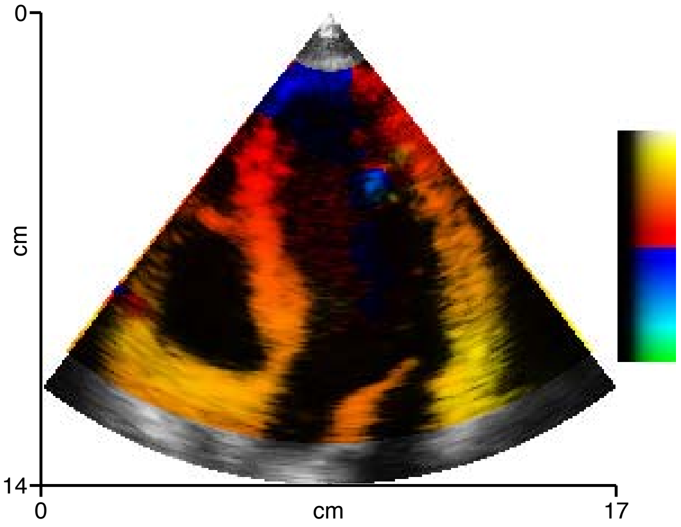

Figure 10: Tissue Doppler image of the left ventricle.

Doppler techniques are then commonly used to quantitatively evaluate the severity of valvular stenoses, leakages, etc. Some important clinical applications of Doppler ultrasound are listed below.

- Cardiology. Detection and assessment of valvular stenoses, regurgitations, shunts, and similar defects that give disturbed flow patterns in the heart.
- Peripheral vascular disease. Detection and assessment of stenoses and aneurysms.
- Radiology. Assessment of malignancy of tumors based on the blood flow.
- Fetal medicine. Early detection of abnormal flow patterns related to high blood pressure in the fetus.

3 Factors Affecting the Quality of Color Flow Imaging

The most basic task of a color flow system is to detect if blood is present or not in a given sample volume. The next task is to calculate unbiased estimates with low variance of the blood velocity and the signal bandwidth. This thesis deals mainly with color flow systems, and in this section we discuss factors that affect the ability of the system to fulfill these goals.

3.1 Noise

There are mainly two forms of noise that corrupt the Doppler signal from blood. Thermal noise in the transducer and front-end electronics limit the lowest Doppler signal strength that can be detected. Thermal noise is modeled as a white Gaussian random process, which means that two different noise samples are statistically independent with a Gaussian probability density function [70]. The second type of noise is the signal from stationary and slowly moving tissue structures, including reverberations caused by multiple reflections. This clutter signal can be 80-100dB stronger than the Doppler signal. The tissue moves more slowly than the blood, thus giving a smaller Doppler shift, and the clutter signal can be removed with a high-pass filter.

Thermal Noise

The received signal is passed through a filter to minimize the noise bandwidth in order to maximize the sensitivity of the instrument. A matched filter maximizes the peak SNR for a known signal in white noise [46]. In ultrasound imaging, the shape of the received signal is, however, not known, and conventional matched filtering is not applicable. Even though the shape of the received signal is unknown, it is shown in [47] that a receiver filter with a rectangular impulse response with duration equal to the pulse length is close to maximizing the signal-to-noise (thermal noise) ratio (SNR).

The SNR can be improved by transmission of pulses with higher power. There are, however, safety limitations on the acoustic intensity [6]. In Doppler applications, the limiting factor is usually the spatial peak of the time averaged intensity, I_{SPTA}. When the PRF is kept constant, I_{SPTA} is proportional to the energy in the transmitted pulse. As long as the sample volume is smaller than the blood vessel, the received signal power is proportional to the pulse energy which is bounded by I_{SPTA}, but the SNR can be increased by decreasing the noise bandwidth. The SNR is therefore improved by decreasing the bandwidth of the pulse; this is equivalent to increasing the pulse length. The improvement in SNR stops when the pulse length is increased to a point where the sample volume becomes larger than the blood vessel. However, for large blood vessels there is a trade-off between sensitivity and radial resolution.

In an acquisition technique called coded excitation, long pulses with high bandwidth are transmitted, but the spatial resolution is retained by deconvolution of the received signal [35]. Since Doppler techniques are limited by the pulse energy, coded excitation will not improve the SNR, but may improve the spatial resolution.

The sensitivity can be improved by injecting ultrasound contrast agents into the blood [55, 65]. This increases the back-scattered power, and thus improves the SNR, but does not reduce the noise power.

Clutter Noise

It is difficult to detect if blood is present in regions with a large clutter-to-signal ratio (CSR), especially when the blood moves with a velocity comparable to the tissue velocity. In this situation, there is a small difference in the Doppler shift from blood and tissue, and the signals are not easily separated with a high-pass filter. Typically only 6-16 pulses, referred to as the packet size, are transmitted in each beam direction when the flow data are acquired. This means that clutter filtering and velocity estimation is performed on only 6-16 samples.

Commonly used filter types for clutter filtering include finite impulse response (FIR) filters [56], infinite impulse response (IIR) filters [56], and polynomial regression filters [40, 44, 72]. Due to the small number of samples, it is important that IIR filters are properly initialized. Such initialization techniques are developed in [26, 32], and applied to color flow imaging in [57, 66].

Tissue motion may lead to “flashing” artifacts in the image. In the periods of the heart cycle with largest tissue motion, the signal from tissue passes through the clutter filter and obscures the display of the blood flow. There are three main sources of tissue motion: The beating of the heart results in large movement of the heart muscle and pulsating vessel walls. Respiration causes movement of the organs both in the chest and abdomen. Finally, the operator may move the probe in search for small blood vessels resulting in movement of the tissue relative to the probe. To improve the clutter rejection when the tissue is moving, it has been suggested that the mean tissue Doppler shift frequency be estimated, and the signal mixed down with this frequency prior to conventional high-pass filtering [71].

Contrast agents increase the strength of the signal from blood, thus reducing the demands of the clutter filter. One of the main applications of contrast imaging is thus to improve the clutter-to-signal ratio to be able to measure blood perfusion [64].

3.2 Bias of Velocity Estimates

There are many algorithms for velocity estimation in color flow imaging, and many of these are discussed by Jensen [42] and Ferrara and DeAngelis [29]. Common to all these algorithms are that the combination of thermal noise, clutter noise, and the clutter filter may lead to bias in the velocity estimate. Unless sufficiently attenuated by the clutter filter, the clutter signal will produce a bias towards zero velocity. On the other hand, high-pass filtered white noise produces a bias towards larger velocities [54, 83]. An algorithm to compensate for this effect has been proposed by Rajaonah et al. [59]. For low blood velocities, the frequency spectrum of the signal may be severely distorted by the clutter filter. Attenuation of the lowest frequencies results in bias towards larger velocities. The clutter filter itself might also introduce bias regardless of the blood velocity and the presence of noise [72, 77].

Direction of arrival processing is a well developed field in array processing used in passive radar and sonar. The similarity between direction of arrival estimation and color flow imaging has been noted in [4, 5], where high resolution estimates are adapted to color flow imaging. It has been proposed that these algorithms be used to estimate several velocity components within the sample volume, and for combined velocity estimation and clutter rejection. However, no clinical results are available with this technique.

3.3 Variance of Velocity Estimates

The variance of the parameter estimates decreases when the number of observations is increased and when the SNR is increased. This means that the variance decreases with increasing packet size. Spatial averaging also reduces the variance [75]. There is thus a trade-off between estimator variance and both temporal and spatial resolution. It is also important that the clutter filter does not reduce the number of samples available to parameter estimation. Advanced algorithms that use samples from several depth ranges to reduce variance are presented by Vaitkus and Cobbold [79, 80].

3.4 Aliasing of Velocity Estimates

Velocity estimation algorithms that are based on transmitting a relatively long pulse and estimating the phase shift from pulse to pulse are referred to as narrowband algorithms [29]. Common to these techniques are that they suffer from aliasing, i.e. a positive velocity is interpreted as a negative velocity and vice versa. The relatively long pulses mean that the SNR is relatively high for these methods. Narrowband velocity estimation can be performed both in the time domain [48] and in the frequency domain [78, 81]. The commonly used "autocorrelation" algorithm [45] is an example of a narrowband algorithm. This mean velocity estimator is equivalent to a first order autoregressive estimate of the mean frequency. A second order autoregressive model for the signal from blood was proposed in [50]. It has also been proposed to use one pole for the clutter signal, and one pole for the signal from blood [1]. However, since the clutter signal is much stronger than the signal from blood, the blood signal pole is shifted toward lower frequencies. Better results were obtained when AR modeling was performed subsequent to a clutter filter.

To avoid aliasing artifacts, several wideband techniques have been proposed [29]. Common to these techniques are that relatively short pulses are transmitted, and that samples from several depth ranges are used in the velocity estimation. Examples of such techniques are the cross-correlation technique [23, 33], speckle tracking [22], the wideband maximum likelihood estimator [30, 31], the butterfly search technique [2, 3], and the extended autocorrelation method [49]. Since short pulses are used, the SNR are poorer compared to the narrowband techniques. Decorrelation due to the presence of velocity gradients and lateral movement as well as the poor SNR may lead to similar effects as aliasing, e.g. the wrong peak is picked in the cross-correlation technique. The wideband techniques have larger computational complexity than the narrowband techniques, and it seems to be difficult to achieve robust non-aliased velocity estimates. The narrowband “autocorrelation” method is thus the most commonly used algorithm in commercial instruments.

3.5 Measuring Only One Velocity Component

Velocity estimation algorithms based on the Doppler shift or the time delay from pulse to pulse only measure the velocity component along the ultrasound beam. The instrument thus provides incomplete information about the flow pattern. This limitation may also lead to a non-intuitive visualization of the flow, i.e. in bent vessels, there will be an abrupt change in color at the point where the vessel is parallel to the transducer surface. Several techniques have been proposed to solve this problem: Compound scanning from two different positions gives velocity components along two different directions [34]. Measurement of the transit-time through the ultrasound beam, which is reflected in an increased bandwidth of the Doppler signal, can be used to find the lateral velocity component [53]. Two-dimensional speckle tracking methods based on frame-to-frame correlation analysis provide both the radial and lateral velocity component [76]. Coherent processing of two sub-apertures of the transducer to create lateral oscillations in the received beam pattern provide quantitative lateral velocity information, including the sign [7, 43]. A common assumption in all these techniques is a uniform velocity field over a large spatial region. None of these algorithms for estimation of two velocity components have yet been implemented on commercial scanners.

3.6 Spatial Resolution

The spatial resolution in ultrasound imaging improves with increasing ultrasound frequency. However, the attenuation also increases with the frequency, and there is therefore a trade-off between spatial resolution and penetration. The length of the transmitted pulse determines the radial resolution, and there is thus a trade-off between radial resolution and sensitivity. With a specified radial resolution there is also a trade-off how the resolution should be divided between the pulse length and spatial filtering. The lateral resolution is determined by the beam density. There is thus a trade-off between image width, lateral resolution, and temporal resolution. Less spatial averaging is required when the estimator variance is small. The spatial resolution is thus indirectly affected by the estimation algorithm, and the potential reduction of available samples after the clutter filter.

3.7 Temporal Resolution

Cardiac hemodynamics demand high temporal resolution; due to the accelerations and decelerations during the cardiac cycle, the temporal resolution in the velocity estimates should be around 10ms [36]. This means that in cardiac applications, the maximum difference in time between two velocity estimates in the same flow image should ideally be less than 10ms. Neglecting the time needed for the B-mode acquisition, this corresponds to a frame rate of 100frames/s. Such a high temporal resolution is hard to achieve in color flow imaging. To correctly measure velocity profiles across valve openings in the heart, it has been necessary to combine measurements from several heart cycles [62]. Another application where high temporal resolution is important is in volume flow measurements using three-dimensional color flow data, where the accuracy improves with increasing frame rate [13].

The total acquisition time equals the sum of the acquisition times for the B-mode image and the flow image. By increasing the width of the transmit beam, and by performing receive beam forming in parallel, several beams can be calculated from one pulse transmission. Parallel beam forming thus reduces the acquisition time for both the B-mode and flow data. The depth and number of beams in the B-mode image determine the acquisition time for this image. The lateral resolution of the B-mode image is commonly reduced to increase the frame rate in color flow imaging.

Several pulses must be transmitted in each beam direction during acquisition of the flow data. The flow acquisition time is therefore much longer than the B-mode acquisition time. To achieve a sufficient frame rate, the lateral resolution is therefore reduced in the flow image compared to the resolution in the B-mode image.

Clutter rejection is harder with a small packet size, and the estimator variance is increased since the estimate is based on fewer samples. To obtain satisfying image quality in “difficult” patients, it is therefore often necessary to increase the packet size, and thus reduce the temporal resolution.

The maximum pulse repetition frequency (PRF) is determined by the image depth. When measuring low velocities it is desirable to reduce the PRF. Without proper action, this may significantly reduce the frame rate. However, if the PRF is reduced by an integer factor k, it is possible to acquire data in $k-1$ other beam direction before returning to the same direction. With this beam interleaving technique, the PRF can be reduced without decreasing the temporal resolution.

3.8 Visualization

The velocity, power and bandwidth of the Doppler signal is combined into a color and superimposed on the B-mode image. The color-map should be designed to ease the visual detection of disturbed flow. The attention of the operator should be drawn to even small jets. To achieve this, disturbed flow may be visualized with a high contrast color, e.g. green as seen in Figure 9 [10].

Another important part of the display system is the algorithm used to decide if flow or tissue should be displayed in a given pixel. This tissue/flow arbitration is closely related to the clutter filtering. The overall impression of the image quality is degraded if false flow pixels are scattered around in a tissue region. The perceived image quality is also improved if there are smooth transitions between flow and tissue at vessel boundaries without "bleeding" into the tissue.

3.9 Tissue Doppler Imaging

Tissue Doppler imaging differs from color flow imaging in several ways. The signal from tissue is the desired signal in tissue Doppler imaging and is not suppressed with a clutter filter. However, in patients with strong stationary reverberation noise, a high-pass filter with narrow stop-band may improve the image quality. The scattered signal from tissue is much stronger than the signal from blood. The SNR in tissue Doppler imaging is therefore significantly higher than the SNR in color flow imaging. A larger pulse bandwidth and thus better spatial resolution is therefore possible in tissue Doppler imaging. To maximize the information on the spatial-temporal relations between the events in the heart muscle during the heart cycle, both high temporal and spatial resolution is desired. High temporal resolution is important to correctly capture the rapid contractions and expansions of the cardiac muscle. High spatial resolution is important when, for example, differences in the velocity across a heart wall is measured.

4 Summary of Papers

This section first gives an overview of how the results in the papers in this thesis contribute toward improving the quality of color flow imaging. After this overview, abstracts of each paper are presented.

Design and Evaluation of Clutter Filters

Papers A-E deal with different aspects of clutter filtering in color flow imaging. The most basic task of a color flow system is to detect if blood is present or not in a given sample volume, and the clutter filter is an important part of this detection.

In Paper A we review and analyze different types of filters suited for high-pass filtering of the short signal sequences that are available in color flow imaging. The study is limited to one-dimensional filters operating on the samples at a fixed depth from subsequent pulse transmissions. The analysis includes finite impulse response (FIR) filters with and without a linear phase response, infinite impulse response (IIR) filters with different types of initialization, and polynomial regression filters. We believe that Paper A is more detailed, and provides analysis of more filter types than previous papers. Paper A thus provides a good theoretical basis when designing clutter filters for color flow imaging.

Paper B presents algorithms to improve the clutter rejection when there is significant movement of the tissue. Examples of this are the moving heart muscle when the coronary arteries are being imaged, or when the operator moves the probe in search for small blood vessels. Previous methods adapt to the tissue movement by mixing down the signal with the estimated mean Doppler shift frequency from tissue[71]. This is most efficient for tissue movements with constant velocity. In Paper B we present algorithms that adapt to accelerated tissue movements, and show that the algorithms improve the clutter rejection in practical imaging situations. The best results were obtained by mixing down the signal with non-constant phase increments estimated from the signal. Subsequent to this down-mixing, the signal can be filtered with any of the high-pass filters analyzed in Paper A. This algorithm has computational complexity suited for real-time processing on an ultrasound scanner.

In Paper C, the detection of blood is formulated as a problem in statistical detection theory. This is an approach commonly used in radar theory. The optimal detector compares the power at the output of a clutter filter to a threshold. The optimal detector structure is thus similar to standard color flow systems, but with a filter that depends on both the clutter and blood signal statistics. In a practical imaging situation, the blood signal statistics are unknown. However, when designing clutter filters it is useful to compare the detection performance to the optimal detector. Such a statistical evaluation is performed in Paper D, where the blood detection performance of several commonly used clutter filters are compared.

In Paper E we present an algorithm that automatically selects the cut-off frequency of polynomial regression filters. There are variable demands on the cut-off frequency in both space and time during the heart cycle, and an adaptive cut-off frequency improves the image quality. In addition, the user interface of the scanner is simplified, since it is not necessary for the user to adjust the cut-off frequency. A simplified version of the algorithm was implemented for real-time processing on the GE Vingmed Ultrasound System Five scanner. The simplification was necessary due to limitations in hardware and available processing time. As a result, there was no significant improvement in the image quality, but the simplification of the user interface was achieved. As more computational power becomes available, the algorithms in Paper B and E could be combined.

A High PRF Technique to Increase the Frame Rate

In Paper F we present and analyze an acquisition technique that improves the temporal resolution in color flow imaging. At the expense of a slight increase in the clutter level, we achieved an increase in the frame rate of 70% when imaging the blood flow through the heart valves with the probe in the apical position. A clinical application of this technique is presented in Paper G. The instantaneous cross sectional velocity profile variability in the left ventricular outlet tract in patients with atrial fibrillation was studied. The study showed no significant difference between two heartbeats of different lengths in patients with atrial fibrillation, and velocity time integrals from heartbeats of different lengths can be averaged also in these patients.

Visualization of Blood Flow Direction

In Paper H we present new signal processing algorithms for visualization of blood flow in ultrasound imaging systems. The technique is called blood motion imaging (BMI). As opposed to conventional color flow imaging, the speckle pattern from the moving blood cells is preserved and enhanced, enabling the user to visually track the blood motion from frame to frame. The technique is applicable both to data acquired using conventional color flow packet acquisition, and to continuously acquired data with uniform time intervals between the samples. The approach is similar to a technique called B-flow that has recently been patented [25]. Both techniques enhance the speckle pattern movement, which is related to the blood cell movement in the blood vessels. However, as opposed to B-flow, BMI calculates several images per packet, giving an improved temporal resolution. BMI can also be combined with conventional color flow velocity estimation. Sliding window processing of the continuously acquired data is unique to BMI. Speckle pattern movement gives the user a correct perception of the blood flow direction and magnitude, and is also useful in separating true blood flow from wall motion artifacts. No attempt was made to measure the lateral velocity component, but BMI may indirectly give the lateral velocity component by combining an angle measurement derived from the speckle motion with the radial velocity component obtained from the Doppler frequency shift.

Increasing the Frame Rate in Tissue Doppler Imaging

The continuous acquisition technique for BMI presented in Paper H, is applied to tissue Doppler imaging (TDI) and strain rate imaging (SRI) in Paper I. Previously, the Doppler and tissue B-mode images have been calculated from different pulse transmissions. The temporal resolution is improved by calculating the Doppler based images from the same pulse transmissions as the tissue B-mode images. This acquisition scheme also reduces the reverberation noise which limits the accuracy of the velocity estimates. When imaging a heart wall, i.e. the interventricular septum, frame rates above 300 frames/second is possible with a lateral resolution equal to a conventional B-mode image. Tissue velocity estimates calculated from these data suffers from a lot of aliasing, but a robust technique is presented that corrects the aliased velocities. A significant advantage is the continuous stream of data with constant sampling intervals. Doppler spectra and sound signals can thus be calculated at arbitrary points in the 2D image.

Paper J presents a clinical study using the acquisition technique presented in Paper I. The spatial-temporal events in the interventricular septum were studied with a temporal and spatial resolution not previously available in tissue Doppler techniques.

Below are the abstracts of the papers in Part 2 of the thesis.

Paper A – Clutter Filter Design for Ultrasound Color Flow Imaging

To get ultrasound color flow images of high quality, it is important to sufficiently suppress the clutter signals originating from stationary and slowly moving tissue. Without sufficient clutter rejection, low velocity blood flow can not be measured, and estimates of higher velocities will have a large bias. The small number of samples available (8-16) makes clutter filtering in color flow imaging a challenging problem. In this paper we review and analyze three classes of filters: FIR, IIR, and regression filters. The quality of the filters was assessed based on the frequency response, as well as on the bias and variance of a mean blood velocity estimator using an autocorrelation technique. With the FIR filters, the frequency response was improved by allowing a non-linear phase response. By estimating the mean blood flow velocity from two vectors filtered in the forward and backward direction, respectively, the standard deviation was significantly lower with a minimum phase filter than with a linear phase filter. For IIR filters applied to short signals, the transient part of the output signal is important. We analyzed zero, step, and projection initialization, and found that projection initialization gave the best filters. For regression filters, polynomial basis functions provide effective clutter suppression. The best filters from each of the three classes gave comparable bias and variance of the mean blood velocity estimates. However, polynomial regression filters and projection initialized IIR filters had a slightly better frequency response than could be obtained with FIR filters.

Paper B – Clutter Filters Adapted to Tissue Motion in Ultrasound Color Flow Imaging

The quality of ultrasound color flow images is highly dependent on sufficient attenuation of the clutter signals originating from stationary and slowly moving tissue. Without sufficient clutter rejection, the detection of low velocity blood flow will be poor, and the velocity estimates will have a large bias. In some situations, e.g. when imaging the coronary arteries or when the operator moves the probe in search for small vessels, there is considerable movement of tissue. It has been suggested that clutter rejection can be improved by mixing down the signal with an estimate of the mean frequency prior to high-pass filtering. In this paper we compare this algorithm with several other adaptive clutter filtering algorithms using both experimental data and simulations. We found that even a slight acceleration of the tissue has a large effect on the clutter rejection. The best results were obtained by mixing down the signal with non-constant phase increments estimated from the signal. This adapted the filter to a possibly accelerated tissue motion, and gave a significant improvement in clutter rejection.

Paper C – Blood Detection Performance in Moving Tissue

A method for evaluating the blood detection performance of general linear clutter filters is described. The detector performance is characterized by a receiver operating characteristic (ROC) which is a plot of the probability of detection, P_D, versus the probability of false alarm, P_F. With a Gaussian signal model, the optimal detector compares the power at the output of a clutter filter to a threshold. The optimal detector structure is thus similar to standard color flow systems, but with a filter matrix that depends on both the clutter and blood signal statistics. It is not possible to implement such a detector, but it gives the performance limit for practical detectors. The performance of a practically realizable adaptive clutter filter is evaluated. This filter compensates for the tissue movement by estimating the correlation matrix of the clutter signal by spatial averaging, and uses the eigenvectors corresponding to the largest eigenvalues as a basis for the clutter space in a regression filter. This basis gives maximum clutter attenuation for a given filter order. Digital RF data from the carotid artery was recorded, and a theoretical model for the blood signal was used to compare the detectors. With large tissue movement, the adaptive filter had almost optimum performance, and was significantly better than the polynomial regression filter.

Paper D – Statistical Evaluation of Clutter Filters in Color Flow Imaging

The filter used to separate blood signals from the tissue clutter signal is an important part of a color flow system. In this paper, statistical detection theory is used to evaluate the quality of the most commonly used clutter filters. The probability of falsely classifying a sample volume as containing blood is kept below a specified threshold. With this constraint, the probability of correctly detecting blood is calculated for all the filters. Using a measured clutter signal, we found that polynomial regression filters and projection-initialized IIR filters are best among the commonly used filters. The probability of correctly detecting blood with velocity 10.1 cm/s was 0.32 for both these filters. The corresponding value for the optimal detector was 0.81, whereas a regression filter that depends on the clutter signal statistics achieved a blood detection probability of 0.72.

Paper E – Automatic Selection of the Clutter Filter Cut-off Frequency in Ultrasound Color Flow Imaging

Unless properly attenuated, the clutter signals originating from stationary and slowly moving tissue cause severe artifacts in ultrasound color flow images. There are varying demands on the cut-off frequency of the clutter filter in both space and time during the heart cycle. In addition, there is a need for user input to set a proper cut-off frequency. To solve these problems, this paper presents an algorithm that automatically chooses the cut-off frequency for each sample volume. The algorithm has low computational complexity, and has been implemented for real-time processing on the GE Vingmed Ultrasound System Five scanner. Filtering with regression filters can be done iteratively, resulting in an increased cut-off frequency for each step in the iteration. Color flow parameter estimates are calculated for each step in the iteration, and are used to determine if sufficient clutter attenuation is obtained. With spatial averaging of the flow parameters in each step, the clutter was sufficiently attenuated, and the blood flow signal was better preserved than with a fixed cut-off filter. Due to limitations in hardware and available processing time, this spatial averaging was not possible in the real time implementation, and the minimum cut-off frequency had to be increased to get sufficient clutter rejection. As a result, the image quality was not significantly improved. However, an important improvement was that the clutter filter was automatically adapted to the signal, with no need for the user to adjust the cut-off frequency.

Paper F – High Frame Rate Color Flow Imaging

This paper presents an acquisition technique that improves the temporal resolution in ultrasound color flow imaging. When the region of interest (ROI) in the color flow image is limited in the depth direction, and is positioned sufficiently deep in the body, it is possible to reduce the acquisition time for the color flow data by 50%. The technique uses a combination of beam interleaving and transmission of pulses with double repetition frequency. After a pulse is transmitted in a first direction, there is time available to receive from a second direction and transmit a new pulse in this direction while waiting for the echo from the first pulse to arrive. The technique is well suited for imaging the blood flow through the heart valves with the probe in the apical position. For this application, an increase in the frame rate of 70% was obtained. The transducer is focused for reception in the first direction, but the beam side lobes will pick up unwanted echoes from the pulse propagating in the second direction. A simulation using the Field II program showed that for scatterers of equal strength, the minimum difference in energy between the desired and undesired signal was 8.9dB for cardiac imaging from the apical position. However, for patients with strong reverberation noise from the body wall, the undesired signal can be considerably stronger. Without sufficient clutter filtering, this reverberation noise gives unreliable velocity estimates, so the technique should be used with care.

Paper G – A New Method Describing Cross-Sectional Blood Flow Velocity Profiles in the Left Ventricular Outflow Tract of Patients with Atrial Fibrillation with the Use of High Frame-Rate 2-Dimensional Color Flow Imaging

A new Doppler method was developed to evaluate the instantaneous cross-sectional velocity profile variability in the left ventricular outlet tract in patients with atrial fibrillation. Blood flow velocities acquired at a high frame rate (> 90 frames/s) from a single heart cycle were used to display the velocity profile. In 9 patients, 2 heart cycles with different R-R interval lengths were recorded in color flow mode in a transthoracic apical 5-chamber and long-axis view. Raw digital ultrasound data were analyzed with an external personal computer. The data indicated a variable skew in the profiles with the highest velocities and velocity-time integral (VTI) most often located in the center and toward the septum. The maximum VTI overestimated the mean VTI by approximately 40%. No significant difference existed between the two heartbeats. Thus the VTI can be averaged from heartbeats of different R-R lengths in atrial fibrillation.

Paper H – Blood Motion Imaging: A New Blood Flow Imaging Technique

In this paper we present new signal processing algorithms for visualization of blood flow in ultrasound imaging systems. As opposed to with conventional color flow imaging, the speckle pattern from the moving blood cells is preserved and enhanced, enabling the user to visually track the blood motion from frame to frame. In conventional color flow imaging, one image is produced from a packet of typically 5-15 pulses transmitted along each scan line in the image. The Doppler shift produced by slowly moving muscular tissue is lower than the Doppler shift produced by the blood flow, and efficient clutter filters are designed to attenuate the clutter signal down to a level much lower than the signal from blood. The signal power after clutter filtering is used to detect points in the image where blood is present. Alternatively, in the power Doppler mode, the signal power is displayed as an image to visualize blood vessels. In order to get reliable detection, substantial temporal and spatial averaging is used, thus limiting the dynamic variation, as well as spatial resolution. This averaging process suppresses the spatial speckle pattern in the signal amplitude. In addition to preserving the speckle pattern, the algorithms described in this paper compute several image frames per packet of pulse transmissions. The perception of movement is further improved if the scatterers in a large spatial region are imaged almost simultaneously. This is obtained by increasing the time between pulse transmissions in the same beam direction, and using a technique called beam interleaving. After transmitting a pulse in a first direction, there is time available to acquire data in several other beam directions before transmitting the next pulse in the first direction. Visualization of the speckle pattern movement gives the user a correct perception of the blood flow direction and magnitude, and is also useful in separating true blood flow from wall motion artifacts.

Paper I – High Frame Rate Tissue Doppler and Strain Rate Imaging

In tissue Doppler and strain rate imaging of the heart, a high frame rate is necessary to capture the rapid relaxations and contractions of the myocardium. Previously, the Doppler and tissue B-mode images have been calculated from different pulse transmissions. To improve the temporal resolution, we present a new acquisition technique where the Doppler based images are calculated from the same pulse transmissions as the tissue B-mode images. By constructing the image from 10-15 transmit beams, frame rates above 300 frames/second are possible when imaging the heart. To get adequate spatial resolution, the small number of transmit beams limits the width of the image, but the image is wide enough to cover a heart wall, i.e. the interventricular septum. The Doppler pulse repetition frequency equals the frame rate and is relatively low. Tissue velocity estimates calculated from these data therefore suffer from aliasing. However, we present a robust technique that corrects the aliased velocities. A significant advantage of the new technique is the continuous stream of data with constant sampling intervals. Doppler spectra and sound signals can thus be calculated at arbitrary points in the 2D image.

Paper J – High Frame Rate Strain Rate Imaging of the Ventricular Septum in Healthy Subjects

The regional function of the left ventricle can be visualized in real-time using the strain rate imaging method. Deformation or strain of a tissue segment occurs over time during the heart cycle. The rate of this deformation (the strain rate) is equivalent to the velocity gradient, and can be estimated using a tissue Doppler technique. In the present study in nine healthy subjects, we have assessed the feasibility of a new strain rate imaging method with a very high frame rate of around 300 frames per second (FPS). Digital radio-frequency (RF) data were acquired for a sector angle of 20°-30° using a high-end ultrasound scanner. The RF data were analyzed using a dedicated software package that displays strain rate images and profiles and calculates quantitative values. Since the ventricular septum is of crucial importance for the left and right ventricular function, we assessed changes in strain rate through the heart cycle of the ventricular septum with the new method. Mean peak systolic strain rate in the healthy subjects was $-1.65 \pm 0.13\text{s}^{-1}$. Mean peak diastolic strain rate during early filling was $3.14 \pm 0.50\text{s}^{-1}$ and mean peak diastolic strain rate during atrial systole was $0.99 \pm 0.09\text{s}^{-1}$. With the new method, we were able to study events and spatial-temporal differences in the heart cycle with duration down to 3.5-3ms, including the pre-ejection period and the isovolumic relaxation period. We found individual differences in the strain rate patterns, but in all subjects, the ventricular contraction started simultaneously in all parts of the septum. After the ejection period, the elongation started before aortic valve closure, in the midinferior septum and propagated towards the apex. In conclusion, high frame rate strain rate imaging makes it possible to study rapid deformation patterns in the heart.

5 Conclusions

Real-time color flow imaging has been available for fifteen years. During this time there has been a significant improvement in the image quality, and the technology is now relatively mature. In the beginning, the processing was performed in hardware. The processing could later be transferred to dedicated programmable digital signal processors. We are now at a point where general purpose computers are fast enough to perform the color flow processing in real time on an ultrasound scanner. This greatly improves the flexibility and eases the development and implementation of new algorithms. The algorithms for improved clutter rejection that are presented in this thesis, have the potential to improve the image quality in color flow imaging. With software based color flow processing, the cost of implementing the algorithms for real-time processing on the scanner should be relatively small. As the computational power increases further, more advanced algorithms can be implemented at a small cost.

The blood motion imaging (BMI) technique is a step forward since it provides a more intuitive display of blood flow compared to conventional color flow imaging. As opposed to conventional color flow imaging, BMI preserves and enhances the speckle pattern. The speckle pattern can be visually tracked from frame to frame, giving the user a correct perception of the blood flow direction and magnitude. BMI is also useful to separate true blood flow from wall motion artifacts. The best results are obtained when imaging the blood flow in peripheral vessels. The lateral movement is clearly visualized, and we get an impression of the parabolic velocity profile across the vessel. In addition to providing an intuitive flow visualization, BMI might ease the detection of abnormal flow pattern such as small jets. A real-time implementation is necessary for a thorough clinical evaluation of BMI.

Assessment of the cardiac function based on ultrasound Doppler methods is a fast developing field. We have described a new method that reduces the noise, and improves the temporal resolution when imaging one heart wall at a time. An increased number of parallel beam forming channels could extend this technique to cover the whole left ventricle with an acceptable spatial resolution. Such a modality would be of great clinical value in, for example, stress-echo examinations.

5.1 Future Directions in Ultrasound Imaging

Ultrasound scanners using two-dimensional transducer arrays for real-time three-dimensional imaging have been available for some years, but the image quality has not been satisfactory. However, the feasible number of beam-forming channels is increasing, and more advanced beam-forming algorithms are being developed. High quality three-dimensional ultrasound imaging systems for both B-mode and color flow are therefore expected in the future. The availability of real-time three-dimensional data of high quality may lead to algorithms for calculating all the components in the three-dimensional blood velocity field. Real-time three-dimensional scanning is likely to be the next major breakthrough in ultrasound color flow imaging.

The first hand-held ultrasound scanners are now commercially available. Such cheap and versatile instruments could bring ultrasound imaging to new fields of medicine such as emergency rescue units and general practitioners. As such markets evolve, we expect a rapid development of the functionality in hand-held instruments. The development might include new Doppler-based imaging modalities specially designed for the applications where handheld instruments are used.

There is currently a rapid development of micromachined ultrasonic transducers built on the surface of a silicon wafer. This means that the transducer and front-end electronics can be integrated on the same silicon chip. Such an integration of the transducer and front-end electronics is interesting both with respect to two-dimensional transducer arrays, and with respect to the cost-effective miniaturization desired for handheld instruments. The development of such transducers might therefore indirectly lead to new and interesting applications of Doppler ultrasound.

References

1. Y. B. Ahn and S. B. Park. Estimation of mean frequency and variance of ultrasonic Doppler signal by using second-order autoregressive model. *IEEE Trans. Ultrason., Ferroelect., Freq. Contr.*, 38(3):172–182, May 1991.

2. S. K. Alam and K. J. Parker. The butterfly search technique for estimation of blood velocity. *Ultrasound Med. Biol.*, 21(5):657–670, 1995.

3. S. K. Alam and K. J. Parker. Reduction of computational complexity in the butterfly search technique. *IEEE Trans. Biomed. Eng.*, 43(7):723–733, July 1996.

4. M. E. Allam and J. F. Greenleaf. Isomorphism between pulsed-wave Doppler ultrasound and direction-of-arrival estimation–Part I: Basic principles. *IEEE Trans. Ultrason., Ferroelect., Freq. Contr.*, 43(5):911–922, Sept. 1996.

5. M. E. Allam, R. Kinnick, and J. F. Greenleaf. Isomorphism between pulsed-wave Doppler ultrasound and direction-of-arrival estimation–Part II: Experimental results. *IEEE Trans. Ultrason., Ferroelect., Freq. Contr.*, 43(5):923–935, Sept. 1996.

6. American Institute of Ultrasound in Medicine. Medical ultrasound safety. Laurel, Maryland, 1994.

7. M. E. Anderson. Multi-dimensional velocity estimation with ultrasound using spatial quadrature. *IEEE Trans. Ultrason., Ferroelect., Freq. Contr.*, 45(3):852–861, May 1998.

8. B. A. J. Angelsen. A theoretical study of the scattering of ultrasound from blood. *IEEE Trans. Biomed. Eng.*, 27(2):61–67, Feb. 1980.

9. B. A. J. Angelsen. *Waves, Signals and Signal Processing in Medical Ultrasonics. Volume I and II.* Dept. of Physiology and Biomedical Engineering, The Norwegian University of Science and Technology (NTNU), Trondheim, Norway, 1995.

10. B. A. J. Angelsen, K. Kristoffersen, and H. Torp. Method of color coding two dimensional ultrasonic doppler velocity images of blood flow on a display. US Patent 4932415, June 1990. Vingmed Sound A/S, Horten, Norway.

11. D. W. Baker and D. W. Watkins. A phase coherent pulse Doppler system for cardiovascular measurement. *Proc. 20th Ann. Conf. on Eng. in Med. and Biol.*, 27, 1967.

12. S. Berg, S. O. Samstad, S. Bjærum, and H. Torp. Quantitative transthoracic three-dimensional colour flow imaging: A new method applied to mitral blood flow. Presented at *12th Symposium on Echocardiology and 9th meeting of the International Cardiac Doppler Society*, Rotterdam, June 25-27, 1997.

13. S. Berg, H. Torp, B. O. Haugen, and S. Samstad. Volumetric blood flow measurement with the use of dynamic 3-dimensional ultrasound color flow imaging. *J. Am. Soc. Echocardiogr.*, 13(5):393–402, May 2000.

14. S. Bjærum and Torp. Method and apparatus for visualization of motion in ultrasound flow imaging using packet data acquisition. US Patent application, Serial No. 09/449,391, filed Nov. 26, 1999.

15. S. Bjærum and Torp. Method and apparatus for visualization of motion in ultrasound flow imaging using continuous data acquisition. US Patent application, Serial No. 09/449,389, filed Nov. 26, 1999.

16. S. Bjærum and H. Torp. Optimal adaptive clutter filtering in color flow imaging. In *Proceedings of the IEEE Ultrasonics Symposium*, volume 2, pages 1223–1226, Oct. 1997.

17. S. Bjærum and H. Torp. Blood detection performance in moving tissue. In *Proceedings of the IEEE Ultrasonics Symposium*, volume 2, pages 1571–1574, Oct. 1998.

18. S. Bjærum and H. Torp. The effect of accelerated tissue motion on clutter rejection in color flow imaging. In *Proceedings of the IEEE Ultrasonics Symposium*, volume 2, pages 1503–1506, Oct. 1999.

19. S. Bjærum and H. Torp. Statistical evaluation of clutter filters in color flow imaging. *Ultrasonics*, 38(1–8):376–380, Mar. 2000.

20. S. Bjærum, H. Torp, and K. Kristoffersen. Clutter filter design for ultrasound color flow imaging. Submitted to *IEEE Trans. Ultrason. Ferroelect. Freq. Contr.*, 2000.

21. S. Bjærum, H. Torp, and K. Kristoffersen. Clutter filters adapted to tissue motion in ultrasound color flow imaging. Submitted to *IEEE Trans. Ultrason. Ferroelect. Freq. Contr.*, 2000.

22. L. N. Bohs, B. H. Friemel, B. A. McDermott, and G. E. Trahey. A real time system for quantifying and displaying two-dimensional velocities using ultrasound. *Ultrasound Med. Biol.*, 19:715–761, 1993.

23. O. Bonnefous and P. Pesqué. Time domain formulation of pulse-Doppler ultrasound and blood velocity estimation by cross correlation. *Ultrason. Imag.*, 8: 73–85, 1986.

24. K. Caidal, E. Kazzam, J. Lidberg, G. Neumann Andersen, J. Nordanstig, S. Rantapaa Dahlqvist, A. Waldenstrom, and R. Wikh. New concept in echocardiography: harmonic imaging of tissue without use of contrast agent. *Lancet*, 352 (9136):1264–1270, Oct. 1998.

25. R. Y. Chiao, A. L. Hall, K. E. Thomenius, M. J. Washburn, and K. W. Rigby. Method and apparatus for enhanced flow imaging in B-Mode ultrasound. US Patent 6074348, June 2000. General Electric Company, Schenectady, N.Y.

26. E. S. Chornoboy. Initialization for improved IIR filter performance. *IEEE Trans. Signal Process.*, 40(3):543–550, Mar. 1992.

27. I. Edler and C. H. Hertz. The use of ultrasonic reflectoscope for the continuous recording of the movement of heart walls. *Kungl. Fysiogr. Sällskap. i Lund Förhandl.*, 24:40–58, 1954.

28. D. H. Evans, W. N. McDicken, R. Skidmore, and J. P. Woodcock. *Doppler Ultrasound, Physics, Instrumentation, and Clinical Applications.* John Wiley & Sons, Inc., New York, 1989.

29. K. Ferrara and G. DeAngelis. Color flow mapping. *Ultrasound Med. Biol.*, 23(3): 321–345, 1997.

30. K. W. Ferrara and V. R. Algazi. A new wideband spread target maximum likelihood estimator for blood velocity estimation–Part I: Theory. *IEEE Trans. Ultrason., Ferroelect., Freq. Contr.*, 38(1):1–16, Jan. 1991.

31. K. W. Ferrara and V. R. Algazi. A new wideband spread target maximum likelihood estimator for blood velocity estimation–Part II: Evaluation of estimators with experimental data. *IEEE Trans. Ultrason., Ferroelect., Freq. Contr.*, 38(1): 17–26, Jan. 1991.

32. R. H. Fletcher and D. W. Burlage. An initialization technique for improved MTI performance in phased array radars. *Proc. IEEE*, 60:1551–1552, Dec. 1972.

33. S. G. Foster, P. M. Embree, and W. D. O'Brien. Flow velocity profile via time-domain correlation: Error analysis and computer simulation. *IEEE Trans. Ultrason., Ferroelect., Freq. Contr.*, 37(2):164–175, May 1990.

34. M. D. Fox. Multiple crossed-beam ultrasound Doppler velocimetry. *IEEE Trans. Sonics Ultrason.*, 25(5):281–286, Sept. 1978.

35. B. Haider, P. A. Lewin, and K. E. Thomenius. Pulse elongation and deconvolution filtering for medical ultrasonic imaging. *IEEE Trans. Ultrason., Ferroelect., Freq. Contr.*, 45(1):98–113, Jan. 1998.

36. L. Hatle and B. Anglesen. *Doppler Ultrasound in Cardiology – Physical Principles and Clinical Applications.* Lea & Feibiger, second edition, 1985.

37. B. O. Haugen, S. Bjærum, S. O. Samstad, T. Skjærpe, and H. Torp. A new method describing cross sectional blood flow velocity profiles in the left ventricular outflow tract from patients with atrial fibrilation using high frame rate two-dimensional color flow imaging. *J. Am. Soc. Echocardiogr.*, 14(1):50–56, Jan. 2001.

38. S. Haykin. *Communication Systems.* John Wiley & Sons, Inc., second edition, 1983.

39. A. Heimdal, A. Støylen, H. Torp, and T. Skjærpe. Real-time strain rate imaging of the left ventricle by ultrasound. *J. Am. Soc. Echocardiogr.*, 11(11):1013–1019, Nov. 1998.

40. A. P. G. Hoeks, J. J. W. van de Vorst, A. Dabekaussen, P. J. Brands, and R. S. Reneman. An efficient algorithm to remove low frequency Doppler signals in digital Doppler systems. *Ultrason. Imag.*, 13(2):135–144, Apr. 1991.

41. D. H. Howry and W. R. Bliss. Ultrasonic visualization of soft tissue structures of the body. *J. Lab. Clin. Med.*, 40:579–592, 1952.

42. J. A. Jensen. *Estimation of Blood Velocities Using Ultrasound.* Cambridge University Press, 1996.

43. J. A. Jensen and P. Munk. A new method for estimation of velocity vectors. *IEEE Trans. Ultrason., Ferroelect., Freq. Contr.*, 45(3):837–851, May 1998.

44. A. P. Kadi and T. Loupas. On the performance of regression and step-initialized IIR clutter filters for color Doppler systems in diagnostic medical ultrasound. *IEEE Trans. Ultrason., Ferroelect., Freq. Contr.*, 42(5):927–937, Sept. 1995.

45. C. Kasai, K. Namekawa, A. Koyano, and R. Omoto. Real-time two-dimensional blood flow imaging using an autocorrelation technique. *IEEE Trans. Sonics Ultrason.*, 32(3):458–464, May 1985.

46. S. M. Kay. *Fundamentals of Statistical Signal Processing: Detection Theory*, volume 2. Prentice Hall, Inc., 1998.

47. K. Kristoffersen. Optimal receiver filtering in pulsed Doppler ultrasound blood velocity measurements. *IEEE Trans. Ultrason., Ferroelect., Freq. Contr.*, 33(1): 51–58, Jan. 1986.

48. K. Kristoffersen and B. A. J. Angelsen. A comparison between mean frequency estimators for multigated Doppler systems with serial signal processing. *IEEE Trans. Biomed. Eng.*, 32(9):645–657, Sept. 1985.

49. X. Lai, H. Torp, and K. K. An extended autocorrelation method for estimation of blood velocity. *IEEE Trans. Ultrason., Ferroelect., Freq. Contr.*, 44(6):1332–1342, Nov. 1997.

50. T. Loupas and W. N. McDicken. Low-order complex AR models for mean and maximum frequency estimation in the context of Doppler color flow mapping. *IEEE Trans. Ultrason., Ferroelect., Freq. Contr.*, 37(6):590–601, Nov. 1990.

51. W. N. McDicken, G. R. Sutherland, C. M. Moran, and L. N. Gordon. Colour Doppler velocity imaging of the myocardium. *Ultrasound Med. Biol.*, 18:651–654, 1992.

52. K. Namekawa, C. Kasai, M. Tsukamoto, and A. Koyano. Real-time blood flow imaging system utilizing autocorrelation techniques. In R. Lerski and P. Morley, editors, *Ultrasound'82*, pages 203–208. Pergamon Press, 1982.

53. V. L. Newhouse, D. Censor, T. Vontz, J. A. Cisneros, and B. B. Goldberg. Ultrasound Doppler probing of flows transverse with respect to beam axis. *IEEE Trans. Biomed. Eng.*, 34(10):779–789, Oct. 1987.

54. A. Nowicki, J. Reid, P. C. Pedersen, A. W. Schmidt, and H. Oung. On the behavior of instantaneous frequency estimators implemented on Doppler flow imagers. *Ultrasound Med. Biol.*, 16(5):511–518, 1990.

55. J. Ophir and K. J. Parker. Contrast agents in diagnostic ultrasound. *Ultrasound Med. Biol.*, 15(4):319–333, 1989.

56. T. W. Parks and C. S. Burrus. *Digital Filter Design.* John Wiley & Sons, Inc., 1987.

57. R. B. Peterson, L. E. Atlas, and K. W. Beach. A comparison of IIR initialization techniques for improved color Doppler wall filter performance. In *1994 IEEE Ultrasonics Symposium Proceedings*, volume 3, pages 1705–1708, Nov. 1994.

58. L. G. Pourcelot. Real-time blood flow imaging. In C. T. Lancee, editor, *Echocardiology*, pages 421–429. Martinus Nijhoff, 1979.

59. J. C. Rajaonah, B. Dousse, and J. J. Meister. Compensation of the bias caused by the wall filter on the mean Doppler frequency. *IEEE Trans. Ultrason., Ferroelect., Freq. Contr.*, 41(6):812–819, Nov. 1994.

60. S. O. Samstad, S. Bjærum, and H. Torp. Cross sectional flow velocity profiles from two-dimensional colour Doppler recorded with high frame rate: A new method applied to mitral blood flow. Presented at *12th Symposium on Echocardiology and 9th meeting of the International Cardiac Doppler Society*, Rotterdam, June 25-27, 1997.

61. S. O. Samstad, S. Bjærum, and H. Torp. Variability of E to A ratio of the mitral blood flow velocity pattern with the intravalvular site of velocity sampling. Presented at *12th Symposium on Echocardiology and 9th meeting of the International Cardiac Doppler Society*, Rotterdam, June 25-27, 1997.

62. S. O. Samstad, O. Rossvoll, H. G. Torp, T. Skjærpe, and L. Hatle. Cross-sectional early mitral flow-velocity profiles from color Doppler in patients with mitral valve disease. *Circulation*, 86(3):748–755, Sept. 1992.

63. S. Satomura. Ultrasonic Doppler method for the inspection of cardiac function. *J. Acoust. Soc. Am.*, 29:1181–1185, 1957.

64. B. Schrope and V. L. Newhouse. Second harmonic ultrasound blood perfusion measurement. *Ultrasound Med. Biol.*, 19:567–579, 1993.

65. P. M. Shah. Contras echocardiography – a historical perspective. In N. C. Nanda, R. Schlief, and B. B. Goldberg, editors, *Advances in Echo Imaging using Contrast Enhancement*, pages 3–9. Kluwer Academic Publishers, second edition, 1997.

66. M. A. Shariati, J. H. Dripps, and W. N. McDicken. Deadbeat IIR based MTI filtering for color flow imaging systems. In *1993 IEEE Ultrasonics Symposium Proceedings*, volume 2, pages 1059–1063, Oct. 1993.

67. S. A. Slørdahl, S. Bjærum, B. H. Amundsen, A. Støylen, A. Heimdal, S. I. Rabben, and H. Torp. High frame rate strain rate imaging of the ventricular septum in healthy subjects. Presented at *19th Congress of the World Federation for Ultrasound in Medicine and Biology*, Florence, 2000.

68. S. A. Slørdahl, S. Bjærum, B. H. Amundsen, A. Støylen, A. Heimdal, S. I. Rabben, and H. Torp. High frame rate strain rate imaging of the ventricular septum in healthy subjects. Submitted to *European Journal of Ultrasound*, 2000.

69. K. Spencer, J. Bednarz, P. G. Rafter, C. Korcarz, and R. M. Lang. Use of harmonic imaging without echocardiographic contrast to improve two-dimensional image quality. *Am. J. Cardiol.*, 82(6):794–799, Sept. 1998.

70. C. W. Therrien. *Discrete Random Signals and Statistical Signal Processing.* Prentice Hall, Inc., 1992.

71. L. Thomas and A. Hall. An improved wall filter for flow imaging of low velocity flow. In *1994 IEEE Ultrasonics Symposium Proceedings*, volume 3, pages 1701–1704, Nov. 1994.

72. H. Torp. Clutter rejection filters in color flow imaging: A theoretical approach. *IEEE Trans. Ultrason., Ferroelect., Freq. Contr.*, 44(2):417–424, Mar. 1997.

73. H. Torp and S. Bjærum. Quality versus framerate in color flow imaging: An experimental study based on offline processing of RF-signals recorded from patients. In *Proceedings of the IEEE Ultrasonics Symposium*, volume 2, pages 1229–1232, Nov. 1996.

74. H. Torp and K. Kristoffersen. Velocity matched spectrum analysis: A new method for suppressing velocity ambiguity in pulsed-wave Doppler. *Ultrasound Med. Biol.*, 21(7):937–944, 1995.

75. H. Torp, K. Kristoffersen, and B. A. J. Angelsen. Autocorrelation techniques in color flow imaging: Signal model and statistical properties of the autocorrelation estimates. *IEEE Trans. Ultrason., Ferroelect., Freq. Contr.*, 41(5):604–612, Sept. 1994.

76. G. E. Trahey, J. W. Allison, and O. T. von Ramm. Angle independent ultrasonic detection of blood flow. *IEEE Trans. Biomed. Eng.*, 34(12):965–967, Dec. 1987.

77. C. Tysoe and D. H. Evans. Bias in mean frequency estimation of Doppler signals due to wall clutter filters. *Ultrasound Med. Biol.*, 21(5):671–677, 1995.

78. P. J. Vaitkus and R. S. C. Cobbold. A comparative study and assessment of Doppler ultrasound spectral estimation techniques part I: Estimation methods. *Ultrasound Med. Biol.*, 14(8):661–672, 1988.

79. P. J. Vaitkus and R. S. C. Cobbold. A new time-domain narrowband velocity estimation technique for Doppler ultrasound flow imaging. Part I: Theory. *IEEE Trans. Ultrason., Ferroelect., Freq. Contr.*, 45(4):939–954, July 1998.

80. P. J. Vaitkus and R. S. C. Cobbold. A new time-domain narrowband velocity estimation technique for Doppler ultrasound flow imaging. Part II: Comparative performance assessment. *IEEE Trans. Ultrason., Ferroelect., Freq. Contr.*, 45(4): 955–971, July 1998.

81. P. J. Vaitkus, R. S. C. Cobbold, and K. W. Johnston. A comparative study and assessment of Doppler ultrasound spectral estimation techniques part II: Methods and results. *Ultrasound Med. Biol.*, 14(8):673–688, 1988.

82. J. J. Wild. The use of ultrasonic pulses for the measurement of biologic tissues and the detection of tissue density changes. *Surgery*, 27:183–188, 1950.

83. J. C. Willemetz, A. Nowicki, J. J. Meister, F. De Palma, and G. Pante. Bias and variance in the estimate of the Doppler frequency induced by a wall motion filter. *Ultrason. Imag.*, 11:215–225, 1989.

84. L. S. Wilson. Description of broad-band pulsed Doppler ultrasound processing using the two-dimensional Fourier transform. *Ultrason. Imag.*, 13:301–315, 1991.

Paper A

Clutter Filter Design for Ultrasound Color Flow Imaging

Steinar Bjærum, Hans Torp and Kjell Kristoffersen[†]

Department of Physiology and Biomedical Engineering,
Norwegian University of Science and Technology, Trondheim, Norway
[†]GE Vingmed Ultrasound,
Horten, Norway

Abstract

To get ultrasound color flow images of high quality, it is important to sufficiently suppress the clutter signals originating from stationary and slowly moving tissue. Without sufficient clutter rejection, low velocity blood flow can not be measured, and estimates of higher velocities will have a large bias. The small number of samples available (8-16) makes clutter filtering in color flow imaging a challenging problem. In this paper we review and analyze three classes of filters: FIR, IIR, and regression filters. The quality of the filters was assessed based on the frequency response, as well as on the bias and variance of a mean blood velocity estimator using an autocorrelation technique. For FIR filters, the frequency response was improved by allowing a non-linear phase response. By estimating the mean blood flow velocity from two vectors filtered in the forward and backward direction, respectively, the standard deviation was significantly lower with a minimum phase filter than with a linear phase filter. For IIR filters applied to short signals, the transient part of the output signal is important. We analyzed zero, step, and projection initialization, and found that projection initialization gave the best filters. For regression filters, polynomial basis functions provide effective clutter suppression. The best filters from each of the three classes gave comparable bias and variance of the mean blood velocity estimates. However, polynomial regression filters and projection initialized IIR filters had a slightly better frequency response than could be obtained with FIR filters.

A shorter version of this paper is submitted to
IEEE Trans. Ultrason., Ferroelect., Freq. Contr.

1 Introduction

In ultrasound Doppler blood flow measurements, the signal scattered from blood is corrupted by signals scattered from muscular tissue such as vessel walls, etc. This clutter signal is typically 40-100dB stronger than the signal from blood. The signal scattered by the rapidly moving blood cells has a larger Doppler frequency shift than the signal reflected from slowly moving tissue. A high-pass filter can therefore be used to separate the signals from blood and tissue. To get adequate frame rates in 2D color flow imaging, only $8-16$ samples are generally available for high-pass filtering. While there are many conventional filter design techniques, all these algorithms consider only the steady state frequency response. For the short signals available in color flow imaging, the transient response is significant, and the steady state response can not be used to compare the filters. In this paper we analyze IIR filters with various initialization techniques [1, 2, 4], FIR filters with and without a linear phase response [7], and regression filters [3, 4, 12] in order to determine which filter is best for clutter filtering in color flow imaging. The paper considers more filter types and goes deeper into the design procedure than previous papers have done [4, 8, 10].

It has been suggested to adapt the clutter filter to the tissue movement by down-mixing the signal with the estimated mean tissue frequency [11]. This paper does not consider such an adaptation to the tissue movement, but down-mixing can be done prior to all the filters considered. Paper [8] suggests initializing an IIR filter to suppress the transient from a complex exponential with frequency equal to the estimated mean frequency. This is called exponential initialization, and results in a non-linear filter and is not considered in this paper. The approach, however, seems similar to down-mixing with the mean frequency prior to a step-initialized IIR filter.

The paper is organized as follows. General theory for linear clutter filters is presented in Section 2. In Sections 3, 4, and 5, FIR, IIR, and regression filters are presented, respectively. Different filters within each of the filter classes are analyzed and compared. The best filters from each class are compared in Section 6, while Section 7 contains the final discussion and conclusions.

2 General Linear Clutter Filters

A 2D color flow imaging system scans the ultrasound beam over the region to be imaged, transmits N pulses in each direction, and estimates the blood flow velocities from the backscattered signals. The number of pulses N will be referred to as the packet size. A well established technique is to estimate the blood flow velocities based on the temporal samples of the complex demodulated signal from fixed positions in space. The clutter filter thus operates on a one-dimensional signal consisting of N temporal samples.

It is convenient to organize the N samples of the complex demodulated Doppler signal in a vector $\mathbf{x} = [x(0), x(1), \ldots, x(N-1)]^T$. A general one-dimensional clutter rejection filter can be described mathematically as a transform on the N-dimensional complex vector space $\mathbb{C}^N$. Restricting the treatment to linear filters, a general linear filtering operation can be expressed by the matrix multiplication

$$\mathbf{y} = \mathbf{A}\mathbf{x} \tag{1}$$

where $\mathbf{A}$ is an $M \times N$ matrix, and the output vector $\mathbf{y} = [y(0), y(1), \ldots, y(M-1)]^T$ has dimension M. With the matrix element in row n and column k denoted by $a(n,k)$, the elements of the output vector are given by

$$y(n) = \sum_{k=0}^{N-1} a(n,k)x(k), \quad n = 0, \ldots, M-1 \tag{2}$$

The filter is linear, but not generally time invariant. It is therefore not possible to define the frequency response as the Fourier transform of an impulse response. For a general linear filter, the frequency response is defined as the power of the output signal when the input is a complex harmonic signal [12] with unit amplitude. A discrete-time complex exponential is defined by

$$x(k) = e^{jk\omega}, \quad k = 0, \ldots, N-1 \tag{3}$$

where $\omega \in [-\pi, \pi]$ is the normalized frequency, and $j = \sqrt{-1}$. With this input signal, the output becomes

$$y_\omega(n) = \sum_{k=0}^{N-1} a(n,k)e^{jk\omega} = A_n(-\omega), \quad n = 0, \ldots, M-1 \tag{4}$$

where $A_n(\omega)$ is the Fourier transform of row n. The frequency response then becomes

$$H_0(\omega) = \frac{1}{M}\sum_{n=0}^{M-1} |y_\omega(n)|^2 = \frac{1}{M}\sum_{n=0}^{M-1} |A_n(-\omega)|^2 \tag{5}$$

The parameters describing the frequency response of a high pass filter are illustrated in Figure 1. The stopband is limited by the stopband cut off frequency ω_s, which should be large enough to remove the clutter signal. The deviation from zero in the stopband is given by d_s, which should be as small as possible to get sufficient clutter rejection. In the passband, all the frequencies should be passed through unaltered which means that d_p should be minimized. Finally, the passband cut off frequency ω_p should be as close as possible to ω_s. This ensures that a maximal range of blood velocities can be measured.

3 Finite Impulse Response (FIR) Filters

As the name implies, the impulse response of an FIR filter is of finite length. The output of a $(K-1)^{\text{th}}$ order FIR filter can therefore be written as the finite convolution sum

$$y(n) = \sum_{k=0}^{K-1} h(k)x(n-k) = \sum_{k=n-K+1}^{n} h(n-k)x(k) \tag{6}$$

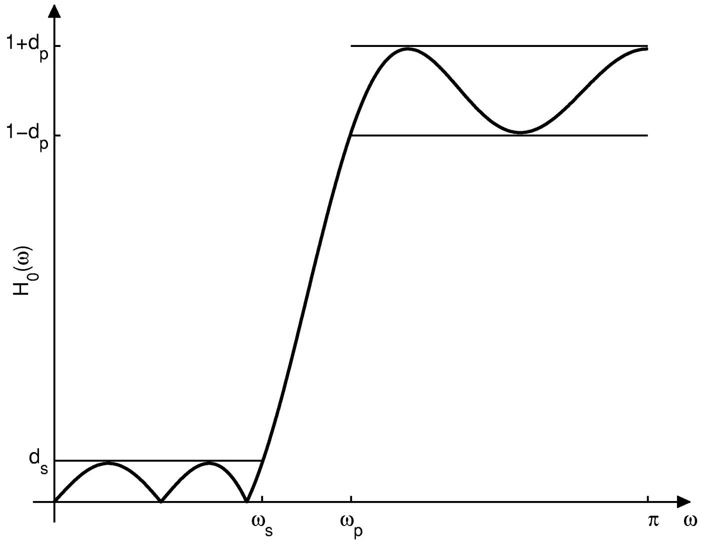

Figure 1: Design parameters for a high pass filter.

A block diagram of an FIR filter of order $K-1$ is shown in Figure 2. The output is not valid until all the filter registers are filled up with input data. With packet size N, and filter order $K-1$, the number of valid output samples is $N-K-1$. It can be shown that for FIR filters, the frequency response defined in Equation 5 becomes $H_0(\omega) = |H(\omega)|^2$, where $H(\omega)$ is the Fourier transform of the impulse response $h(n)$.

3.1 FIR Filters with Linear Phase

A filter has linear phase if the frequency response can be written

$$H(\omega) = G(\omega)e^{j(k_1+k_2\omega)} \tag{7}$$

where $G(\omega)$ is a real function, and k_1 and k_2 are constants. The advantage of linear phase is that in the passband, the frequency response is $H(\omega) \sim e^{j(k_1+k_2\omega)}$. For a signal $x(n)$ consisting only of frequencies in the passband of the filter, the spectrum of

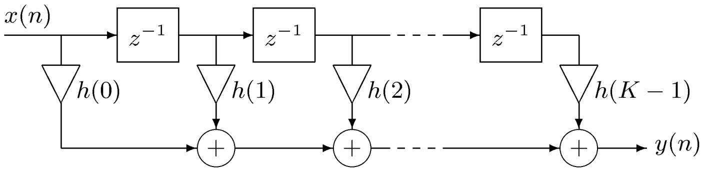

Figure 2: FIR filter of order $K-1$.

Type	$K-1$	$h(n)$	$G(0)$	$G(\pi)$	$Q(\omega)$
1	Even	Symmetric	Unconstrained	Unconstrained	1
2	Odd	Symmetric	Unconstrained	Zero	$\cos\frac{\omega}{2}$
3	Even	Antisymmetric	Zero	Zero	$\sin\omega$
4	Odd	Antisymmetric	Zero	Unconstrained	$\sin\frac{\omega}{2}$

Table 1: Properties of linear phase FIR filters.

the filtered signal is $Y(\omega) \sim X(\omega)e^{j(k_1+k_2\omega)}$. This is just a constant phase shift and a time delay of the input signal, and the wave form is not distorted. An FIR filter with real coefficients has linear phase if the impulse response satisfies the symmetry constraint

$$h(n) = \pm h(K-n-1) \tag{8}$$

resulting in four types of linear phase FIR filters with properties shown in Table 1 [7]. In the $\mathcal{Z}$-plane, Equation 8 forces a zero at $z=(1/r)e^{j\theta}$ if there is a zero at $z=re^{j\theta}$. As we see in Table 1, a high pass filter has to be of type 1 or 4. Many design techniques exist for linear phase FIR filters [7], but we will only consider the design of equiripple filters using the McClellan-Parks algorithm. The amplitude of the frequency response of linear phase FIR filters can be written as

$$G(\omega) = Q(\omega)\sum_{k=0}^{K/2} a_k \cos(k\omega) = Q(\omega)\hat{G}(\omega) \tag{9}$$

where $Q(\omega)$ is defined in Table 1. The specified stop and passbands of the filter define a closed subset $\mathcal{F}$ of the closed interval $0 \leq \omega \leq \pi$. By specifying a desired function $D(\omega)$ and a weighting function $W(\omega)$ on $\mathcal{F}$, the error becomes

$$E(\omega) = W(\omega)(D(\omega) - G(\omega)) = W(\omega)Q(\omega)(D(\omega)/Q(\omega) - \hat{G}(\omega)) \tag{10}$$

The McClellan-Parks algorithm finds the coefficients a_k that minimize

$$\max_{\omega\in\mathcal{F}} |E(\omega)| \tag{11}$$

Since the maximum error is minimized, the error is evenly distributed in $\mathcal{F}$ and the McClellan-Parks algorithm produces equiripple filters [7].

3.2 FIR Filters with Minimum Phase

Linear phase imposes a symmetry constraint on the impulse response as shown in Equation 8. Without any phase constraints, the required order to obtain a specified amplitude response is expected to be reduced. An FIR filter of order $(K-1)$ with optimum amplitude response can be designed as described in [6]. When the phase is neglected, it is equivalent to optimize the squared magnitude of the frequency response which can be written [7, p. 112]

$$|H(\omega)|^2 = \sum_{k=0}^{K-1} a_k \cos(k\omega) \tag{12}$$

First a linear phase filter of order $2(K-1)$ is designed using the McClellan-Parks algorithm. The resulting amplitude response function can be made non-negative by adding a constant value equal to the stopband ripple, and is the magnitude squared frequency response of the desired filter. The next step is thus to factorize this function, which has double zeros on the unit circle corresponding to the stopband zeros, while the zeros determining the passband have mirror symmetry about the unit circle. By picking one of each of the double zeros on the unit circle, and one of each of the symmetric passband zeros, we find the $(K-1)^{\text{th}}$ order filter with optimum amplitude response in the sense specified in Equation 11. By choosing the zeros that are inside the unit circle, we get the minimum phase filter, i.e. the filter with smallest time delay. The minimum phase filter also maximizes the partial energy $E(n) = \sum_{k=0}^{n} |h(k)|^2$ of the impulse response [9], and therefore has the most asymmetric impulse response.

Blood flow parameters are commonly estimated from an estimate of the autocorrelation function of the filtered signal [5]. For an FIR filter, the autocorrelation function of the output signal y is given by

$$R_y(m) = \frac{1}{2\pi} \int_{-\pi}^{\pi} S_x(\omega) |H(\omega)|^2 e^{jm\omega} d\omega \tag{13}$$

when the input signal x has power spectrum $S_x(\omega)$. Since $R_y(m)$ is independent of the phase response of the filter, it is safe to disregard the phase response when designing FIR clutter filters for use together with autocorrelation estimates. The minimum phase filter has a highly asymmetric impulse response function, and the input samples are weighted differently if the impulse response is reversed. The variance might therefore be reduced if the autocorrelation estimate is calculated from two output vectors filtered in the forward and backward direction, respectively. This is investigated in Section 6.

The optimum FIR amplitude response can be compared to the general frequency response defined in Section 2 by writing Equation 5 as

$$\begin{aligned} H_0(\omega) &= \frac{1}{M} \sum_{n=0}^{M-1} |A_n(-\omega)|^2 = \frac{1}{M} \sum_{n=0}^{M-1} \sum_{k=0}^{N-1} b_{nk} \cos(k\omega) \\ &= \frac{1}{M} \sum_{k=0}^{N-1} \sum_{n=0}^{M-1} b_{nk} \cos(k\omega) = \sum_{k=0}^{N-1} c_k \cos(k\omega) \end{aligned} \tag{14}$$

where b_{nk} are constants given by the filter matrix, and $c_k = \sum_{n=0}^{M-1} b_{nk}$. Comparing Equations 12 and 14 we see that the optimum linear clutter filter for packet size N has a frequency response equal to an optimum $(N-1)^{\text{th}}$ order FIR filter when the optimization criterion is as specified in Equation 11. This response can not be obtained with an FIR filter, since at least two output samples are necessary to estimate the blood flow velocity. The optimal response is of value however, since it can be used as a quality measure for other types of filters.

	Min. phase	Lin. phase
ω_p	0.49π	0.58π
d_s [dB]	-87dB	-91dB

Table 2: Optimum linear and minimum phase FIR filters of order 5. Design parameters: minimum $\omega_s = 0.02\pi$, maximum $d_p = 0.5$dB, and minimum $d_s = -80$dB.

3.3 Comparison of Linear and Minimum Phase FIR Filters

When designing both linear- and minimum phase FIR filters, the following parameters defined in Figure 1 were specified:

- Maximum filter order.
- Minimum stopband cut off frequency, ω_s.
- Maximum stopband ripple, d_s.
- Maximum passband ripple, d_p.

With these parameters specified, the minimum passband cut off frequency ω_p was calculated. When the minimum ω_p was found, d_s was minimized without altering the other quantities. Table 2 shows an example of the filter parameters obtained for linear and minimum phase FIR filters of order 5. The corresponding frequency responses are shown in Figure 3, where we see that the passband cut-off frequency decreases from 0.58π to 0.49π when a non-linear phase is allowed. Filters with minimum phase will therefore be used when FIR filters are compared to other filter classes.

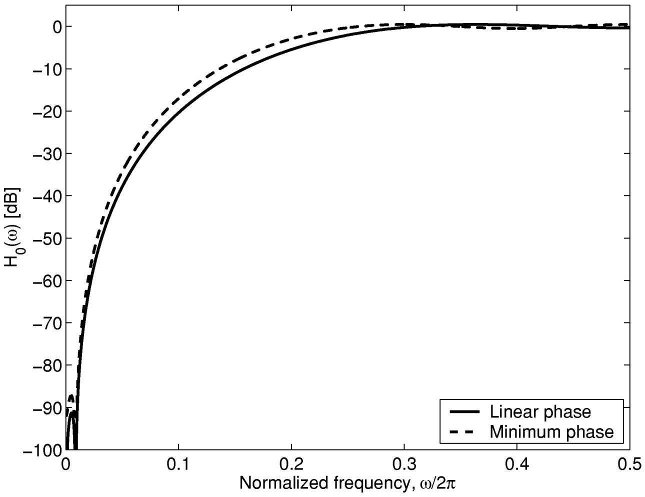

Figure 3: Frequency responses for linear and minimum phase FIR filters of order 5.

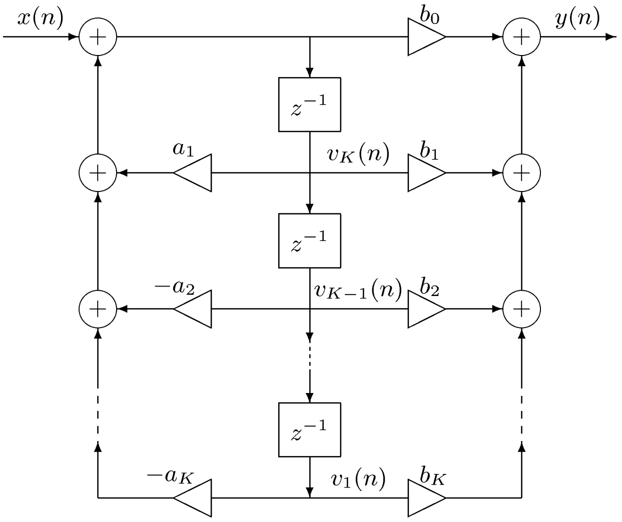

Figure 4: Direct form II realization of IIR filter.

4 Infinite Impulse Response (IIR) Filters

A K^{th} order infinite impulse response (IIR) filter is described by the difference equation

$$y(n) = -\sum_{k=1}^{K} a_k y(n-k) + \sum_{k=0}^{K} b_k x(n-k) \tag{15}$$

where we see that each output sample depends on present and past input samples, as well as past output samples. A direct form II [9] realization of a general IIR filter is shown in Figure 4. The recursive part of the filter causes the response to an impulse input to endure forever, and is the reason why such filters are called IIR filters.

4.1 Steady State and Transient Response

We are interested in input signals of finite length, and will therefore use the one-sided $\mathcal{Z}$-transform in analyzing the system [9]. Transforming Equation 15 gives

$$Y^+(z) = -\sum_{k=1}^{K} a_k z^{-k} \left[Y^+(z) + \sum_{n=1}^{k} y(-n) z^n \right] + \sum_{k=0}^{K} b_k z^{-k} X^+(z) \tag{16}$$

To analyze the transient response, we assume that $x(n)$ has a rational $\mathcal{Z}$-transform, and since it is causal, we may set $X^+(z) = X(z) = N(z)/Q(z)$. The filter has a rational transfer function $H(z) = B(z)/A(z)$ resulting in the following expression for the output signal

$$Y^+(z) = \frac{B(z)}{A(z)} \frac{N(z)}{Q(z)} + \frac{N_0(z)}{A(z)} \tag{17}$$

where $N_0(z) = -\sum_{k=1}^{K} a_k z^{-k} \sum_{n=1}^{k} y(-n)z^n$ depends on the initial values of the filter registers. Assuming no repeated roots in the polynomial $A(z)Q(z)$ and no pole-zero cancellation, a partial fraction expansion gives

$$Y^+(z) = \sum_{k=1}^{K} \frac{A_k}{1 - p_k z^{-1}} + \sum_{k=1}^{K} \frac{Q_k}{1 - q_k z^{-1}} + \sum_{k=1}^{K} \frac{D_k}{1 - p_k z^{-1}} \tag{18}$$

where p_k and q_k are the roots of the polynomials $A(z)$ and $Q(z)$. The last term is due to the nonzero initial conditions. Inverse transformation of Equation 18 gives

$$y(n) = \sum_{k=1}^{K} (A_k + D_k)(p_k)^n u(n) + \sum_{k=1}^{K} Q_k (q_k)^n u(n) = y_{tr}(n) + y_{ss}(n) \tag{19}$$

where $u(n)$ denotes the unit step function. Assuming a stable filter we have $|p_k| < 1$, and the first term vanishes as $n \to \infty$. When the input signal is a sinusoid, the poles q_k fall on the unit circle, and the response persists for all $n \geq 0$. The output is thus divided in a transient part, $y_{tr}(n)$, and a steady state part, $y_{ss}(n)$. The transient part is contained in a K-dimensional vector space spanned by the exponential functions $(p_k)^n$. Both the transient due to the input signal, and the transient due to the non-zero initial conditions are contained in this subspace.

There are many techniques for designing IIR filters based on the steady state magnitude response. Referring to Figure 1, the most common filter types have the following properties [13]:

- Butterworth filters have a monotonic frequency response, and are maximally flat at $\omega = 0$ and at $\omega = \pi$. The first $2N - 1$ derivatives of $|H(\omega)|^2$ are equal to zero at $\omega = 0$ and $\omega = \pi$.
- Chebyshev type I filters have an equiripple passband and a monotonic stopband. The filter is optimal in the sense that among all all-pole filters of order N, this filter has the smallest d_p for fixed ω_s, ω_p, and d_s.
- Chebyshev type II filters have a monotonic passband and an equiripple stopband. The filter is optimal in the sense that among all all-pole filters of order N, this filter has the smallest d_s for fixed ω_s, ω_p, and d_p.
- Elliptic filters have both poles and zeros, and are equiripple in both the passband and the stopband. The filter is optimal in the sense that among all rational transfer functions of a given order, elliptic filters have the smallest d_p for fixed ω_s, ω_p, and d_s.

With an input signal of finite length, the transient response becomes important. Examples of the transient signal for a sinusoidal signal input to Butterworth, Chebyshev, and Elliptic high pass filters of order 3 are shown in Figure 5. As is expected from Equation 19, the Butterworth filter has the smallest transient since among the three filter types, Butterworth filters have poles with the smallest magnitude. Butterworth filters have a wider transition region than the other filters, and there is thus a trade-off between transient duration and magnitude response.

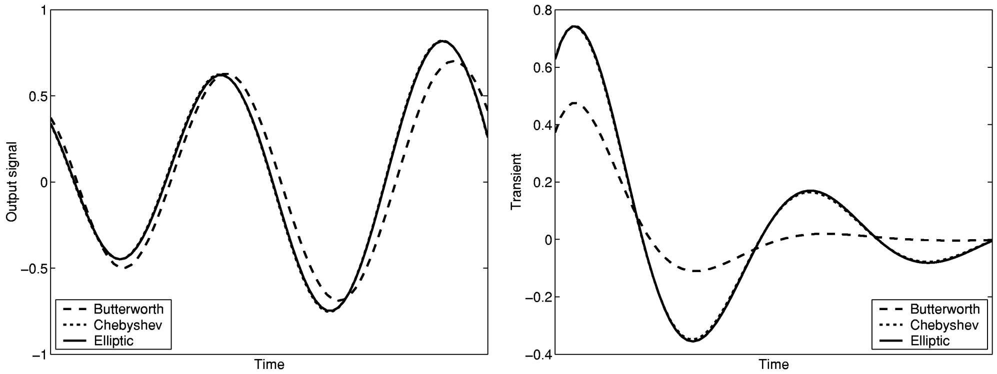

(a) (b)

Figure 5: Filter output (a) and transient signal (b) for the Butterworth, Chebyshev, and Elliptic filters shown in Figure 8. The input signal was $\sin(n\pi/5 + \pi/4)$.

4.2 State Space Formulation

To investigate different techniques for reducing the transient shown in Figure 5, a state space formulation [9] of the IIR filter will be convenient. In Figure 4, the state vector is defined by $\mathbf{v}(n) = [v_1(n)\ v_2(n)\ \dots\ v_K(n)]^T$. The filter is then described by the following state space equations

$$\mathbf{v}(n+1) = \mathbf{F}\mathbf{v}(n) + \mathbf{q}x(n) \tag{20}$$

$$y(n) = \mathbf{g}^T\mathbf{v}(n) + dx(n) \tag{21}$$

where the elements of $\mathbf{F}$, $\mathbf{q}$, $\mathbf{g}$, and d are

$$\mathbf{F} = \begin{bmatrix} 0 & 1 & 0 & \cdots & 0 \\ 0 & 0 & 1 & \cdots & 0 \\ \vdots & \vdots & \vdots & & \vdots \\ 0 & 0 & 0 & \cdots & 1 \\ -a_K & -a_{K-1} & -a_{K-2} & \cdots & -a_1 \end{bmatrix}, \quad \mathbf{q} = \begin{bmatrix} 0 \\ 0 \\ \vdots \\ 0 \\ 1 \end{bmatrix}$$

$$\mathbf{g} = \begin{bmatrix} b_K - b_0 a_n \\ b_{K-1} - b_0 a_{K-1} \\ \vdots \\ b_1 - b_0 a_1 \end{bmatrix}, \quad d = b_0 \tag{22}$$

The state space description of the filter is illustrated in Figure 6. With initial state $\mathbf{v}(0)$, the state at $n > 0$ is given by

$$\mathbf{v}(n) = \mathbf{F}^n\mathbf{v}(0) + \sum_{k=0}^{n-1} \mathbf{F}^{n-1-k}\mathbf{q}x(k) \tag{23}$$

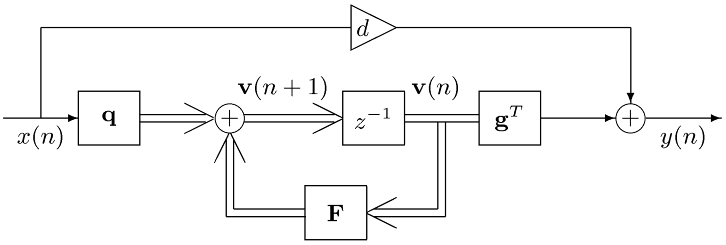

Figure 6: State-space description of IIR filter.

and the filter output is given by

$$y(n) = \begin{cases} \mathbf{g}^T\mathbf{v}(0) + dx(0), & n = 0 \\ \mathbf{g}^T\mathbf{F}^n\mathbf{v}(0) + \sum_{k=0}^{n-1} \mathbf{g}^T\mathbf{F}^{n-1-k}\mathbf{q}x(k) + dx(n), & n > 0 \end{cases} \tag{24}$$

Let the input and output sequences be viewed as $N \times 1$ vectors, $\mathbf{x} = [x(0)\ x(1)\ \ldots\ x(N-1)]^T$, and $\mathbf{y} = [y(0)\ y(1)\ \ldots\ y(N-1)]^T$. Equation 24 can then be written as the matrix-vector equation

$$\mathbf{y} = \mathbf{B}\mathbf{v}(0) + \mathbf{C}\mathbf{x} \tag{25}$$

where

$$\mathbf{B} = \begin{bmatrix} \mathbf{g}^T \\ \mathbf{g}^T\mathbf{F} \\ \vdots \\ \mathbf{g}^T\mathbf{F}^{N-1} \end{bmatrix}, \quad \text{and} \quad \mathbf{C} = \begin{bmatrix} d & 0 & \cdots & 0 & 0 \\ \mathbf{g}^T\mathbf{q} & d & \cdots & 0 & 0 \\ \vdots & \vdots & & \vdots & \vdots \\ \mathbf{g}^T\mathbf{F}^{N-2}\mathbf{q} & \mathbf{g}^T\mathbf{F}^{N-3}\mathbf{q} & \cdots & \mathbf{g}^T\mathbf{q} & d \end{bmatrix} \tag{26}$$

We will now investigate different ways $\mathbf{v}(0)$ can be chosen to minimize the transient.

4.3 Zero Initialization

The initial filter state vector is set equal to the zero vector, $\mathbf{v}(0) = \mathbf{0}$. This is equivalent to assuming that the input signal is identical to zero for $n < 0$. The filtering operation is equal to

$$\mathbf{y} = \mathbf{C}\mathbf{x} \tag{27}$$

where $\mathbf{C}$ is given in Equation 26.

4.4 Step Initialization

The transient response depends on the input signal and can not be removed unless the input signal is completely known. However, the transient can be partially suppressed by using the a priori knowledge available about the input signal. In color flow imaging, the input signal is dominated by the low frequency clutter signal. The input signal is therefore assumed to have a constant value equal to the first signal sample $x(0)$.

For a stable filter, the transient dies out with time, and for a step input, the filter registers converge to constant values. The transient can thus be suppressed by setting the initial filter state equal to the state an infinitely long time after the step is applied at the input. This initial filter state is found by utilizing the final value theorem of the one-sided $\mathcal{Z}$-transform [9]. Transformation of Equation 20 gives

$$\mathbf{V}^{+}(z) = z(z\mathbf{I}-\mathbf{F})^{-1}\mathbf{v}(0) + (z\mathbf{I}-\mathbf{F})^{-1}\mathbf{q}X^{+}(z) \tag{28}$$

and inserting the $\mathcal{Z}$-transform of the assumed input signal gives

$$\begin{aligned}\mathbf{v}_{step}(0) &= \lim_{z\to 1}(z-1)\mathbf{V}^{+}(z)\\ &= \lim_{z\to 1}(z-1)\left(z(z\mathbf{I}-\mathbf{F})^{-1}\mathbf{v}(0) + (z\mathbf{I}-\mathbf{F})^{-1}\mathbf{q}\frac{x(0)z}{z-1}\right)\\ &= x(0)(\mathbf{I}-\mathbf{F})^{-1}\mathbf{q}\end{aligned} \tag{29}$$

Inserting this in Equation 25 the filter with step initialization is given by

$$\begin{aligned}\mathbf{y} &= x(0)\mathbf{B}(\mathbf{I}-\mathbf{F})^{-1}\mathbf{q} + \mathbf{C}\mathbf{x}\\ &= \big(\mathbf{B}(\mathbf{I}-\mathbf{F})^{-1}\mathbf{q}\mathbf{1} + \mathbf{C}\big)\,\mathbf{x}\\ &= \mathbf{A}_s\mathbf{x}\end{aligned} \tag{30}$$

where $\mathbf{1}$ is the $1 \times N$ vector $[1\ 0\ \cdots\ 0]$.

4.5 Projection Initialization

From Equation 19 we see that the transient part of the output signal is of the same form as the response with just a zero input signal. We can further deduce from Equation 25 that the transient is in the subspace spanned by the columns of the matrix $\mathbf{B}$. The projection matrix $\mathbf{P}_B = \mathbf{B}(\mathbf{B}^T\mathbf{B})^{-1}\mathbf{B}^T$ is the projection into this transient subspace [1]. The component of the output signal in the transient subspace is removed by forcing $\mathbf{P}_B\mathbf{y} = \mathbf{0}$. This is obtained by the following initial state vector

$$\mathbf{v}(0) = -(\mathbf{B}^T\mathbf{B})^{-1}\mathbf{B}^T\mathbf{C}\mathbf{x} \tag{31}$$

Inserting this in Equation 25 the filter with projection initialization is given by

$$\mathbf{y} = (\mathbf{I} - \mathbf{B}(\mathbf{B}^T\mathbf{B})^{-1}\mathbf{B}^T)\mathbf{C}\mathbf{x} = \mathbf{A}_p\mathbf{x} \tag{32}$$

4.6 Mirroring of the Input Sequence

The transient decays with time, and the effect of the transient can be reduced by discarding some of the first output samples. This reduction in the number of output samples, however, increases the variance when estimating flow parameters. A better approach is to “increase” the input signal length based on the available samples and then discard the first output samples. One way to obtain this is to mirror the input vector around the first sample, producing the $2N-1$ dimensional vector $\mathbf{x}_m$ as shown

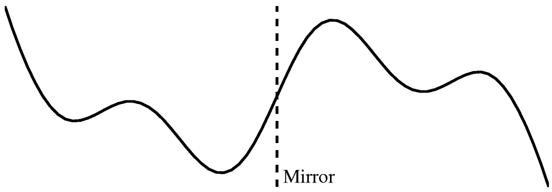

Figure 7: Mirroring of the input sequence around the first sample.

in Figure 7. Mathematically, this mirroring is expressed by the $(2N-1)\times N$ matrix $\mathbf{M}_1$:

$$\mathbf{x}_m = \mathbf{M}_1\mathbf{x}, \quad \text{where} \quad \mathbf{M}_1 = \begin{bmatrix} 2 & 0 & \cdots & 0 & -1 \\ 2 & 0 & \cdots & -1 & 0 \\ \vdots & \vdots & \cdots & \vdots & \vdots \\ 2 & -1 & \cdots & 0 & 0 \\ 1 & 0 & \cdots & 0 & 0 \\ 0 & 1 & \cdots & 0 & 0 \\ \vdots & \vdots & \cdots & \vdots & \vdots \\ 0 & 0 & \cdots & 0 & 1 \end{bmatrix} \tag{33}$$

The matrices in Equation 26 must be adjusted for an input vector of length $2N-1$, and give the output vector $\mathbf{y}_m$. The initial state vector $\mathbf{v}(0)$ is calculated based on $\mathbf{x}_m$. The final output vector $\mathbf{y}$ is the last N samples of $\mathbf{y}_m$. This selection of samples is obtained by the $N\times(2N-1)$ matrix $\mathbf{M}_2$:

$$\mathbf{y} = \mathbf{M}_2\mathbf{y}_m, \quad \text{where} \quad \mathbf{M}_2 = [\mathbf{0}_{N\times N-1}\ \mathbf{I}_{N\times N}] \tag{34}$$

The entire filter including this mirroring operation is given by

$$\mathbf{y} = \mathbf{M}_2\mathbf{B}\mathbf{v}(0) + \mathbf{M}_2\mathbf{C}\mathbf{M}_1\mathbf{x} \tag{35}$$

The matrix $\mathbf{M}_1\mathbf{B}$ has dimensions $N\times N$, while the matrix $\mathbf{M}_2\mathbf{B}$ has dimensions $N\times K$. The mirroring operation can be repeated several times, i.e. the mirrored input vector $\mathbf{x}_m$ can be mirrored to obtain a vector of length $4N-3$.

4.7 Comparison of Initialization Techniques

Examples of frequency responses for Butterworth, Chebyshev, and elliptic filters with different initialization techniques are shown in Figure 8. In this figure we see that for packet size $N=8$, zero initialization results in insufficient stopband rejection. The step initialized filters have a zero at zero frequency, but the stopband is very narrow. The projection initialized filters have a stopband width equal to the steady state response, but with a wider transition region. Frequency responses when the input vector is mirrored are shown in Figure 9. Comparing the responses in Figure 9

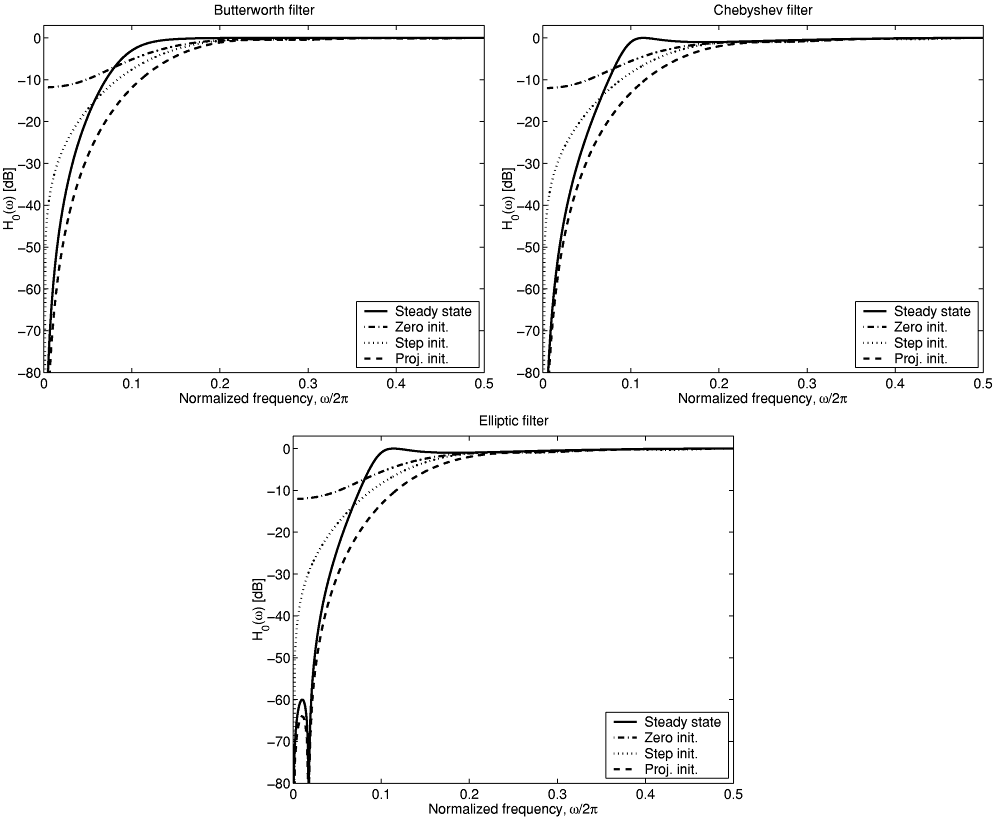

Figure 8: Frequency responses for Butterworth, Chebyshev, and elliptic filters with different initialization techniques. Packet size $N = 8$.

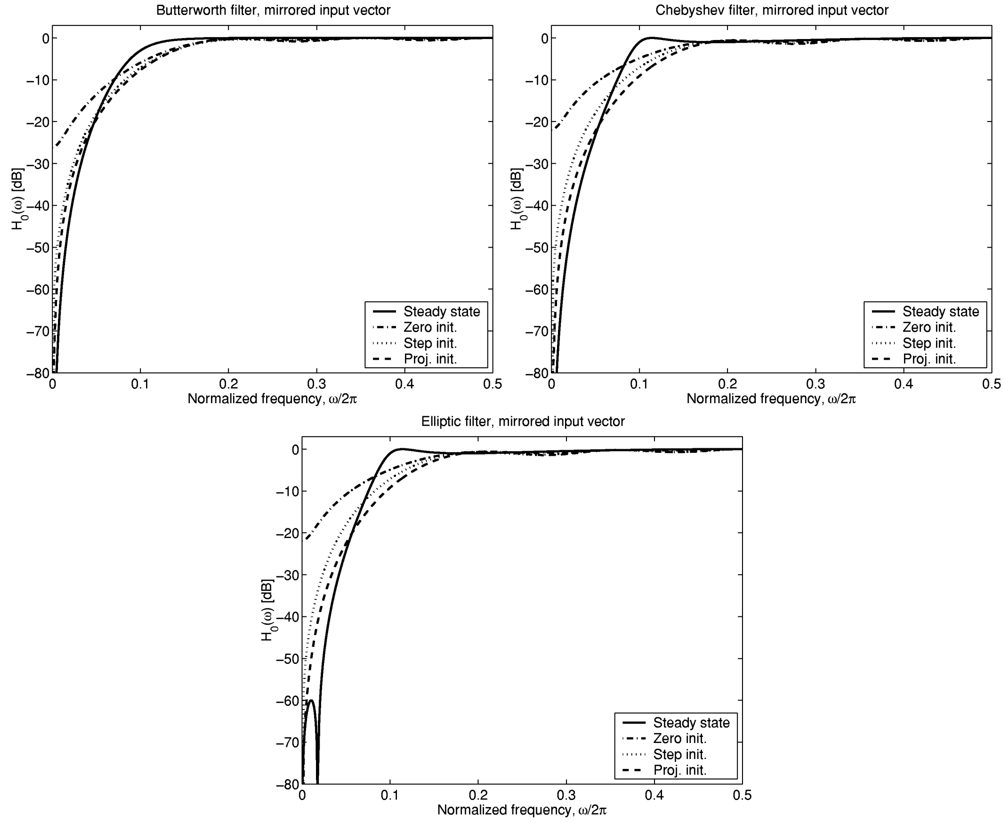

Figure 9: Frequency responses for Butterworth, Chebyshev, and elliptic filters with different initialization techniques when the input signal is mirrored. Packet size $N = 8$.

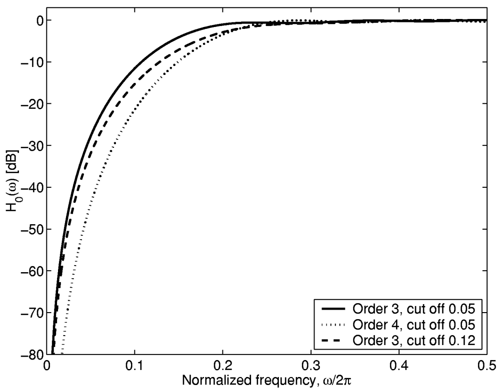

Figure 10: Projection initialized Chebyshev responses as a function of order and steady state cut-off frequency. Packet size $N = 8$.

with those in Figure 8, we see an improvement for zero- and step initialization. For projection initialization, however, mirroring results in a degradation of the response. From Figures 8 and 9, we can conclude that projection initialization without any mirroring of the input vector is the preferred initialization technique for IIR filters. Among the different IIR responses, the Chebyshev response is a good choice since it has a steep transition region and a monotonic stopband. An IIR Chebyshev filter with projection initialization will therefore be used when comparing IIR filters to other filter classes. The stopband width of a projection initialized Chebyshev filter can be increased either by increasing the order or the cut-off frequency of the steady state response. It is, however, not possible to get a significant increase in the −80dB stopband width by increasing the cut-off frequency, the only result is an undesirable widening of the transition region. A better approach is to increase the filter order while keeping the cut-off frequency low. This is illustrated in Figure 10. The frequency responses were also relatively independent of the passband ripple specified for the steady state response. A peak-to-peak ripple of 1dB was used in all the designs of IIR filters.

No symmetry properties can be stated for the rows of an IIR filter matrix. As for minimum phase FIR filters, there is thus a potential reduction of estimator variance if flow parameters are estimated based on two output vectors filtered in the forward and backward direction, respectively. This is investigated in Section 6.

5 Regression Filters

A regression filter calculates the best least-square fit of the signal to a set of curve forms modeling the clutter signal, and subtracts this clutter approximation from the original signal. The curve forms span a subspace of the N-dimensional signal space which we call the clutter space. The best least-square fit is the projection of the signal

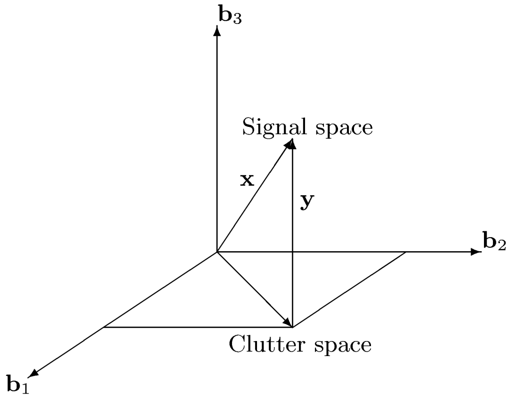

Figure 11: Projection interpretation of regression filters.

into the clutter space, and the filter matrix is given by

$$\mathbf{A} = \mathbf{I} - \sum_{k=0}^{K-1} \mathbf{b}_k \mathbf{b}_k^{*T} \tag{36}$$

where $\mathbf{b}_k$ is a set of orthonormal basis vectors spanning the K-dimensional clutter space, and $\mathbf{I}$ is the identity matrix. This projection interpretation of regression filters is illustrated in Figure 11. The frequency response is

$$H_0(\omega) = 1 - \frac{1}{N} \sum_{k=0}^{K-1} |B_k(\omega)|^2 \tag{37}$$

where $B_k(\omega)$ is the Fourier transform of basis vector k [12]. We see from Equation 37 that to get a high pass filter, the basis vectors should be low-frequency functions. Conventional frequency analysis suggests using low-frequency sinusoids as basis vectors. The regression filter is then equivalent to calculating the Discrete Fourier Transform and then setting the low-frequency coefficients equal to zero prior to the inverse transform. An example of the obtained frequency response is shown in Figure 12a, where we see that this basis does not provide sufficient stopband attenuation. There is a large distance between the zeros in the frequency response, and small attenuation between them. A better frequency response is obtained by increasing the sinusoidal period beyond the packet size. Figure 12b shows the frequency response when the period of the sinusoids is four times the packet size. The zeros come closer together with greater attenuation between them. In the limit, when the period of the sinusoids is increased, they become polynomials within the signal interval. An orthonormal basis is obtained by using the Legendre polynomials as basis vectors, and the resulting filter is called a polynomial regression filter [3, 4, 12]. Frequency responses for polynomial regression filters with different dimensions of the clutter space are shown in Figure 13a. The

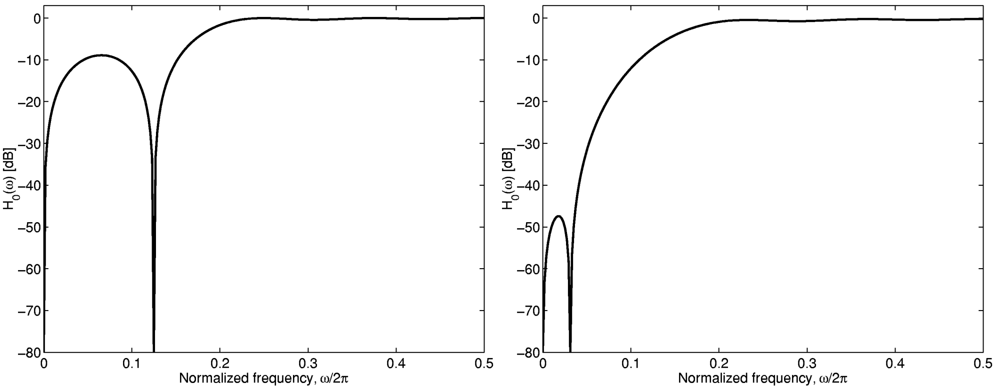

(a) (b)

Figure 12: Frequency responses for regression filters with sinusoidal basis vectors. (a) Sinusoidal period $= N$. (b) Sinusoidal period $= 4N$. Clutter space dimension $K = 3$, and packet size $N = 8$.

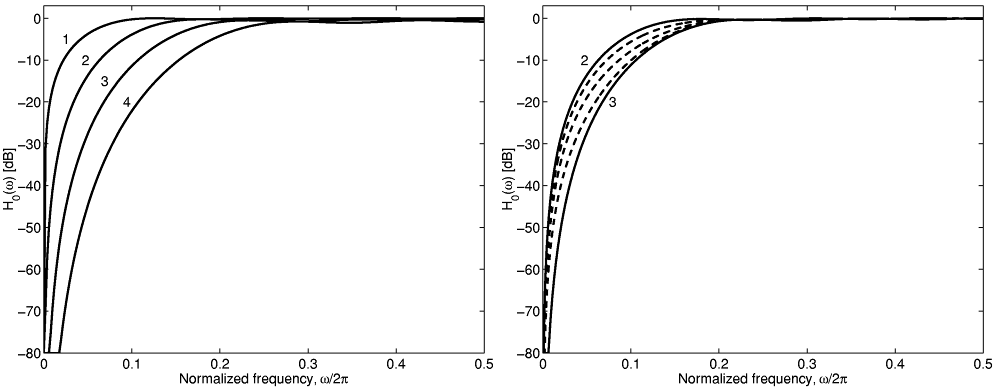

(a) (b)

Figure 13: (a) Frequency responses for polynomial regression filters with packet size $N = 8$. The clutter space dimension is indicated on each curve. (b) Frequency responses for filters described in Equation 38 with $c_0 = c_1 = 1$ and c_2 equal to 0.25, 0.5 and 0.75 are plotted with dashed lines.

polynomial regression filters have a smooth and monotonic frequency response, and a polynomial basis for the clutter space will therefore be used when regression filters are compared to other filter classes. The frequency response of polynomial regression filters changes in discrete steps with clutter space dimension as seen in Figure 13a. The frequency response also varies with packet size. To obtain the same stopband width with a larger packet size, the clutter space dimension has to be increased.

Frequency responses in between those shown in Figure 13a can be obtained by using the filter matrix

$$\mathbf{A} = \mathbf{I} - \sum_{k=0}^{K-1} c_k \cdot \mathbf{b}_k \mathbf{b}_k^{*T} \tag{38}$$

where c_k are real constants. Examples of the resulting frequency responses are shown in Figure 13b for clutter space dimension equal to three, and $c_0 = c_1 = 1$ while c_2 was 0.25, 0.5 and 0.75 in the three examples shown. The −80dB stopband width is not significantly different from the regression filter with clutter space dimension equal to 2. The transition region is, however, significantly wider, and the best performance is obtained with the conventional polynomial regression filter in Equation 36.

The polynomial basis vectors $\mathbf{b}_k$ are either odd or even symmetric, $b(k) = \pm b(N-1-k)$. Using this property in Equation 36, the filter matrix elements satisfy $a(n,k) = a(N-1-n, N-1-k)$. Therefore, a reversal of the input vector only results in a reversal of the output vector. Thus no reduction in estimator variance is obtained by filtering in both the forward and backward direction.

6 Comparison of the Different Filter Classes

In the previous sections, the filters with best frequency responses within the FIR, IIR, and regression filter classes were found. Examples of frequency responses for these three filter classes are shown in Figure 14a for packet size $N = 8$ and in Figure 14b for packet size $N = 16$. The filters were designed with the parameters given in Table 3. These parameters were chosen to achieve filters with comparable frequency responses. The polynomial regression filters have frequency responses almost identical to the projection initialized IIR filters. This is expected since the output vector for both filters is projected into the orthogonal complement of a subspace with low frequency basis functions. The FIR filters have the widest transition regions, and is not the preferred choice based on the frequency response. Figure 14 also contains examples of the power spectra used in the simulations described later in this section.

Blood flow parameters are estimated from the output signal of the clutter filter. It is therefore of interest to see how the clutter filter affects such estimates. A commonly used estimator for the mean velocity in color flow imaging is calculated from an estimate of the autocorrelation function with temporal lag $m = 1$ [5]. Mathematically, the estimator is expressed by

$$\hat{v} = \frac{c}{2f_0T} \cdot \hat{f}_b, \quad \text{where} \quad \hat{f}_b = \arg(\hat{R}(1))/2\pi \tag{39}$$

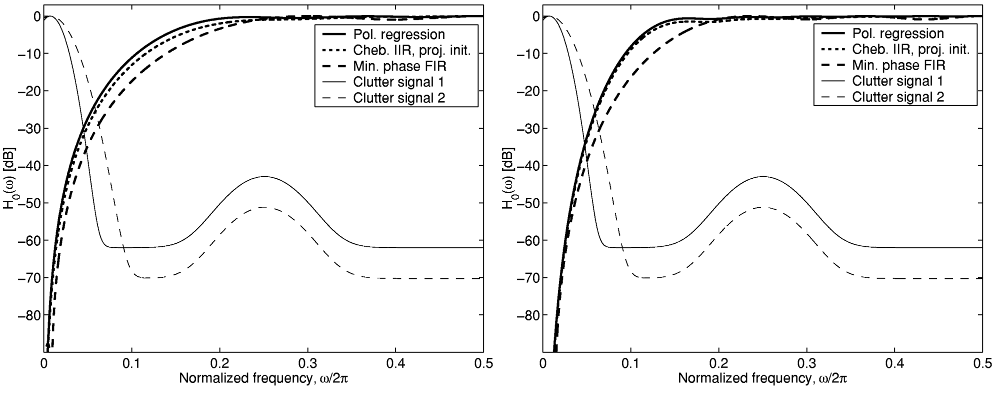

(a) (b)

Figure 14: Comparison of frequency responses of polynomial regression filters, projection initialized IIR Chebyshev filters, and minimum phase FIR filters. (a) Packet size $N = 8$. (b) Packet size $N = 16$. The design parameters are given in Table 3.

Packet size $N = 8$		Packet size $N = 16$	
Filter type	Parameter	Filter type	Parameter
Proj. init. IIR Chebyshev	Order = 3 $\omega_p = 0.2\pi$ $d_p = 0.5$dB	Proj. init. IIR Chebyshev	Order = 5 $\omega_p = 0.1\pi$ $d_p = 0.5$dB
Min. phase FIR	Order = 5 Minimum $\omega_s = 0.02\pi$ Maximum $d_p = 0.5$dB Minimum $d_s = -80$dB Achieved $d_s = -87$dB Achieved $\omega_p = 0.49\pi$	Min. phase FIR	Order = 8 Minimum $\omega_s = 0.03\pi$ Maximum $d_p = 0.5$dB Minimum $d_s = -80$dB Achieved $d_s = -92$dB Achieved $\omega_p = 0.40\pi$
Pol. reg.	Clut. space dim. = 3	Pol. reg.	Clut. space dim. = 5

Table 3: Filter design parameters.

	Clutter signal 1	Clutter signal 2
Clutter-to-flow-signal power ratio, CSR	40dB	50dB
Clutter signal RMS Bandwidth, B_c	0.01PRF	0.015PRF
Clutter signal center frequency, f_c	0.0075PRF	0.0075PRF
Blood signal center frequency, f_b	0 to 0.5PRF	0 to 0.5PRF
Blood signal RMS Bandwidth, B_b	$0.1f_b$	$0.1f_b$

Table 4: Parameters for the simulated spectra. *Clutter signal 1* is plotted with a solid line in Figure 14, while *Clutter signal 2* is plotted with a dashed line.

where c is the sound velocity, f_0 is the ultrasound center frequency, T is the pulse repetition interval, $\hat{R}(1)$ is the autocorrelation estimate, and $\hat{f}_b$ is an estimate of the center frequency of the blood signal. The autocorrelation function can be estimated by the sample mean estimator

$$\begin{aligned}\hat{R}(m) &= \frac{1}{M-m}\sum_{k=0}^{M-m-1} y^*(k)y(k+m)\\ &= \frac{1}{M-m}\sum_{k=0}^{M-m-1}\sum_{j=0}^{N-1}\sum_{n=0}^{N-1} a^*(k,j)a(k+m,n)x^*(j)x(n) \qquad (40)\end{aligned}$$

and we want to investigate how the filter matrix elements $a(k,j)$ influence the mean frequency estimate $\hat{f}_b$. A set of simulations with varying mean blood frequencies was performed with signals having power spectra of the form shown in Figure 14. Both the clutter and blood signal power spectra had a Gaussian shape with parameters given in Table 4. To model the transit time effect, the bandwidth of the blood signal was proportional to the center frequency. The synthetic blood signal was generated by first calculating the Discrete Fourier Transform of a signal consisting of $512 \cdot N$ samples of complex white Gaussian noise. This signal was then multiplied by a mask corresponding to the power spectrum of the blood signal, and transformed back to the time domain. The clutter signal was calculated in a similar manner. Finally, the signal used in the simulations was the sum of these two signals and complex white Gaussian noise, giving a power spectrum as shown in Figure 14. Subdividing this signal into vectors of dimension N, we got 512 realizations of a signal with packet size N. This procedure was repeated 512 times giving a total of 262 144 realizations for each blood signal center frequency. When aliasing of the velocity estimates occurred, $\pm 2\pi$ was added to $\arg(\hat{R}(1))$ in Equation 39 to ensure that the estimates were contained in the interval $[f_b - 0.5, f_b + 0.5]$.

Figure 15 shows the bias and standard deviation of the mean frequency estimate with no clutter signal and a signal-to-noise ratio (SNR) of 30dB. The packet size is $N = 8$. The filters are designed to suppress signals with frequencies in the stopband, and therefore yield a large bias and standard deviation for Doppler frequencies within the stopband. The transition region should be as narrow as possible, and in this region we see that the polynomial regression filter yields a considerably larger bias than the

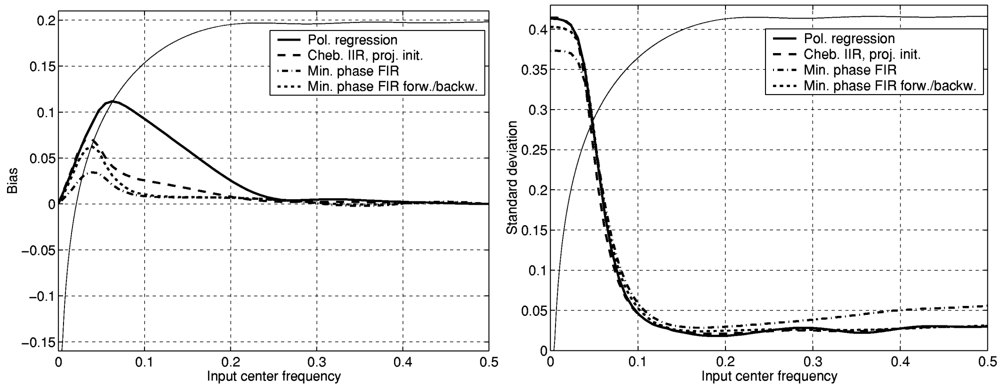

(a) (b)

Figure 15: (a) Bias and (b) standard deviation of the mean frequency estimate for the three different filters in Figure 14a. The frequency of the polynomial regression filter is plotted to indicate the passbands of the filters. No clutter is present and the SNR is 30dB. The packet size is $N = 8$.

other filters. The regression filter also yields bias for a larger range of frequencies. In the passband, however, all the filters yield a negligible bias. For the FIR filter, the standard deviation in the passband is reduced when the estimate is calculated from two vectors filtered in the forward and backward direction. The improvement is largest for high frequencies since the bandwidth of the blood signal is proportional to the center frequency.

Figure 16 shows the results when the SNR is reduced to 6dB. Compared with the results for SNR=30dB, we see that the bias in the transition region and passband increases for all the filters. We also see that the regression filter has the largest bias. The difference in bias between the regression filter and the other filters is, however, much smaller for SNR=6dB which is a realistic signal-to-noise ratio. The standard deviation in the passband increases for all the filters, and the FIR filter yields a considerably higher standard deviation in the passband than the other filters. When the estimate is calculated from two vectors filtered in the forward and backward direction, the standard deviation within the passband is significantly reduced, and is comparable to the IIR and regression filter. For a linear phase FIR filter the standard deviation was approximately equal to the values obtained with a minimum phase filter applied only in the forward direction. For IIR filters there was no significant reduction of the standard deviation when filtering in both the forward and backward direction.

To see how clutter affects the mean frequency estimate, we repeated the simulations including a clutter signal denoted *Clutter signal 1.* To study the decay in performance with increased clutter level, we also performed simulations with *Clutter signal 2* where both the amplitude and bandwidth was increased. The detailed parameters for these two signals are given in Table 4. The results for *Clutter signal 1* are shown in Figure 17

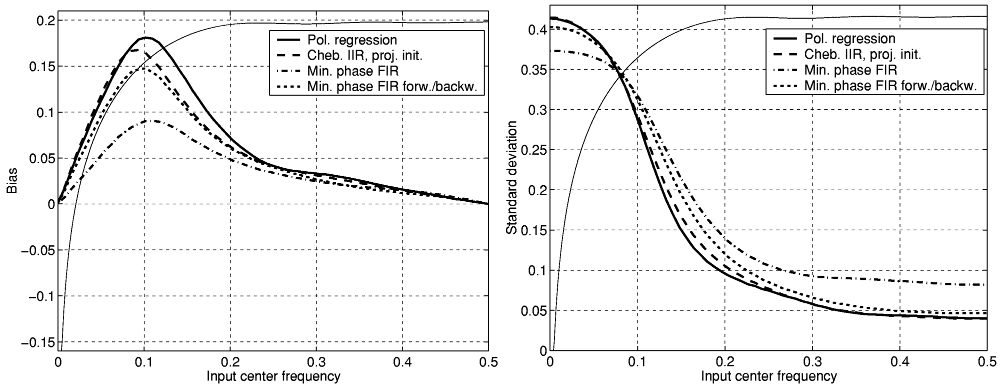

(a) (b)

Figure 16: (a) Bias and (b) standard deviation of the mean frequency estimate for the three different filters in Figure 14a. The frequency of the polynomial regression filter is plotted to indicate the passbands of the filters. No clutter is present and the SNR is 6dB. The packet size is $N = 8$.

where we see that they are very similar to the results with no clutter signal shown in Figure 16. This means that all the filters sufficiently suppress a clutter signal with this amplitude, bandwidth, and center frequency.

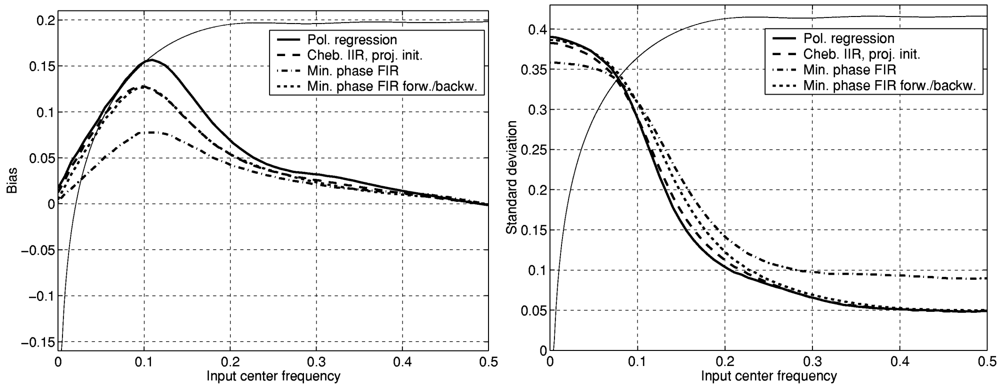

(a) (b)

Figure 17: (a) Bias and (b) standard deviation of the mean frequency estimate with *Clutter signal 1* for the three different filters in Figure 14a. The frequency of the polynomial regression filter is plotted to indicate the passbands of the filters. The SNR is 6dB and the packet size is $N = 8$.

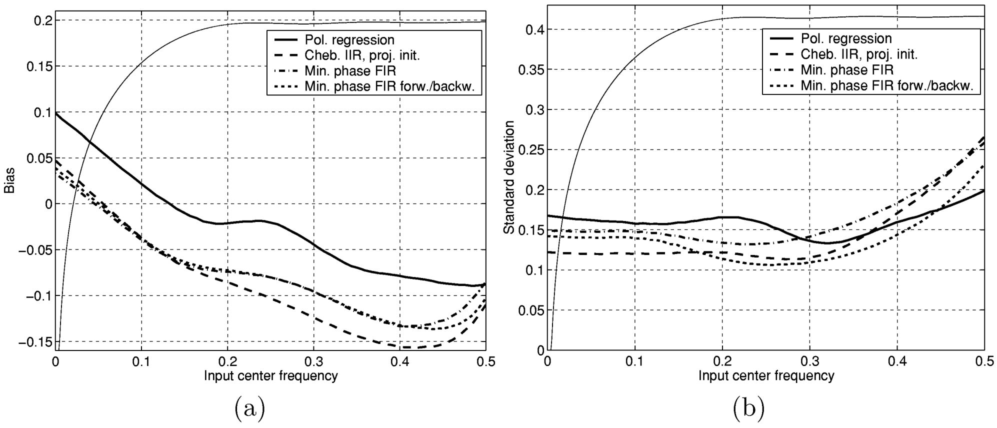

Figure 18: (a) Bias and (b) standard deviation of the mean frequency estimate with *Clutter signal 2* for the three different filters in Figure 14a. The frequency of the polynomial regression filter is plotted to indicate the passbands of the filters. The SNR is 6dB and the packet size is $N = 8$.

The results for *Clutter signal 2* are shown in Figure 18 where we see that the mean frequency estimates are strongly affected by this clutter signal. When studying Figure 14a, we see that the power of *Clutter signal 2* after filtering is above the thermal noise level. This low frequency signal component is an explanation for the significant negative bias in Figure 18a. The standard deviation within the passband is also large for *Clutter signal 2*. Based on the results in Figure 18 it can be concluded that none of the filters sufficiently suppress *Clutter signal 2*. The results also indicate that all the filters break down at approximately the same clutter power, bandwidth and center frequency.

The influence of the packet size on the quality of the mean frequency estimator was investigated by increasing the packet size from 8 to 16. To maintain approximately the same stopband width, the dimension of the clutter space used in the regression filter was increased from 3 to 5. The other filter types were also redesigned with parameters given in Table 3 to get frequency responses similar to the regression filter as shown in Figure 14b. The results for *Clutter signal 1* are shown in Figure 19. When comparing Figure 19a and Figure 17a, we see that the range of frequencies with considerable bias is reduced when the packet size is increased from 8 to 16. This effect is related to the narrower transition region of the filters used for $N = 16$. The standard deviation of the estimates decreases with packet size since the estimates are based on a larger number of samples. The relative advantage achieved by applying the FIR filter in both directions is the same for $N = 8$ and $N = 16$.

The results for *Clutter signal 2* are shown in Figure 20 where we see that all the filters have similar performance and yield a small negative bias for Doppler frequencies within the passband. We also see that the standard deviation is significantly increased

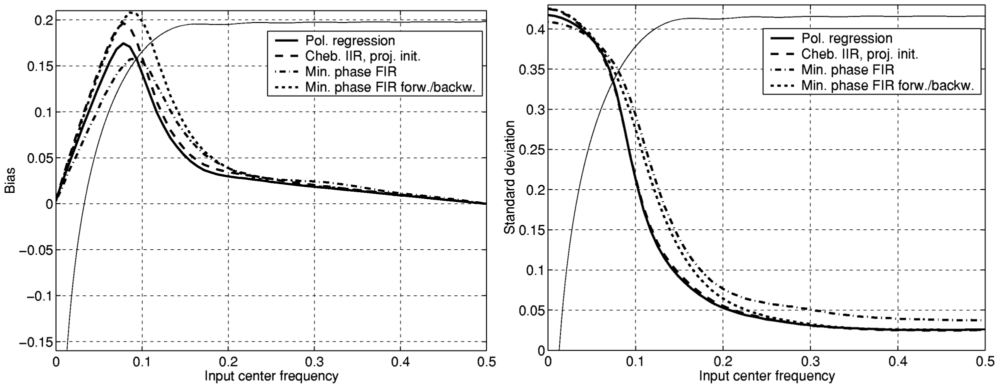

(a) (b)

Figure 19: (a) Bias and (b) standard deviation of the mean frequency estimate with *Clutter signal 1* for the three different filters in Figure 14a. The frequency of the polynomial regression filter is plotted to indicate the passbands of the filters. The SNR is 6dB and the packet size is $N = 16$.

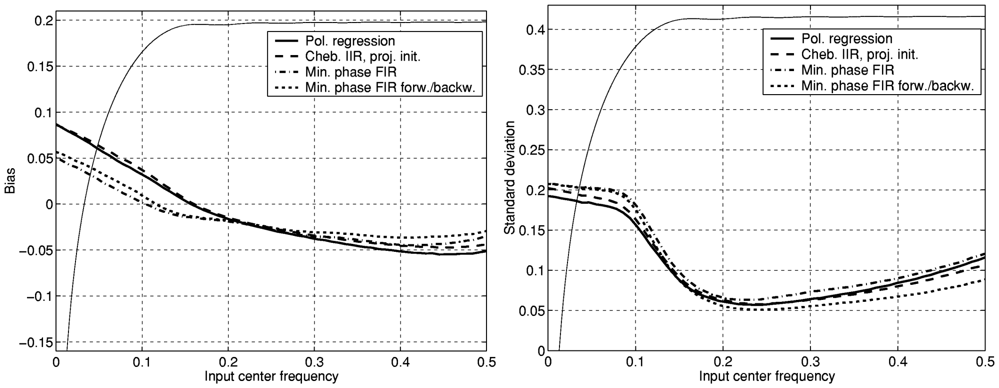

(a) (b)

Figure 20: (a) Bias and (b) standard deviation of the mean frequency estimate with *Clutter signal 2* for the three different filters in Figure 14a. The frequency of the polynomial regression filter is plotted to indicate the passbands of the filters. The SNR is 6dB and the packet size is $N = 16$.

for the highest Doppler frequencies compared to the results for *Clutter signal 1* shown in Figure 19. The filters do not completely suppress the clutter signal, but they perform significantly better than the filters used for packet size $N = 8$. An explanation for this is the wider stopbands of the filters used for $N = 16$.

7 Discussion and Conclusions

The frequency response of FIR filters is improved when a nonlinear phase response is allowed. The commonly used autocorrelation estimates do not depend on the phase response, so a filter with non-linear phase response can safely be chosen. A significant reduction of the variance of the mean frequency estimator was obtained by filtering with a minimum phase filter in both the forward and backward direction. Linear phase FIR filters have symmetric impulse responses, and nothing is gained by filtering in both the forward and backward direction. A large gain in performance can thus be obtained by using a minimum phase filter instead of a linear phase filter.

For short signal lengths, the frequency response for IIR filters is highly dependent on the initialization technique. We found that the best frequency response for IIR filters is obtained when projection initialization is used. The other initialization techniques do not provide a sufficient stopband width for clutter rejection.

Within the class of regression filters, polynomial basis functions were shown to provide useful frequency responses. Polynomial regression filters and projection initialized IIR filters of the same order have almost identical properties. An explanation for this is that the output vector for both filters is projected into the orthogonal complement of a subspace with low frequency basis functions.

Among the three filter classes, polynomial regression filters and projection initialized IIR filters have the best frequency response. For equal stopband width, the transition regions were narrower than for FIR filters. An advantage of FIR filters is the greater flexibility in specifying the filter cut-off frequency, which is also independent of the packet size. To increase the stopband width for projection initialized IIR filters, it was better to increase the filter order than to increase the steady state cut-off frequency.

Simulations were performed to investigate how the bias and standard deviation of the mean frequency estimator were affected by the clutter filters. The simulations showed that for all the filter types, the frequency response is a reliable indicator of the range of blood velocities that can be measured with good quality. For Doppler frequencies within the passband, there was no significant differences in the bias produced by the different filters for realistic noise and clutter levels. The different filter types break down at approximately the same clutter level. IIR and regression filters provide a larger number of output samples than FIR filters provide. The simulations showed that this larger number of samples reduces the variance of the mean frequency estimator within the passband compared to FIR filters. By using a minimum phase FIR filter in both the forward and backward direction, there was, however, no significant difference in variance between the three filter classes. The simulations also showed that the relative performance between the filters did not change significantly with packet size.

When using projection initialization, IIR filters have a computational complexity similar to that of regression filters. The computational complexity is considerably smaller for FIR filters. However, if minimum estimator variance is desired, the FIR filter should be applied twice, and more computations are needed for the autocorrelation estimate.

8 Acknowledgements

This study was supported by the Research Council of Norway. We thank Nancy Lea Eik-Nes for revision of the manuscript.

References

1. E. S. Chornoboy. Initialization for improved IIR filter performance. *IEEE Trans. Signal Process.*, 40(3):543–550, Mar. 1992.

2. R. H. Fletcher and D. W. Burlage. An initialization technique for improved MTI performance in phased array radars. *Proc. IEEE*, 60:1551–1552, Dec. 1972.

3. A. P. G. Hoeks, J. J. W. van de Vorst, A. Dabekaussen, P. J. Brands, and R. S. Reneman. An efficient algorithm to remove low frequency Doppler signals in digital Doppler systems. *Ultrason. Imag.*, 13(2):135–144, Apr. 1991.

4. A. P. Kadi and T. Loupas. On the performance of regression and step-initialized IIR clutter filters for color Doppler systems in diagnostic medical ultrasound. *IEEE Trans. Ultrason., Ferroelect., Freq. Contr.*, 42(5):927–937, Sept. 1995.

5. C. Kasai, K. Namekawa, A. Koyano, and R. Omoto. Real-time two-dimensional blood flow imaging using an autocorrelation technique. *IEEE Trans. Sonics Ultrason.*, 32(3):458–464, May 1985.

6. J. S. Lim and A. V. Oppenheim, editors. *Advanced Topics in Signal Processing.* Prentice Hall, Inc., 1988.

7. T. W. Parks and C. S. Burrus. *Digital Filter Design.* John Wiley & Sons, Inc., 1987.

8. R. B. Peterson, L. E. Atlas, and K. W. Beach. A comparison of IIR initialization techniques for improved color Doppler wall filter performance. In *1994 IEEE Ultrasonics Symposium Proceedings*, volume 3, pages 1705–1708, Nov. 1994.

9. J. G. Proakis and D. G. Manolakis. *Digital Signal Processing, Principles, Algorithms, and Applications.* Macmillan Publishing Company, second edition, 1992.

10. M. A. Shariati, J. H. Dripps, and W. N. McDicken. Deadbeat IIR based MTI filtering for color flow imaging systems. In *1993 IEEE Ultrasonics Symposium Proceedings*, volume 2, pages 1059–1063, Oct. 1993.

11. L. Thomas and A. Hall. An improved wall filter for flow imaging of low velocity flow. In *1994 IEEE Ultrasonics Symposium Proceedings*, volume 3, pages 1701–1704, Nov. 1994.

12. H. Torp. Clutter rejection filters in color flow imaging: A theoretical approach. *IEEE Trans. Ultrason., Ferroelect., Freq. Contr.*, 44(2):417–424, Mar. 1997.

13. P. P. Vaidyanathan. *Multirate Systems and Filter Banks.* Prentice Hall, Inc., 1993.

Paper B

Clutter Filters Adapted to Tissue Motion in Ultrasound Color Flow Imaging

Steinar Bjærum, Hans Torp and Kjell Kristoffersen[†]

Department of Physiology and Biomedical Engineering,
Norwegian University of Science and Technology, Trondheim, Norway
[†]GE Vingmed Ultrasound,
Horten, Norway

Abstract

The quality of ultrasound color flow images is highly dependent on sufficient attenuation of the clutter signals originating from stationary and slowly moving tissue. Without sufficient clutter rejection, the detection of low velocity blood flow will be poor, and the velocity estimates will have a large bias. In some situations, e.g. when imaging the coronary arteries or when the operator moves the probe in search for small vessels, there is considerable movement of tissue. It has been suggested that clutter rejection can be improved by mixing down the signal with an estimate of the mean frequency prior to high-pass filtering. In this paper we compare this algorithm with several other adaptive clutter filtering algorithms using both experimental data and simulations. We found that even a slight acceleration of the tissue has a large effect on the clutter rejection. The best results were obtained by mixing down the signal with non-constant phase increments estimated from the signal. This adapted the filter to a possibly accelerated tissue motion, and gave a significant improvement in clutter rejection.

Submitted to *IEEE Trans. Ultrason., Ferroelect., Freq. Contr.*

1 Introduction

In ultrasound Doppler blood flow measurements, the signal scattered from blood is corrupted by signals scattered from stationary or slowly moving muscular tissue such as vessel walls, and by stationary reverberations. This clutter signal is typically 40-100dB stronger than the signal from blood. The signal scattered by the rapidly moving blood cells has a larger Doppler shift than the signal reflected from slowly moving tissue. A high-pass filter can therefore be used to separate the signals from blood and tissue. Blood velocities are commonly estimated using a mean frequency estimator [5], and to obtain unbiased blood velocity estimates, the clutter signal needs to be attenuated down to the thermal noise level. To get adequate frame rates in 2D color flow imaging, there are typically only 8-16 samples available for high-pass filtering, and efficient clutter filtering is thus a challenging problem.

The signal scattered by moving tissue may have a non-zero mean frequency, and it has been shown that clutter filtering is improved by adapting the filter to the tissue movement [9]. Examples of situations where the tissue movement can be relatively large are imaging of the coronary arteries in the moving heart muscle, and when the operator moves the probe in search of small blood vessels. Adaptation to the tissue movement can be obtained by mixing down the signal with the estimated mean frequency of the clutter signal; this centers the clutter spectrum around zero frequency [9]. After this down-mixing, the clutter can be efficiently attenuated using a high-pass filter with a narrow stop-band, and a broader range of blood velocities can be measured than is possible with a non-adaptive filter.

When imaging low velocity blood flow, the observation time is relatively long, and there might be a considerable acceleration of the tissue during the observation time. We have experienced that it is difficult to obtain sufficient clutter attenuation in such situations, even when down-mixing with the mean frequency is done prior to the high-pass filter. In this paper we propose several new algorithms to improve the clutter rejection when the tissue does not move with constant velocity. The algorithms are based on the fact that a time-varying velocity results in a clutter signal that is a non-stationary stochastic process. We compared the proposed algorithms to each other and to the mean frequency technique by using experimental data recorded while moving the probe in search for small blood vessels in the thyroid gland. To verify the experimental results, we also performed simulations using the Field II program [2].

The paper is organized as follows. First, a model of the Doppler signal is developed in Section 2. The different algorithms are presented in Section 3 before they are compared using experimental data in Section 4. The experimental results are verified by simulations using the Field II program in Section 5. The results are discussed in Section 6, and conclusions are drawn in Section 7.

2 Signal Model

The point scatterer response of an ultrasound imaging system, $e(\mathbf{r}, t)$, is defined as the electrical response in the receiver from a point scatterer at position $\mathbf{r}$. The transducer is positioned at $\mathbf{r} = 0$, and is excited with an electrical pulse at time $t = 0$. Let $o(\mathbf{r}, t)$ be the scattering amplitude which is related to the variation in density and compressibility of the object. To obtain the received signal $x(t)$, the point scatterer response is multiplied with the scattering amplitude $o(\mathbf{r}, t)$ at the time when the transmitted pulse arrives at $\mathbf{r}$, and the product is integrated over space giving

$$x(t) = \int_V e(\mathbf{r}, t) o\left(\mathbf{r}, t - \frac{|\mathbf{r}|}{c}\right) d\mathbf{r} + w(t) \approx \int_V e(\mathbf{r}, t) o\left(\mathbf{r}, \frac{t}{2}\right) d\mathbf{r} + w(t) \tag{1}$$

where c is the speed of sound, and $w(t)$ is white thermal noise. The approximation is valid since the speed of sound is much higher than the scatterer velocity, and it is reasonable to neglect the scatterer movement during the interaction between the sound wave and the scatterer.

The dimensions of the spatial variations in the acoustic parameters of human tissue are much smaller than the spatial resolution of an ultrasound imaging system. The received signal for each point in the image is thus an average of the contribution from a large number of scatterers which makes it convenient to model the scattering medium by a stochastic ensemble. The scattering amplitude function $o(\mathbf{r}, t)$ is thus modeled as a zero-mean random process in space and time, and important results can be obtained from the correlation function defined by

$$R_o(\mathbf{r}, \mathbf{l}, t, \tau) = E\{o(\mathbf{r}, t) o(\mathbf{r} + \mathbf{l}, t + \tau)\} \tag{2}$$

where $\mathbf{l}$ and τ are the lags in the spatial and temporal direction, respectively.

A 2D Doppler imaging system scans the ultrasound beam over the region to be imaged, transmits N pulses in each direction with repetition time T, and estimates the blood flow velocities from the back-scattered signals. For each beam direction there is therefore a two-dimensional signal $x(t, n)$, where t is the time after a pulse transmission, and n is the pulse number. The received signal from pulse n is from Equation 1 equal to

$$x(t, n) = \int_V e(\mathbf{r}, t) o(\mathbf{r}, t/2 + nT) d\mathbf{r} + w(t) \tag{3}$$

and using Equation 2, the autocorrelation function of $x(t, n)$ is given by

$$\begin{aligned} R_x(t, \tau, n, m) &= E\{x(t, n) x(t + \tau, n + m)\} \\ &= \int\int e(\mathbf{r}_1, t) e(\mathbf{r}_2, t + \tau) R_o(\mathbf{r}_1, \mathbf{r}_2 - \mathbf{r}_1, t/2 + nT, \tau/2 + mT) d\mathbf{r}_1 d\mathbf{r}_2 + \sigma_w^2 \delta(m, \tau) \end{aligned} \tag{4}$$

where τ is the lag in "fast" time corresponding to depth in the image, and m is the lag in "slow" time corresponding to the pulse number. The thermal noise is uncorrelated with the back-scattered signal, has variance σ_w^2, and is white, as indicated by the delta function $\delta(m, \tau)$.

2.1 Building Blocks of the Point Scatterer Response

The point scatterer response is a temporal convolution of the following terms [3]:

- The electrical pulse $p(t)$ applied to the transducer.
- The coupling between the electrical signal and mechanical vibrations of the transducer in the transmitting mode $h_{et}(t)$, and in the receiving mode $h_{er}(t)$.
- The acoustical spatial impulse response of the transducer aperture in the transmitting mode $h_{at}(\mathbf{r}, t)$, and in the receiving mode $h_{ar}(\mathbf{r}, t)$. These functions depend on the spatial position of the scatterer, and account for the diffraction and frequency dependent attenuation.
- A temporal filter accounting for the frequency dependent scattering characteristics, $h_s(t)$. The frequency response of the scattering process is modeled to be independent of the spatial position.
- A receive filter, $h_{rec}(t)$, matched to the received pulse bandwidth to optimize the signal-to-noise ratio.

All the temporal signals can be combined into a single signal $y(t)$, and the transmit and receive spatial impulse responses can be combined into a pulse-echo spatial impulse response, $h_{pe}(\mathbf{r}, t)$. The point scatterer response $e(\mathbf{r}, t)$ is then given by

$$e(\mathbf{r}, t) = h_{pe}(\mathbf{r}, t) \underset{t}{*} y(t) \tag{5}$$

where $y(t) = p(t) \underset{t}{*} h_{et}(t) \underset{t}{*} h_s(t) \underset{t}{*} h_{er}(t) \underset{t}{*} h_{rec}(t)$, and $h_{pe}(\mathbf{r}, t) = h_{at}(\mathbf{r}, t) \underset{t}{*} h_{ar}(\mathbf{r}, t)$. The receiver filter can be constructed from a low-pass prototype $h_{LP}(t)$ as shown in Figure 1a, where f_0 is the center frequency of the received signal.

2.2 Statistical Model of a Uniform Scattering Medium with Short Correlation Length

When the scattering amplitude function $o(\mathbf{r}, t)$ has a short spatial correlation length for a fixed time, the correlation function in Equation 2 can be approximated by

$$R_o(\mathbf{r}, \mathbf{l}, t, 0) \approx \sigma_o^2(\mathbf{r}, t)\delta(\mathbf{l}) \tag{6}$$

where $\sigma_o^2(\mathbf{r}, t)$ is the variance of the scattering amplitude function. The approximation is valid when the correlation function is non-zero only for spatial lags much shorter than the wavelength of the imaging system. In a region with uniform scattering properties in space and time, the variance of the scattering amplitude is constant, and the correlation function is further simplified to

$$R_o(\mathbf{r}, \mathbf{l}, t, 0) \approx \sigma_o^2\delta(\mathbf{l}) \tag{7}$$

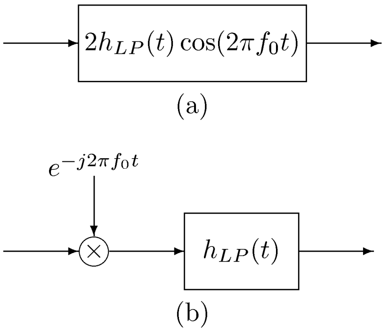

Figure 1: (a) Band-pass receiver filter. (b) Complex demodulation combined with a low-pass receiver filter. The center frequency of the received signal is f_0.

A displacement function $\mathbf{d}(\mathbf{r}, t, \tau)$ is defined such that $\mathbf{r} + \mathbf{d}(\mathbf{r}, t, \tau)$ is the position at time $t + \tau$ of the scatterer which at time t was at the position $\mathbf{r}$. Inserting this displacement function into Equation 7 gives the simplified correlation function

$$R_o(\mathbf{r}, \mathbf{l}, t, \tau) = \sigma_o^2 \delta(\mathbf{l} - \mathbf{d}(\mathbf{r}, t, \tau)) \tag{8}$$

which is valid both for tissue regions with uniform scattering properties and short spatial correlation length, and for blood. Inserting Equation 8 into Equation 4, the correlation function for the received signal becomes

$$R_x(t, \tau, n, m) = \sigma_o^2 \int e(\mathbf{r}, t) e(\mathbf{r} + \mathbf{d}(\mathbf{r}, t/2 + nT, \tau/2 + mT), t + \tau) d\mathbf{r} + \sigma_w^2 \delta(m, \tau) \tag{9}$$

Equation 9 is a great simplification compared to Equation 4, and this simple model of the scattering medium can be used to get important information about the imaging system.

2.3 The Doppler Signal

A well established technique in color flow imaging is to estimate the blood flow velocities based on the temporal samples of the complex demodulated signal from fixed positions in space [5]. Complex demodulation can be combined with the receiver filter as shown in Figure 1b. The clutter filter thus operates on a one-dimensional signal consisting of samples from N consecutive pulse transmissions, and it is convenient to organize these N samples of the complex demodulated Doppler signal for each depth index k in an N-dimensional vector

$$\mathbf{x}_k = [x(2kr_s/c, 0), x(2kr_s/c, 1), \ldots, x(2kr_s/c, N-1)]^T \tag{10}$$

where r_s is the distance between samples in the depth direction. Being a sum of the signals from a large number of independent scatterers, the Central Limit Theorem [7] tells us that $x(t, n)$ is a zero mean Gaussian random process. The vector $\mathbf{x}_k$ contains samples of $x(t, n)$ subsequent to complex demodulation, and has a complex Gaussian probability density function (PDF) with zero mean given by

$$f_{\mathbf{x}_k}(\mathbf{x}_k) = \frac{1}{\pi^N |\mathbf{R}_{x_k}|} e^{-\mathbf{x}_k^{*T} \mathbf{R}_{x_k}^{-1} \mathbf{x}_k} \tag{11}$$

where $\mathbf{x}_k^{*T}$ is the complex conjugated transpose of $\mathbf{x}_k$, and the correlation matrix $\mathbf{R}_{x_k}$ is defined by

$$\mathbf{R}_{x_k} = E\{\mathbf{x}_k \mathbf{x}_k^{*T}\} \tag{12}$$

where $E\{\cdot\}$ denotes the expected value. Equation 11 shows that the PDF of $\mathbf{x}_k$ is completely characterized by the correlation matrix $\mathbf{R}_{x_k}$ where element (i, j) is given by

$$[\mathbf{R}_{x_k}]_{i,j} = R_x(i, j, kr_s/c, 0) \tag{13}$$

where R_x is calculated in Equation 4, or by the simplified expression in Equation 9. In addition to the signal scattered by the moving blood cells, there is a component from the much stronger tissue scatterers, and the signal is also corrupted by reverberations. The signal from tissue together with the reverberation noise will be denoted the clutter signal, and the signal vector is given by

$$\mathbf{x}_k = \mathbf{c}_k + \mathbf{w}_k + \mathbf{b}_k = \mathbf{n}_k + \mathbf{b}_k \tag{14}$$

where $\mathbf{c}_k$ is the clutter signal, $\mathbf{b}_k$ is the signal scattered back from the moving blood cells, $\mathbf{w}_k$ is the thermal noise, and $\mathbf{n}_k$ is the sum of the clutter and thermal noise. The three signal components originate from different sources and are statistically independent. The correlation matrix is then given by

$$\mathbf{R}_{x_k} = \mathbf{R}_{c_k} + \sigma_w^2 \mathbf{I} + \mathbf{R}_{b_k} = \mathbf{R}_{n_k} + \mathbf{R}_{b_k} \tag{15}$$

where $\mathbf{R}_{c_k}$ is the clutter correlation matrix, $\mathbf{R}_{b_k}$ is the blood correlation matrix, σ_w^2 is the noise variance, $\mathbf{I}$ is the identity matrix, and $\mathbf{R}_{n_k}$ is the correlation matrix of the total noise signal.

2.4 Signal Decomposition

The expression for the correlation function in Equation 9 shows that a time-varying displacement function results in a non-stationary signal. To characterize the signal, we will therefore use the Discrete Karhunen-Loève transform (DKLT) which provides a generalization of conventional Fourier analysis for non-stationary random processes [8].

The aim of clutter filters is to attenuate the clutter signal, and the DKLT will be developed for the clutter part of the signal. The DKLT is based on an eigenvector decomposition of the correlation matrix, where the eigenvectors $\mathbf{e}_i$ and eigenvalues λ_i are found by solving the equation

$$\mathbf{R}_c \mathbf{e}_i = \lambda_i \mathbf{e}_i \tag{16}$$

The correlation matrix $\mathbf{R}_c$ is Hermitian symmetric and positive semidefinite [8], and it is possible to find N orthonormal eigenvectors $\mathbf{e}_1, \mathbf{e}_2, \ldots, \mathbf{e}_N$ and a corresponding set of eigenvalues $\lambda_1, \lambda_2, \ldots, \lambda_N$ which are all real and non-negative. In the following discussion, the eigenvalues are ordered in decreasing magnitude, i.e. $\lambda_1 \geq \lambda_2 \geq \ldots \geq \lambda_N$. Defining the eigenvalue and eigenvector matrices by

$$\boldsymbol{\Lambda} = \begin{bmatrix} \lambda_1 & 0 & \cdots & 0 \\ 0 & \lambda_2 & \cdots & 0 \\ \vdots & \vdots & & \vdots \\ 0 & 0 & \cdots & \lambda_N \end{bmatrix} \quad \text{and} \quad \mathbf{E} = \begin{bmatrix} | & | & & | \\ \mathbf{e}_1 & \mathbf{e}_2 & \cdots & \mathbf{e}_N \\ | & | & & | \end{bmatrix} \tag{17}$$

the eigenvalue decomposition of the correlation matrix is given by

$$\mathbf{R}_c = \mathbf{E}\boldsymbol{\Lambda}\mathbf{E}^{*T} \tag{18}$$

The DKLT is a decomposition of the signal along the orthogonal eigenvectors, and is defined by

$$\boldsymbol{\kappa} = \mathbf{E}^{*T}\mathbf{c} \tag{19}$$

The eigenvector matrix is unitary, i.e. $\mathbf{E}^{*T}\mathbf{E} = \mathbf{I}$, and the inverse transform is given by

$$\mathbf{c} = \mathbf{E}\boldsymbol{\kappa} = \sum_{i=1}^{N} \kappa_i \mathbf{e}_i \tag{20}$$

which is termed the Karhunen-Loève expansion. The Karhunen-Loève coefficients are uncorrelated, and related to the eigenvalues by

$$E\{\kappa_i \kappa_j^*\} = \begin{cases} \lambda_i & i = j \\ 0 & i \neq j \end{cases} \tag{21}$$

The total energy in the signal is equal to the sum of the eigenvalues, and the eigenvalue distribution is thus a measure of the bandwidth of the signal. This is a generalization of the Fourier power spectrum which is only defined for stationary signals.

The white noise signal has evenly distributed energy, and the eigenvalue decomposition of $\mathbf{R}_n$ is given by

$$\mathbf{R}_n = \mathbf{E}(\boldsymbol{\Lambda} + \sigma_w^2\mathbf{I})\mathbf{E}^{*T} \tag{22}$$

where we see that the eigenvectors do not change when white noise is added, but the eigenvalues are guaranteed to be strictly positive and $\mathbf{R}_n$ is positive definite.

An illustration of the eigenvalue spectrum for a typical Doppler signal is shown in Figure 2. The energy of the clutter signal from stationary and slowly moving tissue is concentrated in a few eigenvalues corresponding to low-frequency eigenvectors, while the white noise has equal energy along all the eigenvectors. Figure 2 also shows the energy distribution along the clutter eigenvectors for a typical blood signal. Compared to the clutter signal, the signal from the faster moving blood has most of the energy concentrated along eigenvectors with higher frequency content.

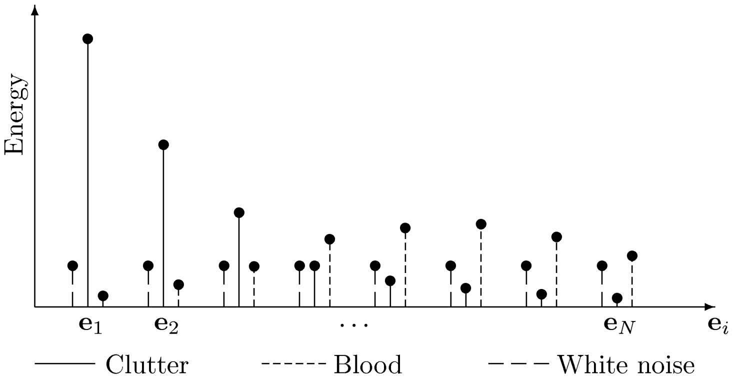

Figure 2: Energy spectrum of a typical Doppler signal.

3 Adaptive Clutter Filters

A general linear filtering operation can be expressed by the matrix multiplication

$$\mathbf{y} = \mathbf{A}\mathbf{x} \tag{23}$$

where $\mathbf{A}$ is an $M \times N$ matrix, and the output vector $\mathbf{y} = [y(0), y(1), \ldots, y(M-1)]^T$ has dimension M. The clutter attenuation can be improved by using a filter matrix that adapts to the clutter signal characteristics. Several such adaptive algorithms are presented in this section.

3.1 Down-mixing with the Mean Doppler Frequency

Using the well established “autocorrelation method” [5], an estimate of the mean frequency of the clutter signal at depth k_0 is given by

$$\hat{\omega}_c = \arg(\hat{R}_{k_0}(1)) \tag{24}$$

where $\hat{R}_{k_0}(1)$ is an estimate of the autocorrelation function with lag equal to one in the temporal direction corresponding to pulse transmissions. This autocorrelation function can be estimated using the unbiased sample mean estimator given by

$$\hat{R}_{k_0}(1) = \frac{1}{2K+1}\frac{1}{N-1}\sum_{k=-K}^{K}\sum_{N=0}^{N-2} x^*(k_0+k, m)x(k_0+k, m+1) \tag{25}$$

where averaging is performed in both space and time. In large vessels, the signal from blood might be comparable in strength to the clutter signal, and to preserve this blood signal, it is important that the filter is not adapted to the blood motion. When spatial averaging with a large number of radial samples K is used, the tissue signal will dominate in the autocorrelation estimate, and adaptation to the tissue movement is ensured. The mixing signal

$$y(k_0, n) = e^{-j\phi(n)} = e^{-j\hat{\omega}_c n} \tag{26}$$

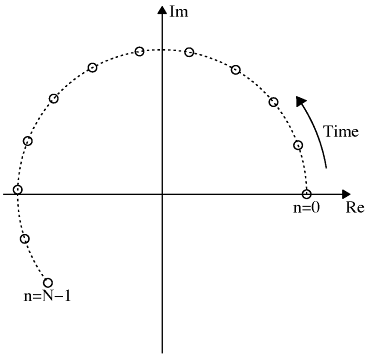

Figure 3: Down-mixing signal with constant phase increments.

is constructed from the estimated mean frequency, and is a phasor spinning round in the complex plane with constant frequency as illustrated in Figure 3. The filtering procedure is summarized in Figure 4, where several types of high-pass filters can be used, e.g. FIR-, IIR- or regression filters. Polynomial regression filters are used in this paper when the adaptive algorithms are compared to each other. The down-mixing is illustrated in the frequency domain in Figure 5 where we see that the clutter can be rejected with a narrower filter after the down-mixing.

3.2 Whitening Filter

The first step in many algorithms for detecting a signal embedded in noise, is to transform the noise signal to white noise [6]. The further optimal detector processing depends on the statistics of the desired signal which are difficult to estimate in our application. In addition to detecting the blood signal, we also want to estimate the mean frequency. Making the noise signal white without significantly altering the blood signal would produce unbiased mean frequency estimates. A filtering operation that whitens the noise is given by

$$\mathbf{y} = \mathbf{E}(\mathbf{\Lambda} + \sigma_w^2\mathbf{I})^{-1/2}\mathbf{E}^{*T}\mathbf{x} \tag{27}$$

where $(\mathbf{\Lambda} + \sigma_w^2\mathbf{I})^{-1/2}$ is diagonal with elements $\sqrt{1/(\lambda_i + \sigma_w^2)}$. For a signal with an energy distribution shown in Figure 2, the output signal has an energy distribution as

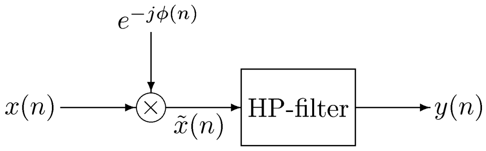

Figure 4: Adaptive clutter filter.

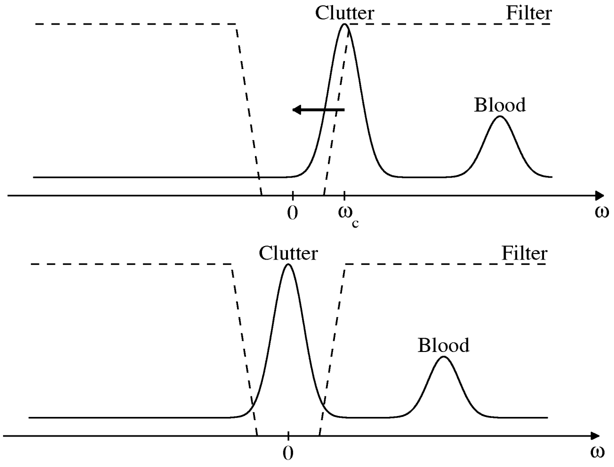

Figure 5: Down-mixing with estimated mean clutter frequency f_c.

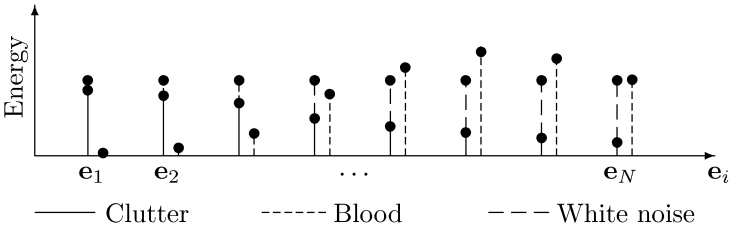

Figure 6: The signal energy distribution after a whitening filter.

shown in Figure 6. The filter has whitened the noise component, but also altered the blood signal. The magnitude of the clutter eigenvalues determines the attenuation of the blood signal. The effect of the filter on the shape of the blood spectrum is small if the blood energy is concentrated along eigenvectors where the corresponding clutter eigenvalues are nearly constant.

In a practical situation the signal statistics are unknown, but the clutter correlation matrix for the sample volume at depth $k_0 r_s/c$ can be estimated by spatial averaging

$$\hat{\mathbf{R}}_{c_{k_0}} = \frac{1}{2K+1} \sum_{k=-K}^{K} \mathbf{x}_{k_0+k} \mathbf{x}_{k_0+k}^{*T} \tag{28}$$

where K is the number of sample volumes in the averaging. Stationarity is not assumed in the estimation of the correlation matrix, and the filter is therefore able to adapt to accelerated tissue movements. The averaging must be performed in an area where the statistical properties of the clutter signal are approximately constant. This is the case with a uniform tissue movement in the averaging area, e.g. probe movement. It is assumed that the power of the blood signal in the averaging region is so small compared to the clutter power that it has a negligible effect on the eigenvectors of the estimated correlation matrix.

As seen in Equation 27, the whitening filter depends on both the eigenvectors and the eigenvalues. The power of the signal varies significantly in space due to speckle effects and the increased attenuation with depth. The clutter level is also lower inside blood vessels. There might therefore be a mismatch between the eigenvalues of the estimated correlation matrix and the power of the clutter signal in a specific sample volume. A filter that depends on only the eigenvectors is therefore desirable.

3.3 Eigenvector Regression Filter

A conventional regression filter fits the signal to a set of curve forms modeling the clutter signal. Filters where the curve forms are polynomials of increasing order are termed polynomial regression filters [1, 4, 10]. The filtered signal is obtained by subtracting this clutter approximation from the input signal. The curve forms span a subspace of the N-dimensional signal space which we call the clutter space, and a K-dimensional clutter approximation is given by

$$\tilde{\mathbf{c}} = \sum_{k=1}^{K} a_k \mathbf{b}_k \tag{29}$$

where $\mathbf{b}_k$ is a set of orthonormal basis vectors spanning the clutter space. The coefficients a_k that minimize the least square error, i.e. $\sum_n |c(n) - \tilde{c}(n)|^2$, are given by the projection of the signal into the clutter space, and the filtering operation is given by

$$\mathbf{y} = \left(\mathbf{I} - \sum_{k=1}^{K} \mathbf{b}_k \mathbf{b}_k^{*T} \right) \mathbf{x} \tag{30}$$

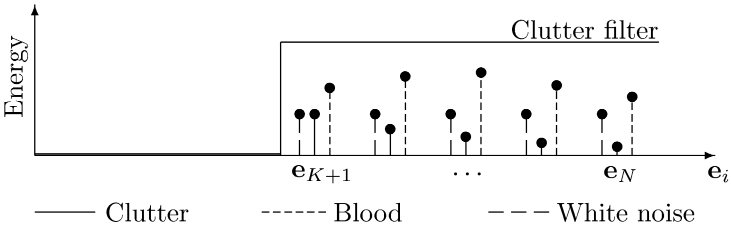

Figure 7: Eigenvector regression filter.

A regression filter can be adapted to the clutter signal by using basis vectors for the clutter space that depend on the clutter statistics. Among all expansions using orthonormal basis functions, the Karhunen-Loève expansion minimizes the mean square error if the expansion is truncated to use fewer than N orthonormal basis functions. This means that the clutter approximation

$$\hat{\mathbf{c}} = \sum_{i=1}^{K} \kappa_i \mathbf{e}_i \tag{31}$$

minimizes the mean square error, i.e. $E\left\{\sum_n |c(n) - \tilde{c}(n)|^2\right\}$. A maximum reduction of clutter energy, given the dimension K, is thus obtained by removing the component of the signal contained in the subspace spanned by $\mathbf{e}_1, \ldots, \mathbf{e}_K$. The filter is described by the projection

$$\mathbf{y} = \left(\mathbf{I} - \sum_{k=1}^{K} \mathbf{e}_k \mathbf{e}_k^{*T}\right) \mathbf{x} \tag{32}$$

and we will refer to it as an eigenvector regression filter. The effect of the eigenvector regression filter on a signal with energy distribution shown in Figure 2, is illustrated in Figure 7 where we see that the filter also removes the component of the blood signal contained in the clutter space. To maximize the range of detectable blood velocities, the clutter space dimension should be minimized. The eigenvector regression filter is optimal in this respect, since for a specified clutter space dimension it maximizes the clutter attenuation.

The correlation matrix can be estimated by spatial averaging as given by Equation 28. An advantage compared to the whitening filter is that the eigenvector regression filter depends only on the shape of the eigenvectors and not the magnitude of the eigenvalues.

3.4 Down-mixing with Varying Phase Increments

Tissue movement with non-constant velocity results in a clutter signal with varying phase increments from sample to sample. Adaptation to such tissue movement is obtained by down-mixing the signal vector $\mathbf{x}$ with a unit amplitude complex vector with varying phase increments as illustrated in Figure 8. The phase increments used

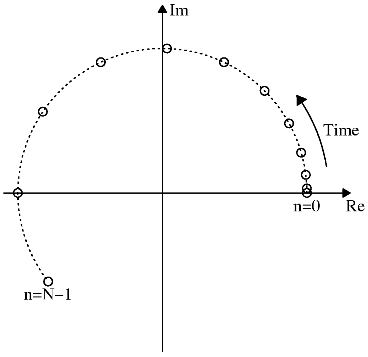

Figure 8: Down-mixing signal for adaptation to an increasing tissue velocity.

for down-mixing at depth k_0 can be found as follows. First estimate the non-stationary correlation function with lag equal to one in the temporal direction corresponding to pulse transmissions. An unbiased estimator for this correlation function is given by

$$\hat{R}_{k_0}(n,1) = \frac{1}{2K+1} \sum_{k=-K}^{K} x^*(k_0+k,n)x(k_0+k,n+1), \quad n = 0,\ldots,N-2 \tag{33}$$

where spatial averaging is performed to avoid adaptation to the blood movement. The phase signal used in the down-mixing in Figure 4 is then given by

$$\phi_R(n) = \begin{cases} 0 & n = 0 \\ \sum_{i=1}^{n} \arg(R_{k_0}(n,1)) & n = 1,\ldots,N-2 \end{cases} \tag{34}$$

By defining the diagonal matrix $\mathbf{M}_{\phi_R(n)}$ with diagonal elements $e^{-j\phi_R(n)}$, the filter including down-mixing can be written as

$$\mathbf{y} = \left(\mathbf{I} - \sum_{k=1}^{K} \mathbf{b}_k \mathbf{b}_k^{*T}\right) \mathbf{M}_{\phi_R(n)} \mathbf{x} \tag{35}$$

For a first order filter, this algorithm is approximately equal to the eigenvector regression filter described in the previous section. The expected value of the non-stationary correlation estimate is given by

$$\begin{aligned} E\{\hat{R}_{k_0}(n,1)\} &= \sum_k \sum_l E\{\kappa_k \kappa_l^*\} e_k(n+1) e_l^*(n) \\ &= \sum_k \lambda_k e_k(n+1) e_k^*(n) \approx \lambda_1 e_1(n+1) e_1^*(n) \end{aligned} \tag{36}$$

where we have used Equations 20 and 21. The phase of the dominant eigenvector vector is

$$\phi_e(n) = \arg(e_1(n)) \tag{37}$$

and from Equation 36 we have

$$\phi_R(n) \approx \phi_e(n) - \phi_e(1) \tag{38}$$

For a small tissue movement, there will be small decorrelation of the clutter signal from sample to sample, and the magnitude of the samples in the dominant eigenvector remains approximately constant. Filtering with a first order eigenvector filter can then be written as approximately

$$\mathbf{y} \approx \mathbf{M}_{-\phi_e(n)} \left(\mathbf{I} - \mathbf{b}_1\mathbf{b}_1^{*T}\right) \mathbf{M}_{\phi_e(n)}\mathbf{x} \tag{39}$$

where $\mathbf{M}_{-\phi_e(n)}$ represents an up-mixing subsequent to the filter. Disregarding this up-mixing, and using the approximation in Equation 38, we see that for a first order filter, the polynomial regression filter with down-mixing using phase increments given in Equation 34 is approximately equal to the eigenvector regression filter. For adaptation to a varying tissue velocity, down-mixing with the phase of the dominant eigenvector is thus an alternative to down-mixing with the phase of the non-stationary correlation estimate.

4 Experimental Results

Digital RF data were recorded with a GE Vingmed Ultrasound System Five scanner using a linear array transducer in color flow modus. The center frequency of the transmitted pulse was 5.7MHz, and the sampling frequency in the depth direction was 3.3MHz. There were 12 pulse transmissions in each beam direction, with a pulse repetition frequency of 1.5kHz. The digital data were stored as complex baseband signals where the in-phase and quadrature signal samples were represented as 16 bit integers. These data were transferred from the scanner and processed on a standard computer using MATLAB. To test the ability of the filters to adapt to the signal, the data were recorded while the probe was being moved in search for small blood vessels in the thyroid gland.

Power Doppler images using the different algorithms are shown in Figure 9 with gain and dynamic range settings equal for all the images. The clutter space dimension is equal to 3 in all the filters, and samples spanning 2cm in the depth direction were used in the spatial averaging in Equations 25, 28, and 33. A small vessel (SV), a large vessel (LV), and a clutter region (C) are marked in all the images. The power in these three regions is tabulated in Table 1. The poorest image quality is obtained for the whitening filter. The gain could be increased to get a brightness level comparable to the other images, but we see that the blood signal to clutter ratio is much lower for this filter. The whitening filter is therefore not investigated in further detail. For this example image, there is no significant improvement by down-mixing with the mean frequency compared to the non-adaptive filter. The three other adaptive filters improve the clutter attenuation by 3dB, but the eigenvector regression filter removes more of the blood signal than the filters that mix down the signal with varying phase increments prior to a polynomial regression filter. The three algorithms which are able to adapt

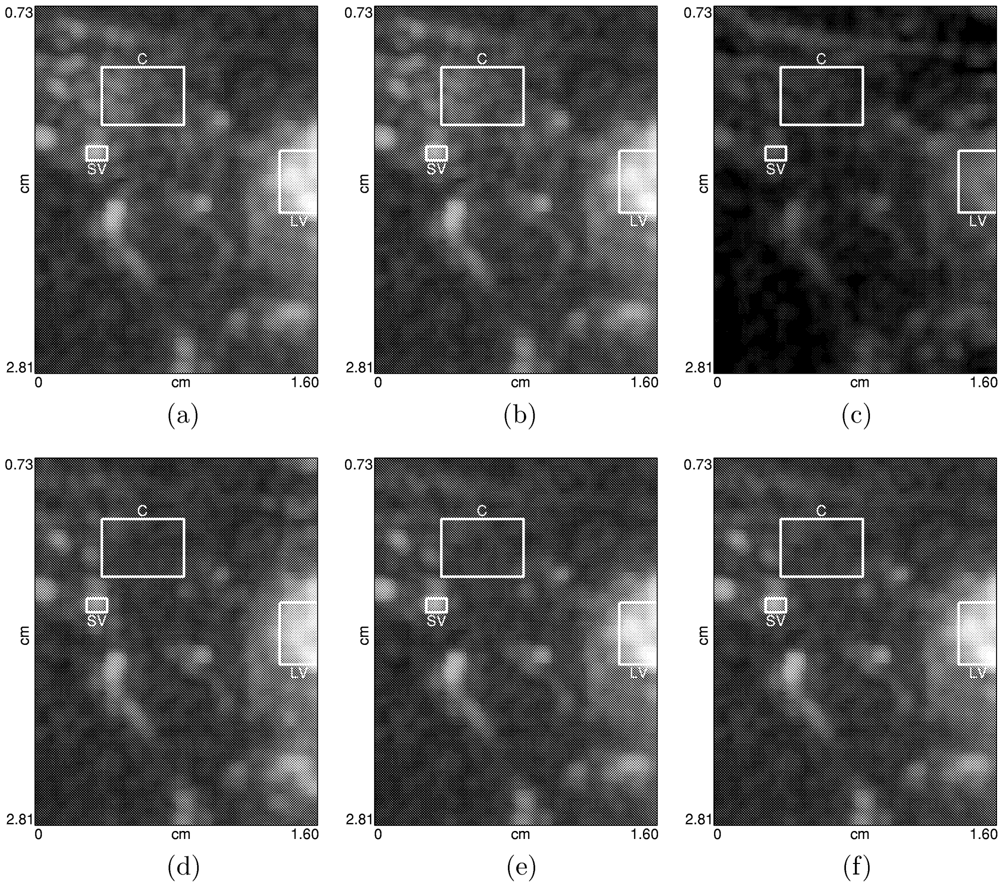

Figure 9: Power Doppler images with a dynamic range of 30dB. The clutter space dimension is equal to 3 in all the filters. The three marked regions contain clutter (C), a small vessel (SV), and a large vessel (LV). (a) Non-adaptive filter. (b) Down-mixing with mean frequency. (c) Whitening filter. (d) Eigenvector regression filter. (e) Down-mixing with phase of dominant eigenvector. (f) Down-mixing with mean non-constant phase increments.

	Large vessel	Small vessel	Clutter
Non-adaptive polynomial regression filter	31.0	24.2	14.7
Down-mixing with mean frequency	31.0	24.2	14.5
Whitening filter	16.2	14.0	9.6
Eigenvector regression filter	29.6	22.0	11.2
Down-mixing with phase of dominant eigenvector	31.0	24.1	11.5
Down-mixing with mean non-constant phase increments	31.0	24.1	11.5

Table 1: Mean power of the Doppler signal in the three regions marked in Figure 9.

to an accelerated tissue motion clearly visualize two small vessels to the left of the indicated clutter region. These two small vessels can not be distinguished from the clutter using the other filters.

More detailed information can be obtained by investigating the filters for a representative sample volume. An example of a signal from a sample volume with moving tissue is shown in Figure 10, where we see that the signal closely follows a circular arc in the complex plane, but that the phase increment between the samples is increasing. This corresponds to an accelerated motion where the velocity increases from 0.13cm/s to 0.22cm/s during the time for the 12 pulse transmissions. The eigenvectors corresponding to the four largest eigenvalues of the correlation matrix estimated for this sample volume are shown in Figure 11, where we see the increasing frequency content of the eigenvectors. The energy spectrums of the signal for the different filters are shown in Figure 12a. For the eigenvector regression filter, Figure 12a shows the energy of the signal along the eigenvectors of the estimated correlation matrix. For the other filters, Figure 12a shows the energy along the polynomial basis vectors subsequent to the different down-mixing techniques. The energy left in the signal after filtering with increasing clutter space dimension is shown in Figure 12b. The eigenvector regression filter needs clutter space dimension $K = 2$ to get sufficient clutter attenuation. This increases to $K = 3$ when down-mixing with varying phase increments is used in com-

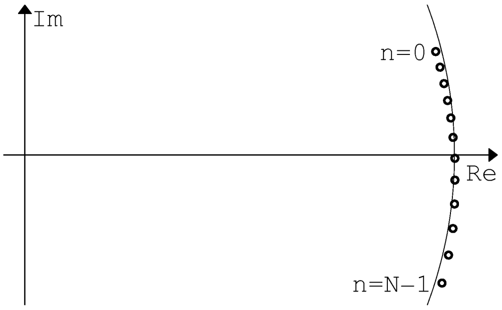

Figure 10: The signal from a representative sample volume.

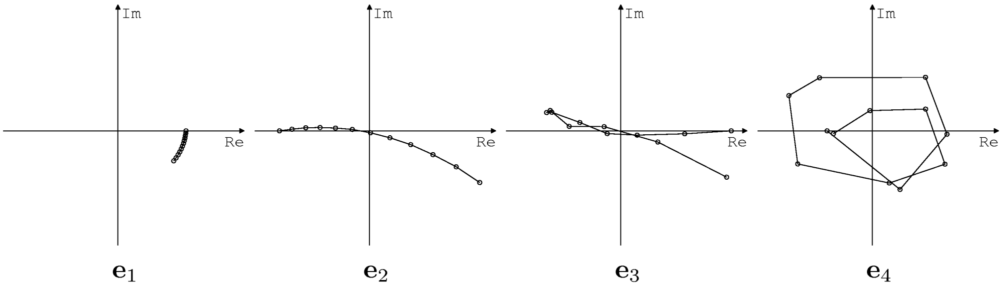

Figure 11: The eigenvectors corresponding to the four largest eigenvalues of the correlation matrix estimated for filtering of the signal in Figure 10.

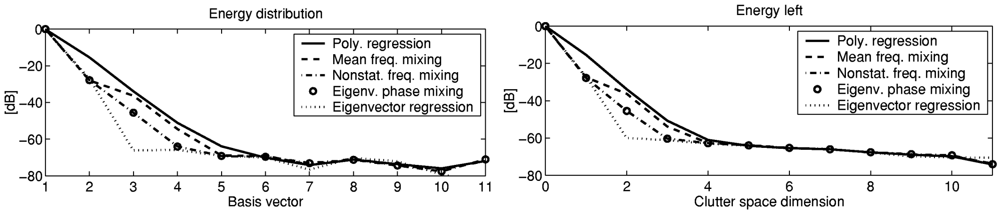

(a) (b)

Figure 12: (a) Energy spectrum for the signal in Figure 10. (b) Energy left after filtering with increased clutter space dimension. Spatial averaging is performed over 2cm in the depth direction in all the estimates.

Center freq.	5.7 MHz
PRF	1.5 kHz
Transducer excitation, $p(t)$	3 period sinusoid
Transducer impulse response, $h_{et}(t) = h_{er}(t)$	Hamming weighted 2 period sinusoid
Receiver filter bandwidth	2MHz
Transducer height	4mm
Element pitch	200μm
Element kerf	20μm
Transmit aperture	18 mm
Receive aperture	12 mm
Transmit focus	50 mm
Receive focus	20 mm
Elevation focus	18 mm
Mathematical element size	$45 \times 50\mu$m
Sampling frequency	200MHz
Sound velocity	1540m/s

Table 2: Field II simulation parameters.

bination with a polynomial regression filter. Down-mixing with the mean frequency does not reduce the necessary clutter space dimension compared to the clutter space dimension that is necessary with a non-adaptive filter.

5 Simulation Results

To verify the experimental results in the previous section, we simulated a similar imaging situation using the point scatterer response model in Equation 5. The received signal from scatterers moving along a straight line through the receive focus as shown in Figure 13 was calculated using the Field II program [2]. This corresponds to imaging just a single muscle fibre, but gives valuable information about the bandwidth of the clutter signal. The parameters used in the simulation are given in Table 2. The total temporal signal $y(t)$ in Equation 5 is shown in both the time and frequency domain in Figure 14. The pulse-echo spatial impulse response function, $h_{pe}(\mathbf{r}, t)$, in Equation 5

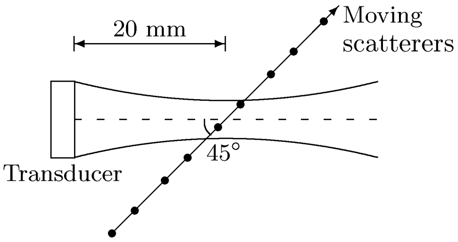

Figure 13: Simulation geometry.

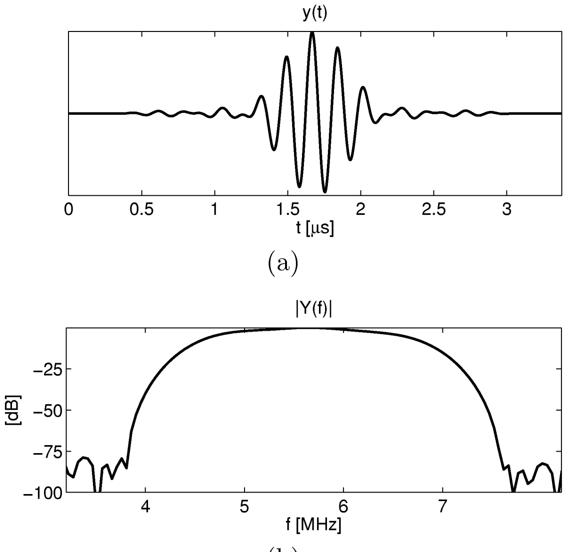

(a)

(b)

Figure 14: (a) The temporal signal $y(t)$ used in the simulations. (b) The frequency spectrum $|Y(f)|$ of $y(t)$.

was calculated using Field II, and Figure 15 shows $h_{pe}(\mathbf{r},t)$ for several points along the line in Figure 13. The signal in Figure 14 was convolved with each of the impulse responses in Figure 15 to get a point scatterer response, $e(\mathbf{r},t)$, for each point along the line. The distance between the points was 0.67μm. The point scatterer responses were sampled at a time after pulse transmission corresponding to the receive focus

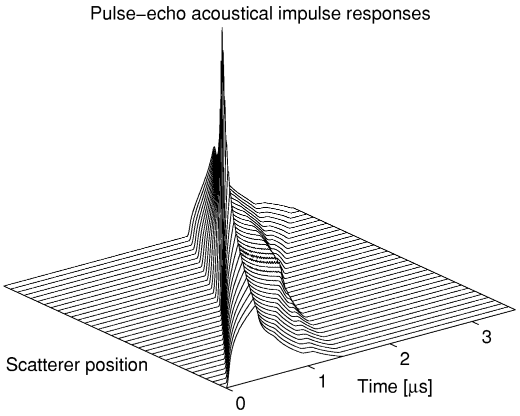

Figure 15: Pulse-echo spatial impulse responses, $h_{pe}(\mathbf{r},t)$, for points along the line in Figure 13. The scatterer in the middle is at receive focus.

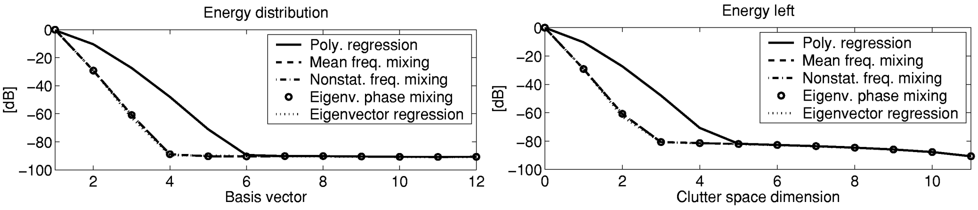

(a) (b)

Figure 16: (a) Energy spectrum. (b) Energy left after filtering with increased clutter space dimension. Constant velocity of 0.3cm/s.

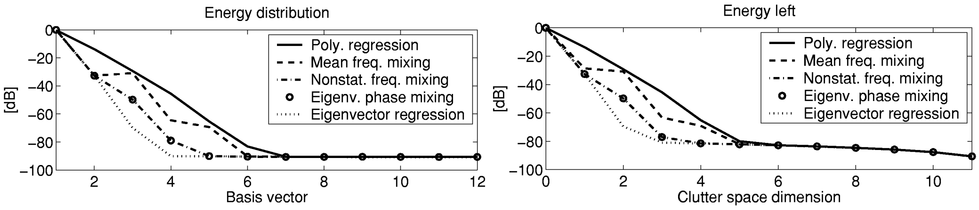

(a) (b)

Figure 17: (a) Energy spectrum. (b) Energy left after filtering with increased clutter space dimension. The velocity increases linearly from 0.1cm/s to 0.3cm/s.

depth. Due to numerical inaccuracies in the Field II calculations, these samples were low-pass filtered to remove high-frequency noise. The resulting data set was used to calculate the correlation function in Equation 13 for different displacement functions. The data were interpolated to get values at all the points resulting from the specified displacement. Since samples were calculated at 0.67μm increments, the interpolation was very accurate. The analysis was limited to a uniform displacement with constant acceleration along the line. White noise was added to the signal to get a signal-to-noise ratio of 80dB.

The correlation matrix was calculated from the correlation function using Equation 13, and was used to compare the clutter filters described in Section 3. The eigenvalues of the correlation matrix used in the eigenvector regression filter, and the energy along each of the polynomial basis vectors used for the other filters, were calculated for different velocities and accelerations. We also calculated the energy left in the signal after filtering with increasing clutter space dimension. The results for a constant velocity with radial component $v = 0.3$cm/s are shown in Figure 16, where we see that all the adaptive filters have equal performance and are significantly better than the non-adaptive polynomial regression filter. Figure 17 shows the results when the radial velocity component increases linearly from $v = 0.1$cm/s at the first pulse transmission to $v = 0.3$cm/s at the last pulse transmission. This is an acceleration corresponding to the signal in Figure 10. The results for the eigenvector regression filter show that there is a slight decrease in the spread of the eigenvalues compared to the spread in Figure 16, but to attenuate the clutter down to the noise level, a clutter space dimension of $K = 3$ is still needed. For the filters using down-mixing with varying phase increments, there is a slight increase in the spread of the energy, and $K = 4$ is necessary. The filter using down-mixing with the mean frequency needs clutter space dimension $K = 5$ which is equal to the necessary clutter space dimension for the non-adaptive filter.

6 Discussion

Down-mixing with the mean frequency results in a surprisingly small improvement in the clutter attenuation as seen by comparing Figure 9a and b. For the signal sample shown in Figure 12, this algorithm needs a filter with the same clutter space dimension as the non-adaptive filter to obtain sufficient clutter suppression. This result is verified by simulations of an accelerated tissue motion as shown in Figures 16 and 17.

The attempt to use a whitening filter for clutter rejection was not successful. This may be explained by the rapid spatial variation in the clutter level. The clutter signal is weighted by the inverted eigenvalues of the estimated correlation matrix as seen in Equation 27. The sum of the eigenvalues equals the mean energy of the signal vectors in the region used to estimate the correlation matrix. In a practical situation, there might be a significant spatial variation in the power of the clutter signal. The clutter level is also lower in sample volumes inside blood vessels. This mismatch between the eigenvalues of the estimated correlation matrix, and the actual clutter power in a specific sample volume, results in too large attenuation of the blood signal as seen in Figure 9c.

The eigenvector regression filter provides maximum reduction of the clutter power for a specified dimension of the clutter space. As opposed to the whitening filter, it depends only on the eigenvectors of the correlation matrix, and is not affected by the spatial variation in the clutter level. The filter adapts to clutter signals with both time-varying amplitude and velocity. It also adapts to clutter signals from scatterers moving with different velocity in different directions. The amount of the blood signal contained in the clutter space and thus removed, is determined by both the dimension of the clutter space, and the shape of the basis vectors spanning the clutter space. The eigenvector regression filter is optimal in the sense that it minimizes the clutter space dimension. However, the blood signal may have a considerable component in the clutter space even though the dimension is minimized. This is the case in the example in Figure 9d. For the eigenvector regression filter, there is a potential pitfall in choosing too high clutter space dimension. The filter might then adapt to and remove the blood signal.

Filters using down-mixing with varying phase increments adapt to clutter signals originating from uniformly moving scatterers with time-varying velocity. Field II simulations showed that even for a small tissue acceleration, there is a large improvement in clutter rejection by using algorithms that adapts to such motions. For the image example in Figure 9, down-mixing with varying phase increments followed by a polynomial regression filter provides clutter rejection that is almost identical to the eigenvector regression filter. The overall image quality is actually superior for the down-mixing algorithms compared to the eigenvector regression filter since the blood signals are better preserved.

7 Conclusions

Several algorithms for adapting the clutter filter in color flow imaging to the tissue movement have been presented and compared to each other using both experimental and simulated data. In situations with constant tissue velocity, down-mixing with the estimated mean frequency results in a significant improvement of the clutter rejection compared to a non-adaptive filter. Our results show, however, that even a slight acceleration of the tissue significantly degrades the efficiency of this algorithm. More sophisticated methods than mean frequency down-mixing are therefore necessary to get sufficient clutter rejection for realistic tissue movements.

The optimum representation property of the Karhunen-Loève transform was used to develop a filter that removes the maximum amount of clutter energy from the signal. This filter is a regression filter with an optimal signal-dependent set of basis vectors. However, our results show that it is difficult to use this filter without removing a non-negligible amount of the signal from blood. This filter also has a large computational complexity.

The best approach is to mix down the signal with varying phase increments calculated from an estimate of the non-stationary correlation function. This adapts the filter to accelerated tissue movements, and is shown to give a significant improvement in the image quality. Considering the rapid development of available computational power, this algorithm has a feasible computational complexity which makes it suitable for real-time processing.

8 Acknowledgements

This study was supported by the Research Council of Norway. We thank Nancy Lea Eik-Nes for revision of the paper.

References

1. A. P. G. Hoeks, J. J. W. van de Vorst, A. Dabekaussen, P. J. Brands, and R. S. Reneman. An efficient algorithm to remove low frequency Doppler signals in digital Doppler systems. *Ultrason. Imag.*, 13(2):135–144, Apr. 1991.

2. J. A. Jensen. Field II, a program for simulating ultrasound systems. The program can be downloaded from `http://www.it.dtu.dk/~jaj/field/field.html`.

3. J. A. Jensen. *Estimation of Blood Velocities Using Ultrasound.* Cambridge University Press, 1996.

4. A. P. Kadi and T. Loupas. On the performance of regression and step-initialized IIR clutter filters for color Doppler systems in diagnostic medical ultrasound. *IEEE Trans. Ultrason., Ferroelect., Freq. Contr.*, 42(5):927–937, Sept. 1995.

5. C. Kasai, K. Namekawa, A. Koyano, and R. Omoto. Real-time two-dimensional blood flow imaging using an autocorrelation technique. *IEEE Trans. Sonics Ultrason.*, 32(3):458–464, May 1985.

6. S. M. Kay. *Fundamentals of Statistical Signal Processing: Detection Theory*, volume 2. Prentice Hall, Inc., 1998.

7. A. Papoulis. *Probability, Random Variables, and Stochastic Processes.* McGraw-Hill, Inc., third edition, 1991.

8. C. W. Therrien. *Discrete Random Signals and Statistical Signal Processing.* Prentice Hall, Inc., 1992.

9. L. Thomas and A. Hall. An improved wall filter for flow imaging of low velocity flow. In *1994 IEEE Ultrasonics Symposium Proceedings*, volume 3, pages 1701–1704, Nov. 1994.

10. H. Torp. Clutter rejection filters in color flow imaging: A theoretical approach. *IEEE Trans. Ultrason., Ferroelect., Freq. Contr.*, 44(2):417–424, Mar. 1997.

Paper C

Blood Detection Performance in Moving Tissue

Steinar Bjærum and Hans Torp
Department of Physiology and Biomedical Engineering
Norwegian University of Science and Technology, N-7005 Trondheim, Norway
E-mail: steinarb@medisin.ntnu.no

Abstract — A method for evaluating the blood detection performance of general linear clutter filters is described. The detector performance is characterized by a receiver operating characteristic (ROC) which is a plot of the probability of detection, P_D, versus the probability of false alarm, P_F. With a Gaussian signal model, the optimal detector compares the power at the output of a clutter filter to a threshold. The optimal detector structure is thus similar to standard color flow systems, but with a filter matrix that depends on both the clutter and blood signal statistics. It is not possible to implement such a detector, but it gives the performance limit for practical detectors. The performance of a practically realizable adaptive clutter filter is evaluated. This filter compensates for the tissue movement by estimating the correlation matrix of the clutter signal by spatial averaging, and uses the eigenvectors corresponding to the largest eigenvalues as a basis for the clutter space in a regression filter. This basis gives maximum clutter attenuation for a given filter order. Digital RF data from the carotid artery was recorded, and a theoretical model for the blood signal was used to compare the detectors. With large tissue movement, the adaptive filter had almost optimum performance, and was significantly better than the polynomial regression filter.

I. INTRODUCTION

In color flow imaging, the blood signal is much weaker than the tissue signal, and it is difficult to detect low velocity blood flow when the Doppler shift from moving tissue is large. This problem occurs when imaging the coronary arteries in the moving heart muscle, and when the operator moves the probe in search for small blood vessels. It has been shown [1, 2, 3] that polynomial regression filtering is an efficient technique for removing the clutter signal. These filters approximate the clutter signal by a polynomial, determined by a least-squares regression analysis, and subtract this clutter estimate from the input signal. In [4] we presented an improved regression filter that adapts to the tissue movement by using a signal dependent basis for the clutter space.

In this paper the optimal blood detector is developed based on statistical detection theory. The assumptions are that the Doppler signal is a complex Gaussian process with independent clutter, white noise, and blood components, and that the signal statistics are known. The optimal detector is shown to consist of a matrix multiplication followed by a power calculation which is then compared to a threshold. Practical detectors have suboptimal clutter filters, but optimal structure. Theory for calculating the detector performance for a general linear clutter filter is developed, and is used to compare the performance of a nonadaptive and adaptive regression filter with the optimal detector.

This paper is organized as follows: The signal model is presented in Section II, followed by development of the detection theory in Section III. In Section IV the performance of the clutter filters is compared to the optimal detector by applying the theory to data recorded from the carotid artery. Further discussion and conclusions are presented in Section V.

II. SIGNAL MODEL

The signal vector $\mathbf{x}$ is the complex demodulated Doppler signal from a single sample volume and consists of N temporal samples. It is a zero mean complex Gaussian process with three independent components, clutter, white noise, and blood

$$\mathbf{x} = \mathbf{c} + \mathbf{n} + \mathbf{b} \tag{1}$$

The signal is characterized by the correlation matrix $\mathbf{R}_x$ which is given by

$$\mathbf{R}_x = \mathbf{R}_c + \sigma_n^2\mathbf{I} + \mathbf{R}_b \tag{2}$$

where $\mathbf{R}_c$ is the clutter correlation matrix, σ_n^2 is the noise variance, $\mathbf{I}$ is the identity matrix, and $\mathbf{R}_b$ is the blood correlation matrix.

0-7803-4095-7/98/$10.00

III. Detection of Blood

In the blood detection problem a decision rule for each sample volume is sought to decide which of the hypotheses

$$\begin{array}{ll} H_0: & \text{No blood is present} \\ H_1: & \text{Blood is present} \end{array} \qquad (3)$$

is true. The observed vector has a complex Gaussian probability density function (PDF) under both hypotheses, but with different correlation matrices

$$\begin{aligned} \mathbf{R}_{x|H_0} &= \mathbf{R}_c + \sigma_n^2\mathbf{I} \\ \mathbf{R}_{x|H_1} &= \mathbf{R}_c + \sigma_n^2\mathbf{I} + \mathbf{R}_b = \mathbf{R}_{x|H_0} + \mathbf{R}_b \end{aligned} \qquad (4)$$

The detector is characterized by the probability of false alarm, P_F, and the probability of detection, P_D, defined by

$$\begin{aligned} P_F &= P(\text{choose } H_1 | H_0 \text{ is true}) \\ P_D &= P(\text{choose } H_1 | H_1 \text{ is true}) \end{aligned} \qquad (5)$$

The performance of a detector is commonly summarized in a receiver operating characteristic (ROC) which is a plot of P_D versus P_F [5].

A. The Optimal Detector

The assumption in this development is that the PDF of the observation vector, $p_{\mathbf{x}|H_i}$, is known under both H_0 and H_1. In this case the Neyman-Pearson lemma [5] tells that P_D is maximized under the constraint $P_F \leq \alpha$ by a likelihood ratio test (LRT) given by

$$\Lambda(\mathbf{x}) = \frac{p_{\mathbf{x}|H_1}(\mathbf{x}|H_1)}{p_{\mathbf{x}|H_0}(\mathbf{x}|H_0)} \underset{H_0}{\overset{H_1}{\gtrless}} \gamma \qquad (6)$$

The Bayes theory of hypothesis testing also leads to an LRT. By taking the logarithm and collecting terms, the LRT for the zero mean Gaussian case can be simplified to [5]

$$l(\mathbf{x}) = \mathbf{x}^{*T}\left(\mathbf{R}_{x|H_0}^{-1} - \mathbf{R}_{x|H_1}^{-1}\right)\mathbf{x} \underset{H_0}{\overset{H_1}{\gtrless}} \eta \qquad (7)$$

where ^{*T} denotes the conjugate transpose. The LRT can be further simplified by solving the generalized eigenvalue problem

$$\mathbf{R}_b\mathbf{E} = \mathbf{R}_{x|H_0}\mathbf{E}\mathbf{\Lambda} \qquad (8)$$

and using the eigenvector matrix $\mathbf{E}$ in the linear transformation $\mathbf{y} = \mathbf{E}^{*T}\mathbf{x}$. This linear transform consists of a stage that whitens the noise, followed by a diagonalization of the transformed blood signal correlation matrix [6]. The correlation matrices under the two hypotheses then become

$$\begin{aligned} \mathbf{R}_{y|H_0} &= \mathbf{I} \\ \mathbf{R}_{y|H_1} &= \mathbf{I} + \mathbf{\Lambda} \end{aligned} \qquad (9)$$

In this new coordinate system, the LRT is simplified to

$$l(\mathbf{y}) = \mathbf{y}^{*T}\left(\mathbf{I} - (\mathbf{I} + \mathbf{\Lambda})^{-1}\right)\mathbf{y} = \sum_{i=1}^{N} \frac{\lambda_i}{1 + \lambda_i}|y_i|^2 \underset{H_0}{\overset{H_1}{\gtrless}} \eta \qquad (10)$$

where y_i are the components of $\mathbf{y}$ and λ_i are the elements of the diagonal eigenvalue matrix $\mathbf{\Lambda}$.

The vector $\mathbf{y} = \mathbf{E}^{*T}\mathbf{x}$ is a zero mean complex Gaussian vector since it is a linear transformation of the zero mean complex Gaussian vector $\mathbf{x}$. The squared magnitude of a complex Gaussian variable is exponentially distributed. This means that under both hypotheses, $l(\mathbf{y})$ is a sum of independent exponentially distributed variables with parameters equal to $(1 + \lambda_i)/\lambda_i$ under H_0 and $1/\lambda_i$ under H_1. The PDF of $l(\mathbf{y})$ can thus be found by a convolution of N exponential distributions with known parameters, resulting in the PDF's $p_{l|H_i}$. The probabilities P_F and P_D can then be found by

$$\begin{aligned} P_F &= \int_{\eta}^{\infty} p_{l|H_0}(l|H_0)dl \\ P_D &= \int_{\eta}^{\infty} p_{l|H_1}(l|H_1)dl \end{aligned} \qquad (11)$$

where η is the threshold in (10).

Because of the noise term, the correlation matrix $\mathbf{R}_{x|H_0}$ in (4) is positive definite [6]. In this case it is shown in [7] that the generalized eigenvalues in (8) are real and that they have the same sign as the ordinary eigenvalues of $\mathbf{R}_b$. Since $\mathbf{R}_b$ is a correlation matrix, it is positive semidefinite which means that it has nonnegative eigenvalues. The λ_i's are therefore guaranteed to be nonnegative and the LRT can be written as

$$l(\mathbf{x}) = \left\|\mathbf{D}\mathbf{E}^{*T}\mathbf{x}\right\|^2 \underset{H_0}{\overset{H_1}{\gtrless}} \eta. \qquad (12)$$

where $\mathbf{D}$ is diagonal matrix with elements $\sqrt{\lambda_i/(1 + \lambda_i)}$. Equation (12) shows that the optimal detector passes the signal through the signal dependent linear filter $\mathbf{D}\mathbf{E}^{*T}$ and compares the resulting power to a threshold as shown in Fig. 1. This

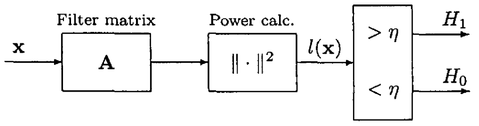

Fig. 1. The structure of the optimal detector. The optimal filter matrix is $\mathbf{A} = \mathbf{D}\mathbf{E}^{*T}$.

is a simple structure, but in practice a suboptimal filter matrix is used since the signal statistics are not known. If the theoretical correlation matrices are replaced by estimates, the resulting test is called a generalized LRT [5]. An estimate of $\mathbf{R}_{x|H_0}$ can be found by spatial averaging

$$\hat{\mathbf{R}}_{x|H_0} = \frac{1}{M}\sum_{i=1}^{M}\mathbf{x}_i\mathbf{x}_i^{*T} \tag{13}$$

in a region containing M sample volumes with approximately constant clutter properties. The noise power, σ_n^2, can be estimated by an average of the smallest eigenvalues of $\hat{\mathbf{R}}_{x|H_0}$. The detector also depends on $\mathbf{R}_b$ which is complicated to estimate because it depends on the signal to be detected. Despite its practical limitations, the optimal detector has theoretical value since it gives the limit of obtainable performance with practical detectors.

B. Practical Detectors

We will now consider detectors with the structure shown in Fig. 1, but with practical filter matrices. The detector can be expressed mathematically as

$$t(\mathbf{x}) = \|\mathbf{A}\mathbf{x}\|^2 \underset{H_0}{\overset{H_1}{\gtrless}} \gamma \tag{14}$$

where $\mathbf{A}$ is a general linear filter matrix [3]. The PDF for the test statistic $t(\mathbf{x})$ under the two hypotheses is found by diagonalizing the correlation matrix of $\mathbf{z} = \mathbf{A}\mathbf{x}$. By similar arguments as for the optimal detector, $t(\mathbf{z})$ is a sum of independent exponentially distributed variables, and the PDFs are found by convolution.

The performance of the detector is determined by the filter matrix $\mathbf{A}$ in (14). The optimal detector is obtained by $\mathbf{A} = \mathbf{D}\mathbf{E}^{*T}$. Regression filters are a class of clutter filters where the filter matrix is given by

$$\mathbf{A} = \mathbf{I} - \mathbf{P} \tag{15}$$

where $\mathbf{P}$ is a projection matrix into a subspace called the clutter space. In polynomial regression filters [1, 2, 3], the K lowest order polynomials are used as a basis for the clutter space. A more effective clutter filter is obtained by using a filter matrix that depends on the clutter signal statistics [4]. In this filter the eigenvectors of $\mathbf{R}_x$ corresponding to the K largest eigenvalues are used as a basis for the clutter space. This filter is optimal in the sense that for a given order K, it removes the best mean square approximation of the clutter signal.

IV. EXPERIMENTAL RESULTS

A. Data Acquisition

Digital RF data was recorded with a VingMed Sound System Five ultrasound scanner using a linear array transducer in color flow modus. The data was recorded with center frequency 5.7MHz, pulselength 0.525μs, radial sampling frequency 2MHz, 9 temporal samples in each sample volume, and pulse repetition frequency 5kHz, giving a Nyquist velocity of 34cm/s. The digital data was stored as complex baseband signals where the in-phase and quadrature signal samples were represented as 16 bit integers. This data was transferred from the scanner and processed on a standard computer using MATLAB.

B. Detection Performance

To evaluate the detectors, data was recorded from the carotid artery with substantial probe movement during the recording. The matrix $\mathbf{R}_{x|H_0}$ in (4) was estimated by spatial averaging in a region with uniform tissue movement as described in (13). The mean tissue movement was estimated to 0.5cm/s. The white noise power σ_n^2 was estimated by averaging the three smallest eigenvalues of $\hat{\mathbf{R}}_{x|H_0}$ resulting in an estimated clutter to white noise ratio of 52dB. The signal from blood was modeled as a single frequency signal, specified by the blood velocity and power. The blood signal to white noise ratio was set to 6dB in all the calculations. ROC's for the optimal detector together with detectors based on standard and adaptive regression filters are shown in Fig. 2 for blood velocity v=10cm/s. The detector based on the adaptive regression filter is seen to be superior to the regression filter with a polynomial basis, and the performance is close to the optimal detector. ROC's for different blood velocities are shown in Fig. 3 for the adaptive filter using order 3. As expected, the performance increases with velocity. Under these conditions, blood with a velocity of v=3.4cm/s can not be detected. Figure 4 shows P_D versus filter order for the adaptive and polyno-

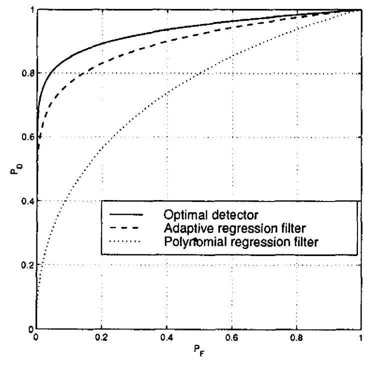

Fig. 2. ROC for the three different detectors. CNR=52dB, SNR=6dB, v=10cm/s, and filter order 3.

mial regression filters. The probability of false alarm P_F is held constant at 0.05 and the blood velocity is 10cm/s. For this blood velocity, the filters have maximum performance for the same filter order, and the adaptive filter is seen to be significantly better than the polynomial regression filter.

V. Discussion and Conclusions

Expressions for calculating the blood detection performance for general clutter filter matrices for a Gaussian signal model have been developed. The theory includes all linear clutter filters, and have been used to compare different regression filters to each other and to the optimal detector. The signal from blood was modeled as a single frequency signal, but a more realistic blood signal model can be used by modifying the blood correlation matrix. We have not considered spatial and temporal averaging which will improve the performance. It is however, expected that an ordering of the detectors by performance will be invariant to averaging. Using the theoretical expressions, we have shown that a considerable performance improvement can be obtained with an adaptive clutter filter when there is large tissue movement.

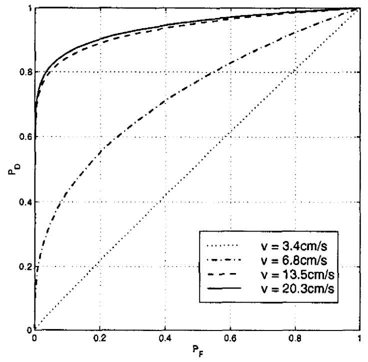

Fig. 3. ROC for the detector based on the adaptive clutter filter. Filter order 3, varying blood velocity.

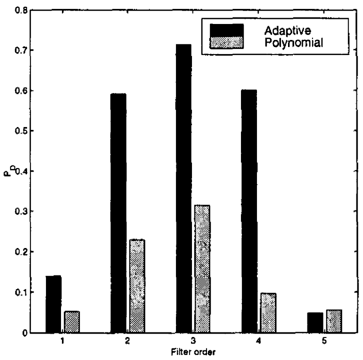

Fig. 4. P_D versus filter order for the adaptive and polynomial regression filter. P_F=0.05 and v=10cm/s.

Acknowledgement — This work was supported by the Norwegian Research Council.

References

[1] A. P. G. Hoeks, J. J. W. van de Vorst, A. Dabekaussen, P. J. Brands, and R. S. Reneman, "An efficient algorithm to remove low frequency Doppler signals in digital Doppler systems," *Ultrason. Imag.*, vol. 13, pp. 135–144, Apr. 1991.

[2] A. P. Kadi and T. Loupas, "On the performance of regression and step-initialized IIR clutter filters for color doppler systems in diagnostic medical ultrasound," *IEEE Trans. Ultrason., Ferroelect., Freq. Contr.*, vol. 42, pp. 927–937, Sep. 1995.

[3] H. Torp, "Clutter rejection filters in color flow imaging: A theoretical approach," *IEEE Trans. Ultrason., Ferroelect., Freq. Contr.*, vol. 44, pp. 417–424, Mar. 1997.

[4] S. Bjærum and H. Torp, "Optimal adaptive clutter filtering in color flow imaging," *Proc. IEEE Ultrason. Symp.*, 1997, vol. 2, pp. 1223–1226.

[5] H. L. Van Trees, *Detection, Estimation, and Modulation Theory, Part I.* John Wiley & Sons, 1968.

[6] C. W. Therrien, *Discrete Random Signals and Statistical Signal Processing.* Prentice Hall, 1992.

[7] G. Strang, *Linear Algebra and its Applications.* Harcourt Brace Jovanovic, third edition, 1988.

Paper D

ELSEVIER

Ultrasonics 38 (2000) 376–380

Ultrasonics

www.elsevier.nl/locate/ultras

Statistical evaluation of clutter filters in color flow imaging

Steinar Bjærum *, Hans Torp

Department of Physiology and Biomedical Engineering, Norwegian University of Science and Technology, N-7489 Trondheim, Norway

Abstract

The filter used to separate blood signals from the tissue clutter signal is an important part of a color flow system. In this paper, statistical detection theory is used to evaluate the quality of the most commonly used clutter filters. The probability of falsely classifying a sample volume as containing blood is kept below a specified threshold. With this constraint, the probability of correctly detecting blood is calculated for all the filters. Using a measured clutter signal, we found that polynomial regression filters and projection-initialized IIR filters are best among the commonly used filters. The probability of correctly detecting blood with velocity 10.1 cm/s was 0.32 for both these filters. The corresponding value for the optimal detector was 0.81, whereas a regression filter that depends on the clutter signal statistics achieved a blood detection probability of 0.72. © 2000 Elsevier Science B.V. All rights reserved.

Keywords: Blood flow; Clutter filters; Doppler; Ultrasound

1. Introduction

In color flow imaging, the signal from blood is much weaker than the signal from tissue. It is therefore difficult to decide if blood is present or not in a given sample volume, especially when imaging small vessels in moving tissue. Commonly used clutter filters to reject the tissue signal are FIR filters, IIR filters with zero-, step-, and projection-initialization, and regression filters. With an efficient clutter filter, the color flow system will reliably detect sample volumes where blood is present. Statistical detection theory can be used to evaluate quantitatively the performance of the different clutter filters, and to find the optimal blood detector. The aim is to maximize the probability of blood detection given a value of the probability of false alarm. It can be shown that, with a Gaussian signal model, the optimal blood detector compares the power at the output of a clutter filter with a threshold. This is a common method used in color flow systems. The optimal clutter filter depends on both the clutter and blood signal statistics and is difficult to implement in practice. In this study we compare the blood detection performance of the different clutter filters with each other and with the optimal filter. In vivo digital RF data are used to calculate the statistics for the tissue signal, and a theoretical signal model is used for the blood. In this way the performance of the different filters is evaluated in different imaging situations.

2. Signal model

The signal vector $\boldsymbol{x}$ is the complex demodulated Doppler signal from a single sample volume and consists of N temporal samples. It is a zero mean complex Gaussian process with three independent components: clutter, white noise, and blood. The signal is characterized by the correlation matrix $\boldsymbol{R}_x$, which is given by

$$\boldsymbol{R}_x = \boldsymbol{R}_\mathrm{c} + \sigma_\mathrm{n}^2 \boldsymbol{I} + \boldsymbol{R}_\mathrm{b}, \tag{1}$$

where $\boldsymbol{R}_\mathrm{c}$ is the clutter correlation matrix, σ_n^2 is the noise variance, $\boldsymbol{I}$ is the identity matrix, and $\boldsymbol{R}_\mathrm{b}$ is the blood correlation matrix.

3. Clutter filters

A general linear filter is described by a matrix multiplication of the signal vector, $\boldsymbol{y} = \boldsymbol{A}\boldsymbol{x}$. The matrix rows are a set of (possibly) different FIR filters for each time instant. With a time variant filter, a frequency response function $H_2(\omega)$ can be defined as the power of the

---

* Corresponding author. Fax: +47-735-98613.
E-mail address: steinarb@medisin.ntnu.no (S. Bjærum)

PII: S0041-624X(99)00153-5

output signal when the input is a complex harmonic signal:

$$H_2(\omega)=\frac{1}{N}(\boldsymbol{A}\boldsymbol{e}_\omega)^{*\mathrm{T}}\boldsymbol{A}\boldsymbol{e}_\omega=\frac{1}{N}\|\boldsymbol{A}\boldsymbol{e}_\omega\|^2, \tag{2}$$

where $\boldsymbol{e}_\omega=[1\ \mathrm{e}^{\mathrm{i}\omega}\cdots\mathrm{e}^{\mathrm{i}(N-1)\omega}]^{\mathrm{T}}$ is a vector of N samples of a complex sinusoid, and $(\boldsymbol{A}\boldsymbol{e}_\omega)^{*\mathrm{T}}$ means that the vector is complex conjugated and transposed. To get a well-defined frequency response for a real valued signal, an ensemble average over all possible phases is necessary, as described in Ref. [1].

3.1. FIR filters

FIR filters are described by the transfer function $H(z)=\Sigma_{k=0}^{M} b_k z^{-k}$, where M is the filter order. It is possible for FIR filters to have a linear phase response by imposing symmetry constraints on the impulse response [2], but for the same order a better amplitude response can be obtained by discarding the phase. The linear phase FIR filters considered in this paper were designed using the McClellan–Parks algorithm [2]. The minimum phase FIR filters were designed by factorization of a linear phase filter of order $2M$ as described in Ref. [3].

The signal consists of N samples, but the first M output samples must be discarded since the output is not valid until the input data reach all the filter registers. This means that only $N-M$ samples are available for estimating flow parameters, resulting in increased estimator variance. The FIR filter can be formulated as an $(N-M)\times N$ matrix with a time-shifted version of the impulse response in each row. For FIR filters, the frequency response defined in Eq. (2) is equal to the squared magnitude of the Fourier transform of the impulse response, $H_2(\omega)=|H(\omega)|^2$.

The frequency responses of linear- and minimum-phase FIR filters of order five in Fig. 1 show that the minimum phase filter has the steepest transition region. It is advantageous with a filter zero at zero frequency since this removes the mean value of the signal, and thus the signal from stationary tissue. This is accomplished by a filter of odd order.

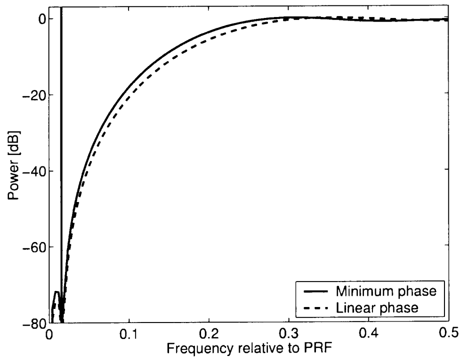

Fig. 1. Frequency responses of fifth-order FIR filters. The vertical line indicates the experimental clutter velocity.

3.2. IIR filters

IIR filters have both zeros and poles, and are described by the transfer function $H(z)=\Sigma_{k=0}^{K} b_k z^{-k}/\Sigma_{k=0}^{K} a_k z^{-k}$, where K is the filter order. Because of the poles, the output consists of a transient signal in addition to the steady state signal. In Ref. [4] a matrix formulation of an IIR filter is developed:

$$\boldsymbol{y}=\boldsymbol{C}\boldsymbol{v}(0)+\boldsymbol{D}\boldsymbol{x}, \tag{3}$$

where $\boldsymbol{v}(0)$ is a vector containing the initial values of the K filter registers. The goal of filter initialization is to choose a value of $\boldsymbol{v}(0)$ that minimizes the transient response. Three different initialization techniques are considered below.

3.2.1. Zero initialization

The filter registers are simply set to zero, $\boldsymbol{v}(0)=\boldsymbol{0}$.

3.2.2. Step initialization

The input signal is assumed to have a constant value equal to the first signal sample $x(0)$. The transient for such a signal is suppressed by setting $\boldsymbol{v}(0)=x(0)\ \boldsymbol{v}_{\mathrm{step}}(\infty)$, where $\boldsymbol{v}_{\mathrm{step}}(\infty)$ is the filter state an infinitely long time after a unit step is applied at the input.

3.2.3. Projection initialization

By setting $\boldsymbol{v}(0)=-(\boldsymbol{C}^{\mathrm{T}}\boldsymbol{C})^{-1}\boldsymbol{C}^{\mathrm{T}}\boldsymbol{D}\boldsymbol{x}$, the output of the projection initialized IIR filter is given by $\boldsymbol{y}=[\boldsymbol{I}-\boldsymbol{C}(\boldsymbol{C}^{\mathrm{T}}\boldsymbol{C})^{-1}\boldsymbol{C}^{\mathrm{T}}]\boldsymbol{D}\boldsymbol{x}$. The matrix $\boldsymbol{C}(\boldsymbol{C}^{\mathrm{T}}\boldsymbol{C})^{-1}\boldsymbol{C}^{\mathrm{T}}$ is recognized as the projection into the range of the matrix $\boldsymbol{C}$, and thus into the K-dimensional subspace containing the transient response [4]. The output of the filter is thus the projection of the steady state response into the orthogonal complement of the transient subspace. In addition to removing the transient signal, the component of the steady state response in the transient subspace is removed.

The frequency response of a fourth-order Chebyshev filter with the different initializations applied to a signal vector of length $N=9$ is shown in Fig. 2 For this short signal length only the projection initialization results in a sufficient stopband width, but the transition band is much wider than expected from the steady state response. The transient dies out with time, but, for this short signal, no significant improvement was obtained by discarding the first samples.

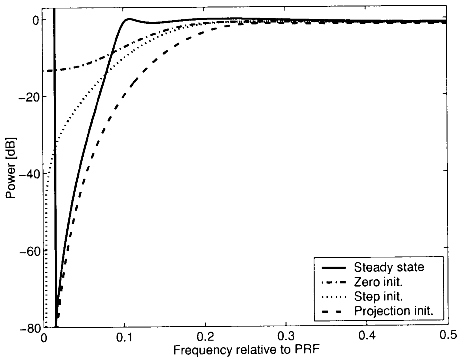

Fig. 2. Frequency responses of a fourth-order Chebyshev filter with different initializations. The signal vector length is $N=9$, and the 1 dB cut-off frequency of the steady state response is 0.1. The vertical line indicates the experimental clutter velocity.

3.3. Regression filters

A regression filter calculates the best least squares fit of the signal to a set of curveforms modeling the clutter space, and subtracts this clutter approximation from the original signal. The curveforms span a subspace of the N-dimensional signal space that we call the clutter space. The regression filter matrix is given by $\boldsymbol{A}=\boldsymbol{I}-\boldsymbol{P}$, where $\boldsymbol{P}$ is a projection matrix into the clutter space. In a polynomial regression filter of order K, the polynomials of order zero to K are used as a basis for a $K+1$-dimensional clutter space [5].

The output vector of both regression filters and projection-initialized IIR filters is contained in a subspace of the N-dimensional vector space. This results in very similar frequency responses, as observed by comparing the response of the third-order polynomial regression filter (four-dimensional clutter space) in Fig. 3 with the response of the projection-initialized IIR filter in Fig. 2.

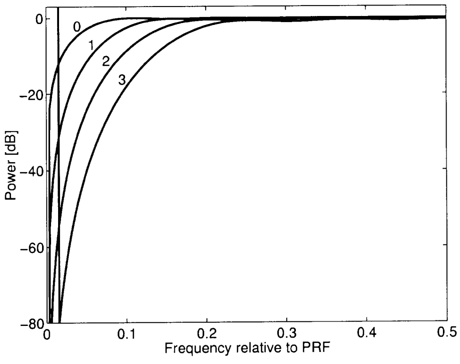

Fig. 3. Frequency responses of polynomial regression filters of order 0–3 with signal vector length $N=9$. The vertical line indicates the experimental clutter velocity.

3.4. An adaptive regression filter

A more efficient clutter filter is obtained by using a filter matrix that depends on the clutter signal statistics [6]. This filter is based on the discrete Karhunen–Loève transform (DKLT) [7], which is a generalization of the discrete Fourier transform for random signals. The DKLT is a signal expansion using the eigenvectors of the correlation matrix as basis vectors. In the adaptive regression filter, the eigenvectors of $\boldsymbol{R}_c$ corresponding to the K largest eigenvalues are used as a basis for the clutter space. This filter is optimal in the sense that, for a given order K, it removes the best statistical mean square approximation of the clutter signal.

4. Detection of blood

In the blood detection problem a decision rule for each sample volume is sought to decide which of the hypotheses

$$H_0\text{: no blood is present} \quad H_1\text{: blood is present} \tag{4}$$

is true. The observed vector is complex Gaussian under both hypotheses, but with different correlation matrices

$$\boldsymbol{R}_{x|H_0}=\boldsymbol{R}_c+\sigma_n^2\boldsymbol{I}$$
$$\boldsymbol{R}_{x|H_1}=\boldsymbol{R}_c+\sigma_n^2\boldsymbol{I}+\boldsymbol{R}_b=\boldsymbol{R}_{x|H_0}+\boldsymbol{R}_b. \tag{5}$$

The detector is characterized by the probability of false alarm P_F and the probability of detection P_D defined by

$$P_F=P(\text{choose } H_1|H_0 \text{ is true})$$
$$P_D=P(\text{choose } H_1|H_1 \text{ is true}). \tag{6}$$

The assumption in the development of the optimal detector is that the probability density function of the observation vector, $p_{x|H_i}$, is known under both H_0 and H_1. In this case the Neyman–Pearson lemma [8] tells us that P_D is maximized under the constraint $P_F\leq\alpha$ by a likelihood ratio test [LRT, $L(x)$] given by

$$L(\boldsymbol{x})=\frac{p_{x|H_1}(\boldsymbol{x}|H_1)}{p_{x|H_0}(\boldsymbol{x}|H_0)}\underset{H_0}{\overset{H_1}{\gtrless}}\gamma. \tag{7}$$

The Bayes theory of hypothesis testing also leads to the LRT in Eq. (8). In Ref. [9] the LRT is simplified to

$$l(\boldsymbol{x})=\|[\boldsymbol{I}-(\boldsymbol{I}+\boldsymbol{\Lambda})^{-1}]^{1/2}\boldsymbol{E}^{*T}\boldsymbol{x}\|^2\underset{H_0}{\overset{H_1}{\gtrless}}\eta, \tag{8}$$

where $l(\boldsymbol{x})$ is a sufficient statistic of the test in Eq. (7), and $\boldsymbol{E}$ and $\boldsymbol{\Lambda}$ solves the generalized eigenvalue problem $\boldsymbol{R}_b\boldsymbol{E}=\boldsymbol{R}_{x|H_0}\boldsymbol{E}\boldsymbol{\Lambda}$. Eq. (8) shows that the optimal detector passes the signal through a signal-dependent filter, and compares the power of the filtered signal to a threshold. Conventional color flow systems have the same structure, but with a suboptimal filter matrix. The probabilities of detection and false alarm can be calculated as described in Ref. [9] and used to compare the detector performance of the different filters.

5. Experimental results

5.1. Data acquisition

To evaluate the detectors, digital RF data were recorded using a GE Vingmed Ultrasound System Five ultrasound scanner with a linear array transducer. The data were recorded from the thyroid gland with substantial probe movement during the recording. The scanner was set up with center frequency 5.7 MHz, pulse length 0.525 μs, radial sampling frequency 2 MHz, nine temporal samples in each sample volume, and pulse repetition frequency 5 kHz, giving a Nyquist velocity of 34 cm/s. The digital data were stored as complex baseband signals where the in-phase and quadrature signal samples were represented as 16 bit integers. This data were transferred from the scanner and processed on a standard computer using MATLAB.

An estimate of $\boldsymbol{R}_{x|H_0}$ was found by spatial averaging in a region with approximately constant clutter properties. The white noise power σ_n^2 was estimated by averaging the three smallest eigenvalues of $\boldsymbol{R}_{x|H_0}$, resulting in an estimated clutter to white noise ratio of 52 dB. The mean tissue movement was estimated to 1.0 cm/s. The signal from blood was modeled as a single frequency signal, specified by the blood velocity and power. The blood signal to white noise ratio was set to 6 dB in all the calculations.

5.2. Filter performance

The filter performances are summarized in Table 1. The probability of false alarm is kept constant at $P_F = 0.05$, and the probability of detection P_D is calculated for the different filters and different blood velocities. As expected, the performance improves with increased blood velocity for all the filters. For our clutter signal, the step-initialized IIR filter has poor performance for all the blood velocities. The clutter is not sufficiently rejected, as can be explained by the narrow stopband for step initialization seen in Fig. 2. There was no significant increase in the −40 dB stopband width for step initialization by increasing the steady state cutoff frequency and/or the filter order. An improvement is expected by increasing the number of signal samples, but even for 32 signal samples the stopband is very narrow, as shown in Ref. [4]. Only narrowband clutter signals can thus be sufficiently rejected by step-initialized IIR filters. The FIR filters have poor performance for low velocities. The polynomial regression filter and the projection-initialized IIR filter have similar performances and are best among the non-adaptive filters for low velocities. For higher velocities, the FIR filters are slightly better. For all the non-adaptive filters there is a slight variation in P_D for large velocities. This variation seems to coincide with the passband ripple. The adaptive regression filter has an overall higher P_D than any of the non-adaptive filters, with a very large improvement for the lowest blood velocities.

6. Conclusions

Among the non-adaptive clutter filters, the projection initialized IIR and polynomial regression filters provide the largest overall probability of blood detection. FIR filters are inferior for low blood velocities, with a small improvement by allowing non-linear phase. For IIR filters, projection initialization was the only initialization scheme resulting in reliable blood detection with the measured clutter signal. However, owing to the initialization, there is no longer any computational advantage in using an IIR filter compared with a regression filter. The adaptive regression filter is relatively close to the optimum detector. In the given clutter conditions it is

Table 1
Probability of detection P_D for different filters and blood velocities. The probability of false alarm is kept constant at $P_F = 0.05$

Velocity (cm/s)	P_D						
	Optimal	Adap. regression	Poly. regression	Proj. init. IIR	Step init. IIR	FIR min. phase	FIR lin. phase
6.8	0.50	0.34	0.07	0.07	0.05	0.06	0.06
10.1	0.81	0.72	0.32	0.32	0.05	0.23	0.16
13.5	0.88	0.81	0.65	0.65	0.05	0.57	0.49
16.9	0.90	0.81	0.74	0.74	0.05	0.73	0.70
20.3	0.92	0.82	0.73	0.72	0.05	0.77	0.77
23.7	0.92	0.82	0.75	0.73	0.05	0.75	0.80
27.0	0.92	0.82	0.75	0.74	0.05	0.72	0.79
30.4	0.92	0.83	0.75	0.73	0.05	0.73	0.77

the only filter able to detect blood with velocity 10 cm/s, but at a very high computational cost.

References

[1] H. Torp, Clutter rejection filters in color flow imaging: a theoretical approach, IEEE Trans. Ultrason. Ferroelectr. Freq. Contr. 44 (1997) 417–424.

[2] J.G. Proakis, D.G. Manolakis, Digital Signal Processing, Principles, Algorithms, and Applications, second ed.Macmillan, New York, 1992.

[3] J.S. Lim, A.V. Oppenheim (Eds.), Advanced Topics in Signal Processing, entice Hall, Englewood Cliffs, NJ, 1988.

[4] E.S. Chornoboy, Initialization for improved IIR filter performance, IEEE Trans. Signal Process. 40 (1992) 543–550.

[5] A.P.G. Hoeks, J.J.W. van de Vorst, A. Dabekaussen, P.J. Brands, R.S. Reneman, An efficient algorithm to remove low frequency Doppler signals in digital Doppler systems, Ultrason. Imag. 13 (1991) 135–144.

[6] S. Bjærum, H. Torp, Optimal adaptive clutter filtering in color flow imaging, Proc. IEEE Ultrason. Symp. 2 (1997) 1223–1226.

[7] C.W. Therrien, Discrete Random Signals and Statistical Signal Processing, Prentice Hall, Englewood Cliffs, NJ, 1992.

[8] H.L. Van Trees, Detection, Estimation, and Modulation Theory, vol. 1, Wiley, 1968.

[9] S. Bjærum, H. Torp, Blood detection performance in moving tissue, Proc. IEEE Ultrason. Symp. 2 (1998) 1571–1574.

Paper E

Automatic Selection of the Clutter Filter Cut-off Frequency in Ultrasound Color Flow Imaging

Steinar Bjærum, Hans Torp,
Torbjørn Bakke[†] and Kjell Kristoffersen[†]

Department of Physiology and Biomedical Engineering,
Norwegian University of Science and Technology, Trondheim, Norway
[†]GE Vingmed Ultrasound,
Horten, Norway

Abstract

Unless properly attenuated, the clutter signals originating from stationary and slowly moving tissue cause severe artifacts in ultrasound color flow images. There are varying demands on the cut-off frequency of the clutter filter in both space and time during the heart cycle. In addition, there is a need for user input to set a proper cut-off frequency. To solve these problems, this paper presents an algorithm that automatically chooses the cut-off frequency for each sample volume. The algorithm has low computational complexity, and has been implemented for real-time processing on the GE Vingmed Ultrasound System Five scanner. Filtering with regression filters can be done iteratively, resulting in an increased cut-off frequency for each step in the iteration. Color flow parameter estimates are calculated for each step in the iteration, and are used to determine if sufficient clutter attenuation is obtained. With spatial averaging of the flow parameters in each step, the clutter was sufficiently attenuated, and the blood flow signal was better preserved than with a fixed cut-off filter. Due to limitations in hardware and available processing time, this spatial averaging was not possible in the real time implementation, and the minimum cut-off frequency had to be increased to get sufficient clutter rejection. As a result, the image quality was not significantly improved. However, an important improvement was that the clutter filter was automatically adapted to the signal, with no need for the user to adjust the cut-off frequency.

1 Introduction

In ultrasound Doppler blood flow measurements, the signal scattered from blood is corrupted by signals scattered from stationary or slowly moving muscular tissue such as vessel walls, and by stationary reverberations etc. The signal scattered by the rapidly moving blood cells has a larger Doppler shift than the signal reflected from slowly moving tissue. Thus, a high-pass filter can be used to separate the signals from blood and tissue. The blood velocities are commonly estimated using a mean frequency estimator [4]. To obtain unbiased blood velocity estimates, the clutter signal needs to be attenuated down to the thermal noise level. To get adequate frame rates in 2D color flow imaging, there are typically only 8-16 samples available for high-pass filtering. The clutter signal is typically 40-100dB stronger than the signal from blood, and it is difficult to get sufficient clutter attenuation without also removing the signal from slow blood flow. The lower limit of measurable blood velocities increases with the clutter filter cut-off frequency which therefore should be kept as low as possible.

There are varying demands on the cut-off frequency of the clutter filter in both space and time. For sample volumes inside small blood vessels, the beam side lobes pick up a strong signal from the surrounding tissue, resulting in a higher clutter level in the coronary arteries than in the ventricle. The temporal variability is caused by the changing tissue velocity during the heart cycle. With too low a cut-off frequency, the moving tissue is colored, giving a false indication of blood flow. With too high a cut-off frequency, the low velocity blood flow in small vessels is not detected. An algorithm that chooses a proper cut-off frequency based on the signal at hand would therefore be of great value. With such an adaptive filter, there would be fewer artifacts in the image. As an added benefit, the button controlling the cut-off frequency could be removed from the scanner. The image quality thus becomes less dependent on user skill.

Polynomial regression filters are known to be efficient clutter filters for ultrasound color flow imaging [2, 3, 6]. In this paper we present an algorithm that automatically chooses the cut-off frequency for polynomial regression filters for each sample volume. The algorithm has low computational complexity, and has been implemented for real-time processing on the GE Vingmed Ultrasound System Five scanner.

Section 2 contains a short review of the basics of color flow imaging. The adaptive algorithm is developed in Section 3, and a short description of the real-time implementation is given in Section 4. Experimental data recorded during the imaging of a coronary artery were used to compare the adaptive algorithm to fixed cut-off filters. The results are presented and discussed in Section 5, and conclusions are drawn in Section 6.

2 Signal Model and Parameter Estimation

A 2D color flow imaging system scans the ultrasound beam over the region to be imaged, transmits N pulses in each direction, and estimates the blood flow velocities based on the back scattered signals. The number of pulses N will be referred to as the packet size. After sampling in the depth direction, a two-dimensional signal

$x(k,n)$ is available for each beam direction, where k is the depth index, and n is the temporal index. A well established technique is to estimate the blood flow velocities from the temporal samples of the complex demodulated signal from each range gate [4]. The clutter filter thus operates separately on the signals from each depth k, and it is convenient to organize the N samples of the complex demodulated Doppler signal in an N-dimensional vector

$$\mathbf{x}_k = [x(k,0), x(k,1), \ldots, x(k,N-1)]^T \tag{1}$$

Only the signal from a single depth is used when describing the algorithm, and the depth index k is dropped in the rest of the paper. A general linear filtering operation can be expressed by the matrix multiplication

$$\mathbf{y} = \mathbf{A}\mathbf{x} \tag{2}$$

where $\mathbf{A}$ is an $M \times N$ matrix, and the output vector $\mathbf{y} = [y(0), y(1), \ldots, y(M-1)]^T$ has dimension $M \leq N$.

Color flow parameter estimates are commonly based on estimates of the autocorrelation function with temporal lag equal to zero and one [4]. These autocorrelation values can be estimated using the unbiased sample mean estimator given by

$$\hat{R}(m) = \frac{1}{M-m} \sum_{n=0}^{M-1-m} y^*(n) y(n+m), \quad m = 0, 1 \tag{3}$$

The estimate of the signal power, $\hat{R}(0)$, is used to determine if blood is present in the sample volume, while an estimate of the velocity is found from $\hat{R}(1)$ by

$$\hat{v} = \frac{c}{4\pi f_0 T} \cdot \arg(\hat{R}(1)) \tag{4}$$

where c is the sound velocity, f_0 is the center frequency of the ultrasound signal, and T is the time between pulse transmissions. To minimize the blood velocity estimation bias, it is important that the clutter filter does not remove more of the signal than strictly necessary. A clutter filter that automatically chooses the minimum stop-band width would therefore be convenient.

3 Automatic Selection of the Clutter Filter Cut-off Frequency

A regression filter calculates the best least-square fit of the signal to a set of curve forms modeling the clutter signal, and subtracts this clutter approximation from the original signal. The curve forms span a subspace of the N-dimensional signal space which we will call the clutter space. The best least-square fit to the clutter curve forms is the projection of the signal into the clutter space, and the filtering operation is given by

$$\mathbf{y}_K = \mathbf{A}_K \mathbf{x} = \left(\mathbf{I} - \sum_{k=1}^{K} \mathbf{b}_k \mathbf{b}_k^{*T} \right) \mathbf{x} \tag{5}$$

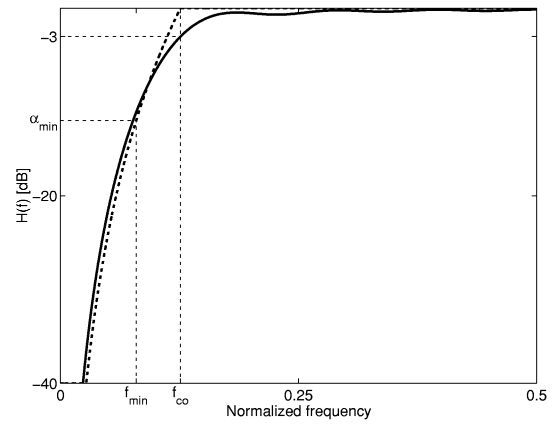

Figure 1: Frequency response of a polynomial regression filter, together with the approximation in Equation 7. Packet size $N = 10$, and clutter space dimension $K = 3$.

where $\mathbf{b}_k$ is a set of orthonormal basis vectors spanning the K-dimensional clutter space, $\mathbf{I}$ is the identity matrix, and ^{*T} denotes complex conjugation and transposition. Polynomial regression filters use polynomials of increasing order as basis functions $\mathbf{b}_k$, and are shown in [2, 3, 6] to be efficient clutter filters.

A frequency response for a general linear filter is in [6] defined as the power of the output signal when the input is a complex harmonic signal with unit amplitude. The -3dB cut-off frequency f_{co} of polynomial regression filters increases with an increasing clutter space dimension K, and decreases with an increasing packet size N. A reasonable approximation for f_{co} is therefore given by [5]

$$f_{co} \approx a \cdot \frac{K}{N} \tag{6}$$

where a is a constant that needs to be determined. The exact value of f_{co} was calculated when K was varied from 1 to 4, and N from 8 to 12. From these values, the best least-square approximation was found to be $a = 0.42$. The steepness of polynomial regression filters below the cut-off frequency is approximately $-6 \cdot K$dB per octave, and an approximation of the amplitude response of such filters is given by

$$H_{\text{appr}}(f) = \begin{cases} \left(\frac{f}{f_{co}}\right)^K & , \quad |f| < f_{co} \\ 1 & , \quad |f| \geq f_{co} \end{cases} \tag{7}$$

A plot of $|H_{\text{appr}}(f)|^2$ together with the exact frequency response is shown in Figure 1 for $N = 10$ and $K = 3$. As seen in Figure 1, the approximation is quite accurate, and the accuracy is similar for other values of K and N.

With the basis vectors for the clutter space as a starting point, a complete set of N orthonormal basis vectors $\mathbf{b}_1, \ldots, \mathbf{b}_N$ can be found and the signal vector $\mathbf{x}$ can be written as

$$\mathbf{x} = \sum_{k=1}^{N} \mathbf{b}_k^{*T}\mathbf{x} \cdot \mathbf{b}_k, \quad \text{where} \quad \mathbf{b}_i^{*T}\mathbf{b}_j = \begin{cases} 1 & \text{for } i = j \\ 0 & \text{for } i \neq j \end{cases} \tag{8}$$

The filtered vector with clutter space dimension k can then be written as

$$\mathbf{y}_k = \sum_{n=k+1}^{N} \mathbf{b}_n^{*T}\mathbf{x} \cdot \mathbf{b}_n = \mathbf{y}_{k-1} - \mathbf{b}_k^{*T}\mathbf{x} \cdot \mathbf{b}_k \tag{9}$$

Because of the orthonormality of the basis vectors, $\mathbf{b}_k^{*T}\mathbf{x} \cdot \mathbf{b}_k = \mathbf{b}_k^{*T}\mathbf{y}_{k-1} \cdot \mathbf{b}_k$, and the regression filtering can be done iteratively by

$$\begin{aligned} \mathbf{y}_0 &= \mathbf{x} \\ \mathbf{y}_k &= \mathbf{y}_{k-1} - \mathbf{b}_k^{*T}\mathbf{y}_{k-1} \cdot \mathbf{b}_k, \quad k = 1, \ldots, K \end{aligned} \tag{10}$$

The cut-off frequency can be adapted to the signal by stopping the iteration when the output signal satisfies certain criteria. Such an algorithm is shown as Algorithm 1, and should be studied with reference to Figure 1. For an efficient implementation, the values of $\tan(2\pi f_{\text{min}})$ should be calculated in advance and put in an array indexed by the filter order.

With large tissue movements, K_{max} might be reached without sufficient clutter attenuation, and the sample volume might be colored giving a false indication of blood flow. In the line marked $(*)$, the autocorrelation estimates $\hat{R}(0)$ and $\hat{R}(1)$ are given values ensuring that no flow is displayed in this sample volume. Such a removal of tissue motion artifacts can also be done when using a filter with a fixed cut-off frequency as shown in Algorithm 2. This algorithm ensures that no flow is indicated in sample volumes with too low velocity or too high power. When judging the power, the algorithm incorporates the attenuation caused by the clutter filter. Using such an algorithm is important to get a fair comparison between filters with fixed and variable cut-off frequencies.

4 Real-time Implementation

Algorithm 1 was implemented on the color flow processing board on the GE Vingmed Ultrasound System Five scanner. The color flow processing in this scanner is done on a board with several Texas Instruments TMS320C31 [1] digital signal processors operating in parallel. There is a C-compiler for this processor, but to get the most effective code, the programming was done using the assembly language for the TMS320C31 processor.

5 Experimental Results

To test the automatic cut-off frequency selection algorithm, and to compare it with images using fixed cut-off filters, digital RF-data were recorded for off-line processing.

Automatic selection of cut-off frequency

$P_{\max}$ Power threshold. Signals from blood must have power below this threshold.

$\alpha_{\min}$ Velocity threshold. Signals from blood must have mean frequency above the frequency corresponding to this filter attenuation.

$K_{\min}$ Minimum clutter space dimension.

$K_{\max}$ Maximum clutter space dimension.

Algorithm:

```
$k = K_{\min}$
$\mathbf{y}_{k-1} = \mathbf{A}_{k-1}\mathbf{x}$
while  $k \leq K_{\max}$  do
    $f_{co} = 0.42 \cdot \frac{k}{N}$
    $f_{\min} = f_{co} \cdot 10^{\min(\alpha_{\min}+3,0)/20k}$
    $\mathbf{y}_k = \mathbf{y}_{k-1} - \mathbf{b}_{k-1}\mathbf{b}_k^{*T}\mathbf{y}_k$
    $\hat{R}(0) = \frac{1}{M}\sum_{n=0}^{M-1} y_k^*(n) y_k(n)$
    $\hat{R}(1) = \frac{1}{M-1}\sum_{n=0}^{M-2} y_k^*(n) y_k(n+1)$
    if  ( $\hat{R}(0) > P_{\max}$ )  OR  ( $|Im\{\hat{R}(1)\}| < \tan(2\pi f_{\min}) \cdot Re\{\hat{R}(1)\}$ )
        $k = k + 1$
    else
        return $\hat{R}(0)$ and $\hat{R}(1)$
    end
end
$\hat{R}(0) = 1,\ Re\{\hat{R}(1)\} = 1,\ Im\{\hat{R}(1)\} = 0$        (*)
return $\hat{R}(0)$ and $\hat{R}(1)$
```

Algorithm 1: Automatic selection of cut-off frequency.

The data were recorded while imaging a coronary artery using a phased array transducer in color flow mode with acquisition parameters as shown in Table 1. Figure 2 shows the region where the RF-data were recorded. The digital data were stored as complex base band signals where the in-phase and quadrature signal samples were represented as 16 bit integers. These data were transferred from the scanner and processed

Center freq.	3.3 MHz
Radial sampling freq.	5 MHz
Pulse repetition freq.	2 kHz
Packet size	10

Table 1: Data acquisition parameters.

Tissue motion artifact removal

Parameters:

$P_{\max}$	Power threshold. Signals from blood must have power below this threshold.
$\alpha_{\min}$	Velocity threshold. Signals from blood must have mean frequency above the frequency corresponding to this filter attenuation.
K	Clutter space dimension.

Algorithm:

```
$f_{co} = 0.42 \cdot \frac{K}{N}$
$f_{\min} = f_{co} \cdot 10^{\min(\alpha_{\min}+3,0)/20K}$
$f = \arg \hat{R}(1)/2\pi$
if ( $\hat{R}(0) > P_{\max}$ ) OR ( $|f| < f_{\min}$ )
    OR $\Big($ ( $|f| < f_{co}$ ) AND $\Big($ $\hat{R}(0) > P_{\max} \cdot (f/f_{co})^{2K}$ $\Big)\Big)$
        $\hat{R}(0) = 1,\ Re\{\hat{R}(1)\} = 1,\ Im\{\hat{R}(1)\} = 0$
end
```

Algorithm 2: Tissue motion artifact removal.

on a standard computer using MATLAB.

The off-line algorithms were identical to the real-time algorithms, but off-line processing is necessary to be able to test the different algorithms on the same data. 32-bit floating point numbers are used in the processing on the scanner, while 64-bit floating point numbers are used in the off-line processing. This difference should, however, have an equal effect on all the algorithms, and should not influence the comparison of the algorithms.

Seven consecutive power Doppler images using polynomial regression filters with a fixed cut-off frequency are shown in Figures 3 to 6. Spatial averaging of $\hat{R}(0)$ and $\hat{R}(1)$ was done using three points in both the depth and lateral directions. The gain setting was equal, and the dynamic range was set to 30dB in all the power Doppler images. Comparing Figures 3 and 4, we see that a clutter space dimension of $K = 4$ is necessary to get sufficient attenuation of the clutter signal. The difference in clutter rejection is clearly evident in the lower right corner of frame 1, and in the upper left part of frames 2-4. Frame 1 in Figures 5 and 6 shows that the signal from moving tissue was efficiently removed by Algorithm 2, where $\alpha_{\min} = -4$dB was used. Unfortunately, the signal within the ventricle was also partly removed as is most clearly seen in frames 4-6.

The algorithm for automatic selection of cut-off frequency, shown as Algorithm 1 was used with parameter values given in Table 2. Comparing the results in Figures 7 and 8, we see a clear improvement when spatial averaging of $\hat{R}(0)$ and $\hat{R}(1)$ is done in the adaptive algorithm. Unfortunately, this is not possible in the real-time imple-

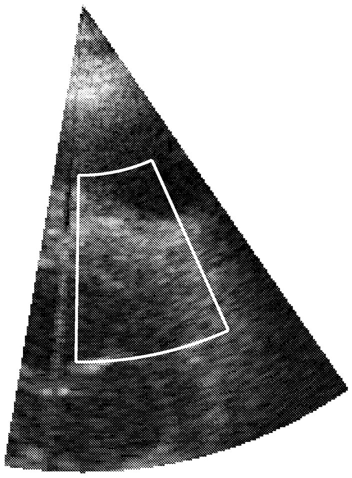

Figure 2: Indication of the region where RF-data were recorded. The region contains a coronary artery in the myocardium.

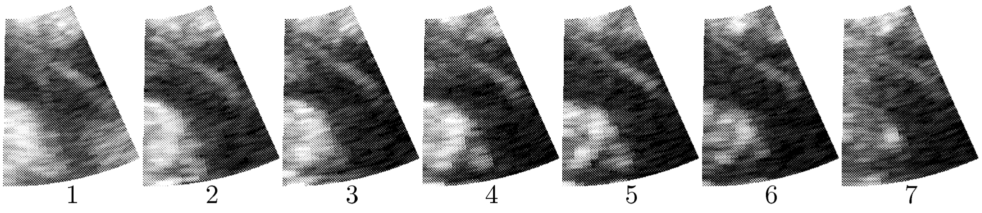

Figure 3: Filter with clutter space dimension equal to three. No tissue motion artifact removal.

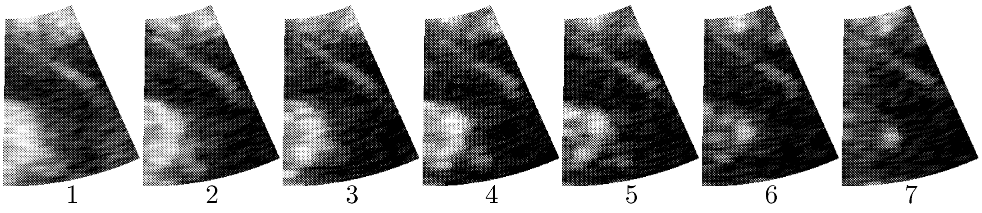

Figure 4: Filter with clutter space dimension equal to four. No tissue motion artifact removal.

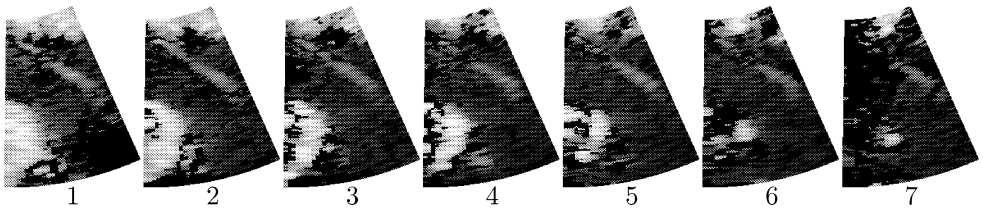

Figure 5: Filter with clutter space dimension equal to three. Removal of tissue motion artifact.

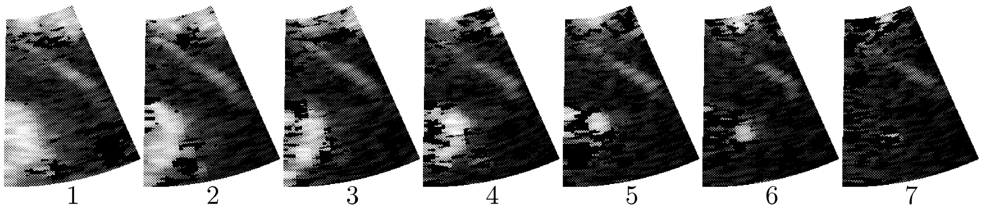

Figure 6: Filter with clutter space dimension equal to four. Removal of tissue motion artifact.

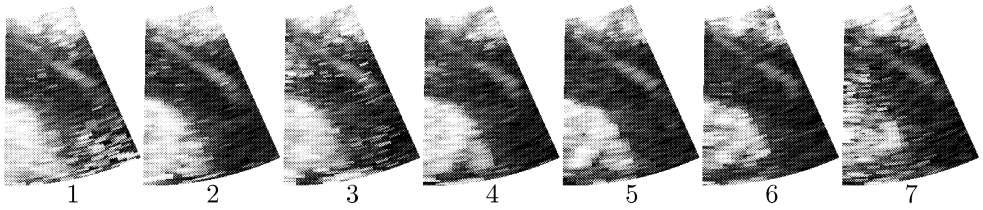

Figure 7: Filtering with automatic cut-off frequency selection.

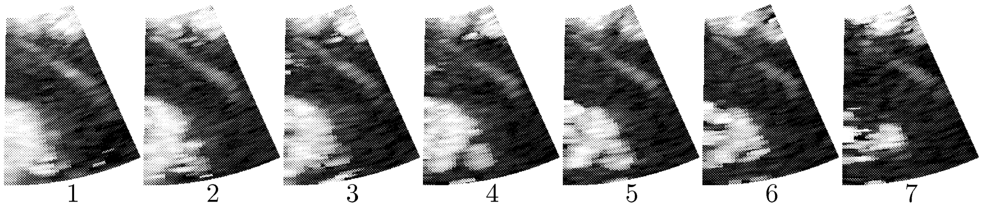

Figure 8: Filtering with automatic cut-off frequency selection using 4×4 spatial averaging of $\hat{R}(0)$ and $\hat{R}(1)$ in the adaptive algorithm.

P_{pre}	P_{max}	α_{min}	K_{min}	K_{max}	P_{nb}	R_{nb}
85dB	40dB	-4dB	1	5	0	5

Table 2: Parameters used in the algorithm for automatic cut-off frequency selection.

mentation of the algorithm due to the hardware architecture. To see how well the cut-off frequency is adapted to the signal, the selected clutter space dimension with and without spatial averaging is visualized in Figures 9 and 10, where the advantage of spatial averaging is clearly seen. Without spatial averaging, there are some sample volumes whose filter order is too low, as can be seen especially in the lower right corner of frame 1. This low filter order results in poor clutter rejection as seen in Figure 7. Figures 9 and 10 also show that the lowest filter order is generally correctly chosen inside the ventricle, and that a lower order is used inside the coronary artery than in other regions of the myocardium. Comparing the images in Figure 4 and 8, we see that the filter with a variable cut-off frequency provides clutter attenuation similar to that of the fixed filter, but preserves the flow in the ventricle considerably better since a lower cut-off frequency is used in these regions. This is most clearly seen in frames 5-7. The clutter rejection of the adaptive filter without spatial averaging is improved by increasing the minimum order to $K_{\text{min}} = 3$ as shown in Figure 11, where the image quality is comparable to the images with fixed $K = 4$ in Figure 4. However, the filter used in Figure 11 automatically adapts to the signal, and sufficient filtering is obtained without the need for the user to adjust the cut-off frequency.

The signal and the effect of filtering for three different regions in the image are shown in Figure 12, where the different demands on clutter space dimension are clearly illustrated. A clutter space dimension of 4 is necessary in the myocardium, while this value results in an unnecessary high attenuation of the blood signal in the ventricle and the coronary artery, and also affects the velocity estimate.

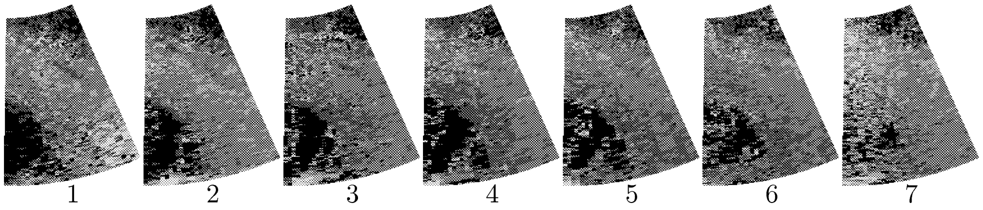

Figure 9: Selected clutter space dimension. The gray scale value increases with an increase in clutter space dimension (from 1 to 5).

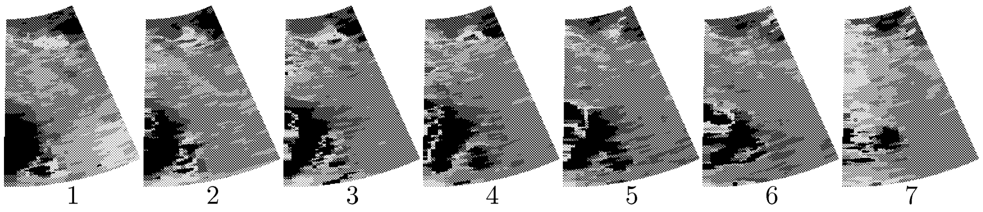

Figure 10: Selected clutter space dimension using 4 × 4 spatial averaging of $\hat{R}(0)$ and $\hat{R}(1)$ in the adaptive algorithm. The gray scale value increases with an increase in clutter space dimension (from 1 to 5).

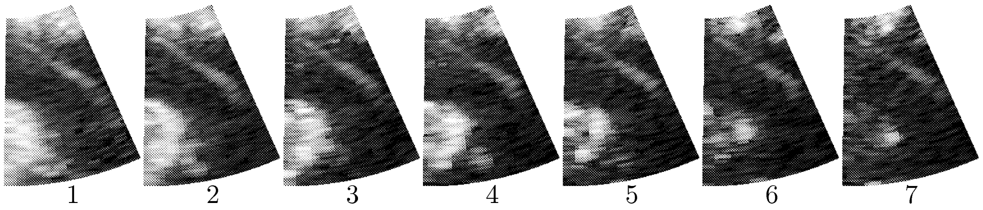

Figure 11: Filtering with automatic cut-off frequency selection. Compared to Figure 7, K_{min} is increased from 1 to 3.

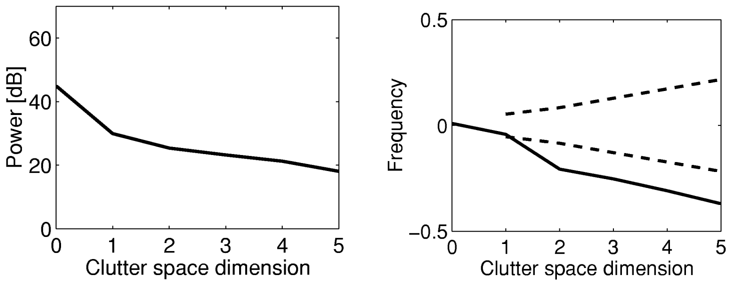

(a) Ventricle.

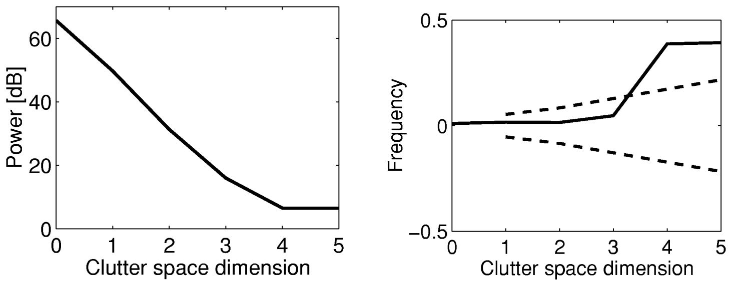

(b) Myocardium.

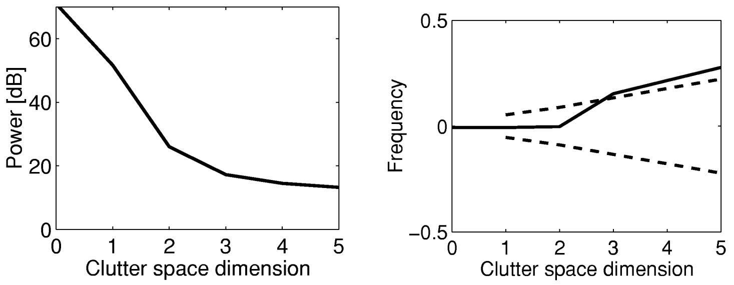

(c) Coronary artery.

Figure 12: Power and mean frequency of the signal after filtering with increasing clutter space dimension. Three different spatial locations: (a) Inside the blood pool in the ventricle. (b) Inside the myocardium. (c) Inside a coronary artery.

6 Conclusions

An algorithm has been developed for automatic selection of the cut-off frequency when polynomial regression filters are used for clutter filtering in ultrasound color flow imaging. With regression filters, the filtering can be done iteratively with successively higher cut-off frequencies. By calculating color flow parameter estimates for each step in the iteration, the filtering can be terminated when these parameters indicate that sufficient clutter attenuation has been obtained. The algorithm has relatively low computational complexity, and has been implemented for real-time processing on the GE Vingmed Ultrasound System Five scanner.

When spatial averaging of the autocorrelation estimates is done in the cut-off selection algorithm, the image quality is better than that which is obtained with fixed cut-off filters. The adaptive algorithm provides sufficient clutter attenuation while preserving the blood flow signal in areas with a low clutter level. This spatial averaging is unfortunately not possible in the real-time implementation of the algorithm where the minimum cut-off frequency needs to be increased to get sufficient clutter rejection. Without spatial averaging in the adaptive algorithm, the quality is comparable to fixed cut-off filters. However, an important advantage is that the clutter filter automatically adapts to the signal, and there is no need for the user to adjust the cut-off frequency.

7 Acknowledgements

This study was supported by the Research Council of Norway. We thank Nancy Lea Eik-Nes for revision of the paper.

References

1. Texas Instrument TMS320C31 Digital Signal Processor. Data sheet, user guide, and other documentation are available at Texas Instruments' website `http://focus.ti.com/docs/prod/productfolder.jhtml?genericPartNumber=TMS320C31`.

2. A. P. G. Hoeks, J. J. W. van de Vorst, A. Dabekaussen, P. J. Brands, and R. S. Reneman. An efficient algorithm to remove low frequency Doppler signals in digital Doppler systems. *Ultrason. Imag.*, 13(2):135–144, Apr. 1991.

3. A. P. Kadi and T. Loupas. On the performance of regression and step-initialized IIR clutter filters for color Doppler systems in diagnostic medical ultrasound. *IEEE Trans. Ultrason., Ferroelect., Freq. Contr.*, 42(5):927–937, Sept. 1995.

4. C. Kasai, K. Namekawa, A. Koyano, and R. Omoto. Real-time two-dimensional blood flow imaging using an autocorrelation technique. *IEEE Trans. Sonics Ultrason.*, 32(3):458–464, May 1985.

5. K. Kristoffersen and S. Holm. Mapping user interface controls to hardware. Technical report, Vingmed Sound, 1997.

6. H. Torp. Clutter rejection filters in color flow imaging: A theoretical approach. *IEEE Trans. Ultrason., Ferroelect., Freq. Contr.*, 44(2):417–424, Mar. 1997.

Paper F

High Frame Rate Color Flow Imaging

Steinar Bjærum, Hans Torp,
Kjell Kristoffersen[†] and Dagfinn Sætre[†]

Department of Physiology and Biomedical Engineering,
Norwegian University of Science and Technology, Trondheim, Norway
[†]GE Vingmed Ultrasound,
Horten, Norway

Abstract

This paper presents an acquisition technique that improves the temporal resolution in ultrasound color flow imaging. When the region of interest (ROI) in the color flow image is limited in the depth direction, and is positioned sufficiently deep in the body, it is possible to reduce the acquisition time for the color flow data by 50%. The technique uses a combination of beam interleaving and transmission of pulses with double repetition frequency. After a pulse is transmitted in a first direction, there is time available to receive from a second direction and transmit a new pulse in this direction while waiting for the echo from the first pulse to arrive. The technique is well suited for imaging the blood flow through the heart valves with the probe in the apical position. For this application, an increase in the frame rate of 70% was obtained. The transducer is focused for reception in the first direction, but the beam side lobes will pick up unwanted echoes from the pulse propagating in the second direction. A simulation using the Field II program showed that for scatterers of equal strength, the minimum difference in energy between the desired and undesired signal was 8.9dB for cardiac imaging from the apical position. However, for patients with strong reverberation noise from the body wall, the undesired signal can be considerably stronger. Without sufficient clutter filtering, this reverberation noise gives unreliable velocity estimates, so the technique should be used with care.

1 Introduction

When using ultrasound color flow imaging to measure blood flow in the heart, it is important to have high temporal resolution. This is especially so when investigating the details in the cross-sectional velocity distribution through the heart valves. The velocities across the valve opening should be measured as simultaneously as possible, and this velocity profile should be updated as often as possible to capture the rapid flow changes during the heart cycle. Previously, ECG triggered techniques have been used for such measurements [10]. Another application where high temporal resolution is desired is in volume flow measurements using three-dimensional color flow data [1].

In pulsed wave spectrum Doppler measurements, the maximum velocity that can be measured without aliasing is called the Nyquist velocity, and is determined by the pulse repetition frequency (PRF) together with the transmitted ultrasound frequency. The depth down to the sample volume determines the maximum PRF. Increasing the PRF above this limit will create an extra sample volume closer to the transducer, causing a range ambiguity concerning which range the sampled signal is coming from. It is often possible, however, to position the transducer so that there is little or no blood flow in the extra sample volume, and the high PRF (HPRF) technique can be used to measure high blood velocities [4]. The HPRF technique is an alternative to continuous wave (CW) Doppler for measuring high velocities. CW Doppler does not suffer from aliased velocities, but does not provide any range resolution of the measurements.

A 2D Doppler imaging system scans the ultrasound beam over the region to be imaged, transmits a number of pulses in each direction, and estimates the blood flow velocities from the back scattered signals. When measuring low velocities, the PRF can be decreased from the maximum value given by the depth. If the PRF is decreased by a factor k, there is time to acquire data in $k - 1$ other beam directions before transmitting the next pulse in the first direction. This beam interleaving technique [2] maintains the frame rate even though the PRF is reduced.

In this paper we use a combination of the HPRF technique and beam interleaving to reduce the acquisition time for the color flow image by a factor of two without altering the PRF of pulses transmitted in the same direction. The technique is applicable when the region of interest (ROI) is short in the depth direction, and is positioned sufficiently deep in the body. This means that the technique is well suited for imaging the blood flow through the heart valves with the probe in the apical position. The reduction in acquisition time is obtained by having two pulses propagating simultaneously. After a pulse is transmitted in a given direction, there is time available to receive echoes from another direction and transmit a new pulse in this direction while waiting for the echo from the first pulse to arrive back to the transducer. Since the acquisition time for the color flow data is halved, a substantial increase in the frame rate is achieved.

The acquisition technique is described in Section 2 where we find the restrictions on the ROI, and work through an example showing the increase in frame rate. Having two pulses propagating simultaneously may lead to artifacts in the image, and in Section 3 the interference between the two pulses are simulated using the Field II program [6]. Some examples of clinical applications are mentioned in Section 4 before the paper is concluded in Section 5.

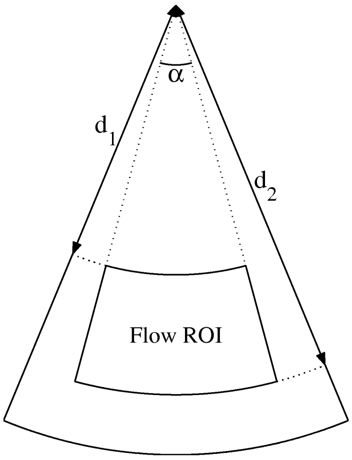

Figure 1: Tissue B-mode and color flow image sectors.

2 Data Acquisition

The restrictions on the depth and length of the ROI for the high frame rate acquisition technique will be discussed based on the geometry shown in Figure 1, and the timing diagram shown in Figure 2. The pulse repetition time for each beam direction, T_B, is determined by the desired maximum depth d_2 of the flow ROI

$$T_B = 2d_2/c + T_{D2} \tag{1}$$

where c is the sound velocity and T_{D2} is the delay between the end of reception and the transmission of a new pulse. The minimum T_{D2} is determined by how fast the front-end electronics can switch between reception and transmission. It might, however, be desirable to use a longer T_{D2} to ensure sufficient attenuation of the echoes from this pulse before a new pulse is transmitted.

By increasing the start depth of the ROI, there is time available to receive and transmit in another direction as illustrated in Figure 2. The minimum depth d_1 down to the ROI is given by

$$\begin{aligned} d_1 &= c(T_B/2 + T_P + T_{D1})/2 \\ &= d_2/2 + c(T_P + T_{D1} + T_{D2}/2)/2 \end{aligned} \tag{2}$$

where Equation 1 is inserted in the second step.

Looking at Figure 2, we see that there are $T_B/2$ seconds between the transmission of the pulses in beam direction 1 and 2. When the reception beam is focused in direction 1, the pulse transmitted in direction 1 will be called the primary pulse, and the pulse transmitted in direction 2 will be called the secondary pulse. The difference in depth

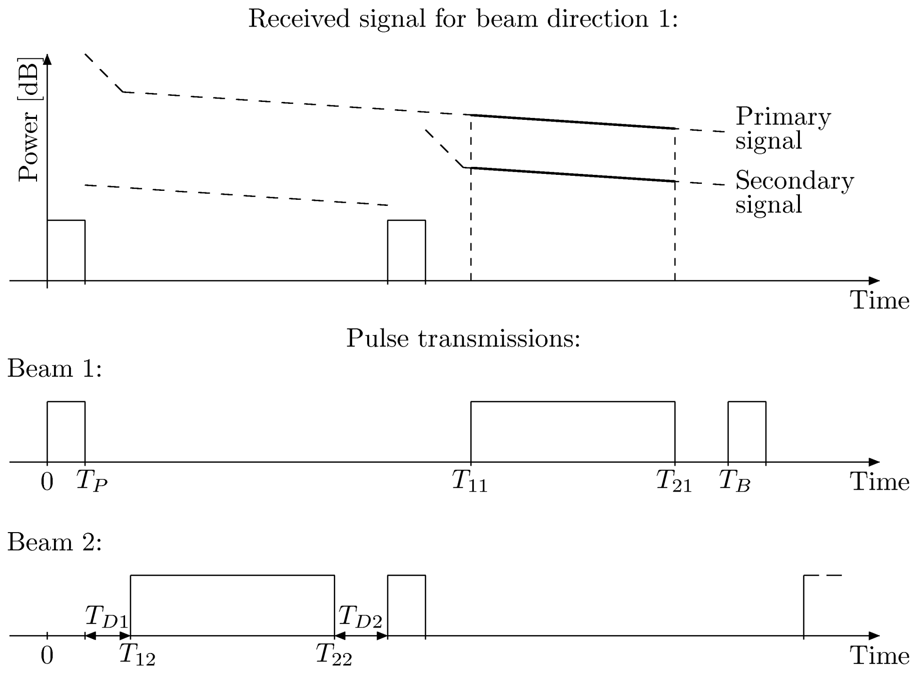

T_P: Pulse length
T_{11}: Start of reception in beam 1, $T_{11} = 2d_1/c$
T_{21}: End of reception in beam 1, $T_{21} = 2d_2/c$
T_B: Pulse repetition time, T_B =1/PRF
T_{12}: Start of reception in beam 2
T_{22}: End of reception in beam 2
T_{D1}: Delay between transmission and reception
T_{D2}: Delay between reception and transmission

Figure 2: Timing diagram.

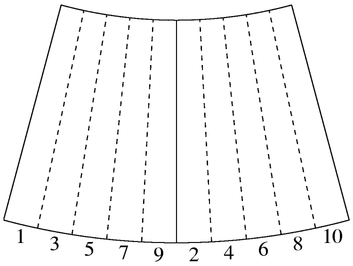

Figure 3: Beam sequencing. Pulses propagate simultaneously in directions 1 and 2, 3 and 4, and so on.

to the primary pulse and secondary pulse is given by

$$\begin{aligned}\Delta d &= cT_B/4 \\ &= d_2/2 + cT_{D2}/4\end{aligned} \tag{3}$$

and is an important quantity when calculating the interference from the secondary pulse. The reception beam is focused to receive the echoes from the primary pulse in beam direction 1, but the beam side lobes will pick up echoes from the secondary pulse propagating in direction 2. The total signal is thus a sum of the primary and secondary signal as illustrated in Figure 2. To get the smallest possible interference from the secondary pulse, beam 1 and 2 should be separated to the maximum. The best scan sequence is shown in Figure 3, where pulses propagate simultaneously in directions 1 and 2, 3 and 4, and so on. The directions of two simultaneously propagating pulses are separated by an angle $\alpha/2$ where α is the sector angle of the flow image. The interference between the two pulses is investigated in more detail in Section 3.

Example:

We will now work through an example to show the limitations of the ROI, and to demonstrate how much the frame rate is increased with the new acquisition technique for a setup suitable for imaging of the blood flow through either the mitral or aortic valve with the probe in the apical position.

A pulse with three periods at 2.5MHz is suited for cardiac color flow imaging. With sound velocity $c = 1540$m/s, this gives a pulse length of $T_P = 1.2\mu s$. The ROI needs to extend down to a depth of $d_2 = 15$cm, and setting $T_{D2} = 5.2\mu$s, gives a pulse repetition time of $T_B = 200\mu$s. Assuming $T_{D1} = T_P$, the minimum start depth of the ROI becomes $d_1 = 7.9$cm. Fortunately, an ROI from 7.9cm to 15cm is sufficient when imaging the flow through the heart valves from the apical view in typical patients. The difference in depth down to the two pulses is $\Delta d = 7.55$cm.

For conventional acquisition, the total acquisition time for one image frame is given by

$$T_{\text{Frame}} = T_{\text{tissue}} + T_{\text{flow}} = \frac{N_{\text{tissue}}}{M} T_{\text{B,tissue}} + \frac{N_{\text{flow}} N_{PS}}{M} T_{\text{B,flow}} \tag{4}$$

where N_{tissue} and N_{flow} are the number of beams in the tissue and flow image, $T_{\text{B,tissue}}$ and $T_{\text{B,flow}}$ are the beam acquisition times, M is the number of parallel receive beam forming channels, and N_{PS} is the number of pulse transmissions (packet size) in each beam direction to estimate the blood velocities. Parallel receive beam forming means that multiple receive beams are calculated per transmit beam.

The number of beams in the image is determined by the image sector width and the beam density. Reasonable values of the beam densities can be found as follows: In the far-field, the angular beam pattern is equal to the Fourier transform of the aperture. Focusing brings the far-field to the focus, and the angular beam width in focus is determined by the main lobe width of the Fourier transform of the window function used for apodizing the aperture. With wave length λ, and aperture size D, the angular beam width is $\theta = k \cdot (\lambda/D)$, where k depends on the apodization and the definition of the beam width (-3dB or -6dB). A 2cm aperture with Hamming apodization gives $\theta_{-3\text{dB}} = 2.3°$. Nyquist sampling then corresponds to an angle increment between beams of $\alpha = 1.15°$. To get a slight over-sampling, we choose one tissue B-mode beam per degree. Lower resolution is required for the flow image, where we choose 0.6 beams per degree. An image sector of 20° has a width of 4.1cm at 12cm depth. This is wide enough to cover the heart valves, but to ease the navigation, a 30° tissue B-mode sector is convenient. Blood velocity estimates of good accuracy can be obtained with $N_{PS} = 8$ which will be used in our calculations.

Assuming equal depth of the B-mode and flow images, and setting $T_{\text{B,tissue}} = T_{\text{B,flow}} = 200\mu\text{s}$, gives the following acquisition time for a 30° B-mode sector:

$$T_{\text{tissue}} = \frac{30}{2} 200\mu\text{s} = 3.0\text{ms} \tag{5}$$

The flow acquisitor time becomes:

$$\begin{aligned} T_{\text{flow}} &= \tfrac{12 \cdot 8}{2} 200\mu\text{s} = 9.6\text{ms} && \text{for a } 20° \text{ flow sector} \\ T_{\text{flow}} &= \tfrac{18 \cdot 8}{2} 200\mu\text{s} = 14.4\text{ms} && \text{for a } 30° \text{ flow sector} \end{aligned} \tag{6}$$

The new acquisition technique reduces T_{flow} by 50%, giving the improvement in frame rate shown in Table 1. The significant improvement in temporal resolution given in Table 1 is important when studying the details of the flow through the heart valves.

Frame rates [frames/second]

20° flow sector		30° flow sector	
Conventional	Improved	Conventional	Improved
79.4	128.2	57.5	98.0

Table 1: Improvements in frame rate with the new acquisition technique.

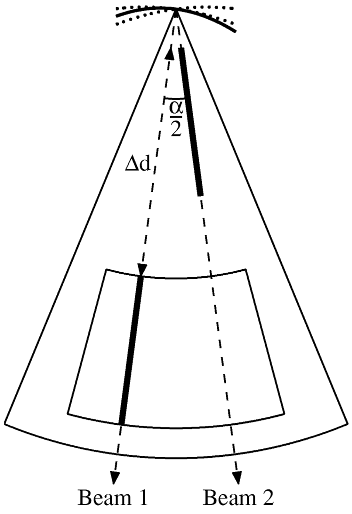

Figure 4: Geometry of simultaneously propagating pulses.

3 Simulation of Artifacts Caused by the Acquisition Technique

The geometry of the acquisition technique described in Section 2 is shown in Figure 4. Pulses are transmitted with fixed transmit focus, while dynamic focusing is used on reception. Transmit focusing is illustrated with dotted transducers in Figure 4, and receive focusing is illustrated with a solid transducer. The transducer is focused for reception of the primary signal in beam direction 1, but the beam side lobes will pick up echoes from the secondary pulse propagating in direction 2. To investigate the importance of this undesired secondary signal, simulations were performed using the Field II program [6]. This program uses the spatial impulse response technique to calculate acoustic fields. The simulation parameters are shown in Table 2. Using T_B =1/PRF= 200μs in Equation 3, the secondary pulse has propagated Δd = 7.7cm shorter than the primary pulse, and the attenuation level becomes important when calculating the primary and secondary signals. An attenuation level of 0.5dB/MHz·cm is commonly used in ultrasound imaging. In this application, however, the difference in the propagation path between the primary and secondary pulse is mainly through the blood in the left ventricle. In [7, p. 30], the attenuation in blood is given as 0.17-0.24dB/MHz·cm, and we made a conservative choice of 0.3dB/MHz·cm in our simulations. The attenuation was calculated based on the mean frequency of the pulse, without any shaping of the pulse frequency spectrum.

In addition to the sector width, both the elevation and transmit focus will influence the relative strength between the primary and secondary signal. Tables 3–6 show the energy difference between the primary signal received from point scatterers located

Center frequency	2.5MHz
Transducer impulse response	Hanning weighted 2 period sinusoid
Transducer excitation	3 period sinusoid
Transducer height	13mm
Element pitch ($\lambda/2$)	308μm
Element kerf ($\lambda/20$)	30.8μm
Number of elements	64
Mathematical element size ($\lambda/20$)	30.8μm
Sampling frequency	100MHz
Sound velocity	1540m/s
Attenuation	0.3dB/MHz·cm
PRF	5kHz

Table 2: Field II simulation parameters.

at depths of 8-15cm, and the secondary signals from equal point scatterers at corresponding depths. From these results an elevation focus at 8cm and a transmit focus at 16cm are good choices, and we see that a 30° image sector should be used since the secondary signal is considerably lower than the secondary signal in a 20° image sector. An increase in the sector width increases the angle $\alpha/2$ in Figure 4, resulting in less interference from the secondary pulse.

In addition to the results shown in Tables 3–6, we found a slight increase in the energy difference when the pulse length was increased to four periods. However, increasing the pulse length degrades the radial resolution. The tabulated values are for a primary pulse propagating in beam direction 5 in Figure 3, and for a secondary pulse propagating in beam direction 6. There was no significant change in the values when beam directions 1 and 2 were simulated; this means that the values are uniform in the lateral direction.

Figure 5 shows the primary signal received from point scatterers located at depths

	Energy difference [dB]				
	Transmit focus				
Depth [cm]	8	10	12	14	16
8	15.2	14.7	13.7	12.7	11.7
9	11.3	11.6	11.1	10.4	9.8
10	6.8	7.6	7.6	7.3	6.9
11	0.0	1.3	1.9	2.3	2.3
12	0.2	2.9	2.7	2.2	1.8
13	−2.9	2.1	4.8	5.8	5.9
14	−3.4	0.6	3.2	5.0	6.2
15	−2.8	0.4	2.6	4.1	5.2

Table 3: Energy differences between primary and secondary signals. Sector width 20° and elevation focus 8cm.

	Energy difference [dB]				
	Transmit focus				
Depth [cm]	8	10	12	14	16
8	15.1	14.6	13.7	12.6	11.7
9	11.0	11.2	10.7	10.1	9.4
10	8.8	9.6	9.6	9.3	8.9
11	8.4	9.6	10.1	10.4	10.4
12	7.6	10.5	10.4	10.0	9.5
13	3.2	8.0	10.7	11.8	11.9
14	1.7	5.6	8.2	10.0	11.2
15	1.8	4.9	7.0	8.5	9.6

Table 4: Energy differences between primary and secondary signals. Sector width 30° and elevation focus 8cm.

	Energy difference [dB]				
	Transmit focus				
Depth [cm]	8	10	12	14	16
8	14.5	14.0	13.0	11.9	10.9
9	9.9	10.2	9.7	9.1	8.4
10	4.8	5.4	5.3	4.9	4.5
11	−6.0	−4.6	−3.9	−3.5	−3.4
12	−3.9	−1.3	−1.6	−2.0	−2.4
13	−6.1	−1.1	1.6	2.6	2.7
14	−6.0	−2.0	0.6	2.4	3.6
15	−4.9	−1.7	0.4	1.9	3.0

Table 5: Energy differences between primary and secondary signals. Sector width 20° and elevation focus 6cm.

	Energy difference [dB]				
	Transmit focus				
Depth [cm]	8	10	12	14	16
8	14.4	13.9	12.9	11.9	10.9
9	9.3	9.5	9.1	8.4	7.8
10	7.2	7.9	7.8	7.4	7.0
11	2.6	3.8	4.5	4.7	4.8
12	3.5	6.2	6.1	5.7	5.3
13	0.1	4.9	7.6	8.6	8.8
14	−0.7	3.1	5.7	7.5	8.7
15	−0.3	2.8	4.8	6.3	7.4

Table 6: Energy differences between primary and secondary signals. Sector width 30° and elevation focus 6cm.

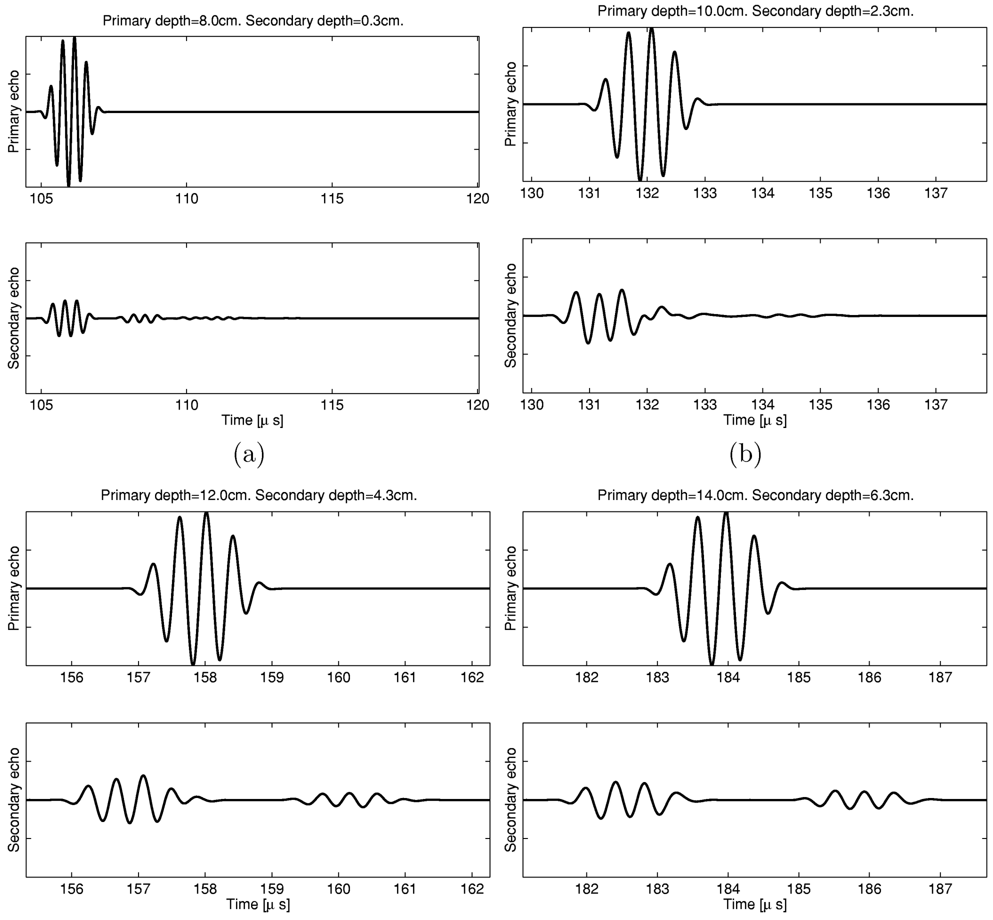

(a) (b) (c) (d)

Figure 5: Primary and secondary echoes for a 30° sector width. The elevation and transmit focus are at 8cm and 14cm respectively.

of 8-14cm, together with the secondary signals for a 30° sector width and elevation and transmit focus at 8cm and 16cm respectively. For each depth, the signals are normalized relative to each other.

Taking the strong scatterers in the body wall into consideration, the secondary signal might be considerably stronger than the primary signal for the smaller depths in the ROI. The clutter level can be significantly increased, and the stop band width of the clutter filter might have to be increased to get sufficient clutter attenuation. This means that low velocity blood flow may be difficult to measure. At depths where the secondary pulse has reached the ventricle, both pulses are scattered mainly by blood, and Table 4 shows that the primary signal is much stronger than the secondary signal. The secondary signal will not significantly influence the mean velocity estimates.

4 Clinical Applications

The stroke volume can be calculated by integrating the blood flow velocities through either the mitral or aortic valve in space and time during the heart beat. Velocity time curves can be obtained using spectral Doppler measurements. Assuming a flat velocity distribution, an estimate of the stroke volume is found by integrating a representative velocity time curve and multiplying the result with the estimated cross-sectional area [11]. The accuracy of the result depends on how well the cross-sectional velocity distribution fits the assumption.

Spectral Doppler measurements of the flow through the mitral valve is used to assess the diastolic function of the left ventricle [3, p. 151–155]. With a non-uniform cross-sectional velocity distribution, such measurements will be sensitive to the placement of the sample volume.

The examples mentioned above show that an efficient technique for investigating the cross-sectional velocity distribution through the heart valves is of clinical importance. Previously, ECG-triggered techniques have been used because of the limited temporal resolution in color flow imaging [10]. The acquisition technique described in this paper provides a temporal resolution that makes ECG-triggered techniques obsolete. The technique has been successfully used for investigations of both mitral [8, 9] and aortic [5] cross-sectional velocity distributions.

A three-dimensional color flow technique has recently been presented for volume flow measurements [1]. The accuracy of the three-dimensional technique depends on the temporal resolution, and the acquisition technique described in this paper might improve the accuracy of the 3D flow estimates.

5 Conclusions

An acquisition technique giving improved temporal resolution in ultrasound color flow imaging has been presented. The technique is based on having two pulses propagating simultaneously in different directions, and is applicable when the flow ROI is positioned deep in the image and extends only up to roughly half the maximum ROI depth. After a pulse is transmitted in a first direction, there is time available to receive and transmit in a second direction while waiting for the echo from the first pulse to arrive back to the transducer. With such beam interleaving, the acquisition time for the flow image is reduced by 50%. A disadvantage of the technique is that the echo from the second pulse which is picked up by the side lobes of the receive beam focused in the first direction, interferes with the desired primary echo.

Imaging of the blood flow through the heart valves with the probe in the apical position satisfies the ROI constraints. With a 30° tissue B-mode sector, and a 30° flow ROI extending from 7.9cm to 15cm, the frame rate was increased from 58 to 98frames/second by using the new acquisition technique. Simulations of this imaging geometry showed that for equal scatterers, the energy difference between the primary and secondary signals varies slightly with depth within the ROI. The minimum value of 8.9dB indicates that the secondary signal has a small effect on the flow estimates. In patients with strong reverberation noise from the body wall, the secondary signal might be considerably stronger. However, the reverberations vary slowly with time, and can be removed by a clutter filter. Due to the increased clutter level, the performance of the clutter filter becomes more critical when the proposed acquisition technique is used.

6 Acknowledgements

This study was supported by the Research Council of Norway. We thank Nancy Lea Eik-Nes for revision of the paper.

References

1. S. Berg, H. Torp, B. O. Haugen, and S. Samstad. Volumetric blood flow measurement with the use of dynamic 3-dimensional ultrasound color flow imaging. *J. Am. Soc. Echocardiogr.*, 13(5):393–402, May 2000.
2. R. H. Chesarek. Ultrasound imaging system for relatively low-velocity blood flow at relatively high frame rates. US Patent 4888694, Dec. 1989. Quantum Medical Systems, Inc., Issaquah, Wash.
3. H. Feigenbaum. *Echocardiography.* Lea & Feibiger, fifth edition, 1994.
4. L. Hatle and B. Anglesen. *Doppler Ultrasound in Cardiology – Physical Principles and Clinical Applications.* Lea & Feibiger, second edition, 1985.
5. B. O. Haugen, S. Bjærum, S. O. Samstad, T. Skjærpe, and H. Torp. A new method describing cross sectional blood flow velocity profiles in the left ventricular outflow tract from patients with atrial fibrilation using high frame rate two-dimensional color flow imaging. *J. Am. Soc. Echocardiogr.*, 14(1):50–56, Jan. 2001.
6. J. A. Jensen. Field II, a program for simulating ultrasound systems. The program can be downloaded from `http://www.it.dtu.dk/~jaj/field/field.html`.
7. J. A. Jensen. *Estimation of Blood Velocities Using Ultrasound.* Cambridge University Press, 1996.
8. S. O. Samstad, S. Bjærum, and H. Torp. Cross sectional flow velocity profiles from two-dimensional colour Doppler recorded with high frame rate: A new method applied to mitral blood flow. Presented at *12th Symposium on Echocardiology and 9th meeting of the International Cardiac Doppler Society*, Rotterdam, June 25-27, 1997.
9. S. O. Samstad, S. Bjærum, and H. Torp. Variability of E to A ratio of the mitral blood flow velocity pattern with the intravalvular site of velocity sampling. Presented at *12th Symposium on Echocardiology and 9th meeting of the International Cardiac Doppler Society*, Rotterdam, June 25-27, 1997.

10. S. O. Samstad, O. Rossvoll, H. G. Torp, T. Skjærpe, and L. Hatle. Cross-sectional early mitral flow-velocity profiles from color Doppler in patients with mitral valve disease. *Circulation*, 86(3):748–755, Sept. 1992.

11. T. Skjærpe. Principles of volume flow measurements. In J. R. T. C. Roelandt, G. R. Sutherland, S. Iliceto, and D. T. Linker, editors, *Cardiac Ultrasound*, pages 199–205. Churchill Livingstone, 1993.

Paper G

A New Method Describing Cross-Sectional Blood Flow Velocity Profiles in the Left Ventricular Outflow Tract of Patients with Atrial Fibrillation with the Use of High Frame-Rate 2-Dimensional Color Flow Imaging

Bjørn Olav Haugen, Steinar Bjærum[†], Stein Olav Samstad,
Terje Skjærpe and Hans Torp[†]

Department of Cardiology and Lung Medicine
Norwegian University of Science and Technology, Trondheim, Norway
[†]Department of Physiology and Biomedical Engineering,
Norwegian University of Science and Technology, Trondheim, Norway

Abstract

A new Doppler method was developed to evaluate the instantaneous cross-sectional velocity profile variability in the left ventricular outlet tract in patients with atrial fibrillation. Blood flow velocities acquired at a high frame rate (> 90 frames/s) from a single heart cycle were used to display the velocity profile. In 9 patients, 2 heart cycles with different R-R interval lengths were recorded in color flow mode in a transthoracic apical 5-chamber and long-axis view. Raw digital ultrasound data were analyzed with an external personal computer. The data indicated a variable skew in the profiles with the highest velocities and velocity-time integral (VTI) most often located in the center and toward the septum. The maximum VTI overestimated the mean VTI by approximately 40%. No significant difference existed between the two heartbeats. Thus the VTI can be averaged from heartbeats of different R-R lengths in atrial fibrillation.

Journal of the American Society of Echocardiography, 14(1):50–56, Jan. 2001

1 Introduction

Stroke volumes can be calculated from echocardiographic measurements of the velocity-time integral (VTI) in the left ventricular outflow tract (LVOT) and the subvalvular diameter, assuming a circular outflow tract and a flat velocity profile [5]. However, several reports have shown a nonuniform velocity profile in the LVOT in persons in sinus rhythm [1, 6, 7]. These studies assumed constant R-R intervals, and no beat-to-beat variability of the velocity profile. With these assumptions, one velocity profile was calculated by interpolation of color flow velocity samples from several heartbeats. The previous method cannot be used in patients with irregular heart rhythm, and to our knowledge, no data exist on the possible beat-to-beat variability of the velocity profile in the LVOT in such patients. To calculate cardiac output from echocardiographic measurements of stroke volume, the VTI must be averaged from 5 to 10 heartbeats to compensate for the variability in blood flow [5]. If the profile is skewed, and the skew changes from stroke to stroke in an unpredictable manner, another uncertainty and limitation is introduced in the pulsed wave Doppler technique.

We have developed a new method that uses blood flow velocity estimates acquired at a high frame rate (≥ 90 frames/s) from one heart cycle. A similar method has been applied in studies of the instantaneous cross-sectional velocity profile in the mitral blood flow of persons in sinus rhythm [3].

The purpose of our study was to develop a fast and easy method to study the instantaneous cross-sectional blood flow velocity profile in the LVOT in patients with atrial fibrillation. The method was applied to 9 patients, and velocity profiles from 2 consecutive heartbeats of different R-R interval lengths were compared to assess any possible differences in the velocity profile.

2 Methods

Informed, written consent was obtained from each subject in accordance with the regional ethical committee on human research.

2.1 Subjects

Nine patients with atrial fibrillation and no significant heart valve disease or other structural heart disease were consecutively included before elective DC cardioversion at the department of cardiology, University hospital of Trondheim, Norway. The group comprised 7 men and 2 women (mean age 62 years, range 41 to 75). The mean heart rate was 88 bpm (range 65 to 110).

2.2 Equipment

A digital ultrasonographic scanner (System Five, GE Vingmed Ultrasound, Horten, Norway) with a 2.5-MHz phased-array transducer was used for all echocardiographic measurements. Digital image data were transferred to an external personal computer and analyzed with MATLAB (The MathWorks, Inc, Natick, Mass) software. To obtain the information needed from 1 heartbeat to construct the instantaneous cross-sectional velocity profile, we used software developed for high frame-rate imaging as described below.

2.3 Instrument Setting

Recordings of tissue images were obtained in second harmonic imaging mode with a transducer transmittal frequency of 1.7 MHz. For color flow imaging, the center frequency of the transmitted pulse was 2.5 MHz. The radial sample volume length was 0.8 mm.

2.4 Data Acquisition

The subjects were examined in the left lateral decubital position. To reduce cardiac movement, the recordings were done in held end-expiration. Ultrasonographic data were acquired in an apical 5-chamber view and an apical long-axis view. To get as high a frame-rate as possible during recordings of aortic blood flow, a prototype data acquisition technique was used, which provided an increased frame-rate with a moderate decrease in spatial resolution. The sector angle was set to a minimum, and the region of interest minimized to cover the LVOT to obtain a rate of ≥ 90 frames/s, and a time delay less than 6 ms over the flow sector was achieved. Thus, from a single heart beat, blood flow velocities from various positions within the LVOT were recorded with a resolution better than 6 ms at each point.

We scrolled the replay memory in the digital ultrasonographic scanner to find the longest R-R interval. The subsequent R-R interval was short. The digital image data from the 3 subsequent heartbeats corresponding to these 2 R-R intervals were transferred from the ultrasonographic scanner to an external personal computer.

2.5 Data Processing

For each sample volume, the flow information was encoded in a 16-bit “word”. This data format ensures adequate resolution for both the power and velocity estimates. The data were visualized and processed with the use of software written in the MATLAB language. By performing angle correction, flow velocities perpendicular to arbitrary lines in the image could be plotted as a function of time. Detection of large discontinuities in the velocity estimates enabled correction for aliasing caused by high velocities. This way, the color flow data could be used in the quantitative analysis of the flow pattern through the aortic valve.

Tissue priority and flow gain were adjusted to make sure that the flow was within the anatomic borders. The systolic periods from 2 subsequent heartbeats were studied. Measurements were obtained for the R-R interval, defined as the time from the previous heartbeat to the one studied. A line across the LVOT was drawn 0.5 to 1 cm proximal to the insertion of the aortic valve (Figure 1), and cross-sectional velocities were extracted from this line and visualized with color M-mode echocardiography (Figure 2). The line was fixed and did not track the tissue during systole. Blood flow velocities from any

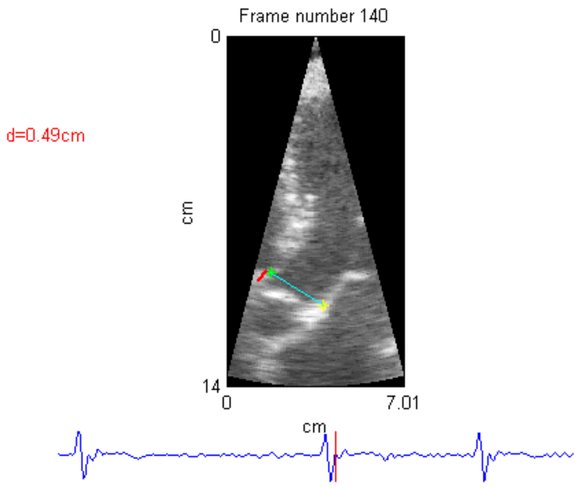

Figure 1: A line across the LVOT was drawn 0.5 cm proximal to the insertion of the aortic valve, and cross-sectional velocities were extracted from this line.

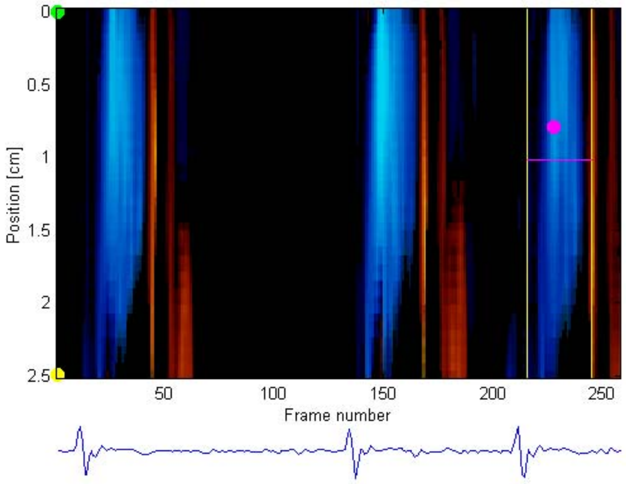

Figure 2: Cross-sectional blood flow velocities encoded as color flow from the left ventricular outflow tract obtained in a 5-chamber view in a patient with atrial fibrillation. The *blue area limited by yellow lines* represents the systolic period. The *green marker* is located at the septum. The *yellow marker* is located laterally. The *pink marker* is located at the point of maximum velocity and represents the maximum velocity-time integral. The *pink line* represents the maximum velocity-time integral.

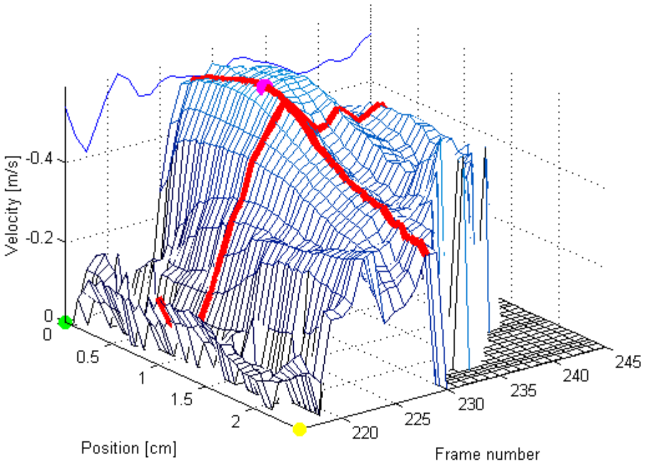

Figure 3: The instantaneous cross-sectional velocity profile in systole limited by *yellow lines* in Figure 2. The *red line crossing the picture along the axis marked position* represents time of maximum velocity. The *pink marker* represents the maximum velocity. The *red line along the axis marked frame number* represents the position of maximum velocity-time integral.

given time interval (in our setting, during systole) were analyzed by extracting the data as illustrated in Figure 2. The following heartbeat was treated in the same manner.

The instantaneous cross-sectional velocity profile was reconstructed by plotting blood flow velocities against time and position along the diameter of the LVOT (Figure 3). Figure 4 shows the velocity profile from 2 heartbeats of different R-R interval lengths (long and short). As a quantitative assessment of the velocity distribution, any possible skew was described by comparing the ratio of the maximum VTI to the mean velocity integral, and the maximum velocity to the mean velocity. Furthermore, the position of the maximum velocity and the maximum VTI along the cross-sectional line was noted. Finally, we calculated the part of the line that crossed the LVOT in which values between the maximum VTI and maximum VTI−20% were detected (Figure 5).

2.6 Statistical Analysis

Data from 2 different heartbeats were compared with the paired t-test (null hypothesis: there is no difference between the 2 heartbeats; alternate hypothesis: there is a difference). The level of significance was chosen at $P < .05$.

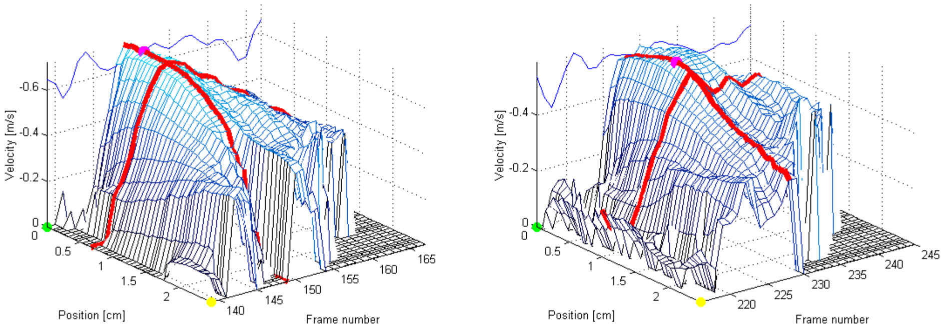

Systole 1

Systole 2

Figure 4: The instantaneous cross-sectional velocity profiles from 2 heartbeats with different R-R interval lengths in a patient with atrial fibrillation. Blood flow velocities are plotted against time and position along the diameter of the left ventricular outflow tract. The highest blood flow velocities are located toward the intraventricular septum.

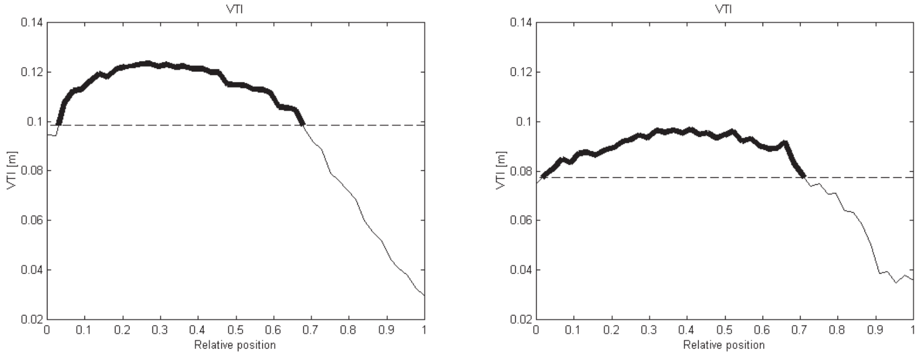

(a)

(b)

Figure 5: The relative length of *(VTI max to VTI max−20%)/Total diameter*. Five-chamber view. The *x-axis* represents the line across the left ventricular outflow tract. *Point 0* is located at the septum and *1* at the lateral end. The *bold part of the curve* is the interval *VTI max to VTI max−20%*. a. Heartbeat 1. The relative length of (VTI max to VTI max−20%)/Total diameter= 0.65. b. Heartbeat 2. The relative length of (VTI max to VTI max−20%)/Total diameter= 0.69. *VTI*, velocity-time integral.

3 Results

The data indicated a nonuniform velocity distribution with the highest velocities and VTI located in the center of the LVOT and toward the intraventricular septum. The maximum VTI overestimated the mean VTI by approximately 40% in both planes. At peak flow, the maximum velocity overestimated the mean velocity by approximately 50% in the apical long-axis view and by about 60% in the 5-chamber view. The line from the septum to the middle part of the LVOT covered VTI values from maximum to 20% below maximum.

No significant difference was found at the 5% level between the 2 heartbeats in any of the calculated variables, except the difference in R-R interval length. However, the ratios of maximum velocity/mean velocity recorded in the apical long-axis view showed a difference of $P = .05$, close to significance.

Tables 1 through 4 present the data from the recordings of 2 different heartbeats obtained in 2 orthogonal planes, a 5-chamber view, and the apical long-axis view. The recordings were obtained at high frame-rate (mean 100 frames/s, range 90 to 115). The mean time resolution was 10 ms (range 8.7 to 11 ms).

	Heart beat 1	Heart beat 2	95% CI difference in mean	*P* value
RR length (s)	0.93	0.59	0.21 to 0.48	.0001
$\frac{\text{Length of (VTI max to VTI max}-20\%)}{\text{Total line}}$	0.56	0.44	−0.03 to 0.25	.1
Max VTI/mean VTI	1.38	1.49	−0.61 to 0.38	.62
Max V/mean V	1.37	1.67	−0.59 to −0.01	.05

Table 1: The recordings from two different heartbeats in 9 patients with atrial fibrillation (apical long-axis view). In calculations of the relative length of (VTI max to VTI max−20%)/Total line, point 0 is located to the anterior, and 1 is located at the posterior end. *RR*, Time interval between two R complexes in the electrocardiogram; *VTI*, velocity-time integral; *V*, velocity; *max*, maximum.

	Heart beat 1	Heart beat 2	95% CI difference in mean	*P* value
RR length (s)	0.94	0.61	0.18 to 0.47	.001
$\frac{\text{Length of (VTI max to VTI max}-20\%)}{\text{Total line}}$	0.56	0.63	−0.16 to 0.06	.07
Max VTI/mean VTI	1.32	1.42	−0.06 to 0.24	.19
Max V/mean V	1.8	1.32	−0.59 to 1.53	.33

Table 2: The recordings from two different heartbeats in 9 patients with atrial fibrillation (5-chamber view). In calculations of the relative length of (VTI max to VTI max−20%)/Total line, point 0 is located to the anterior, and 1 is located at the posterior end. *RR*, Time interval between two R complexes in the electrocardiogram; *VTI*, velocity-time integral; *V*, velocity.

Relative position of the maximum velocity along the line crossing the LVOT	Heart beat 1	Heart beat 2	95% CI difference in mean	*P* value
Five-chamber view	0.43	0.41	−0.26 to 0.19	.74
Apical long-axis view	0.35	0.53	−0.09 to 0.33	.24

Table 3: The recordings from two different heartbeats in 9 patients with atrial fibrillation. In the relative position of the maximum velocity, point 0 is located at the septal/anterior, and 1 is located at the lateral/posterior end. *LVOT*, Left ventricular outflow tract.

Relative position of the maximum VTI along the line crossing the LVOT	Heart beat 1	Heart beat 2	95% CI difference in mean	*P* value
Five-chamber view	0.44	0.47	−0.24 to 0.19	.76
Apical long-axis view	0.34	0.44	−0.28 to 0.07	.22

Table 4: The recordings from two different heartbeats in 9 patients with atrial fibrillation. In the relative position of the maximum VTI, point 0 is located at the septal/anterior, and 1 is located at the lateral/posterior end. *LVOT*, Left ventricular outflow tract; *VTI*, velocity-time integral

4 Discussion

In this study, we have presented a fast and easy method to describe instantaneous cross-sectional blood flow velocity profiles in the LVOT of patients with atrial fibrillation. At 90 frames/s and above, the time resolution was better than 11 ms. The influence of the sweep time delay was strongly reduced and therefore disregarded in our study. Thus, it was possible to display the instantaneous velocity profile from the recording of a single heart cycle. Because we compared 2 heartbeats, any possible influence in the skew caused by sweep time delay would influence both heartbeats. This was a more feasible method than previous methods in which color flow velocity samples from several heartbeats with regular R-R intervals were interpolated to construct the instantaneous cross-sectional velocity profile [1, 2, 4, 6, 7].

In conventional pulsed wave Doppler techniques, 5 to 10 heartbeats are averaged in patients with atrial fibrillation to ensure a reliable measure of cardiac output. We did not find any significant difference in the blood flow velocity profile in 2 consecutive heartbeats of different R-R interval lengths. One potential implication of this finding is that when measuring blood flow velocities with the pulsed Doppler technique, the sample volume can be fixed in the same position along the diameter of the LVOT during the recording. The maximum VTI has been described in 2 settings: the relative position of maximum VTI, and the part of the line that crosses the LVOT in which values between maximum VTI and maximum VTI − 20% were measured. The maximum VTI was a robust parameter as opposed to the mean VTI because of less dependence of the high pass filter limit. Furthermore, the maximum VTI was less sensitive to poor differentiation of tissue and blood flow velocities. The mean VTI was measured for comparison with previous works. The Doppler sample volume is fixed during recording of blood flow velocities, but the heart is moving.

The introduction of the parameter *Length of (VTI max to VTI max−20%)/total line*, illustrates that the acceptance of a potential variation of 20% in the calculation of stoke volume likely enables the sample volume to actually detect these velocities along the diameter. If this distance is short, it would be difficult to detect blood flow velocities within this range, and the estimate of the VTI would be less precise. As shown in Tables 1 and 2, the line from the septum to the middle part of LVOT covers VTI values from maximum to 20% below. The skew in the velocity profile has been described in patients in sinus rhythm as previously mentioned and must be kept in mind when sampling blood flow velocities with the use of the pulsed Doppler technique.

5 Study Limitations

The results describing the velocity profiles must be interpreted cautiously because a limited number of patients were included in this study. Each patient analysis was limited to 2 cardiac cycles. However, we scrolled the replay memory in the digital ultrasonographic scanner to find the longest R-R interval. The subsequent R-R interval was significantly shorter. Thus, the probability of detecting differences in the velocity profile was maximized.

The cross-sectional velocity profile was recorded in 2 orthogonal planes; thus a complete 3-dimensional velocity profile was not studied. It is not possible to generalize our findings to all patients with atrial fibrillation, as they might represent a selected group.

6 Conclusion

We have developed a fast and easy method that enables the study of the instantaneous cross-sectional velocity profile in patients with atrial fibrillation. The velocity profiles were skewed with the maximum velocity and VTI most often located in the middle of the LVOT and toward the septum. The maximum VTI overestimated the mean VTI by approximately 40%.

No differences existed in these measures in 2 consecutive heartbeats of different R-R interval lengths. Thus, according to our results, measurements from heartbeats of different R-R interval lengths can be averaged without moving the pulsed wave sample volume along the diameter of the LVOT.

Acknowledgements

The authors would like to thank Stig Arild Slørdahl, MD, PhD, with the Department of Physiology and Biomedical Engineering, Norwegian University of Science and Technology, Trondheim, Norway, for reviewing our manuscript. This study was supported by grants from The Norwegian Council for Cardiovascular Diseases.

References

1. O. Rossvoll, S. Samstad, H. G. Torp, D. T. Linker, T. Skjærpe, B. A. J. Angelsen, and L. Hatle. The velocity distribution in the aortic anulus in normal subjects: Quantitative analysis of two-dimensional Doppler flow maps. *J. Am. Soc. Echocardiogr.*, 4:367–378, 1991.

2. S. O. Samstad, J. Bathen, O. Rossvoll, H. G. Torp, T. Skjaerpe, and L. Hatle. Impact of changes in heart rate and stroke volume on the cross sectional flow velocity distribution of diastolic mitral blood flow. a study on 6 patients with pacemakers programmed at different heart rates. *Int. J. Card. Imaging*, 8:75–83, 1992.

3. S. O. Samstad, S. Bjærum, and H. Torp. Cross sectional flow velocity profiles from two-dimensional colour Doppler recorded with high frame rate: A new method applied to mitral blood flow. Presented at *12th Symposium on Echocardiology and 9th meeting of the International Cardiac Doppler Society*, Rotterdam, June 25-27, 1997.

4. S. O. Samstad, O. Rossvoll, H. G. Torp, T. Skjærpe, and L. Hatle. Cross-sectional early mitral flow-velocity profiles from color Doppler in patients with mitral valve disease. *Circulation*, 86(3):748–755, Sept. 1992.

5. T. Skjærpe. Principles of volume flow measurements. In J. R. T. C. Roelandt, G. R. Sutherland, S. Iliceto, and D. T. Linker, editors, *Cardiac Ultrasound*, pages 199–205. Churchill Livingstone, 1993.

6. R. Wiseth, S. Samstad, O. Rossvoll, H. G. Torp, T. Skjærpe, and L. Hatle. Cross–sectional left ventricular outflow tract velocities before and after aortic valve replacement: A comparative study with two-dimensional Doppler ultrasound. *J. Am. Soc. Echocardiogr.*, 6(3):279–285, 1993.

7. Y. Q. Zhou, S. Faerestrand, K. Matre, and S. Birkeland. Velocity distributions in the left-ventricular outflow tract and the aortic anulus measured with Doppler color-flow mapping in normal subjects. *Eur. Heart J.*, 14(9):1179–1188, Sept. 1993.

Paper H

Blood Motion Imaging: A New Blood Flow Imaging Technique

Steinar Bjærum and Hans Torp

Department of Physiology and Biomedical Engineering,
Norwegian University of Science and Technology, Trondheim, Norway

Abstract

In this paper we present new signal processing algorithms for visualization of blood flow in ultrasound imaging systems. As opposed to with conventional color flow imaging, the speckle pattern from the moving blood cells is preserved and enhanced, enabling the user to visually track the blood motion from frame to frame. In conventional color flow imaging, one image is produced from a packet of typically 5-15 pulses transmitted along each scan line in the image. The Doppler shift produced by slowly moving muscular tissue is lower than the Doppler shift produced by the blood flow, and efficient clutter filters are designed to attenuate the clutter signal down to a level much lower than the signal from blood. The signal power after clutter filtering is used to detect points in the image where blood is present. Alternatively, in the power Doppler mode, the signal power is displayed as an image to visualize blood vessels. In order to get reliable detection, substantial temporal and spatial averaging is used, thus limiting the dynamic variation, as well as spatial resolution. This averaging process suppresses the spatial speckle pattern in the signal amplitude. In addition to preserving the speckle pattern, the algorithms described in this paper compute several image frames per packet of pulse transmissions. The perception of movement is further improved if the scatterers in a large spatial region are imaged almost simultaneously. This is obtained by increasing the time between pulse transmissions in the same beam direction, and using a technique called beam interleaving. After transmitting a pulse in a first direction, there is time available to acquire data in several other beam directions before transmitting the next pulse in the first direction. Visualization of the speckle pattern movement gives the user a correct perception of the blood flow direction and magnitude, and is also useful in separating true blood flow from wall motion artifacts.

1 Introduction

Ultrasound blood flow imaging is based on detection and measurement of the Doppler shift created by moving scatterers. This Doppler shift is utilized to suppress the signal from slowly moving muscular tissue, in order to detect the presence of blood, and is also used to quantify the actual blood velocity in each point of an ultrasound image. Unfortunately, the Doppler frequency shift is only sensitive to the velocity component along the ultrasonic beam. Possible velocity components transversal to the beam are not detectable from the received Doppler signal. In standard color flow imaging, the Doppler shift is estimated from the received signal generated by a number of transmitted pulses, and visualized using a color scale. In some situations, the blood flow direction can be measured from the vessel geometry, but this is difficult to do automatically, especially when the vessel geometry is not clearly visible in the image. Standard color flow imaging often gives confusing blood velocity visualization, e.g. due to changes in the angle between the blood flow and the ultrasonic beam. Even though the velocity magnitude is constant in a curved blood vessel the Doppler shift, and therefore also the color, changes along the vessel. In the power Doppler mode this confusion is removed by discarding the measured Doppler shift from the display, but these images do not contain any directional information.

There is a considerable interest in a possible measurement of the transversal velocity component in ultrasound flow imaging, and a number of methods have been proposed.

1. Compound scanning from two different positions gives two velocity components. To get sufficient difference in the angle between the two velocity components, the distance between the two sub-apertures needs to be relatively large. However, in cardiac imaging the size of the transducer is limited by the space between the ribs. Additional problems with this technique is the time lag between the measurement of the two velocity components, and the limited field of view [7].

2. Measurement of transit-time through the ultrasound beam, which is reflected in an increased bandwidth of the Doppler signal. This method has very low accuracy, does not yield flow direction, and will only work in regions with rectilinear and laminar flow [13].

3. Two-dimensional speckle tracking methods based on frame-to-frame correlation analysis has been proposed by several authors [18]. This method can be used both for the RF-signal and the amplitude detected signal.

4. Coherent processing of two sub-apertures of the transducer to create lateral oscillations in the received beam pattern. This method is described by two authors [1, 10], and gives quantitative lateral velocity information, including the sign. The main drawback of this method is poor lateral resolution, which limits its use for imaging.

Although these techniques address the same problem, the solution presented in this paper is fundamentally different from the techniques above. Rather than trying to estimate the lateral velocity component, we present algorithms for enhancing the speckle pattern movement, which is related to the blood cell movement in the blood vessels. The approach is similar to a technique called B-flow that has recently been patented [4].

In ultrasound imaging, the returned echoes are processed coherently, and there are variations in the intensity due to constructive and destructive interference of the sound waves scattered back from a large number of scatterers. These variations in intensity are often termed the “speckle pattern”. When there is a slight displacement of the scatterers (the red blood cells), there will be a corresponding displacement of the speckle pattern. By preserving, enhancing, and visualizing the speckle pattern from moving scatterers and displaying a stream of such images, an intuitive display of the blood flow is obtained. This method will be referred to as “blood motion imaging” (BMI) and enables the operator to see the blood flowing in the image, although no attempt is made to measure the lateral velocity component. However, BMI may indirectly give the lateral velocity component by combining an angle measurement derived from the speckle motion with the radial velocity component obtained from the Doppler frequency shift. In addition to providing correct perception of the blood flow direction and magnitude, BMI is also useful in separating true blood flow from wall motion artifacts.

BMI processing can be applied both to data which are uniformly sampled in time, and to data acquired using conventional color flow “packet” acquisition. Different pulse transmissions can be used for the tissue and BMI data, enabling different optimization of the tissue and flow pulses. The first stage in the BMI processing is temporal high-pass filtering to attenuate the signal from stationary and slowly moving scatterers. The high-pass filtered data can be processed by using conventional B-mode techniques, or, in order to accentuate the speckle pattern, more advanced processing such as amplitude normalization can be performed. It is also possible to combine BMI with conventional color flow velocity estimates. The tissue and flow images can be combined additively into either a gray scale or color image. Alternatively, a decision can be made for each pixel if it is a tissue or flow pixel. The uniformly sampled data are processed using a sliding window, and the frame rate becomes equal to the pulse repetition frequency (PRF). For the packet data, BMI processing produces several image frames per packet, whereas conventional color flow imaging produces only one image frame per packet. The time between each of the BMI frames from one packet equals the inverse of the PRF within the packet. In order to visualize the motion, the display frame rate must be reduced substantially, e.g. from 1kHz PRF to 30Hz frame rate. For real-time display, a lot of data must be discarded, but for slow motion replay, a larger fraction or all of the recorded frames can be used.

As mentioned above, B-flow uses a similar approach as BMI for blood flow visualization. There are, however, several differences between B-flow and BMI regarding data acquisition and signal processing. In B-flow, one high-pass filtered sample is calculated by a weighted average over a packet of samples. The tissue structures are visualized by perturbing one of the filter weights. This adds the high-pass filtered data to the unfiltered data from one of the pulse transmissions within each packet. The resulting sample undergoes conventional B-mode processing. Since the tissue and flow images are calculated from the same pulse transmissions, it is not possible to use different tissue and flow pulses. The main difference between B-flow and BMI is that in B-flow only one image per packet is produced. This means that there is a larger displacement between each frame, and thus a larger decorrelation of the speckle pattern which potentially makes it harder to follow the speckle movement from image to image. With only one image per packet, each packet can contain only a small number of samples to get an adequate frame rate. This makes it difficult to sufficiently attenuate the signal from slowly moving tissue. The B-flow patent does not mention any combination with color flow velocity estimates.

This paper is organized as follows. The data acquisition and basic principles of BMI are described in Section 2. A more detailed description of the signal processing in BMI is given in Section 3, while clinical applications are discussed in Section 4. Possible improvements and new applications of BMI are discussed in Section 5 before the paper is concluded in Section 6.

2 Data Acquisition

The data used to calculate blood motion images are acquired in the same manner as data used for conventional color flow imaging. The ultrasound beam is scanned over the region to be imaged, and a series of N pulses are transmitted in each beam direction of the flow image. For each flow image, one tissue B-mode scan is performed, and the flow and B-mode data are combined to visualize both the blood flow and the tissue structures.

The number N will be referred to as the packet size. The time T between two pulses within a packet is called the pulse repetition time, and the inverse of this time is called the pulse repetition frequency (PRF). The ultrasound pulse needs to propagate a distance equal to twice the image depth d_{max} before a new pulse can be transmitted. The maximum possible PRF is thus given by

$$\text{PRF}_{\text{max}} = \frac{1}{T} = \frac{c}{2d_{\text{max}}} \tag{1}$$

where c is the sound velocity. By decreasing the PRF with a factor k, it is possible to use a technique called beam interleaving [3]. After transmitting a pulse in a first direction, there is time to acquire data in $k-1$ other beam directions before transmitting the next pulse in the first direction. These k beams are called an interleave group (IG), and the number k is called the interleave group size (IGS) and can be expressed by

$$\text{IGS} = \left\lfloor \frac{\text{PRF}_{\text{max}}}{\text{PRF}} \right\rfloor \tag{2}$$

where $\lfloor \cdot \rfloor$ means nearest integer towards $-\infty$. The number of interleave groups N_{IG} in one image is given by

$$N_{\text{IG}} = \frac{N_{\text{beams}}}{\text{IGS}} \tag{3}$$

where N_{beams} is the number of beams determined by the image width. The principle of beam interleaving is illustrated in Figure 1, where the numbers in the different beam

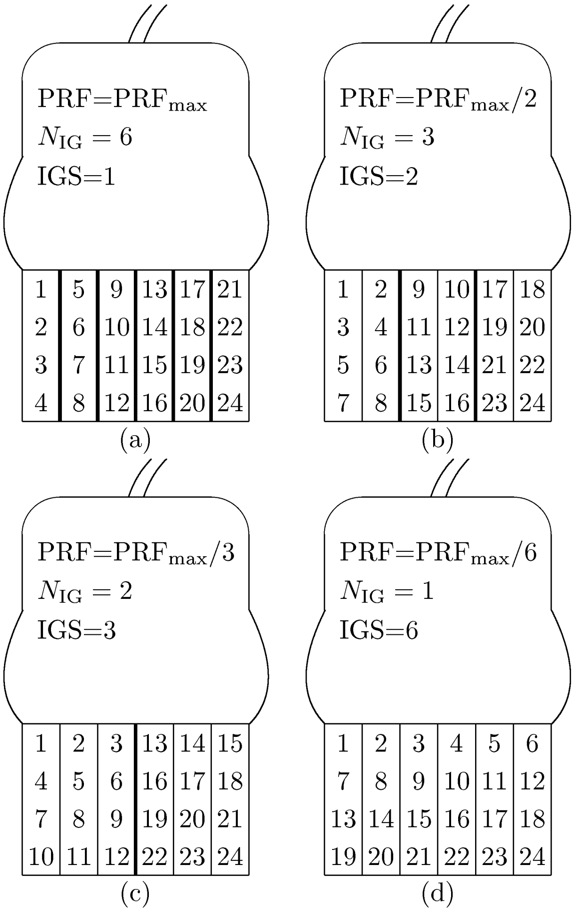

1	5	9	13	17	21
2	6	10	14	18	22
3	7	11	15	19	23
4	8	12	16	20	24

(a)

1	2	9	10	17	18
3	4	11	12	19	20
5	6	13	14	21	22
7	8	15	16	23	24

(b)

1	2	3	13	14	15
4	5	6	16	17	18
7	8	9	19	20	21
10	11	12	22	23	24

(c)

1	2	3	4	5	6
7	8	9	10	11	12
13	14	15	16	17	18
19	20	21	22	23	24

(d)

Figure 1: Beam interleaving in 2D Doppler acquisition with 6 beam directions and packet size $N = 4$. The numbers indicate the sequence of the 24 pulses.

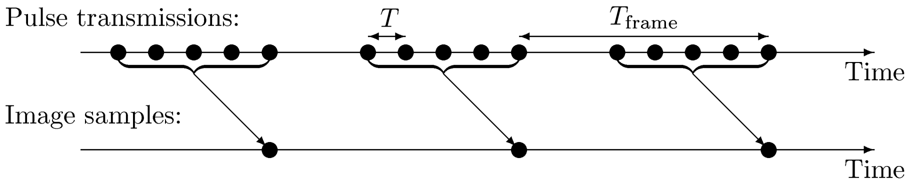

Figure 2: The timing of pulse transmissions vs. image samples in one sample volume in conventional color flow imaging. One image sample is calculated per packet of pulse transmissions.

directions indicate the timing of the transmitted pulses. Parts of the tissue B-mode image may be acquired between the different flow interleave groups, or the whole B-mode image is acquired after one entire flow image acquisition. Either way, there is one B-mode image recording per flow image (which consists of N pulses in each direction). With a low PRF, the image consists of just a few interleave groups. It is advantageous with a large IGS since there is a small time difference between neighboring beams within an IG. The scatterers in a spatial region with width determined by the IGS are imaged almost simultaneously, and the movement of the scatterers can be visually tracked from frame to frame.

By using a relatively broad transmit beam, it is possible to have several receive beams per transmit beam by using simultaneous beamforming in slightly different directions. With k parallel beamforming channels, the frame rate is increased by a factor k for the same number of receive beams.

The timing of pulse transmissions in one beam direction, together with the calculated image data in conventional color flow imaging is shown in Figure 2. During the time T_{frame} in Figure 2, flow data are acquired in all the other beam directions, and the tissue B-mode data are also acquired. The corresponding timing for BMI is shown in Figure 3, where we see that several flow images are calculated for each signal packet. Only one B-mode scan is performed per flow packet, and interpolation is needed to obtain one B-mode image for each flow image. Alternatively, the B-mode image can be calculated from the same data as the flow image, resulting in a higher frame rate. The disadvantage of this approach is that the B-mode image can not be wider than the flow

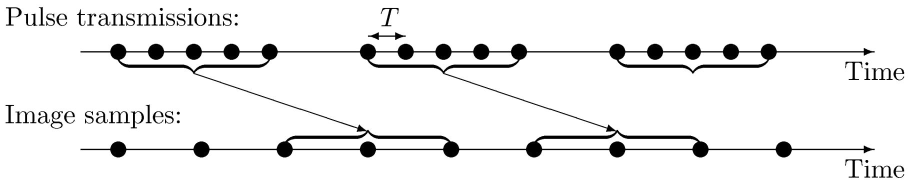

Figure 3: The timing of pulse transmissions vs. image samples in one sample volume in BMI packet acquisition. Several image samples are calculated per packet of pulse transmissions.

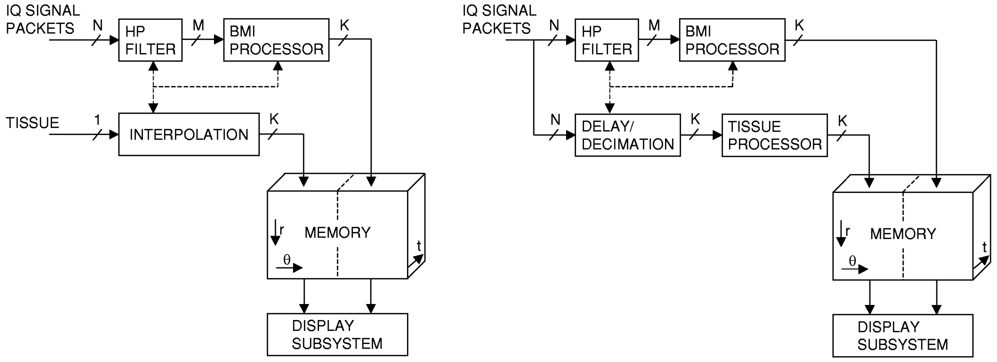

(a) (b)

Figure 4: Overview of BMI processing for packet data acquisition. (a) Separate tissue B-mode scan. (b) BMI and tissue B-mode from the same data.

image, and the B-mode resolution can not be higher than the flow image resolution.

An overview of BMI systems using packet data acquisition is shown in Figure 4. The input data are the beamformed, complex demodulated, and time-gain compensated IQ signal packet containing samples in time from one sample volume with sampling frequency equal to the PRF. The signal packet forms a complex valued signal vector with dimension equal to the packet size N, where the samples have a zero mean complex Gaussian probability density function (PDF). The same processing is performed on the signal from all the sample volumes in the image. Several images ($K > 1$) per packet may be displayed, as opposed to conventional color flow imaging where only one image per packet is displayed. With separate tissue B-mode acquisition, the tissue data need to be interpolated in time to get one tissue frame for each flow frame as shown in Figure 4a. The number of BMI frames K might be smaller than the packet size N. When the B-mode images are calculated from the same data as the BMI images, the two data streams need to be synchronized to get matching BMI and tissue frames as shown in Figure 4b.

2.1 Continuous Acquisition

Combining a low PRF and small depth with a narrow image sector, it is possible with just one IG as illustrated in Figure 1d, where we see that the entire flow image is scanned between two pulse transmissions in the same direction. After N flow pulses are transmitted in each beam direction, a B-mode scan is performed, and there is a time delay until the next N flow pulses are transmitted. Uniform sampling in time can be achieved in several ways. One possibility is to perform a B-mode scan for each flow scan. Another option is to skip the separate B-mode scan and generate the tissue B-mode image from the flow data. Acquisition schemes where there is a continuous stream of flow data with uniform sampling interval, will be called continuous acquisition as opposed to conventional color flow packet acquisition. With continuous acquisition,

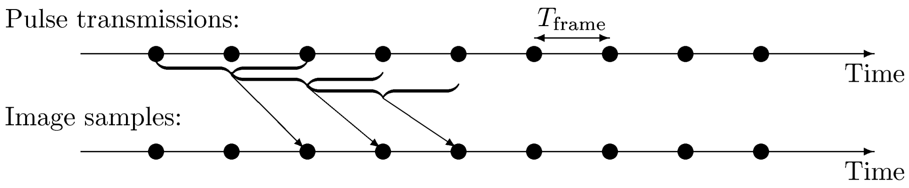

Figure 5: The timing of pulse transmissions vs. image samples in one sample volume for continuous BMI acquisition. The image samples are calculated using a sliding window approach.

the PRF is equal to the frame rate. The timing of the pulse transmissions in one beam direction for continuous data acquisition is shown in Figure 5, where we see that the BMI images are calculated using a sliding window approach. BMI systems using continuous data acquisition are illustrated in Figure 6 where for each sample volume there is a continuous stream of data with uniform sampling interval. The scheme with separate B-mode acquisition shown in Figure 6b corresponds to packet acquisition with $N = 1$.

2.2 Coded Excitation

In BMI it is important to have as high spatial resolution as possible, and a short pulse should be used. For patient safety reasons, there is a limit on the amplitude of the transmitted pulse. This means that the transmitted power decreases with pulse length, resulting in a poorer signal-to-noise ratio (SNR). However, several coded excitation techniques exist [8] to improve the SNR without increasing the amplitude of the transmitted pulse. BMI is ideally suited for coded excitation techniques, and the BMI

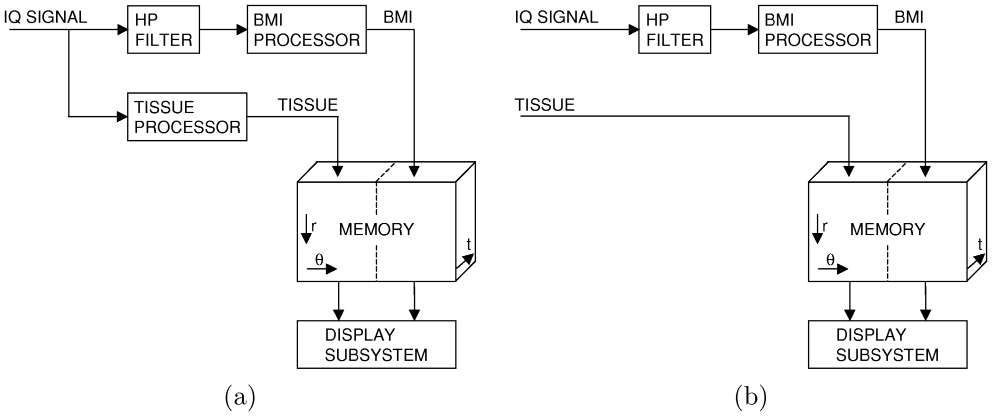

Figure 6: Overview of BMI processing for continuous data acquisition. (a) BMI and tissue B-mode images are calculated from the same data. (b) Separate tissue B-mode scan.

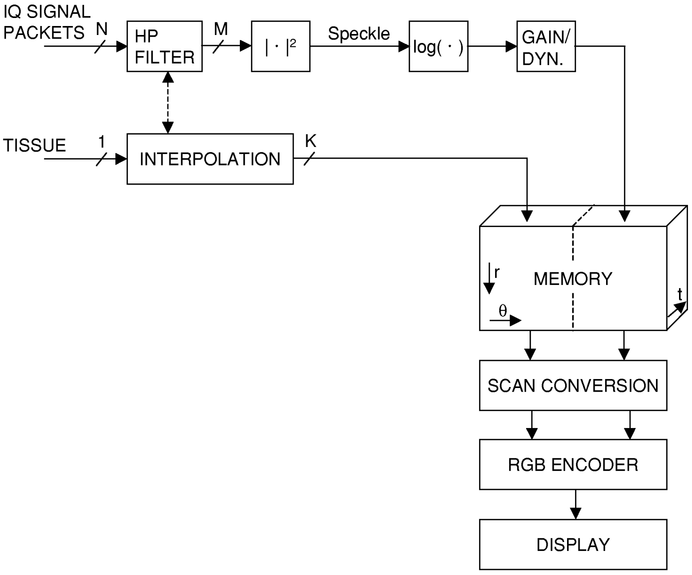

Figure 7: Basic BMI processing.

processing described in the next section will not be not altered if the input signal is acquired using coded excitation techniques to improve the SNR.

3 Signal Processing in BMI

A block diagram of a basic form of the 'BMI processor' in Figure 4 is shown in Figure 7, and is recognized as tissue B-mode processing of the high-pass filtered data. In the following sections, we will investigate the high-pass filter in more detail, and present more advanced 'BMI processors' than the one shown in Figure 7.

3.1 High-pass Filtering

As seen in Figure 7, the first stage in the BMI processing is temporal high-pass filtering. Figure 8a shows a tissue B-mode image of the carotid artery. The corresponding B-mode image calculated from high-pass filtered data is shown in Figure 8b where the signal from the moving blood is significantly stronger than the signal from the surrounding tissue.

Commonly used high-pass filters in color flow imaging are finite impulse response (FIR) filters, infinite impulse response (IIR) filters with different types of initialization [5, 6], and polynomial regression filters [9, 11, 17]. All these types of filters can be used in BMI. However, BMI depends on the similarity of the speckle pattern in subsequent images. The processing should be equal for subsequent images, and FIR filters are preferred since they are the only filters that are time invariant for signals of finite length.

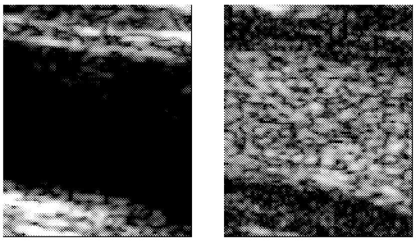

(a) (b)

Figure 8: Carotid artery. (a) Tissue B-mode image. (b) Tissue B-mode image calculated from temporally high-pass filtered data.

An FIR filter is described by an impulse response function $h(n),\ n = 0, \dots, L-1$, where $L-1$ is the filter order. With input signal $x(n),\ n = 0, \dots, N-1$, the output signal $y(n)$ is given by the convolution sum

$$y(n) = \sum_{k=0}^{L-1} h(k)x(n-k) \tag{4}$$

Each output sample $y(n)$ is a weighted sum of the previous L input samples $x(n), \dots, x(n-L+1)$, and the output sample $y(L-1)$ is the first output sample that does not depend on any $x(n)$ for $n < 0$. This means that the first $L-1$ output samples, $y(0), \dots, y(L-2)$, need to be discarded. With packet size N, the number of samples subsequent to the high-pass filter is reduced to $M = N - (L-1)$ as indicated in Figure 7.

Subsequent to the high-pass filter in Figure 7, the squared magnitude $|y(n)|^2$ is calculated. The expected value of $|y(n)|^2$ is the mean power in the signal, and is also equal to the autocorrelation function at lag zero, $R(0) = E\{|y(n)|^2\}$. We will later use estimates of the autocorrelation function at lag one to estimate the blood velocity and combine these estimates with BMI. The autocorrelation function of the output signal is related to the filter transfer function $H(\omega)$ and the power spectrum of the input signal $S_x(\omega)$ by

$$R_y(l) = \mathcal{F}^{-1}\left\{|H(\omega)|^2 S_x(\omega)\right\} \tag{5}$$

where $\mathcal{F}^{-1}$ denotes the inverse Fourier transform. Equation 5 shows that the autocorrelation function does not depend on the phase response of the filter. In [2] we have shown the advantage of using FIR filters with a non-linear phase response compared to the more commonly used linear-phase FIR filters. The improvement in the frequency response with non-linear phase is illustrated in Figure 9 for fourth order equiripple FIR filters. Equiripple filters minimize the maximum error in the pass- and stop-band [14]. The pass-band width of the filters in Figure 9 was maximized within the constraints of at least 80dB attenuation in the stop-band from 0 to 0.005, and maximum 1dB peak-to-peak ripple in the pass-band.

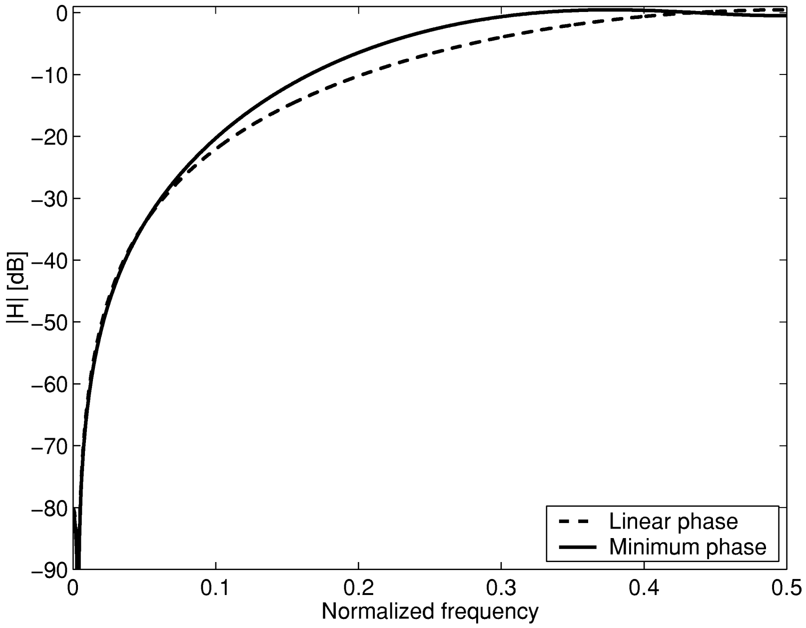

Figure 9: FIR high-pass filters of order 4.

3.2 High-pass Filter Effects on the Speckle Signal

High-pass filtering is necessary to remove the signal from stationary and slowly moving tissue scatterers. In this section we will investigate how the high-pass filter affects the desired speckle pattern from moving blood.

A coordinate system for the imaging system is shown in Figure 10 where x, y, and z are the coordinates in the lateral, elevation and radial directions, respectively. Assume that a linear shift-invariant imaging system with point-spread function $p(x, y, z)$ is used to image the object $o(x, y, z, t)$. The image plane is positioned at $y = 0$, and the object is imaged with a time T between the image frames. For frame n at time nT the image

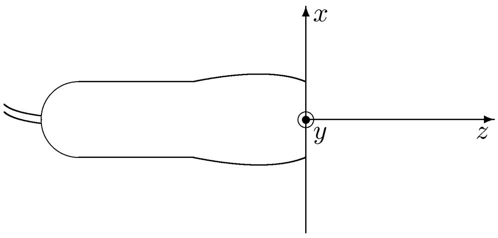

Figure 10: Imaging coordinate system.

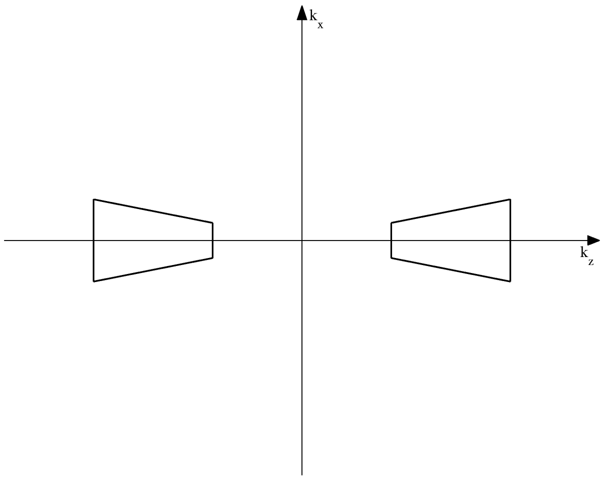

Figure 11: Illustration of the Fourier spectrum of an ultrasound image prior to amplitude detection.

operation is expressed by the convolution

$$i(x, z, t_0) = p(x, y, z) \underset{x,y,z}{*} o(x, y, z, nT)|_{y=0} \tag{6}$$

Fourier-transformation of the spatial variables gives

$$I(k_x, k_z, nT) = \int P(k_x, k_y, k_z) O(k_x, k_y, k_z, nT) dk_y \tag{7}$$

Such an image spectrum prior to amplitude detection is illustrated schematically in Figure 11. The band-pass nature of the signal in the k_z-direction is due to the ultrasound pulse which is a band-pass signal. With a velocity $\mathbf{v} = [v_x, v_y, v_z]$, the object is translated a distance $\mathbf{v}T$ between image frames. The spectrum including the temporal angular frequency ω becomes

$$I(k_x, k_z, \omega) = \int P(k_x, k_y, k_z) O(k_x, k_y, k_z, nT) \delta(\omega - k_x v_x - k_y v_y - k_z v_z) dk_y \tag{8}$$

where δ is the Dirac delta-function. The further analysis is simplified by assuming zero velocity transverse to the image plane, i.e. $\mathbf{v} = [v_x, 0, v_z]$. The resulting spectrum can be written

$$I(k_x, k_z, \omega) = \int P(k_x, k_y, k_z) O(k_x, k_y, k_z, nT) dk_y \ \delta(\omega - k_x v_x - k_z v_z) \tag{9}$$

and is illustrated in Figure 12. Movement transverse to the image plane broadens the spectrum in both the k_x and k_z direction.

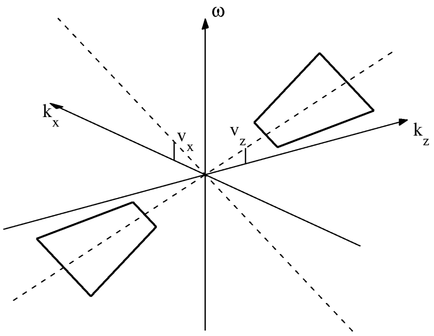

Figure 12: Image spectrum with radial and lateral movement of the object.

The images are sampled with sampling frequency $1/T$ in the temporal direction, and the spectrum in Figure 12 is therefore periodic with period $2\pi/T$ in the ω-direction, although only one period is shown. The high-pass filter is a one-dimensional filter operating in the temporal direction, and with transfer function $H(\omega)$, the spectrum of the filtered images becomes

$$I(k_x, k_z, \omega) = \int P(k_x, k_y, k_z) O(k_x, k_y, k_z, nT) dk_y \; H(\omega) \delta(\omega - k_x v_x - k_z v_z) \qquad (10)$$

The effect of the high-pass filter on the spectrum in Figure 12 is illustrated in Figure 13. The high-pass filter is represented by two planes that remove the part of the signal contained in the interval $[-\omega_c, \omega_c]$. Two-dimensional projections of the spectrum in Figure 13 are shown in Figure 14. As seen in Figure 14a, both the power and the bandwidth are decreased when the velocity is so small that parts of the signal spectrum are in the stop-band of the filter. The reduction in bandwidth means that the speckle is smeared out, and the speckle movement might be harder to perceive since the spatial dimensions of the speckle become large compared to the displacement from frame to frame. Due to aliasing, the high-pass filter also modifies the signal from scatterers

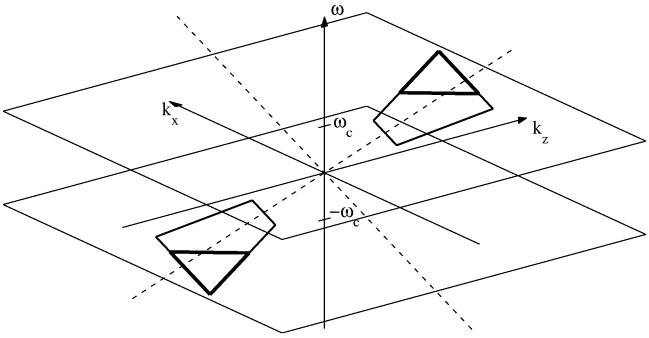

Figure 13: The effect of the high-pass filter on the spectrum in Figure 12.

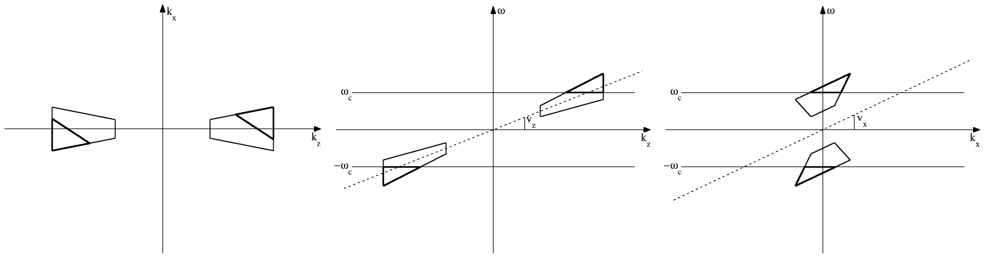

(a) (b) (c)

Figure 14: 2D projections of the 3D spectrum in Figure 13.

moving with a velocity giving Doppler frequencies close to multiples of the sampling frequency. The signal is demodulated and amplitude detected before it is displayed. This centers the signal around zero frequency in the k_z-direction, and is not included in the spectra shown above.

3.3 Amplitude Normalization

There is a time-gap between the IQ signal packets in Figure 7 which produces a discontinuity of the signal from packet to packet. The squared magnitude of the high-pass filtered signal from a representable sample volume is shown in Figure 15, where we see that the mean power varies significantly from packet to packet. To get a smooth temporal display, this fluctuation in the mean power needs to be compensated for. A method to solve this problem is described next.

The IQ signal is a random signal with a zero mean complex Gaussian probability

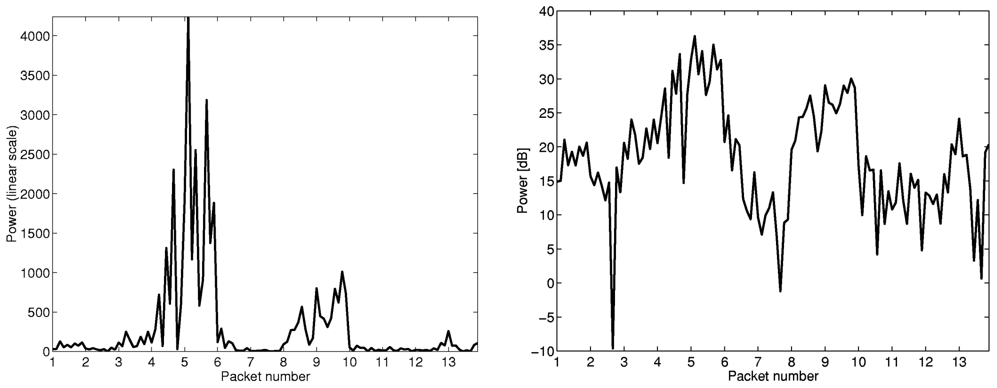

(a) (b)

Figure 15: The magnitude squared of the high-pass filtered signal. (a) Linear scale. (b) dB scale.

distribution. The high-pass filtering is a linear operation, and the signal $y(n)$ at the filter output is also a zero mean complex Gaussian process that can be written

$$y(n) = u(n) + iv(n) \tag{11}$$

where $u(n)$ and $v(n)$ are zero mean real Gaussian processes that are statistically independent [16]. The expected value, and the mean square value are given by

$$\begin{aligned} E\{y(n)\} =& E\{u(n)\} + iE\{v(n)\} = 0 \\ E\left\{|y(n)|^2\right\} =& E\left\{u(n)^2\right\} + E\left\{v(n)^2\right\} = \sigma_u^2 + \sigma_v^2 = 2\sigma_u^2 = 2\sigma_v^2 \end{aligned} \tag{12}$$

where $\sigma_u^2 = \sigma_v^2$ are the variances of $u(n)$ and $v(n)$, respectively. Normalizing the squared magnitude by the mean we get

$$z(n) = \frac{|y(n)|^2}{E\{|y(n)|^2\}} = \frac{1}{2}\left(\frac{u(n)^2}{\sigma_u^2} + \frac{v(n)^2}{\sigma_v^2}\right) \tag{13}$$

The random variable $2z(n)$ is χ^2-distributed with 2 degrees of freedom since it is the sum of the square of two independent Gaussian variables with zero mean and variance equal to one [15]. This gives the following PDF of $z(n)$

$$f_Z(z) = e^{-z} \tag{14}$$

In dB-scale, the variable becomes

$$w(n) = g(z(n)) = 10\log(z(n)) = 10\log(|y(n)|^2) - 10\log\left(E\{|y(n)|^2\}\right) \tag{15}$$

and the inverse of this transformation is given by $z(n) = h(w(n)) = 10^{w(n)/10}$. The PDF of $w(n)$ is then found by [15]

$$\begin{aligned} f_W(w) =& |h'(w)| \cdot f_U(h(w)) \\ & \frac{\ln(10)}{10} 10^{w/10} e^{-10^{w/10}} \end{aligned} \tag{16}$$

The PDF in Equation 16 is shown in Figure 16 together with a histogram of the transformed data from a representable image frame. Figure 16 shows close agreement between the experimental data and the theoretical PDF.

A method for performing the normalization described above is shown in Figure 17, and the signal plotted in Figure 15 is used to illustrate the algorithm. The mean power is estimated for each packet by

$$\hat{R}(0) = \frac{1}{M}\sum_{m=0}^{M-1} |x(m)|^2 \tag{17}$$

and subtracted from the speckle signal in the log-domain. The mean power in each packet is shown as the piece-wise constant signal in Figure 18. The normalized speckle signal corresponding to Equation 15 is obtained at point 3 in Figure 17, and is plotted

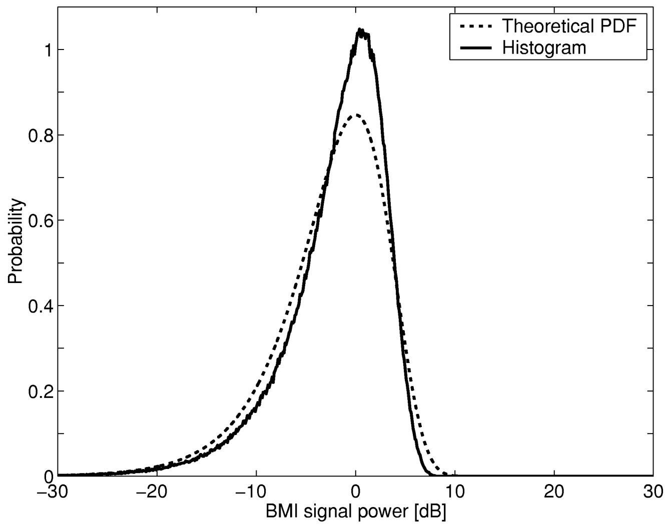

Figure 16: The PDF $f_W(w)$ together with a histogram of the data from a representable image frame.

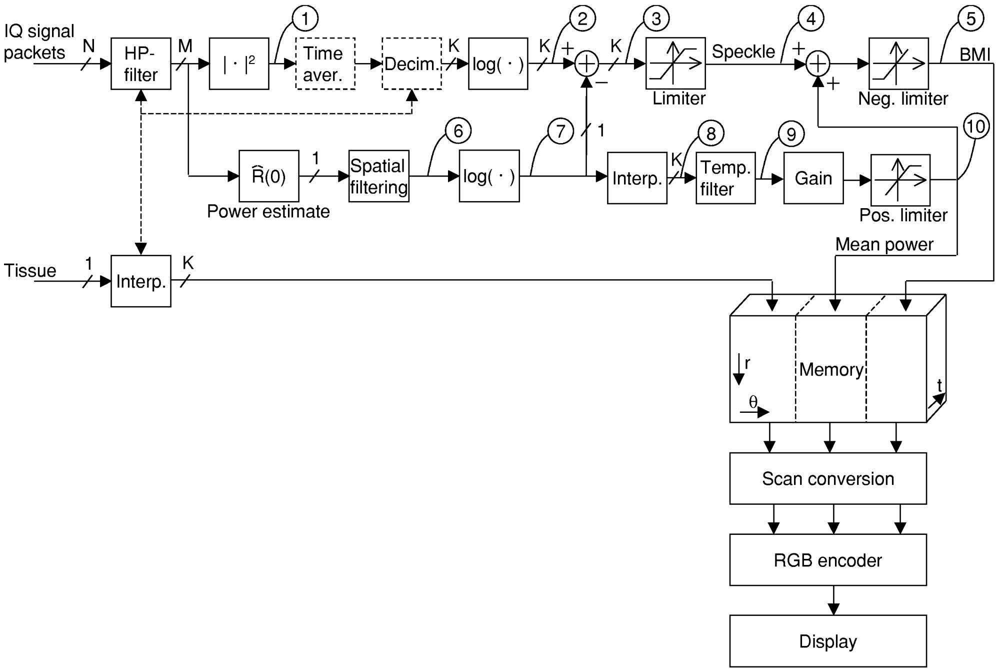

Figure 17: BMI processing of packet data with amplitude normalization.

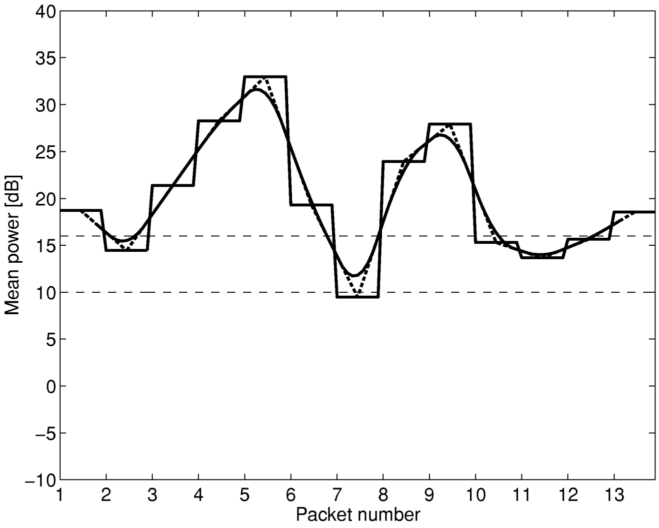

Figure 18: The piecewise constant signal is the mean power in each packet. This is the signal at point 7 in Figure 17. The interpolated mean power signal with (point 9 in Figure 17) and without (point 8 in Figure 17) temporal smoothing is also shown.

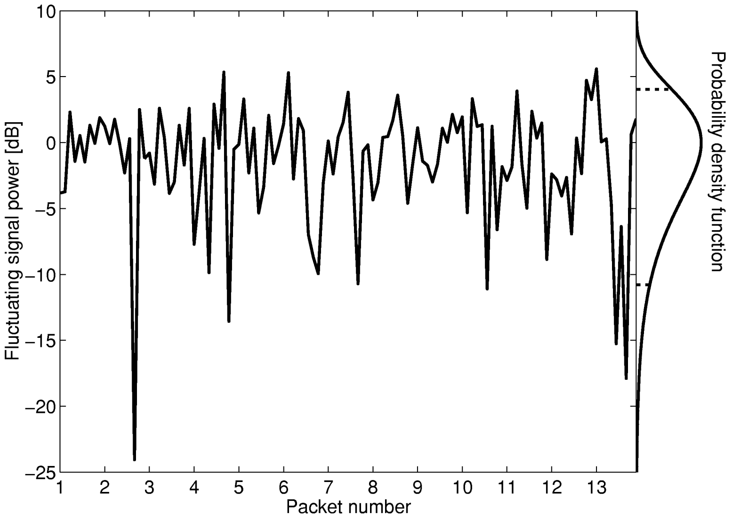

Figure 19: The normalized signal at point 3 in Figure 17.

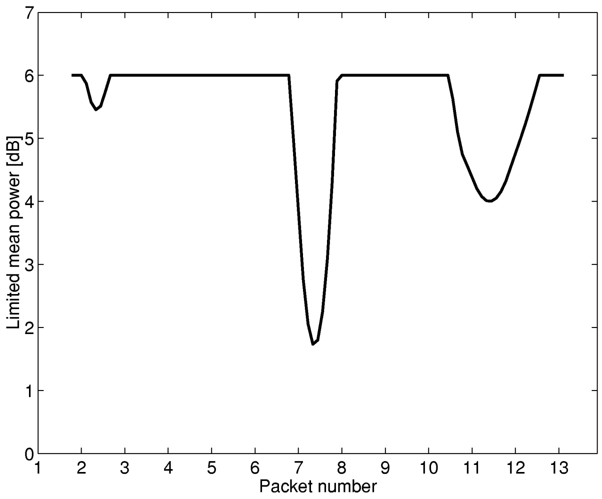

Figure 20: Limited mean power signal.

in Figure 19. The PDF in Equation 16 is superimposed to the right in Figure 19, and the signal can be limited to lie within a certain confidence interval as illustrated by the dashed lines. This limited speckle signal corresponds to point 4 in Figure 17. The speckle signal can be visualized in the flow image display by modifying the color pixel value in the areas of the image where blood flow is detected. One way of obtaining this effect is to combine the mean signal power with the speckle signal into one value, which controls, for instance, the brightness of the pixel value. Since there is only one mean power sample for each packet, the mean power signal is interpolated in time to get the same number of mean power samples as speckle signal samples. The interpolated signal at point 8 in Figure 17 is plotted with a thick dotted line in Figure 18 which also shows the smoothed signal at point 9. The gain and dynamic range of the mean power signal may be adjusted as in conventional color flow imaging. The signal is limited to a maximum positive value given by the gain and dynamic range, but the negative signal values are not limited to zero. The interpolated, smoothed, and limited mean power signal at point 10 in Figure 17 is shown in Figure 20. The gain in this example is equal to -10dB, and the signal is limited to a dynamic range of 6dB as illustrated with the dashed lines in Figure 18. The speckle signal is added to the mean signal, and the negative values are set equal to zero. When the mean signal has maximum value, the total signal spans the dynamic range of the display. When the mean signal is less than maximum, the smallest part of the total signal is lost. This is the BMI signal at point 5 in Figure 17, and is shown in Figure 21. Compared to Figure 15b, there is much less variation in the mean power, while the fluctuations are retained.

A power normalization algorithm simpler than that described in Figure 17 is as follows. The speckle signal is calculated as in point 3 in Figure 17, and the BMI signal is calculated as the sum of this speckle signal and a low-pass filtered version of the original signal at point 2. In this way the interpolation is avoided.

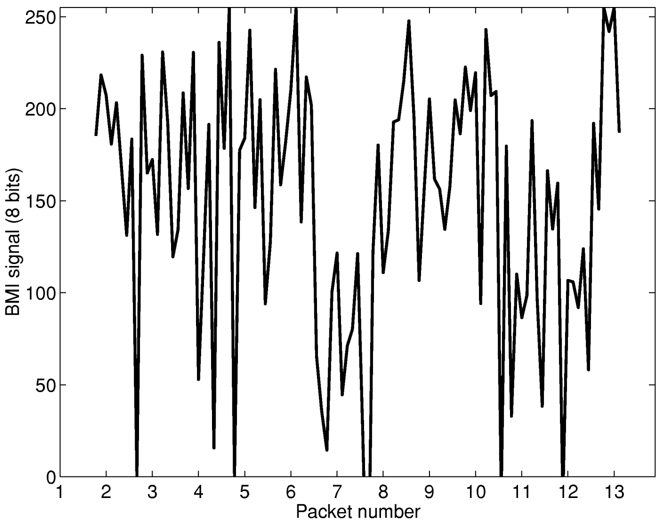

Figure 21: BMI signal.

3.4 BMI Combined with Velocity Estimates

In addition to the processing described above, it is possible to use the conventional autocorrelation algorithm [12] to estimate the radial velocity component. One estimate of the autocorrelation function at temporal lag equal to one is found for each packet using the unbiased sample mean estimator given by

$$\hat{R}(1) = \frac{1}{M-1} \sum_{m=0}^{M-2} x^*(m)x(m+1) \tag{18}$$

This complex valued autocorrelation estimate is interpolated in time to obtain one estimate for each BMI sample. The estimate of the radial velocity component is calculated from the phase of the autocorrelation values by

$$\hat{v} = \frac{c}{4\pi f_0 T} \cdot \arg(\hat{R}(1)) \tag{19}$$

where c is the sound velocity, f_0 is the center frequency of the ultrasound signal, and T is the pulse repetition time. This velocity estimate is then combined with the BMI signal in the display subsystem. A block diagram illustrating the combination of velocity estimates and the BMI signal is shown in Figure 22.

The interpolation of the autocorrelation estimates can be avoided by calculating instantaneous autocorrelation estimates by

$$\hat{R}_n(1) = x^*(n)x(n+1) \tag{20}$$

and then applying temporal averaging across packet boundaries to reduce the variance.

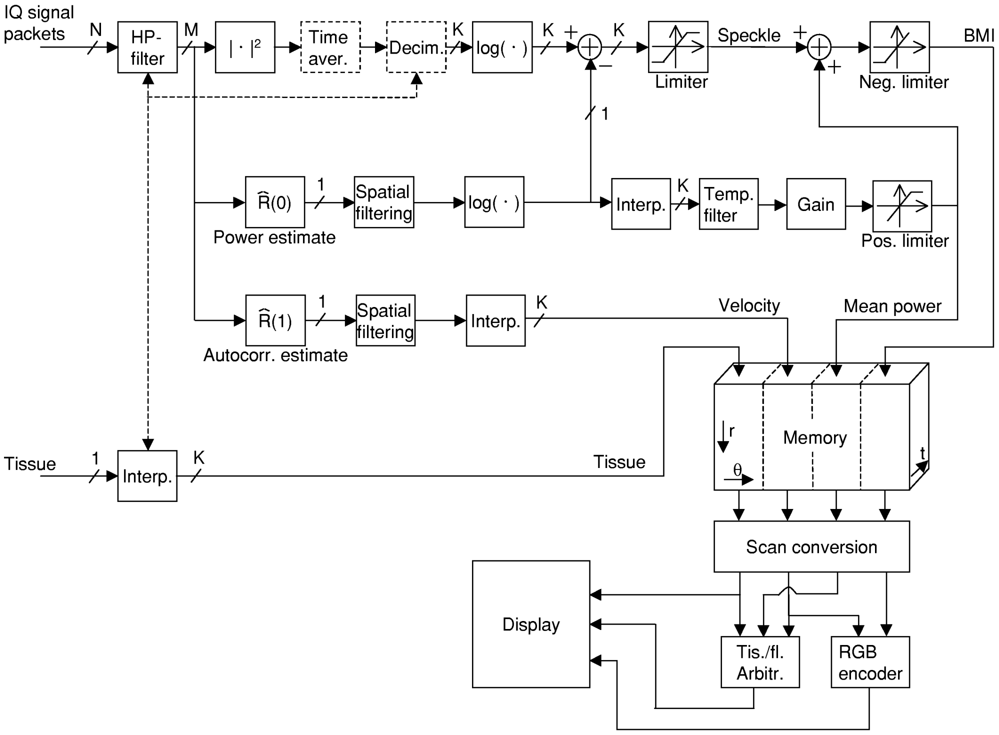

Figure 22: BMI with amplitude normalization, combined with velocity estimates.

3.5 Display Algorithms

The first stage in the display system is to scanconvert the images. The scanconverter maps the data from beam-depth format to rectangular coordinates with correct spatial dimensions. The scanconverted tissue and BMI images are then combined into a single gray scale or color image.

For the algorithms that do not incorporate velocity estimation, a simple additive combination of the BMI and tissue images is possible. One example of how the RGB-components can be calculated is given by

$$\mathrm{R} = 4 \times \mathrm{BMI} + 2 \times \mathrm{tissue}, \quad \mathrm{G} = \mathrm{BMI} + 4 \times \mathrm{tissue}, \quad \mathrm{B} = 4 \times \mathrm{tissue} \tag{21}$$

which gives high contrast between the blood flow and the surrounding tissue. A combination producing a gray scale image is also possible.

Another possibility is to make a decision for each pixel, whether tissue or flow should be displayed. This tissue/flow arbitration is based on the tissue, mean power, and velocity signal. The RGB values of the flow pixels are determined by the BMI and the velocity signal. The color is chosen based on the velocity, while the BMI signal determines the brightness of the color.

Spatial averaging is necessary to reduce the variance in the velocity estimates. Together with the limited resolution of ultrasound imaging systems, blood flow might be visualized outside the anatomical borders of the blood vessels. A similar artifact resulting from limited resolution and insufficient clutter attenuation, is that the estimated blood velocity does not approach zero towards the vessel boundary. The velocity is calculated in Equation 19, where we see that addition of a real quantity to $\hat{R}(1)$ reduces the magnitude of $\arg(\hat{R}(1))$ and thus the velocity. The velocity can be forced towards zero at the vessel boundary by adding a fraction of a spatial averaged tissue image to $\hat{R}(1)$. The spatial averaging extends the vessel border inside the vessel, and the estimated velocities are reduced in this area. In the middle of the vessel, the tissue signal is weak, giving a small modification of $\arg(\hat{R}(1))$. However, with a strong reverberation signal inside the vessel, there might be an undesirable alteration of the velocity estimate.

3.6 Temporal Processing

Temporal averaging and/or decimation may be done on the signal at point 1 in Figure 17. Temporal averaging within a signal packet produces traces in the speckle along the direction of the blood flow. However, temporal averaging across packets destroys the speckle pattern. Since the averaging must be performed within each packet, the averaging filter needs to be initialized for each packet, and a number of samples equal to the averaging window length must be discarded in each packet. Further decimation may be necessary to get a frame rate suitable for real time display. By averaging over the entire packet, the result is one sample per packet. The only difference between the signals at 2 and 7 in Figure 17 is then the spatial averaging at 6. When the signal at point 3 in Figure 17 is used as the power signal in standard color flow imaging, stripes along the flow direction are visible in the color flow images. This processing is very similar to the processing in conventional color flow imaging.

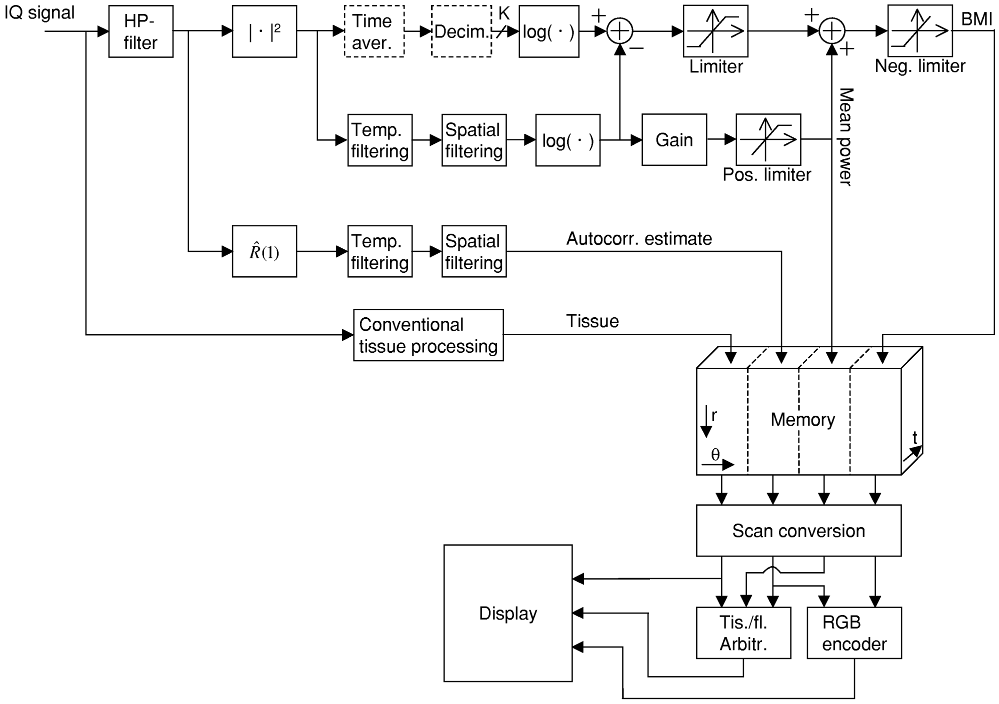

Figure 23: Advanced BMI processing of data from continuos acquisition.

3.7 Continuous Acquisition

The data from continuous acquisition are not divided into packets, and do not suffer from temporal discontinuities. This simplifies the processing, which can be performed with a sliding window as illustrated in Figure 5. The mean power of the signal varies during the heart cycle, and amplitude normalization can be performed inside a sliding window of length N as shown in Figure 23. A combination with velocity estimates is also possible with continuous acquisition as illustrated in Figure 23.

4 Clinical Applications

It is hard to get a correct impression of BMI from still images. We have therefore made a web page containing BMI loops for the clinical applications discussed in the following sections. The web page can be found at `http://www.ifbt.ntnu.no/~steinarb/bmi/`.

4.1 Peripheral Vessels

BMI has been successfully applied to imaging of peripheral vessels using both packet and continuous acquisition. The vessels are located at relatively shallow depths so that relatively large interleave group sizes with sufficient PRF are possible.

The lateral velocity component is clearly visualized, and we get an impression of the parabolic velocity profile across the vessel. Compared to conventional color flow imaging, BMI provides a more intuitive display since the images contain a motion corresponding to the flow of the red blood cells. Disturbed flow patterns are more easily detected than they are with color flow since both the color and speckle pattern are altered.

The benefit of the amplitude normalization algorithm is evident in the examples of the brachialis artery: The stepping artifact between the packets is reduced, and there is a more uniform amplitude during the heart cycle. The web page contains several examples of temporal averaging and decimation.

4.2 Transthoracic Cardiac Imaging

The blood flow inside the heart is more complicated than the flow in peripheral vessels. In cardiac applications there is more flow transversal to the imaging plane, and there will thus be more decorrelation of the speckle from frame to frame. The heart also lies deeper in the body, and the reduced PRF increases the decorrelation in addition to reducing the interleave group size. It is therefore hard to visually track the speckle pattern when imaging flow inside the heart. However, there will be an even stronger speckle decorrelation in regions with disturbed flow resulting from valve stenoses or insufficiencies, than in regions with more regular flow. The increase in speckle fluctuations might ease the detection of small jets.

The web page contains two examples of aortic insufficiencies, one moderate and one small. The increased temporal variation of the speckle pattern in the jet areas is clearly seen. A sensation of the jet direction is also obtained. Using the algorithm described in Section 3.5, we have also obtained nice transitions between the flow and tissue.

4.3 Transesophageal Cardiac Imaging

In transesophageal imaging, the transducer is positioned closer to the flow in the heart, and a pulse with higher center frequency can be used. This gives higher spatial resolution, which is important for BMI. The reduced depth also means that large interleave group sizes is possible when keeping the same PRF. However, the ability to visually follow the speckle movement is still limited by the decorrelation caused by out of plane movement.

The web page contains several examples of cardiac blood flow imaged from the esophagus. Compared to the transthoracic images, the speckle pattern has smaller spatial dimensions due to the increased frequency. The speckle pattern is more “noisy” in the jet regions, and a nice visualization of the disturbed flow is obtained.

4.4 Pediatrics

Congenital heart diseases lead to complicated geometry and flow patterns. The small dimensions in the child’s heart give the same advantages regarding BMI as transesophageal imaging. With the improved ability of BMI to visualize disturbed flow, we hope that it can ease the detection of shunts and other abnormalities. The web page contains some preliminary examples of BMI applied to cardiac flow measurements in a small baby.

5 Discussion

We have described processing of the beamformed, complex demodulated, and time-gain compensated IQ signal packets. Alternatively, the processing can be done on the real valued RF data without complex demodulation. In both alternatives, a band-pass filter can be used to filter out frequency bands around a desired multiple or fraction of the transmitted frequency. Such (sub)harmonic filtering is important when BMI is combined with ultrasound contrast agents.

The speckle signal is calculated by amplitude detection of the high-pass filtered IQ-signal. More advanced processing could be done to increase the bandwidth of the speckle which might ease the perception of speckle movement. Spectral analysis similar to the analysis in Section 3.2 might be useful when developing improved speckle amplitude processing.

Several forms of temporal averaging and decimation were described in Section 3.6, but we think that an improved display is possible with more advanced temporal processing, and further work should be done in this area. It could be possible to color code the “age” of the speckle to visualize both the direction and magnitude of the flow. Improved still image visualization should also be developed.

The BMI processing and display techniques can be applied in all combinations of imaging modalities where conventional color flow is used. Examples are M-mode and spectrum Doppler. Combination with spectrum Doppler is especially interesting, since accurate angle correction is easier to perform when the lateral blood flow is visualized with BMI.

BMI processing can be used in combination with ultrasound contrast imaging. The contrast agent enhances the scattering from blood, which increases the sensitivity and makes clutter filtering less critical. The BMI method may be used in combination with several methods for contrast enhancement using a sequence of transmit pulses per scan line, including fundamental and second harmonic power Doppler, the pulse-inversion technique, and coded excitation. Variations of the echo from pulse to pulse caused by movement and/or destruction of the contrast particles create changes in the speckle pattern in the image, making visual detection of small concentrations of contrast agent easier. In intermittent imaging, which is often used for contrast imaging, the BMI method is of special importance. With BMI processing, several images are displayed for each recorded data set, giving a more continuous stream of images, where speckle fluctuations indicate the presence of contrast agent.

6 Conclusions

BMI is a new variant of color flow imaging which preserves, enhances, and visualizes the speckle pattern movement resulting from the flowing red blood cells. The method is sensitive to flow in all directions, and provides a more intuitive display of the blood flow compared to conventional color flow imaging which is only sensitive to flow along the beam direction. Although the lateral velocity component is visualized, no attempt is made to measure this component qualitatively. However, BMI may indirectly give the lateral velocity component by combining an angle measurement derived from the speckle motion, with the radial velocity component obtained from the Doppler frequency shift. In addition to providing a more intuitive display of the flow in peripheral vessels, we hope that BMI will ease the detection of disturbed flow in cardiac applications. In systems with software based flow processing, only small modifications are necessary since the data acquisition is the same as in color flow imaging. Such a real time implementation of the algorithms is necessary for a thorough clinical evaluation of the method.

7 Acknowledgements

This study was supported by the Research Council of Norway. We thank Nancy Lea Eik-Nes for revision of the paper.

References

1. M. E. Anderson. Multi-dimensional velocity estimation with ultrasound using spatial quadrature. *IEEE Trans. Ultrason., Ferroelect., Freq. Contr.*, 45(3):852–861, May 1998.

2. S. Bjærum, H. Torp, and K. Kristoffersen. Clutter filter design for ultrasound color flow imaging. Submitted to *IEEE Trans. Ultrason. Ferroelect. Freq. Contr.*, 2000.

3. R. H. Chesarek. Ultrasound imaging system for relatively low-velocity blood flow at relatively high frame rates. US Patent 4888694, Dec. 1989. Quantum Medical Systems, Inc., Issaquah, Wash.

4. R. Y. Chiao, A. L. Hall, K. E. Thomenius, M. J. Washburn, and K. W. Rigby. Method and apparatus for enhanced flow imaging in B-Mode ultrasound. US Patent 6074348, June 2000. General Electric Company, Schenectady, N.Y.

5. E. S. Chornoboy. Initialization for improved IIR filter performance. *IEEE Trans. Signal Process.*, 40(3):543–550, Mar. 1992.

6. R. H. Fletcher and D. W. Burlage. An initialization technique for improved MTI performance in phased array radars. *Proc. IEEE*, 60:1551–1552, Dec. 1972.

7. M. D. Fox. Multiple crossed-beam ultrasound Doppler velocimetry. *IEEE Trans. Sonics Ultrason.*, 25(5):281–286, Sept. 1978.

8. B. Haider, P. A. Lewin, and K. E. Thomenius. Pulse elongation and deconvolution filtering for medical ultrasonic imaging. *IEEE Trans. Ultrason., Ferroelect., Freq. Contr.*, 45(1):98–113, Jan. 1998.

9. A. P. G. Hoeks, J. J. W. van de Vorst, A. Dabekaussen, P. J. Brands, and R. S. Reneman. An efficient algorithm to remove low frequency Doppler signals in digital Doppler systems. *Ultrason. Imag.*, 13(2):135–144, Apr. 1991.

10. J. A. Jensen and P. Munk. A new method for estimation of velocity vectors. *IEEE Trans. Ultrason., Ferroelect., Freq. Contr.*, 45(3):837–851, May 1998.

11. A. P. Kadi and T. Loupas. On the performance of regression and step-initialized IIR clutter filters for color Doppler systems in diagnostic medical ultrasound. *IEEE Trans. Ultrason., Ferroelect., Freq. Contr.*, 42(5):927–937, Sept. 1995.

12. C. Kasai, K. Namekawa, A. Koyano, and R. Omoto. Real-time two-dimensional blood flow imaging using an autocorrelation technique. *IEEE Trans. Sonics Ultrason.*, 32(3):458–464, May 1985.

13. V. L. Newhouse, D. Censor, T. Vontz, J. A. Cisneros, and B. B. Goldberg. Ultrasound Doppler probing of flows transverse with respect to beam axis. *IEEE Trans. Biomed. Eng.*, 34(10):779–789, Oct. 1987.

14. A. V. Oppenheim, R. W. Schafer, and J. R. Buck. *Discrete-Time Signal Processing.* Prentice Hall, Inc., second edition, 1999.

15. A. Papoulis. *Probability, Random Variables, and Stochastic Processes.* McGraw-Hill, Inc., third edition, 1991.

16. C. W. Therrien. *Discrete Random Signals and Statistical Signal Processing.* Prentice Hall, Inc., 1992.

17. H. Torp. Clutter rejection filters in color flow imaging: A theoretical approach. *IEEE Trans. Ultrason., Ferroelect., Freq. Contr.*, 44(2):417–424, Mar. 1997.

18. G. E. Trahey, J. W. Allison, and O. T. von Ramm. Angle independent ultrasonic detection of blood flow. *IEEE Trans. Biomed. Eng.*, 34(12):965–967, Dec. 1987.

Paper I

High Frame Rate Tissue Doppler and Strain Rate Imaging

Steinar Bjærum, Andreas Heimdal, Hans Torp,
Brage H. Amundsen, Stig A. Slørdahl and Bjørn Olstad[†]

Department of Physiology and Biomedical Engineering,
Norwegian University of Science and Technology, Trondheim, Norway
[†]Department of Computer and Information Science,
Norwegian University of Science and Technology, Trondheim, Norway

Abstract

In tissue Doppler and strain rate imaging of the heart, a high frame rate is necessary to capture the rapid relaxations and contractions of the myocardium. Previously, the Doppler and tissue B-mode images have been calculated from different pulse transmissions. To improve the temporal resolution, we present a new acquisition technique where the Doppler based images are calculated from the same pulse transmissions as the tissue B-mode images. By constructing the image from 10-15 transmit beams, frame rates above 300 frames/second are possible when imaging the heart. To get adequate spatial resolution, the small number of transmit beams limits the width of the image, but the image is wide enough to cover a heart wall, i.e. the interventricular septum. The Doppler pulse repetition frequency equals the frame rate and is relatively low. Tissue velocity estimates calculated from these data therefore suffer from aliasing. However, we present a robust technique that corrects the aliased velocities. A significant advantage of the new technique is the continuous stream of data with constant sampling intervals. Doppler spectra and sound signals can thus be calculated at arbitrary points in the 2D image.

1 Introduction

Ultrasound Doppler techniques have been used with success in two-dimensional imaging of blood flow velocities [1]. More recently, there has been a rapid development in using Doppler techniques in the assessment of myocardial function. Spectral Doppler can be used to measure the tissue velocity at discrete positions in the myocardium, but the sample volume needs to be moved around to assess the regional function. Two-dimensional tissue Doppler imaging (TDI) can be used to assess regional myocardial function [4], and has proven to be of significant clinical value. Additional information can be obtained by imaging the rate of deformation of the myocardium; this is called strain rate imaging (SRI) in [2]. SRI may ease the differentiation of active elongation or contraction from passive motion induced by elongation or contraction in other parts of the myocardium [2].

The rapid accelerations in the myocardium demand imaging systems with high temporal resolution. Conventional systems trade off temporal resolution with spatial resolution in the tissue B-mode and/or the Doppler image. In this paper we present a new acquisition technique which uses the same data for both tissue B-mode imaging, TDI, and SRI. For an image sector wide enough to cover a heart wall, this technique provides frame rates exceeding 300 frames/second with high spatial resolution for both the B-mode and Doppler image. As an added benefit, the technique also provides a continuous stream of data with constant sampling intervals. Doppler spectra and sound signals can therefore be calculated from the 2D data, thus avoiding separate data acquisitions for these modalities.

Sections 2 and 3 present the basics of tissue Doppler and strain rate imaging, including how these quantities are estimated. Then the new acquisition method is described and compared to conventional 2D Doppler acquisition in Section 4. Section 5 compares TDI/SRI calculated from the second harmonic and fundamental signal, and we find a significant quality improvement of SRI when the second harmonic signal is used. The tissue velocity estimates suffer from aliasing since the pulse repetition frequency is relatively low. A robust technique that corrects the aliased velocities is presented in Section 6. In Section 7, examples of Doppler spectra calculated from the 2D data are shown, and in Section 8 we describe how tissue velocity and strain rate sound signals can be generated. Section 9 contains examples of clinical applications of high frame rate TDI/SRI. The paper is concluded in Section 10.

2 Tissue Doppler Imaging

In 2D ultrasound imaging, the ultrasound beam is scanned over the region to be imaged. For each image frame, the tissue velocities at points along each beam direction are estimated based on the received signals from a packet of $N \geq 2$ pulse transmissions in this direction. The time T between two pulses within a packet is called the pulse repetition time. The time between two pulse packets in the same direction is equal to the time between two image frames, T_{frame}. After sampling the signal at depth increments r_s, there is a two-dimensional signal $x_l(k, n)$ for each frame and each beam

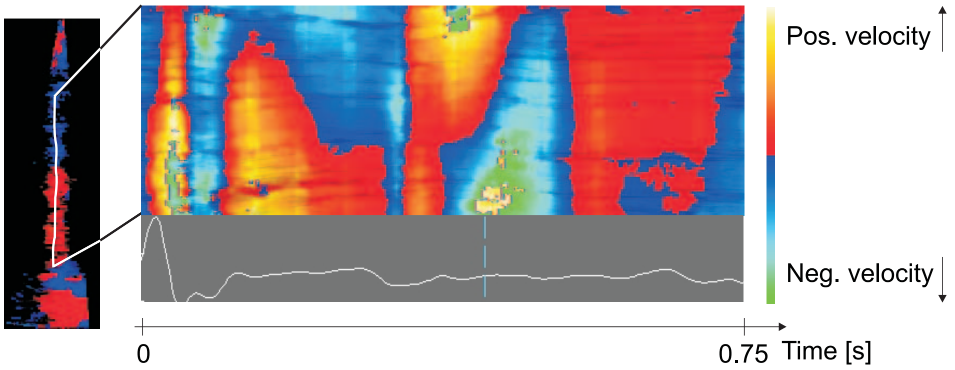

Figure 1: Example of a tissue Doppler M-mode image. The velocities in the septum of the heart during one heartbeat are visualized. The frame rate is 266 frames/second.

direction, where l is the frame number, k is the depth index, and n is the temporal index corresponding to pulse transmissions. A commonly used velocity estimator is based on estimates of the autocorrelation function with temporal lag equal to one [3]. This autocorrelation value can be estimated at depth kr_s and time lT_{frame} using the unbiased sample mean estimator given by

$$\hat{R}_{k,l}(1) = \frac{1}{N-1} \sum_{n=0}^{N-2} x_l^*(k,n) x_l(k,n+1) \tag{1}$$

where N is the number of pulses in each packet. Based on $\hat{R}_{k,l}(1)$, an estimate of the velocity component along the beam direction is calculated by

$$\hat{v}(k,l) = \frac{c}{4\pi f_0 T} \cdot \arg(\hat{R}_{k,l}(1)) \tag{2}$$

where c is the sound velocity, and f_0 is the center frequency of the received ultrasound signal. The phase angle $\arg(\hat{R}_{k,l}(1))$ is contained in the interval $[-\pi, \pi]$. If the velocity is so large that the phase shift from pulse to pulse is larger than π, aliasing occurs, i.e. a positive velocity is interpreted as a negative velocity and vice versa. The maximum unaliased velocity is called the Nyquist velocity and is given by

$$v_{\text{Nyq}} = \frac{c}{4 f_0 T} \tag{3}$$

The tissue velocities are encoded using colors, and superimposed on the tissue B-mode image. A common colormap is to let red correspond to velocities towards the probe, and let blue correspond to velocities away from the probe. The magnitude of the velocity determines the hue and saturation of the color, while the tissue intensity determines the intensity of the color. To get both temporal and spatial information in one image, the velocities along a curved line following an anatomical structure in the 2D image can be imaged versus time as shown in Figure 1. This is called a color M-mode image, and in Figure 1 we see the velocities in the septum of the heart during one heartbeat.

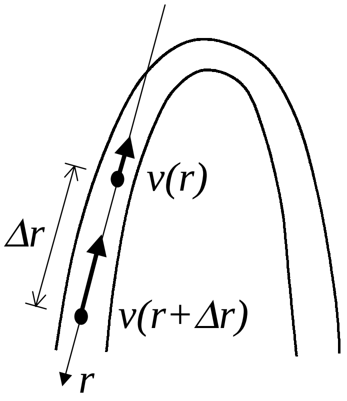

Figure 2: Illustration of the velocities used in the strain rate estimate in Equation 4.

3 Strain Rate Imaging

The strain rate (SR) is equivalent to the spatial gradient of the velocity [2]. Estimates of the velocity component along the beam direction are available from tissue Doppler imaging, and an approximation to the strain rate at depth kr_s and time lT_{Frame} is given by

$$\text{SR}(k,l) \approx \frac{v(k,l) - v(k+\Delta k, l)}{\Delta k \cdot r_s} \tag{4}$$

where $\Delta k \cdot r_s$ is a small radial lag as illustrated in Figure 2. Combining Equations 2 and 4, an estimator of strain rate suitable for real time implementation is given by

$$\hat{\text{SR}}(k,l) = \frac{c}{4\pi f_0 T \Delta k r_s} \cdot \arg\left(\sum_{m=0}^{K-1} \hat{R}^*_{k+m,l}(1) \hat{R}_{k+m+\Delta k,l}(1) \right) \tag{5}$$

where averaging is performed over K radial samples to reduce variance. Aliasing of the strain rate estimates occurs if the mean difference between the phase angle of $\hat{R}_{k,l}(1)$ and $\hat{R}_{k+\Delta k,l}(1)$ exceeds π.

Strain rate can be visualized using a color technique similar to TDI. A strain rate M-mode of the septum is shown in Figure 3, where blue corresponds to local shortening (negative SR), red corresponds to local elongation, and green corresponds to zero deformation.

4 Data Acquisition

When imaging down to a depth r, the minimum time between pulse transmissions is $T_{\min} = 2r/c$. For the heart, the depth r is approximately 15cm, and with sound velocity $c = 1540$m/s, the minimum time between pulse transmissions is $T_{\min} \approx 200\mu$s. With an ultrasound center frequency of 2MHz, this gives a Nyquist velocity of 96cm/s

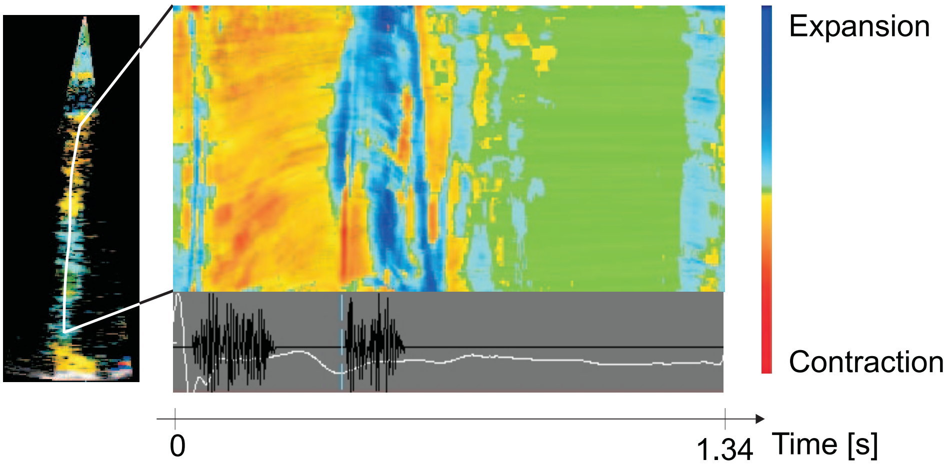

Figure 3: Example of a strain rate M-mode image. The strain rates in the septum of the heart during one heartbeat are visualized. The frame rate is 323 frames/second.

which is suitable for blood velocity imaging. The timing of the pulse transmissions in one beam direction is illustrated in Figure 4 when $N = 3$ pulses are used for each velocity estimate. During the time $T_{\text{frame}} - NT$, both the Doppler data in the other beam directions and the tissue B-mode data are acquired. If the Nyquist velocity can be reduced by a factor M, T can be increased by the same factor M. This means that during the time T between two pulse transmissions in the same beam direction, there is time to acquire data in $M - 1$ other beam directions. The tissue velocities are much smaller than the blood velocities, and by allowing some aliasing, the Nyquist velocity can be reduced by a factor $M \sim 10$. By restricting the Doppler image to consist of only M beams, the entire Doppler image can be scanned before two pulses are fired in the same beam direction. If the velocities are estimated based on N pulse transmissions, there are N Doppler scans between each tissue B-mode scan.

In 2D blood flow imaging, the optimal transmitted pulses for the tissue B-mode and Doppler image are different. One reason for this is that to get a sufficient signal-to-noise ratio (SNR), higher power has to be transmitted for Doppler imaging than for tissue B-mode imaging. There are, however, safety limitations on the transmitted pulse amplitude, so the power is increased by increasing the pulse length. Increasing the pulse length also decreases the noise bandwidth, giving a further increase in the

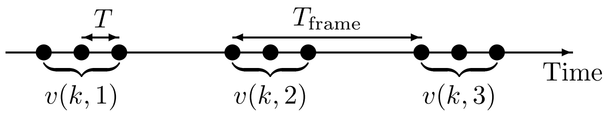

Figure 4: The timing of $N = 3$ pulses fired in the same beam direction for conventional 2D Doppler imaging.

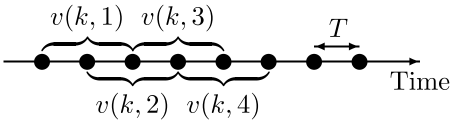

Figure 5: Sliding window velocity estimation of data with constant sampling intervals.

SNR. B-mode images calculated from these long Doppler pulses would have reduced radial resolution. Fortunately, when imaging tissue velocities, the signal-to-noise ratio is much higher than it is for blood velocity imaging. Both the tissue B-mode and the Doppler image can therefore be calculated from the same pulse transmissions without any degradation of the image quality. If a small bandwidth is required in Doppler algorithms, the signal can be band pass filtered and still have sufficient SNR. The penalty for using the same pulses is that the tissue B-mode image sector is restricted to be of equal size as the Doppler image sector.

Without a separate tissue B-mode scan, there is a continuous stream of data $x(k,l)$ with constant sampling intervals in the temporal direction. The autocorrelation estimate can then be calculated using a sliding window technique given by

$$\hat{R}_{k,l}(1) = \frac{1}{N-1} \sum_{n=0}^{N-2} x^*(k,l+n)x(k,l+n+1) \tag{6}$$

One image is thus calculated for each Doppler scan, and the frame rate is $1/T$ as illustrated in Figure 5. The conventional method needs M Doppler scans and one tissue B-mode scan before a new image is calculated, and the frame rate is $1/(MT + T_{\text{tissue}})$, where T_{tissue} is the time needed for the tissue B-mode scan. The difference in the timing of the velocity estimates obtained with the conventional and the new acquisition technique is clearly seen by comparing Figures 4 and 5.

Another advantage of the new acquisition scheme is a potential reduction of reverberation artifacts. Figure 4 illustrates the pulse timing of the conventional acquisition scheme, and we see that the scanning history is different for the different pulses in the same beam direction. A time varying reverberation signal might therefore exist. In the new acquisition scheme, the scanning history is equal for all the pulses, and the reverberation signal is constant in time.

A disadvantage of the new acquisition scheme is the limited number of transmit beams $N \sim 10$ available. The distance between neighboring beams must be small to get good lateral resolution for the tissue image, and this acquisition method is therefore only suited for a narrow image sector. With a relatively wide transmit beam, and receive beam-forming performed in parallel, several beams can be calculated from one pulse transmission. Using two parallel beam-forming channels, around 20 beams are available, which is sufficient for a 20 degree image sector. Fortunately, this is wide enough to individually image the different walls of the heart with a spatial resolution of the Doppler image that is equal to the tissue image resolution.

Digital ultrasound data were recorded using a GE Vingmed System Five scanner to test the described acquisition scheme. The digital data were stored as complex base band signals where the in-phase and quadrature signal samples were represented as 16 bit integers. These data were transferred from the scanner and processed on a standard computer using MATLAB.

5 Fundamental vs. Second Harmonic Imaging

The tissue image quality is improved when a band pass filter centered at twice the transmitted frequency is applied to the received signal. A brief explanation of this is as follows. Second harmonic frequency components are generated by non-linear wave propagation, and the second harmonic generation increases with wave amplitude and propagation distance. The most severe reverberation noise is generated while the pulse propagates through the body wall. The propagation distance from the probe to the reverberating layers in the body wall is, however, so small that the second harmonic signal level is low, and the reverberation noise is reduced compared to the fundamental frequency band. The second harmonic image also has better lateral resolution since the sidelobe power level is not high enough to generate second harmonic frequency components.

To test if the quality of TDI and SRI is improved by using the second harmonic signal, we recorded data with acquisition parameters as shown in Table 1. By using band pass filters centered around f_{TX} and $2f_{\mathrm{TX}}$, the fundamental and second harmonic signals could be obtained from the same data. The tissue images were calculated using the second harmonic signal, while TDI/SRI was tested on both the fundamental and second harmonic signals. A comparison using this data is not completely fair since a higher f_{TX} is preferable for fundamental imaging, but the comparison provides valuable information.

Examples of TDI and SRI M-modes using the two frequency bands are shown in Figure 6 where we see that the velocity estimates are of good quality using either the fundamental or second harmonic signal. There is, however, some aliasing due to the low pulse repetition frequency. Because of a doubling of f_0, the Nyquist velocity for the second harmonic signal is half of the Nyquist velocity for the fundamental signal. As seen in Figure 6, the strain rate estimates are considerably better when the second harmonic signal is used instead of the fundamental signal. Since the strain rate values are calculated as a difference between two velocity values, there are no severe aliasing problems caused by using the second harmonic signal for SRI when the radial distance $\Delta k r_s$ in Figure 2 is small.

Transmit frequency, f_{TX}	1.67MHz
No. of periods in pulse	1.5
Demodulation frequency	2.5MHz
Demodulation bandwidth	2MHz

Table 1: Wide band acquisition parameters.

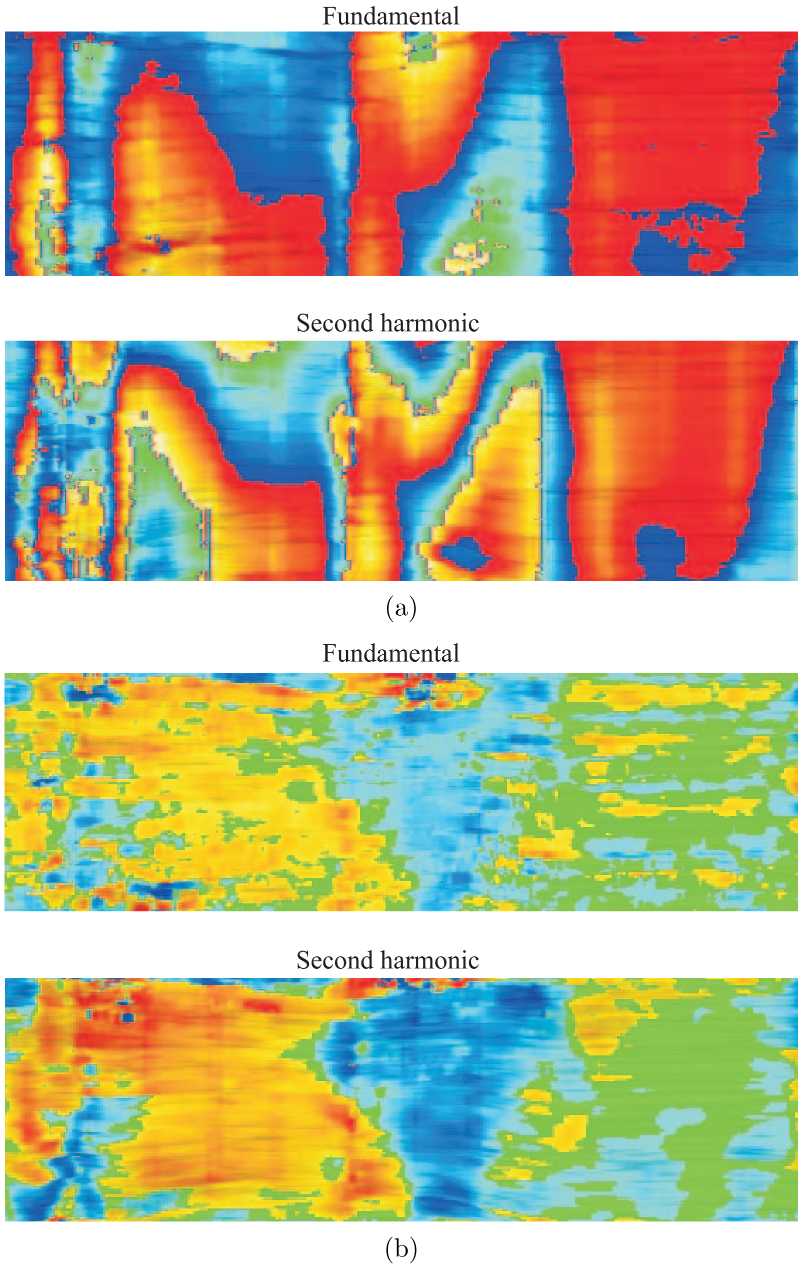

Figure 6: Example of M-modes using the fundamental and second harmonic signal. (a) TDI. (b) SRI.

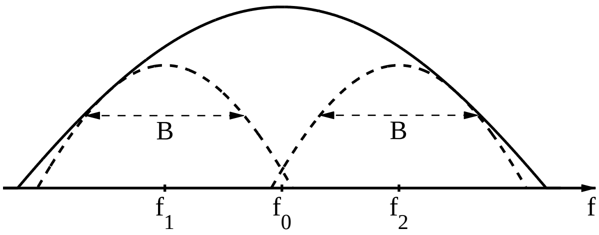

Figure 7: Aliasing correction using two subbands.

6 Anti-aliasing Techniques for TDI

The aliasing artifacts of the TDI images can be corrected for by using a method similar to the one described in [5]. Correcting aliased velocities is easier for tissue Doppler imaging than for blood flow imaging since the signal-to-noise ratio is much higher. In addition, the bandwidth of the Doppler signal is lower when tissue velocities are measured than when blood flow is measured. All the tissue scatterer in one sample volume moves with approximately the same velocity, while blood scatterers might move in several different directions with different velocities resulting in a large bandwidth of the Doppler signal.

The received signal has frequency content centered around f_0, and can be filtered with two narrow band filters centered at the frequencies f_1 and f_2 as illustrated in Figure 7. Two autocorrelation estimates, $\hat{R}^{f_1}_{k,l}(1)$ and $\hat{R}^{f_2}_{k,l}(1)$, are calculated from these two narrow band signals using Equation 6. The difference between the phase angle of these two autocorrelation estimates can be found from Equation 2 and is equal to

$$\arg(\hat{R}^{f_2}_{k,l}(1)) - \arg(\hat{R}^{f_1}_{k,l}(1)) = \frac{4\pi T}{c}(f_2 - f_1) \cdot \hat{v}_{12}(k,l) \tag{7}$$

An estimator of the velocity based on the two subband signals is thus given by

$$\hat{v}_{12}(k,l) = \frac{c}{4\pi(f_2 - f_1)T} \arg(\hat{R}^{f_1}_{k,l}(1)^* \hat{R}^{f_2}_{k,l}(1)) \tag{8}$$

where the Nyquist velocity

$$\hat{v}^{12}_{\mathrm{Nyq}} = \frac{c}{4(f_2 - f_1)T} \tag{9}$$

is increased with a factor $f_0/(f_2 - f_1)$ compared to Equation 3. The band pass filtering used to obtain the subband signals unfortunately reduces the spatial resolution of the velocity estimate. To regain spatial resolution, the velocity estimate $\hat{v}_{12}$ is used to correct the velocity estimate based on the original wide band signal centered at f_0. For each (possibly aliased) velocity estimate, several candidate velocities are found as

$$\hat{v}(k,l) = \frac{c}{4\pi f_0 T}(\arg(\hat{R}_{k,l}(1)) + 2n\pi), \quad -N_{\max} \le n \le N_{\max} \tag{10}$$

where $N_{\max} \le \left\lfloor \frac{f_0}{f_2 - f_1} - 1 \right\rfloor$, and $\lfloor \cdot \rfloor$ means nearest integer towards $-\infty$. Next, the candidate velocity $\hat{v}(k,l)$ that is closest to the unaliased velocity estimate $\hat{v}_{12}(k,l)$ is

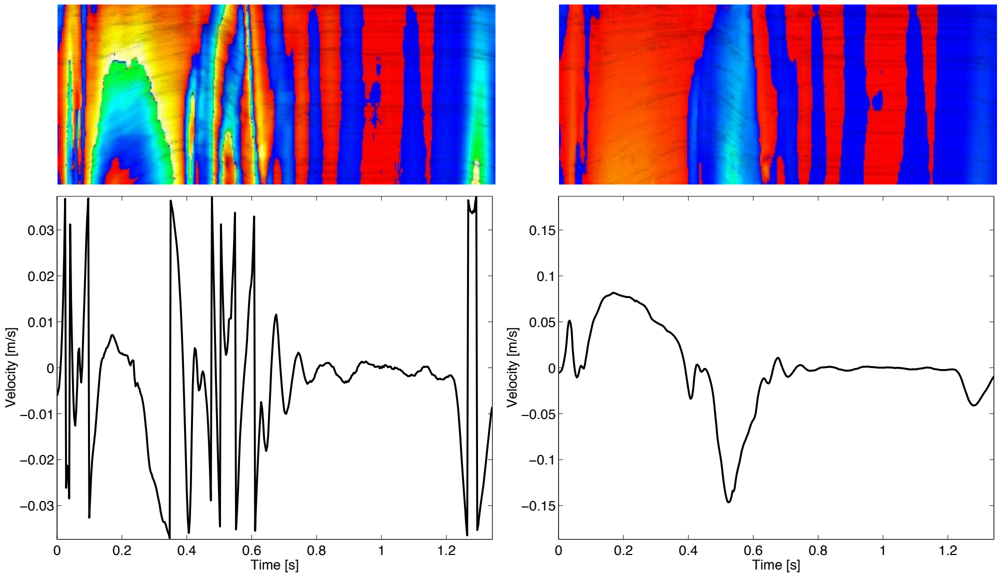

(a) (b)

Figure 8: TDI M-modes and velocity traces before (a) and after aliasing correction (b).

chosen. The spatial resolution of the original velocity estimate is kept, while avoiding the problem of aliasing.

The difference in Doppler shift increases with the distance between f_1 and f_2. Since the thermal noise and estimator variance are independent of the values of f_1 and f_2, best results were obtained when f_1 and f_2 was relatively far from each other. There is thus a trade-off between the increase of the Nyquist velocity and the robustness of the algorithm. We also obtained best results with a relatively small bandwidth B. A small bandwidth results in a minimal overlap between the bands, and the noise in the two bands becomes uncorrelated.

Examples of TDI M-modes and velocity curves before and after aliasing correction are shown in Figure 8. The velocities are estimated from a second harmonic signal centered at $f_0 = 3.3$MHz with frame rate 323frames/second. The sampling frequency after complex demodulation was 2MHz. The subband signals were obtained from the baseband signal using 10th order Hamming weighted rectangular band-pass filters with bandwidth $B = 75$kHz, and center frequencies corresponding to $f_1 = 2.9$MHz and $f_2 =$3.7MHz respectively. Some velocities are aliased twice, but the described algorithm provides a robust correction. The Nyquist velocities for the fundamental signal, the second harmonic signal, and when the correction algorithm is used on the second harmonic signal are shown in Table 2. Using the correction algorithm, the second harmonic signal can be used for TDI without aliasing artifacts. This is important when TDI and SRI are calculated from the same data, since Figure 6 shows an improvement

	v_{Nyq}
Fundamental, $f_0 = 1.67$MHz	7.5cm/s
Second harmonic, $f_0 = 3.33$MHz	3.7cm/s
Sec. harm. with correction algo. $f_1 = 2.9$MHz and $f_2 = 3.7$MHz	15.5cm/s

Table 2: Nyquist velocities.

in the quality of SRI when the second harmonic signal is used. The algorithm also corrects for the increase in aliasing artifacts when a wider sector, and thus a larger time T between pulse transmissions, is used.

7 Calculating Doppler Spectra From the 2D Data

The acquisition scheme provides a continuous stream of samples with constant sampling intervals as illustrated in Figure 5, and Doppler spectra can therefore be calculated from the 2D data. Compared to mean velocity curves, Doppler spectra visualize all the different velocities within the sample volume. Reverberations corrupt mean velocity estimates, but can be visually differentiated from true tissue velocities in a Doppler spectrum. The temporal resolution is poorer for Doppler spectra than for mean velocity curves since a larger number of temporal samples are needed to calculate a spectrum than to calculate a mean velocity value.

Because of the low pulse repetition frequency, conventional Doppler spectra suffer from aliasing, but it is possible to extract the correct velocity by stacking several spectra on top of each other. A technique called *Velocity-matched spectrum analysis*, which suppresses aliasing artifacts, is described in [7]. The idea is to use several range samples, and track the movement of the scatterers for each velocity component in the spectrum. Examples of conventional and velocity-matched spectra are shown in Figure 9. Both techniques give good results, with slightly narrower spectra for the velocity-matched technique. The correct velocity waveform stands out more clearly in the velocity-matched technique, since the aliased spectra are smeared out compared to the correct spectrum.

8 Making Sound from Tissue Velocity and Strain Rate Data

In addition to calculating Doppler spectra, a sound signal can also be generated from the continuous stream of data. Doppler sound has been used for a long time in blood flow measurements, and gives a direct sensation of the blood flow velocity. This also applies to tissue velocities and strain rates. Below is a brief description of the signal processing necessary to generate a sound signal letting the clinician use his ears in addition to his eyes when measuring tissue velocities and strain rates.

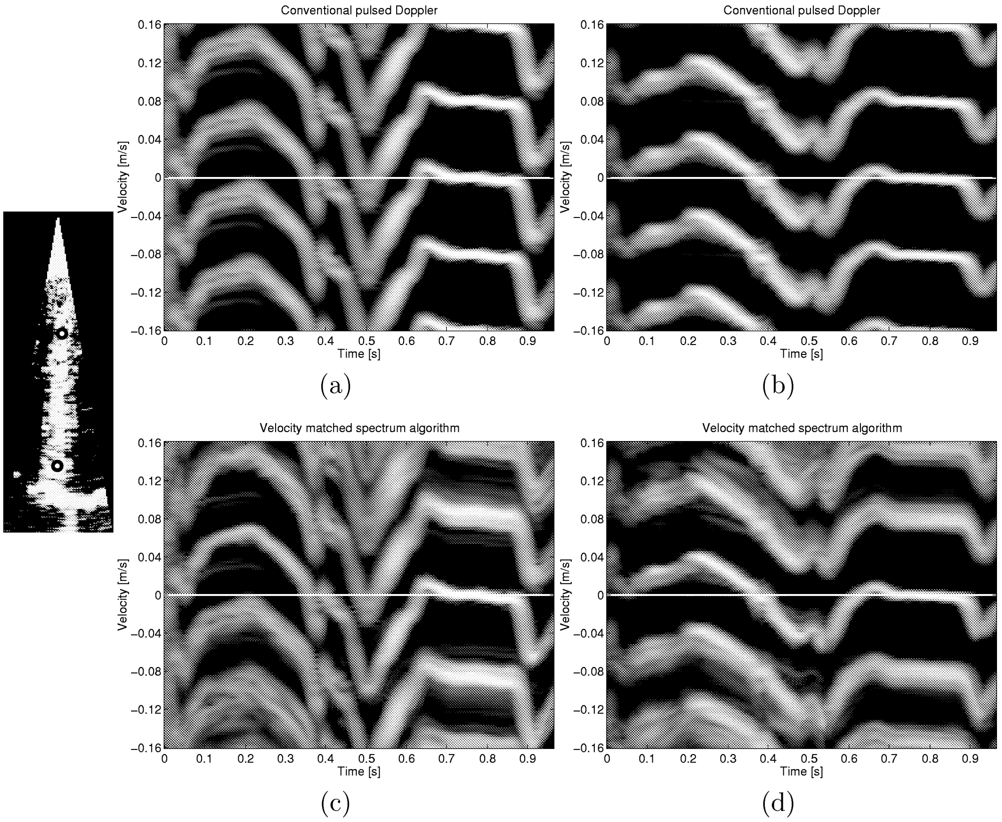

Figure 9: Tissue Doppler spectra. (a) and (b): Conventional algorithm. (c) and (d): Velocity-matched algorithm. Spectra (a) and (c) are from the basal part of the septum, while spectra (b) and (d) are from the apical part as illustrated in the image to the left.

Tissue Doppler Sound

Let $y(k,l) = \hat{R}_{k,l}(1)$, and let $z(k,l)$ be the corresponding "aliasing corrected $\hat{R}_{k,l}(1)$" given by

$$z(k,l) = |\hat{R}_{k,l}(1)|e^{j(\arg(\hat{R}_{k,l}(1))+2n\pi)/(2N_{\max}+1)\pi} \tag{11}$$

where n is chosen as described in relation to Equation 10. A phasor spinning around with frequency proportional to the mean velocity estimate is given by

$$s_{\hat{R}(1)}(k,l) = |z(k,l)|e^{j\cdot\sum_{m=-\infty}^{l}\arg(z(k,l))} \tag{12}$$

and a sound signal can be generated based on $s_{\hat{R}(1)}(k,l)$. Another option is to generate the sound directly from the complex base band signal $x(k,l)$. An aliasing corrected version of $x(k,l)$ can be calculated by

$$s_x(k,l) = x(k,l)\cdot e^{-j\arg(y(k,l))}\cdot e^{j\arg(z(k,l))} \tag{13}$$

where the signal is mixed down with the aliased mean frequency and mixed up again with the aliasing corrected mean frequency. The velocity spread around the mean velocity is kept, and sound based on s_x is less "synthetic" than sound based on $s_{\hat{R}(1)}$. The rest of the processing is the same regardless of the choice between $s_{\hat{R}(1)}$ and s_x, and the notation s will be used for both signal types.

The temporal sampling frequency of $s(k,l)$ is equal to the frame rate, and the signal needs to be interpolated to a higher sampling frequency, i.e. 8kHz. A typical blood velocity of 1m/s gives a Doppler shift of 3.90kHz for an ultrasound frequency of 3MHz, while a typical tissue velocity of 0.1m/s only gives a Doppler shift of 390Hz. A relative change in frequency $\Delta f/f$ is easy to detect for the human ear when f is large, and the Doppler signal from blood flow does not need any manipulation of the frequency. Changes in the tissue Doppler frequency are, however, difficult to detect without increasing the frequency. Following this interpolation, the instantaneous frequency is thus increased by a factor N_f

$$s_{N_f}(k,l) = |s(k,l)|e^{jN_f\cdot\arg(s(k,l))} \tag{14}$$

where the constant N_f is chosen to increase the maximum frequency up to, but not exceeding, half the new sampling frequency.

Velocities towards the probe give positive Doppler shifts, while velocities away from the probe give negative Doppler shifts. This directional information can be obtained from the complex base band signal by splitting the signal in one part containing the positive frequencies, and one part containing the negative frequencies. These two signal components can then be fed to the two channels in a stereo sound system. The splitting of the signal is obtained by

$$s_{\text{left}}(k,l) = \mathcal{H}\{Re(s(k,l))\} + Im(s(k,l)) \tag{15}$$

$$s_{\text{right}}(k,l) = \mathcal{H}\{Im(s(k,l))\} + Re(s(k,l)) \tag{16}$$

where $\mathcal{H}\{\cdot\}$ denotes the Hilbert transform in the temporal direction, and Re and Im denote the real and imaginary part, respectively.

Strain Rate Sound

We assume here that aliasing does not occur for the strain rate estimates. Referring to Equation 5, let $u(k,l) = \sum_{m=0}^{K-1} \hat{R}^*_{k+m,l}(1)\hat{R}_{k+m+\Delta k,l}(1)$. A phasor spinning around with frequency proportional to the strain rate is then given by

$$s_{\hat{SR}}(k,l) = \sqrt{|u(k,l)|}e^{j\cdot\sum_{m=-\infty}^{k} \arg(u(k,m))} \tag{17}$$

Since $u(k,l)$ is the product of two correlation estimates, the square root is applied to get a dynamic range of the sound signal that is proportional to the amplitude of the signal $x(k,l)$. It is also possible to generate a strain rate sound signal directly from the complex base band signal $x(k,l)$ by calculating

$$s_{x_{SR}}(k,l) = \frac{x^*(k,l)x(k+\Delta k,l)}{\sqrt{|x^*(k,l)x(k+\Delta k,l)|}} \tag{18}$$

The further processing is equal to that described above for the velocity sound signal, giving contraction and expansion signals in the two stereo channels.

9 Clinical Applications

The new acquisition scheme provides data that are ideally suited for investigating the relaxation and contraction patterns of the myocardium. The advantage of the improved temporal resolution is illustrated in Figure 10 where an SRI M-mode with 323frames/second is decimated to 65 and 25frames/second. We see that, for instance, the precise position of the start of the relaxation can only be found with the highest frame rate. A clinical study using this acquisition technique to study the spatial-temporal patterns of the deformation events in the ventricle during the heart cycle is presented in [6].

In stress-echo examinations, there is limited time available for data acquisition, and the clinician concentrates on getting B-mode tissue images of high quality. Using the acquisition technique described in this paper, the clinician can optimize the tissue B-mode images when the data are recorded, and later obtain additional information, since both TDI/SRI, Doppler spectra, and Doppler sound can be calculated from the same data.

Because of both the high temporal and spatial resolution, we believe that this imaging modality also can be a valuable tool when investigating the electrical conduction system in the heart.

10 Conclusions

A new acquisition scheme has been presented which provides TDI and SRI images with a higher temporal resolution ($>$ 300frames/second) than has previously been available. The TDI/SRI images are calculated from the same data as the tissue B-mode images and has the same spatial resolution. The technique is limited to a small image sector,

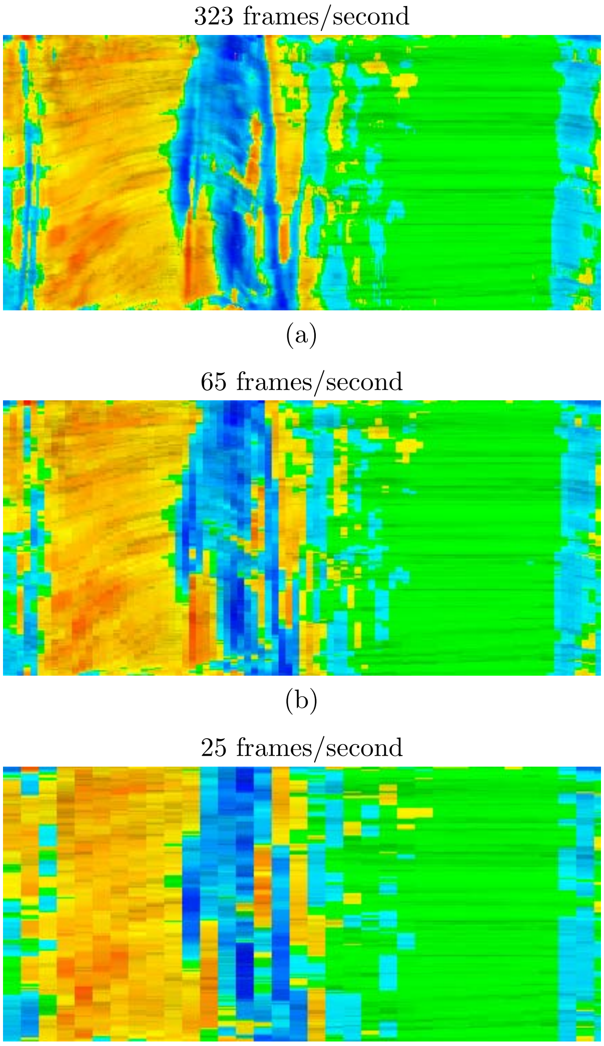

323 frames/second

(a)

65 frames/second

(b)

25 frames/second

(c)

Figure 10: (a) SRI M-mode with 323 frames/second. (b) The M-mode in (a) decimated to 65 frames/second. (c) The M-mode in (a) decimated to 25 frames/second corresponding to video frame rate.

but is ideally suited for studying the timing of the relaxations and contractions in the rapidly moving myocardium.

The SRI quality was found to be significantly improved when second harmonic imaging was used. The pulse repetition frequency is equal to the frame rate, and is relatively low. This results in aliasing artifacts in TDI, especially when second harmonic imaging is used. A method has been presented to correct for this aliasing, and for a typical signal, the Nyquist limit was increased from 3.7cm/s to 15.5cm/s. The algorithm was demonstrated to work robustly even for velocities that were aliased several times.

The new acquisition technique provides a continuous stream of samples with constant sampling intervals. Doppler spectra can thus be calculated from the 2D data, and visualizes the velocity spread instead of just the mean velocity available from velocity traces based on TDI. This is an advantage when reverberations are present, because reverberations corrupt mean velocity estimates, but in a Doppler spectrum they can visually be differentiated from true tissue velocities. A method to generate tissue Doppler and strain rate sound signals at arbitrary points in the 2D image has also been presented. However, the clinical benefit of such sound signals has not yet been proven.

11 Acknowledgements

This study was supported by the Research Council of Norway. We thank Nancy Lea Eik-Nes for revision of the paper.

References

1. K. Ferrara and G. DeAngelis. Color flow mapping. *Ultrasound Med. Biol.*, 23(3): 321–345, 1997.

2. A. Heimdal, A. Støylen, H. Torp, and T. Skjærpe. Real-time strain rate imaging of the left ventricle by ultrasound. *J. Am. Soc. Echocardiogr.*, 11(11):1013–1019, Nov. 1998.

3. C. Kasai, K. Namekawa, A. Koyano, and R. Omoto. Real-time two-dimensional blood flow imaging using an autocorrelation technique. *IEEE Trans. Sonics Ultrason.*, 32(3):458–464, May 1985.

4. W. N. McDicken, G. R. Sutherland, C. M. Moran, and L. N. Gordon. Colour Doppler velocity imaging of the myocardium. *Ultrasound Med. Biol.*, 18:651–654, 1992.

5. H. J. Nitzpon, J. C. Rajaonah, C. B. Burckhardt, B. Dousse, and J. J. Meister. A new pulsed wave Doppler ultrasound system to measure blood velocities beyond the Nyquist limit. *IEEE Trans. Ultrason., Ferroelect., Freq. Contr.*, 42(2):265–279, Mar. 1995.

6. S. A. Slørdahl, S. Bjærum, B. H. Amundsen, A. Støylen, A. Heimdal, S. I. Rabben, and H. Torp. High frame rate strain rate imaging of the ventricular septum in healthy subjects. Submitted to *European Journal of Ultrasound*, 2000.

7. H. Torp and K. Kristoffersen. Velocity matched spectrum analysis: A new method for suppressing velocity ambiguity in pulsed-wave Doppler. *Ultrasound Med. Biol.*, 21(7):937–944, 1995.

Paper J

High Frame Rate Strain Rate Imaging of the Ventricular Septum in Healthy Subjects

Stig A. Slørdahl, Steinar Bjærum, Brage H. Amundsen,
Asbjørn Støylen[†], Andreas Heimdal, Stein Inge Rabben and Hans Torp
Department of Physiology and Biomedical Engineering,
Norwegian University of Science and Technology, Trondheim, Norway
[†]Department of Cardiology, University Hospital of Trondheim
Norwegian University of Science and Technology, Trondheim, Norway

Abstract

The regional function of the left ventricle can be visualized in real-time using the strain rate imaging method. Deformation or strain of a tissue segment occurs over time during the heart cycle. The rate of this deformation (the strain rate) is equivalent to the velocity gradient, and can be estimated using a tissue Doppler technique. In the present study in nine healthy subjects, we have assessed the feasibility of a new strain rate imaging method with a very high frame rate of around 300 frames per second (FPS). Digital radio-frequency (RF) data were acquired for a sector angle of 20°-30° using a high-end ultrasound scanner. The RF data were analyzed using a dedicated software package that displays strain rate images and profiles and calculates quantitative values. Since the ventricular septum is of crucial importance for the left and right ventricular function, we assessed changes in strain rate through the heart cycle of the ventricular septum with the new method. Mean peak systolic strain rate in the healthy subjects was $-1.65 \pm 0.13\mathrm{s}^{-1}$. Mean peak diastolic strain rate during early filling was $3.14 \pm 0.50\mathrm{s}^{-1}$ and mean peak diastolic strain rate during atrial systole was $0.99 \pm 0.09\mathrm{s}^{-1}$. With the new method, we were able to study events and spatial-temporal differences in the heart cycle with duration down to 3.5-3ms, including the pre-ejection period and the isovolumic relaxation period. We found individual differences in the strain rate patterns, but in all subjects, the ventricular contraction started simultaneously in all parts of the septum. After the ejection period, the elongation started before aortic valve closure, in the midinferior septum and propagated towards the apex. In conclusion, high frame rate strain rate imaging makes it possible to study rapid deformation patterns in the heart.

Submitted to *European Journal of Ultrasound*

1 Introduction

The regional function of the left ventricle can be visualized in real-time using the strain rate imaging method [8]. Deformation or strain of a tissue segment changes with time during the heart cycle. The rate of this deformation (the strain rate) is equivalent to the velocity gradient, and can be estimated using tissue Doppler data. Strain rate imaging is a new ultrasound method for evaluating regional function and agrees fairly well with standard echocardiography in grading regional wall function [14] as well as with reference to coronary angiography [15]. Strain rate imaging provides both quantitative measurements of local deformation rates, and semi-quantitative information about the regional function.

With magnetic resonance imaging it is possible to measure wall deformation in three dimensions [2], but the current frame rates of 20 FPS are too low to resolve myocardial mechanical events and peak velocities. An advantage of strain rate imaging is the high frame rate. With a decreased spatial resolution 130 FPS is possible when acquiring tissue Doppler images of the whole left ventricle. Ultrasound tissue Doppler techniques can thus be used to reveal the complex spatial-temporal patterns of the deformation events in the ventricle during the heart cycle.

The longitudinal motion of the heart shows a descent of the base towards the apex during systole, with a reverse movement during the two main phases of diastole; i.e. early filling and atrial systole, while the apex remains almost stationary throughout the heart cycle [10]. Although longitudinally directed fibers comprise only a small portion of the myocardial mass, several studies have shown that the systolic displacement of the atrioventricular plane towards the apex is an important component of the pump function of the left ventricle [1, 13].

Strain rate imaging is best for studying longitudinal deformation of the left ventricle. This makes the method suitable for studying the time-course of mechanical events in the heart, as they generally progresses along the length of the ventricle. The ventricular septum regulates ventricular stroke volumes to maintain proper balance between systemic and pulmonic circulation [11]. The ventricular septum is therefore of crucial importance for both the left and right ventricular function. Endocardial mapping in humans in sinus rhythm with normal left ventricles has also shown that one out of two endocardial breakthroughs of the ventricular activation sequence is on the midinferior septum [6]. This means that the septum is of particular interest when the timing of events is studied.

In order to study the complex patterns of events in the left ventricle during the heart cycle, the frame rate should be as high as possible. We have developed a new strain rate imaging method with frame rates around 300 FPS and spatial resolution equal to a tissue B-mode image of high quality. The aim of the current study was to evaluate the feasibility of this imaging technique to study timing and fast changes in regional function through both the systolic and diastolic phases of the heart cycle. Since the new method depends on a narrow image sector, we chose to study changes in strain rate in the ventricular septum, as this wall is the most readily accessible, as well as the most interesting from a physiological point of view.

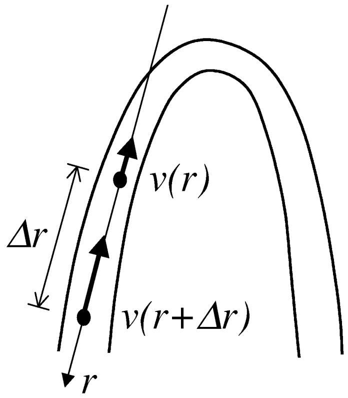

Figure 1: Illustration of the velocities used in the strain rate estimate in Equation 1.

2 Materials and Methods

Strain Rate Imaging

The strain rate (SR) is equivalent to the spatial gradient of the velocity. The strain rate is estimated from the velocity, v, at two points along the ultrasound beam, as described in Equation 1:

$$\mathrm{SR} \approx \frac{v(r) - v(r+\Delta r)}{\Delta r} \tag{1}$$

where r is the distance along the beam, and Δr is the small offset between the two points illustrated in Figure 1. In this study, the offset distance was 6mm. Negative strain rate corresponds to a shortening of the tissue segment, whereas positive strain rate corresponds to an elongation. The strain rate is visualized using a color scheme where red corresponds to negative and blue corresponds to positive strain rate values.

Data Acquisition and Signal Processing

To achieve frame rates above 300 FPS, a System Five scanner (GE Vingmed Ultrasound, Horten, Norway) with customized software was used. Digital radio-frequency (RF) data were acquired for off-line processing. The digital data were stored as complex base band signals where the in-phase and quadrature signal samples were represented as 16 bit integers. These data were transferred from the scanner and processed on a standard personal computer using MATLAB (The MathWorks, Inc., Natick, Massachusetts, USA) software.

A new acquisition technique was used, where the strain rate images were calculated from the same RF-data as the tissue B-mode images. With this technique, the pulse repetition frequency (PRF) becomes equal to the B-mode frame rate. Two-dimensional images of the ventricular septum were obtained from a four-chamber apical view and the image sector was placed with the septum in the center giving a small angle between

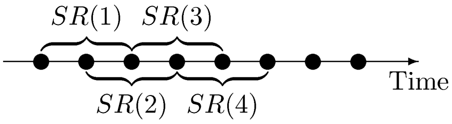

Figure 2: Sliding window estimation of strain rate from data with constant sampling intervals.

the septum and the ultrasound beam. An image sector of 20°- 30° was sufficient to cover the whole width of the septum, and frame rates above 300 FPS were obtained. Strain rate estimation involves calculation of a difference between two velocity estimates. An estimator described by Heimdal [7] ensures that aliasing of the strain rate estimates is avoided as long as the difference between the two velocities is below the Nyquist limit. Since the velocity difference is small for small offset distances, no severe aliasing artifacts in the strain rate images were experienced with frame rates exceeding 300 FPS.

Without separate pulse transmissions to acquire the strain rate and B-mode data, and by using second harmonic data acquisition, the reverberation noise was reduced compared to conventional strain rate data acquisition. Within the narrow image sector, we thus obtained high quality strain rate estimates with spatial resolution equal to the tissue B-mode image.

From the continuous stream of data with constant sampling intervals, the strain rate estimates were calculated using a sliding window technique as illustrated in Figure 2. A continuous stream of data is very convenient for temporal processing, and also makes it possible to calculate Doppler spectra and sound signals at arbitrary points within the image sector.

After signal processing in MATLAB, the data were written to files on the GE Vingmed EchoPac format, and analysed using a protoype software package from GE Vingmed (Horten, Norway).

Study subjects

Nine healthy and physically active male volunteers (mean body surface area 1.96m^2) without any evidence of cardiac disorders were studied. All volunteers were in normal sinus rhythm and gave informed consent to participate in the study. Standard phonocardiogram was used to determine the aortic valve closure and standard two-dimensional echocardiography was used to visualize and detect mitral valve opening since the anterior mitral valve leaflet was seen in the strain rate images.

3 Results

In all the healthy subjects we were able to acquire strain rate images of the ventricular septum with a higher temporal resolution than previously published. In all the subjects, the isovolumic contraction with shortening of the ventricular septum started almost simultaneously at all levels from base to apex, followed by a slight, equally simultaneous recoil (Figure 3). Similarly, the shortening during ejection started almost simultaneously. The elongation of the septum started in the midinferior septum, and even before the isovolumic relaxation as shown by the phonocardiogram in Figure 4. The two main phases of diastole; i.e. early filling and atrial systole, were clearly demonstrated in all subjects. However, the deformation patterns were not similar in the subjects. In diastasis (the slow filling phase) the strain rate was almost zero. Mean peak systolic strain rate in the healthy subjects was $-1.65 \pm 0.13\mathrm{s}^{-1}$. Mean peak diastolic strain rate during early filling was $3.14 \pm 0.50\mathrm{s}^{-1}$ and mean peak diastolic strain rate during atrial systole was $0.99 \pm 0.09\mathrm{s}^{-1}$. In Figure 5 we have compared a high temporal resolution (high frame rate) strain rate imaging M-mode with M-modes of lower frame rates. The M-mode was calculated from data acquired with a frame rate of 323 FPS (a) and these data were then decimated down to frame rates of 65 FPS (b) and 25 FPS (c).

4 Discussion

This study shows the feasibility of studying rapid deformation patterns in the heart with a new strain rate imaging method with very high frame rates. The method has a superior temporal resolution as illustrated in Figure 5. The frame rate of 25 FPS corresponds to the frame rate of data recorded on video tape. The precise spatial position of the start of the elongation of the septum can only be found with the highest frame rate. A smoother display of the M-modes in Figure 5b and c can be achieved by temporal and spatial interpolation. However, Figure 5 illustrates the temporal information contained in the raw data for different frame rates.

It is a fundamental problem with the currently available strain rate methods in ultrasound that only one out of possibly nine strain components can be measured at one time. However, the clinical relevance of the method is promising [14–16] and with frame rates above 300 FPS the potential for quantification of the regional myocardial function is even greater than with the currently available methods. The spatial resolution with this method is equal to the B-mode resolution and is superior to conventional strain rate imaging.

This study shows the feasibility of high frame rate strain rate imaging, with a possibility of studying events and temporal-spatial inequalities of down to 3ms duration. It is important to realize that strain rate imaging shows only deformation. Shortening may either be contraction or elastic recoil after stretching. In systole, the isovolumic contraction started almost simultaneously judged by a shortening followed by a short simultaneous elongation which we believe is a recoil before the ejection phase. As the ventricle shortens during the isovolumic contraction period, this is in accordance with the ventricle assuming a more spherical shape. The shape and geometry of the ventricle, arrangement of the fiber bundles in the wall and the nonuniform stress distribution at rest are all major determinants of the ventricular contraction-relaxation pattern. These structural features result in nonuniform configurational changes during systole, when the left ventricle changes shape [3]. In addition, the mechanical performance of the

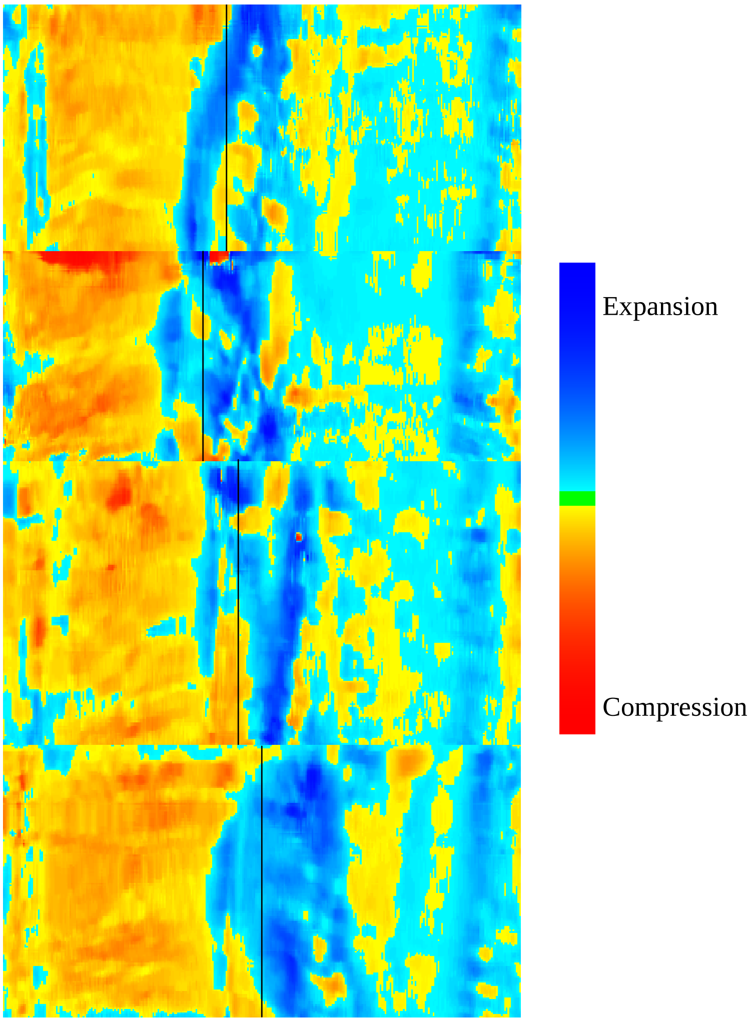

Figure 3: Strain rate imaging M-mode of the ventricular septum for one heart cycle in four healthy subjects from the apical part at the top of each image to the basal part at the bottom. Start is at the R-wave of the QRS complex and the vertical line marks the mitral valve opening determined from the 2-dimensional image. To the right is the colour scale where cyan to blue corresponds to positive strain rate values and orange to blue corresponds to negative strain rate values.

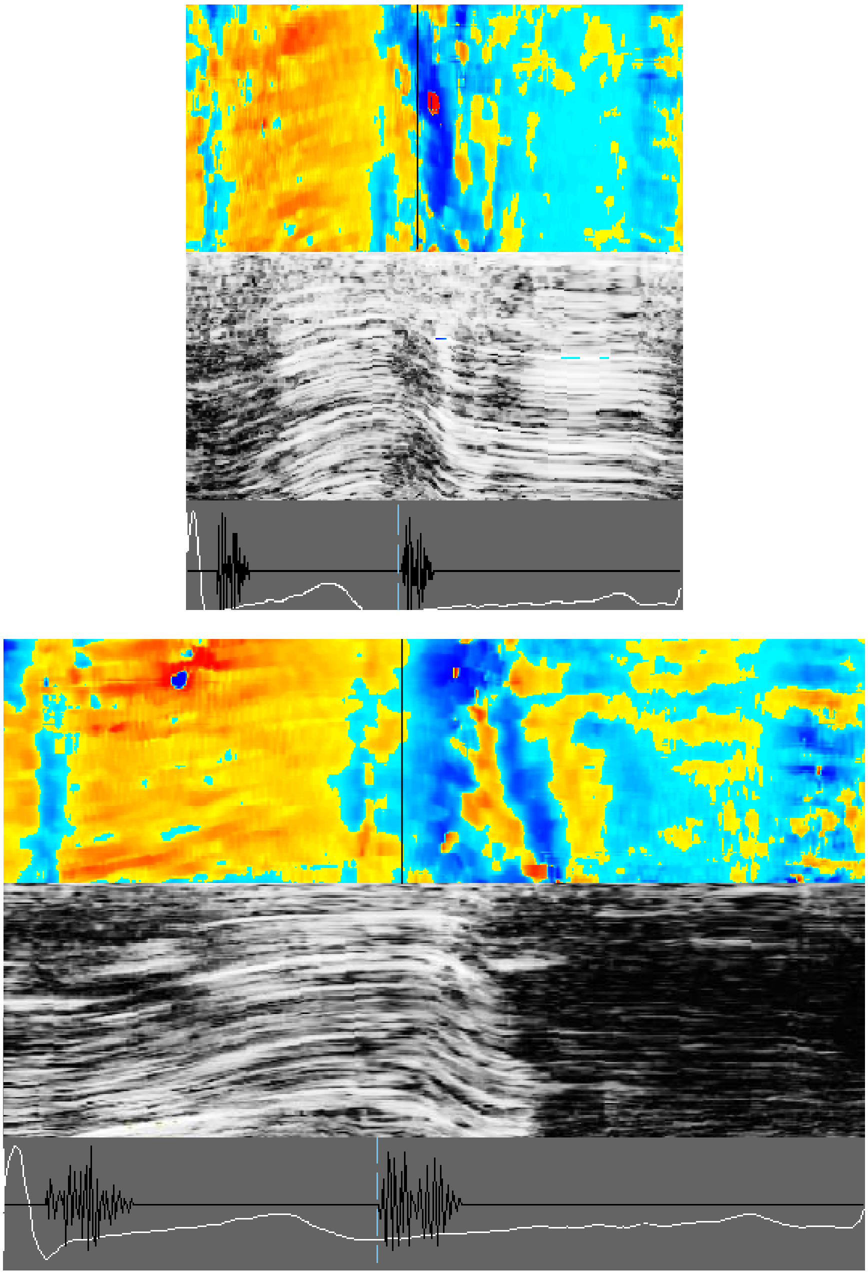

Figure 4: Strain rate imaging M-mode of the ventricular septum for one heart cycle in two healthy subjects in a similar way as in Figure 3, but with tissue priority in the middle and standard phonocardiogram in the bottom image.

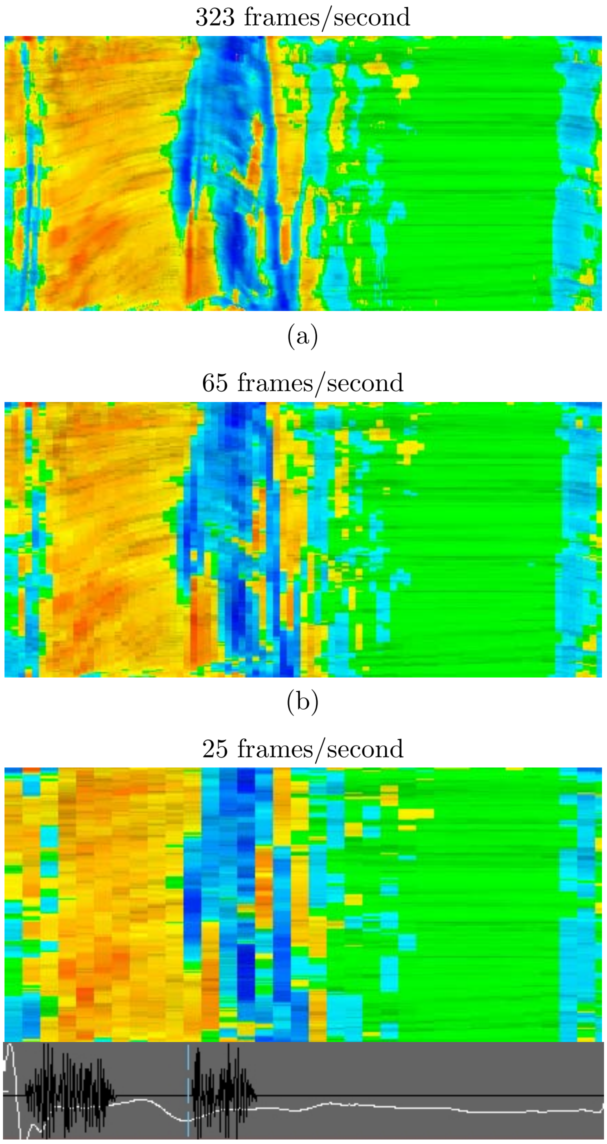

(a)

(b)

(c)

Figure 5: (a) A strain rate imaging M-mode calculated from data with a frame rate of 323 FPS. (b) A strain rate imaging M-mode from the data in (a), but decimated down to 65 FPS. (c) A strain rate imaging M-mode from the data in (a), but decimated down to 25 FPS. No interpolation is performed in the visualization of the M-modes. Green colour in these strain rate imaging M-modes corresponds to strain rates values around zero (see the colour scheme in Figure 3)

myocardium in different layers of the ventricular wall is not uniform. The nonuniform changes in the septum are not so easily seen with the strain rate imaging method in the beginning of systole. Earlier studies have shown that the nonuniformity is more pronounced at higher loading conditions, being most marked during relaxation [9].

The exact onset of diastole is controversial and varies according to the definitions described by Wiggers [18] which includes isovolumic relaxation time in systole, Brutsaert et al. [4, 5] which includes rapid filling phase in systole according to the triple control of relaxation, or using a clinical definition. Using the clinical definition, diastole is divided into two phases with an isovolumic relaxation period from aortic valve closure to mitral valve opening and an auxotonic period from mitral valve opening to mitral valve closure. These phases are demonstrated in Figure 4 and this study shows that elongation starts even before the isovolumic relaxation period. In the auxotonic period this method demonstrates clearly the three events with rapid filling phase, slow filling phase (diastasis) and the atrial filling phase. The slow filling phase is earlier described to account for only 5% of the total filling [12]. In the slow filling phase the peak strain rate fluctuated around zero and this indicates hardly any changes in length in this phase of diastole.

The new strain rate imaging method with very high frame rates show individual differences in the healthy subjects with regards to the contraction-relaxation patterns. A possible explanation is the nonuniform configuration of the myocardium and that we can only measure one of the strain components. In healthy subjects no fundamental differences in the myocardial structure or performance is expected. Strain rates in the directions transverse to the ultrasound beam as well as shear strain rates are not currently accessible in simultaneous recordings, but we still believe that strain rate imaging can be an important tool in physiologic research.

Mean peak systolic strain rate and mean peak diastolic strain rate of the rapid filling phase were somewhat higher than earlier published values obtained with lower frame rates [15, 17]. The reason can be that it is easier to get peak strain rates with this new method if there are peaks of very short duration. It may also be that the lower noise level leads to recognition of peak strain rate that has previously been classified as noise. However, in this study, the center of the sector is oriented along the septum, while the previous studies utilised standard apical planes with the sector center in mid-chamber. This may account for a larger angle and hence, lower measured values. High frame rate strain rate imaging therefore seems to have the potential of providing additional physiological information compared to standard strain rate imaging and of course compared to standard echocardiography. Its main advantages seem to be the high time resolution with respect to the location of the start and the propagation of events in the myocardium. This may be especially promising in the field of arrythmias and conduction abnormalities. With around 3 ms between the strain rate images, one should be able to track the mechanical events following the depolarization wave.

A limitation of this method is the sector angle of 20°-30°. This was sufficient to cover the ventricular septum from an apical view, but makes it impossible to study more than one wall of the left ventricle at a time. Increasing the sector width reduces either the spatial resolution or the frame rate.

References

1. M. Alam, C. Hoglund, and C. Thorstrand. Longitudinal systolic shortening of the left ventricle: An echocardiographic study in subjects with and without preserved global function. *Clin. Physiol.*, 12(4):443–452, July 1992.

2. R. Beyar, E. P. Shapiro, W. L. Graves, W. J. Rogers, W. H. Guier, G. A. Carey, R. L. Soulen, E. A. Zerhouni, M. L. Weisfeldt, and J. L. Weiss. Quantification and validation of left-ventricular wall thickening by a three-dimensional volume element magnetic resonance imaging approach. *Circulation*, 81(1):297–307, Jan. 1990.

3. D. L. Brutsaert. Nonuniformity: A physiologic modulator of contraction and relaxation of the normal heart. *J. Am. Coll. Cardiol.*, 9(2):341–348, Feb. 1987.

4. D. L. Brutsaert, F. Rademakers, and S. U. Sys. Triple control of relaxation: implication in cardiac disease. *Circulation*, 69:190–196, 1984.

5. D. L. Brutsaert and S. U. Sys. Relaxation and diastole of the heart. *Physiol. Rev.*, 69(4):1228–1315, Oct. 1989.

6. D. M. Cassidy, J. A. Vassallo, F. E. Marchlinski, W. J. Untereker, and M. E. Josephson. Endocardial mapping in humans in sinus rhytm with normal left ventricles: activation patterns and characteristics of electrograms. *Circulation*, 70:37–42, 1984.

7. A. Heimdal. *Doppler based ultrasound imaging methods for noninvasive assessment of tissue viability.* PhD thesis, Norwegian University of Science and Technology, 1999.

8. A. Heimdal, A. Støylen, H. Torp, and T. Skjærpe. Real-time strain rate imaging of the left ventricle by ultrasound. *J. Am. Soc. Echocardiogr.*, 11(11):1013–1019, Nov. 1998.

9. P. R. Housmans, L. H. S. Chuck, V. A. Claes, and D. L. Brutsaert. Non-uniformity of contraction and relaxation of mammalien cardiac muscle. In G. H. Pollack and H. Sugi, editors, *Contractile mechanisms in muscle*, pages 837–840. Plenum Press, New York, 1984.

10. C. J. Jones, L. Raposo, and D. G. Gibson. Functional importance of the long axis dynamics of the human left ventricle. *Br. Heart J.*, 63(4):215–220, Apr. 1990.

11. S. Lundback. Cardiac pumping and function of the ventricular septum. *Acta Physiol. Scand. Suppl.*, 550:1–101, 1986.

12. L. H. Opie. *The heart: physiology, from cell to circulation.* Lippincott-Raven, Philadelphia, third edition, 1998.

13. J. S. Simonson and N. B. Schiller. Descent of the base of the left ventricle: an echocardiographic index of left ventricular function. *J. Am. Soc. Echocardiogr.*, 2 (1):25–35, Jan. 1989.

14. A. Stoylen, A. Heimdal, K. Bjornstad, H. G. Torp, and T. Skjaerpe. Strain rate imaging by ultrasound in the diagnosis of regional dysfunction of the left ventricle. *Echocardiography*, 16(4):321–329, 1999.

15. A. Stoylen, A. Heimdal, K. Bjornstad, R. Wiseth, H. Vik-Mo, H. Torp, B. Angelsen, and T. Skjaerpe. Strain rate imaging by ultrasound in the diagnosis of coronary artery disease. Accepted for publication in *J. Am. Soc. Echocardiogr.*, 2000.

16. A. Stoylen, S. Slordahl, G. K. Skjelvan, A. Heimdal, and T. Skjaerpe. Strain rate imaging in normal and reduced diastolic function: Comparison with pulsed Doppler tissue imaging of the mitral annulus. Accepted for publication in *J. Am. Soc. Echocardiogr.*, 2000.

17. J. U. Voigt, M. F. Arnold, M. Karlsson, L. Hübbert, T. Kukulski, L. Hatle, and G. R. Sutherland. Assessment of regional longitudinal myocardial strain rate derived from Doppler myocardial imaging indexes in normal and infarcted myocardium. *J. Am. Soc. Echocardiogr.*, 13(6):588–598, June 2000.

18. C. J. Wiggers. Studies on the consecutive phases of the cardiac cycle. *Am. J. Physiol.*, 563:415–459, 1921.